Technische Universität München
TUM School of Life Sciences

TUM

Tailoring cellulose nanocrystals' size distribution and suspension stability for efficient isolation and utilization in advanced materials

Christoph Metzger

This page intentionally left blank.

Acknowledgements

Abstract

Cellulose nanocrystals (CNCs) are nanorods, which are derived from bio-based resources. They are considered sustainable high-performance building blocks for multiple applications in advanced materials; and they receive increasing attention based on their remarkable properties in academia and industry. For example, CNCs have great potential as reinforcing filler in polymer nanocomposites, if they are well-dispersed. Furthermore, they are constituted as important materials platform in biomedical devices, electronics and sensors, and emulsions and foams. CNCs are commonly isolated from biomass by sulfuric acid-catalyzed hydrolysis, yielding highly crystalline and electrostatically stabilized nanoparticles in colloidal suspension. Current challenges, which limit their use, originate from their propensity for lateral agglomeration, susceptibility to cluster formation in high ionic strength environments, intrinsically broad particle size distribution, and complex characterization, among others. Thus, the objectives of this thesis were to explore agglomeration behavior of CNCs in the presence of secondary sulfates, as well as effects of ultrasonication on particle size distribution and colloidal stability of CNCs. Furthermore, salt containing CNCs were applied to polymeric materials to improve their barrier properties and mechanical properties.

In the first part of this thesis, agglomeration and individualization of CNCs were investigated. It was found that electrostatic charge screening, cluster formation, and matching affinities control CNC agglomeration in the presence of sulfates. Critical salt concentrations—at CNC agglomeration and peptization—were identified for four different sulfates, and, subsequently, used for process design, based on neutralization of reactant solutions. This was an effort to accelerate product separation at low reactant consumption for overall efficient CNC production. Furthermore, particle size distribution and stability of CNCs were modified by applying ultrasound treatment to purified CNC suspensions. It was found that increasing ultrasound energy input facilitates CNC cluster dispersion. Simultaneously, long-term stability increased with increasing ultrasound energy input. In the same study, multi-detector asymmetrical flow field-flow fractionation (AF4) was used to determine CNC properties in their native never-dried state.

In the second part of this thesis, CNCs from neutralization-based isolation were applied onto hydrophobic polymer films and incorporated into hydrophilic nanocomposites to determine effects of residual salt on processing and performance. In both use cases, advanced materials based on salt containing CNCs showed improved performance, compared to CNC-free materials, and thereby proved good spreadability and dispersibility.

The work overall presented in this thesis yields new insight into CNC processing and properties at different stages of production and application. For example, studying ultrasonication in combination with multi-detector AF4 provides expanded knowledge on a critical and, so far, deficiently investigated unit operation during CNC isolation. Furthermore, successful application of salt containing CNCs in polymeric materials provides foundation for future process development, from which a variety of advanced materials can be produced; and it is proof of concept toward process development of low-cost and efficient CNC production.

Kurzzusammenfassung

Cellulose-Nanokristalle (CNCs) sind stäbchenförmige Nanopartikeln, die aus nachwachsenden Rohstoffen isoliert werden. Sie haben ein vielseitiges physikalisch-chemisches Eigenschaftsprofil und werden als nachhaltige, leistungsfähige Bausteine für eine Vielzahl von Anwendungen in neuen Materialien betrachtet. Aufgrund ihrer hohen mechanischen Festigkeit besitzen CNCs beispielsweise großes Potential als verstärkender Füllstoff in Polymer-Nanokompositen—vorausgesetzt, sie sind in der Matrix gut dispergierbar. Gegenwärtige Herausforderungen, die den Einsatz von CNCs einschränken, ergeben sich aus ihrer Anfälligkeit zur Clusterbildung in Umgebungen mit hoher Ionenstärke. Intrinsisch breite Partikelgrößenverteilungen (PGV) und Schwierigkeiten bei deren Charakterisierung stellen weitere Einschränkungen dar. In diesem Kontext richten sich die Forschungsziele dieser Arbeit auf das Agglomerationsverhalten von CNCs in Anwesenheit von Sulfaten. Des Weiteren wurde der Effekt von Ultraschallbehandlung auf die PGV und Suspensionsstabilität untersucht. Außerdem wurden salzhaltige CNCs in polymeren Materialien verarbeitet mit dem Ziel, deren Barriere- und mechanischen Eigenschaften zu verbessern.

Im ersten Teil der Arbeit wurde das Agglomerationsverhalten von CNCs untersucht. Es zeigte sich, dass Sulfate durch elektrostatische Ladungsabschirmung und Prinzipien der chemischen Verwandtschaft von Sulfatgruppen und Gegenionen Clusterbildung initiieren. Kritische Salzkonzentrationen, bei denen Agglomeration oder Peptisierung eintrat, wurden ermittelt, um einen effizienten Isolationsprozess zu entwerfen. Dieser basiert auf Neutralisierung der Reaktionslösung, um das Produkt mit geringem Zeit- und Ressourcenaufwand abzutrennen. In einer weiteren Studie wurde Ultraschall eingesetzt, um PGV und Suspensionsstabilität zu manipulieren. Es wurde festgestellt, dass ein höherer Energieeintrag die Dispersion von CNC-Clustern erleichtert. Zudem nahm die Langzeitstabilität der Suspensionen zu. Zur Untersuchung der Agglomeration von CNCs in ihrem nativen, suspendierten Zustand wurde asymmetrische Fluss-Feld-Fluss-Fraktionierung (AF4) mit optischen Detektoren gekoppelt.

Im zweiten Teil der Arbeit wurden CNCs isoliert und mittels Neutralisation abgetrennt. Anschließend wurden die Partikeln auf hydrophobe Polymerfilme aufgetragen und in hydrophile Nanokomposite eingearbeitet. Besonderes Augenmerk lag auf dem Einfluss des Restsalzgehalts auf die Prozessierbarkeit und die Anwendungseigenschaften. In beiden Fällen zeigte sich, dass die Leistungsfähigkeit der CNC-haltigen Materialien im Vergleich zu CNC-freien Pendants verbessert wurde. Dies wurde auf gute Prozessierbarkeit und Dispergierbarkeit der Suspensionen zurückgeführt.

Die vorgestellten Arbeiten liefern neue Einblicke in die Herstellung, Verarbeitung und Eigenschaften von CNCs. Dazu wurden verschiedene Prozessschritte untersucht und praktische Anwendungen in neuen Materialien demonstriert. Beispielsweise wurde der Einfluss der Ultraschallbehandlung zur Individualisierung von CNCs untersucht. Obwohl homogene und reproduzierbare Produkteigenschaften maßgeblich durch diesen Prozessschritt bestimmt werden, wurde ihm in der Literatur bisher nur wenig Beachtung geschenkt. Die erfolgreiche Leistungssteigerung von polymeren Materialien durch Zugabe von salzhaltigen CNCs bietet außerdem eine nachhaltige Basis zur Entwicklung einer Vielzahl neuer Materialien mit geringem ökologischem Fußabdruck.

Contents

1. Introduction and objectives

1.1. Scientific framework

Cellulose nanocrystals (CNCs) are bio-based nanorods with diameters ranging from 3 to 50 nm and high aspect ratio (*1*). CNCs have unique or enhanced properties, similar to other advanced materials (AdMs); and they are superior to conventional materials or provide unusual properties to a product. CNCs can be utilized as sustainable building blocks to improve performance of numerous materials. Potential fields of application are polymer nanocomposites, gas barrier films, electronics and sensors, biomedical devices, emulsions, foams, and rheology modifiers, among many more (*2, 3*).

CNCs' impact on performance of AdMs highly depends on the way CNCs are produced. Conceptualizing such a process, from a chemical-engineering perspective, requires comprehension of mutual relation of process, structure, properties, and performance of a material (*4–6*) (Figure 1): Nowadays, a *process* for manufacturing AdMs not only has economic constraints. Furthermore, rising awareness of environmental aspects demands environmentally friendly, sustainable, safe, and healthy process design, yielding recyclable products and byproducts at low consumption of raw materials. Tailoring material *structure* and *properties* on the nano- and mesoscale requires careful process design and control over multiple length and time scales: operating conditions and design parameters of the process are applied at the macroscale; however, structural changes, which determine product properties, occur at the micro-, meso- and nanoscale. In addition, transport phenomena may affect conversion kinetics over multiple time scales. Required *performance* of AdMs, as structural or functional building blocks in actual engineering applications, determine their properties and, therefore, the whole process chain reciprocally.
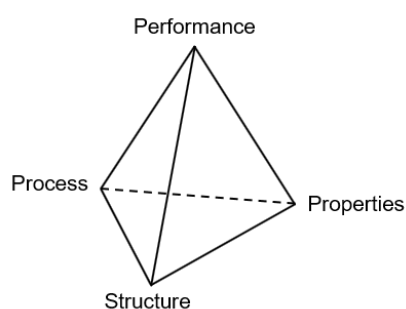
Figure 1: Graphical representation of interrelationship of process, structure, properties, and performance in materials science and engineering (*5*).

This dissertation investigates process conditions during CNC production for better comprehension of the process-structure and the structure-property relationship. In this context, it aims at an economically feasible process design, which provides well-dispersed CNCs at high yield. Furthermore, effects of CNCs in gas barrier films and polymer nanocomposites were demonstrated to emphasize their beneficial effect on advanced materials' performance.

1.2. Overview

Throughout the 20th century, global use of materials has increased eightfold to almost $60 \cdot 10^9$ tons per annum, driven by rapid population and economic growth (*7*). Today, more than 70% of total materials consumption is satisfied by nonrenewable materials (*8*). Raising concerns about consumption of nonrenewable petroleum-based materials and accruing nondegradable plastic wastes trigger political, scientific, and industrial action on a global scale; toward an increasing use of renewable materials and sustainable processes for development of AdMs. Consequently, environmentally compatible bio- and nanomaterials, and eco-friendly processes have been identified to play substantial roles in at least three of the 17 Sustainable Development Goals of the United Nations (*9*). Among these goals, more efficient use of Earth's resources and improvement of quality of life until 2030 involves industry, innovation, and infrastructure (goal 9); sustainable cities and communities (goal 11); and responsible consumption and production (goal 12). Similarly, the European Union has set goals for a knowledge-based bio-economy, in which sustainable materials and processes play an integral role (*10, 11*).
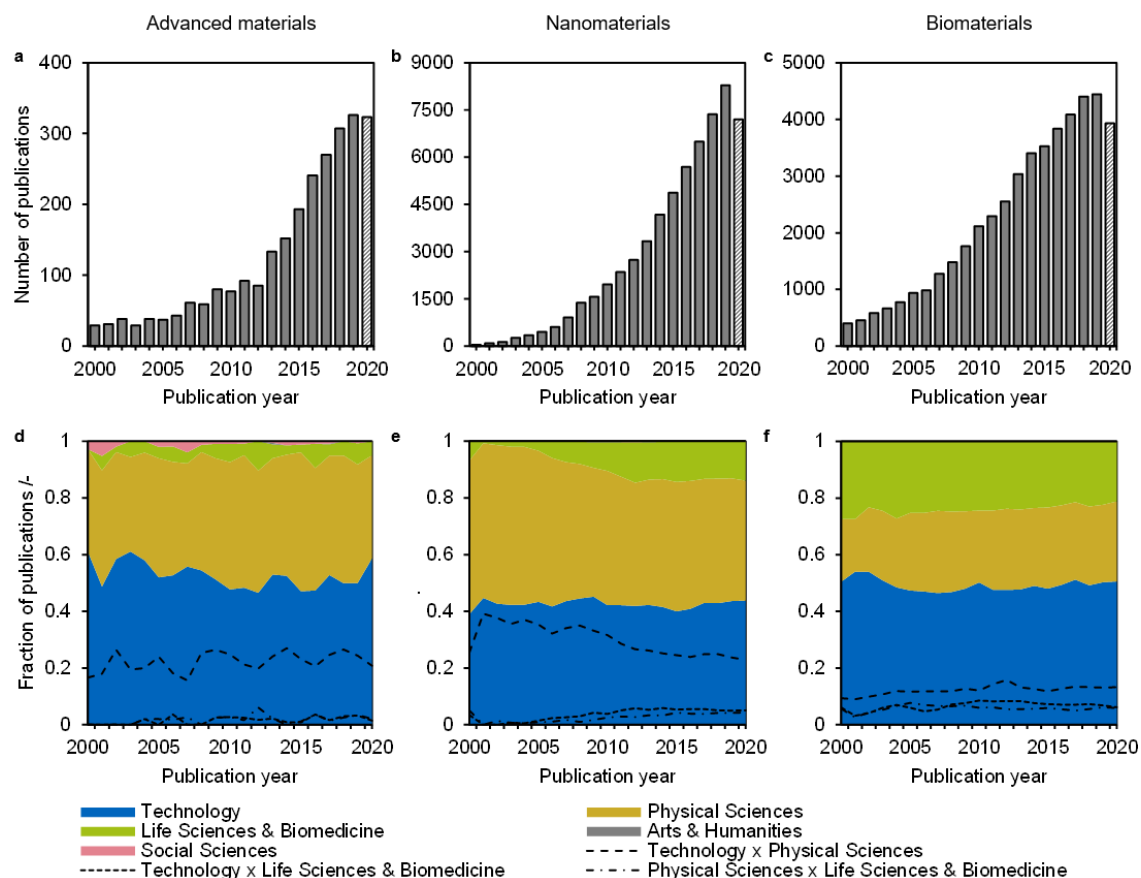
Figure 2: Bibliometric analysis of peer-reviewed original research articles. From left to right: advanced materials, nanomaterials, and biomaterials. The evolution of annual publication number is shown at the top. Publication distribution across different subject categories and their proportion associated with more than one category is shown at the bottom. All data was retrieved from the Web of Science Core Collection (WoS-CC) (*12*) on 15 August 2021. Subject categories were derived from research areas on the journal level, according to Clarivate Analytics (*13*). Data processing is outlined in section 9.1.

In accordance with these political goals, interdisciplinary scientific interest on AdMs and, particularly, on nanomaterials and sustainable biomaterials, has gained momentum over the past 20 years. Figure 2 (a-c) display the evolution of the annual number of peer-reviewed original research articles, involving each of these material classes. Steady increase of annual publication number emphasizes their increasing scientific relevance.[a] Figure 2 (d-f) illustrates the annualized publication distribution across different scientific subject categories. Research on each material class was mainly driven by engineering and technological studies, as well as the physical sciences. It comes as no surprise that the fields of life sciences and biomedicine play an important role in research on biomaterials. Ongoing endeavors to utilize nanomaterials in consumer products and, in particular, medical applications, is reflected in the increasing publication number in the fields of life sciences and biomedicine, which addressed development of manufactured nanomaterials (MNMs), as well as their impact on human health and environment. Interdisciplinary research on each material class was mainly found between technology and physical sciences.

Contributions of MNMs toward sustainable development and economic benefits have mainly been associated with their prospective performance (*14*). However, for comprehensive assessment of MNMs in terms of sustainability, it is necessary to reveal their cumulative environmental impact of their full life cycle (*15, 16*). Life-cycle assessment (LCA) methodology is defined in ISO 14044 (*17–19*); it comprises goal definition, inventory analysis, impact assessment, and respective interpretation. Thus, all stages of MNMs—from initial extraction of raw materials through to end-of-life disposal of the final product—need to be considered. In the context of an LCA, it has been shown that cellulose has great potential as starting material for development of sustainable processes and MNMs with low environmental impact (*20*).

Many of cellulose's inherent material functions, which it has in its native surroundings, are desired in high-value material applications: it is produced by plants and animals as structural components, membranes, and protective barriers around cells. Furthermore, it functions as energy storage and contributes to metabolic bioprocesses (*21*). Therefore, cellulose is traditionally actively used in many technological fields, such as paper products, fibers, consumables, building materials, pharmaceuticals, and in biofuel conversion. Cellulose is also utilized as precursor for chemically modified synthetic fibers, for example nitrocellulose and rayon, in various industrial and textile applications. Abundance of cellulose makes it an almost inexhaustible raw material. It has been estimated that every year 10^{11}–10^{12} t of biomass are produced by photosynthesis (*22, 23*). 40% of produced biomass were the polysaccharides cellulose (33%) and starch (7%) (*24*). However, only about 3% of these was used in non-food applications (*25*).

---

[a] Bibliometric indicators are explained in Appendix 9.1. It is assumed that the actual publication number on each material class is higher, and there is a significant overlap between them. However, infometric analyses unveiled a qualitative lack of comprehensive keyword indexing and keyword normalization. This may not be the indexing database operator's fault, but rather caused by transferring errors from the journals' databases to the indexing database, and authors' limited use of appropriate keywords.
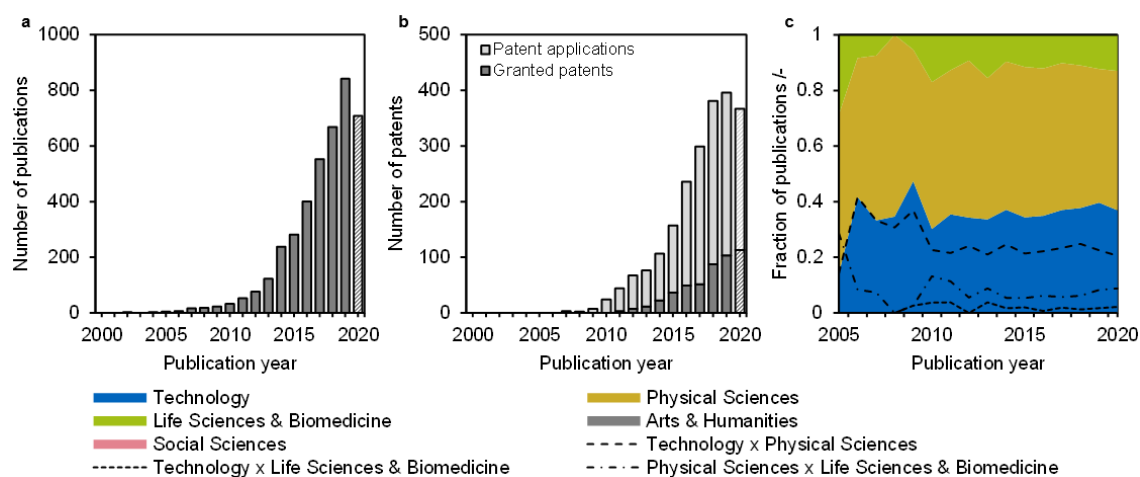
Figure 3: Bibliometric analysis of (a) peer-reviewed original articles on CNCs and (b) granted patents and applications on CNCs. All data in (a) was retrieved from the WoS-CC (*12*) on 15 August 2021. Data shown in (b) was retrieved from The Lens (*26*) on 15 August 2021. (c) Research areas of peer-reviewed original research articles on the journal-level were extracted for data, which was retrieved from the WoS-CC and peer-reviewed original research articles cited in patents.

Over the past decade, scientific interest emerged on cellulose nanomaterials (CNMs) and, in particular, cellulose nanocrystals (CNCs). CNCs feature high strength, low density, high absorbency, and self-assembly properties in colloids and thin films. Their physical and chemical properties make them attractive building blocks in high-performance applications as reinforcing filler in nanocomposites, stabilizer in emulsions and gels; and in mesoporous photonic films, electronic materials, and prospective biomedical and pharmaceutical use cases (*27*). Figure 3 (a) illustrates evolution of the annual number of original research articles on CNCs. Research dominantly referred to CNC isolation methods from biomass and utilization of new cellulose sources, chemical derivatization techniques, application of CNCs in nanocomposites, and characterization techniques. This research has mainly been performed in the fields of polymer science, chemistry, and materials science; within the physical sciences and technological research (Figure 3 (c)).

Abundancy of feedstock, auspicious performance in advanced materials, and potentially low environmental impact are favorable premises for industrial endeavors toward CNC commercialization. Demand for adoption of CNCs can be derived from efforts of pioneering companies to protect intellectual property. Only 25 entities filed 25% of all patents involving CNCs, and the next 25% of patents were submitted by 96 other entities. Evolution of the annual patent application number and granted patents involving CNCs is illustrated in Figure 3 (b). Over the past five years, patent-to-publication ratio (PPR) leveled around ~0.5, and it was greater than 0.75 between 2010 and 2012.[b] Patents, and original research articles cited by patents, predominantly addressed CNC isolation, chemical derivatization, and their application in nanocomposites (*29*). Therefore, focus of scientific research and industrial efforts indicate great extent of harmonization, between academia and industry. While CNCs are considered as ready for products (*30,*

---

[b] PPR represents corporate activity on a specific topic. Low values indicate focus on academic research and development of knowledge, whereas high values indicate industrial attention on application of knowledge (*28*). Exemplarily, polyethylene, as well-established material, had a PPR of 18.9 in 2019. In the same year, advanced nanomaterials, such as graphene, carbon nanotubes, and aerogels, had PPRs of 1.0, 1.8, and 4.3, respectively. Lithium ion technology, instancing advanced platform technologies, had a PPR of 4.9 in 2019.

31), and beneficial market projections have been made (*32, 33*), some challenges remain to bridge the gap between academia and their future commercial implementation (*34*):

Current CNC production processes lack competitive cost effectiveness, are too low in scale, and require transition from batch to continuous design (*30, 31, 35–39*). LCA of CNCs, involving environmental and health impacts, is object of equally prioritized research (*20, 30, 31, 38, 40–44*). Providing CNCs with functional properties by chemical derivatization could expand their compatibility further and, therefore, facilitate implementation in high added-value products (*36, 38*). These goals are accompanied by efforts for regulation and standardization of CNCs (*1, 35, 45–49*), and development of techniques for their complex characterization (*42, 44, 45, 48*). These challenges were overall equally put forth in roadmaps of industrial associations, involved in economic utilization of CNMs and CNCs; namely, the Alliance for Pulp & Paper Technology Innovation (APPTI) (*50*), the Bio-based Industries Joint Undertaking (BBI JU) (*51*), the Nanocellulose Forum (NCF) (*52*), and the Technical Association of the Pulp and Paper Industry (TAPPI) (*53*).

1.3. Thesis objectives

As an emerging bio-based nanomaterial, CNCs have potential use cases as building blocks in numerous applications. However, further development of these applications necessitates deeper understanding of the impact of CNC production process on particles' structure and properties. Moreover, successful commercial adoption of CNCs requires comprehension of the structure-property relationship of CNCs, to tailor performance of advanced materials. Therefore, the overall objective of this thesis was to investigate impacts of unit operations during CNC production—namely neutralization and ultrasonication—on structure and properties of aqueous CNC suspensions. Furthermore, effects of processing on CNC structure and, therefore, suspension properties, as well as performance in advanced materials, was elucidated. The specific goals of this work were as follows:

(I) Develop efficient downstream processing strategy, based on CNC agglomeration behavior. Electrostatically stabilized CNCs in aqueous suspension are susceptible to agglomeration, already at low ionic strength. While particle agglomeration is unwanted in the product, it can be exploited for efficient product separation during downstream processing. This work aimed at understanding CNC agglomeration behavior in the presence of sulfates, and targeted use of particle agglomeration in process design was evaluated.

(II) Thoroughly characterize effects of ultrasonication on CNC suspension properties. Ultrasound is commonly applied to CNC suspensions to individualize nanoparticles and to tailor their properties. Therefore, it is essential to understand the treatment's effect on CNC size distribution and stability in their native suspended state. Herein, colloidal CNCs were characterized by asymmetrical flow field-flow fractionation, regarding short-term and long-term effects of ultrasonication on suspension properties.

(III) Demonstrate CNC performance in advanced materials. Based on the structure-property relationship, CNC performance depends on their state of agglomeration, which is governed by ionic strength, among others. In this work, process design from **goal I** was implemented to produce CNCs, which contain residual salt. Subsequently, polymer films were coated with CNCs and polymer nanocomposites reinforced with CNCs were manufactured. Oxygen barrier performance and mechanical reinforcement effects of CNCs were linked to nanoparticle suspension processability.

1.4.   Thesis outline

This thesis is cumulative and composed of four peer-reviewed papers. Its aim is to contribute toward better comprehension of the interrelationship of process, structure, properties, and performance of CNCs, for their use in advanced materials.

Chapter 2 – Background and literature review. This chapter provides a thorough examination of concepts and literature relevant to structure, properties, and performance of cellulose, CNMs, and CNCs. The complete process chain—from raw material to CNCs, which are implementable in advanced materials, along with characterization techniques—is introduced, based on extensive literature review. Contemporary challenges, related to CNC processing and performance assessment, are presented.

Chapter 3 – Actionable goals and methods. This chapter highlights actionable issues to overcome the limitations of CNCs, which are presented in chapter 2, and it constitutes the comprehensive motivation of the thesis. Furthermore, an overview of applied methods for CNC production and characterization is presented, along with methods for processing and characterization of CNC-based nanocomposites.

Chapter 4 – Results. This chapter contains copies of each peer-reviewed paper, along with brief summaries on respective motivation, hypotheses, and findings. Additional subject-specific knowledge and detailed descriptions of used materials and methods, as well as supporting information, is provided in each paper.

Chapter 5 – Concluding remarks. This chapter discusses and summarizes major contributions of this thesis. Potential future work toward improved understanding of process, structure, properties, and performance of CNCs, along with use in advanced materials, are presented.

2. Background and literature review

2.1. Cellulose

2.1.1. Cellulose structure

Biomass has evolved in plants, animals, and algae with several chemical and structural mechanisms over multiple length scales, to avert microbial or enzymatic degradation (*54*). Concerning cellulose, recalcitrance against chemical and biological hydrolysis is determined by its structure on the molecular level. Native cellulose is a semi-crystalline polycarbohydrate of β-D-glucopyranose monomers, with theoretical density of 1.6 g cm^{-3} (*55*). Cellulose chains are formed by β-1,4-glycosidic linkage between C_1 and C_4 atoms of two consecutive glucose monomers through polycondensation (Figure 4). Since condensation reactions release a water molecule, these monomers are referred to as anhydroglucose units (AGUs). The glycosidic bond undergoes spontaneous hydrolysis at a very low rate, giving it a half-life of 5–8 · 10^6 years under neutral conditions (*56, 57*). Repeated units of cellulose are referred to as AGUs, with the chemical formula $(C_6H_{10}O_5)_n$ (*58*). Furthermore, each cellulose chain has a reducing end group with the chemical formula $C_6H_{10}O_6$, which is a β-D-glucopyranose unit in equilibrium with the aldehyde function. Each chain is terminated by a non-reducing end, with an anomeric C atom and chemical formula $C_6H_{10}O_5$.

Non-reducing end Repeated unit Reducing end
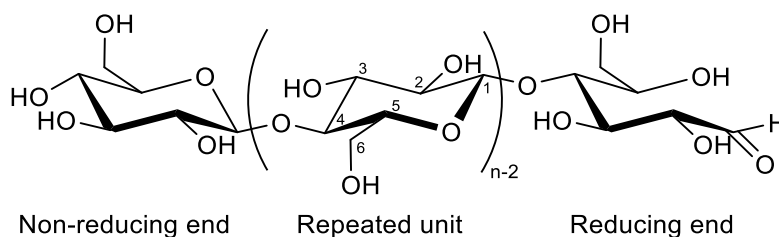
Figure 4: Molecular cellulose structure, with the number of AGUs corresponding to chain length, n; and numbering of the six carbon atoms, where C_1 is part of an aldehyde group.

Intra- and intermolecular forces determine chain configuration and supramolecular structure of elementary fibrils (*59, 60*). Hydrogen bonds of the primary hydroxy functional group at C_6 and both secondary hydroxy functional groups at C_2 and C_3, between AGUs and adjacent chains, form a network, in which only oxygen atoms of glycosidic bonds take no part in (Figure 5). The intramolecular hydrogen bond between the hydroxy group at C_3 and the ring oxygen atom of the consecutive AGU determines relative orientation of both monomers, and contributes to chain rigidity (*61*). AGUs are twisted by 26° to each other (*62*), making cellulose chains cylindrical helixes with two-fold screw axis symmetry (*63–66*). Chain twist propagates structural chirality and chiral interaction of cellulose in supramolecular elementary fibrils (*67, 68*). Another intramolecular hydrogen bond occurs between hydroxy groups at C_2' and C_6. Extended chains and inherently rigid glycosidic bonds favor formation of fibrous cellulose structures (*69*). Spatial ordering within elementary fibrils is established, when van der Waals forces induce two-dimensional sheet formation of parallelly arranged chains (*70, 71*). Chains within each sheet are linked via intermolecular hydrogen bonds between C_3'' and C_6, and short-range order is established (*62, 72*). Crystalline elementary fibrils are then formed by convergence of ordered regions. Cohesion of crystalline cellulose is determined by intermolecular

hydrogen bonds and attractive London dispersion forces (*70, 73–76*). The bond network accounts for absence of cleavage planes and contributes to mechanical strength of crystalline cellulose. Furthermore, surface hydroxy groups are involved in interfacial phenomena, and they determine swelling, wetting, degradation, and thermal properties of cellulose (*77*).
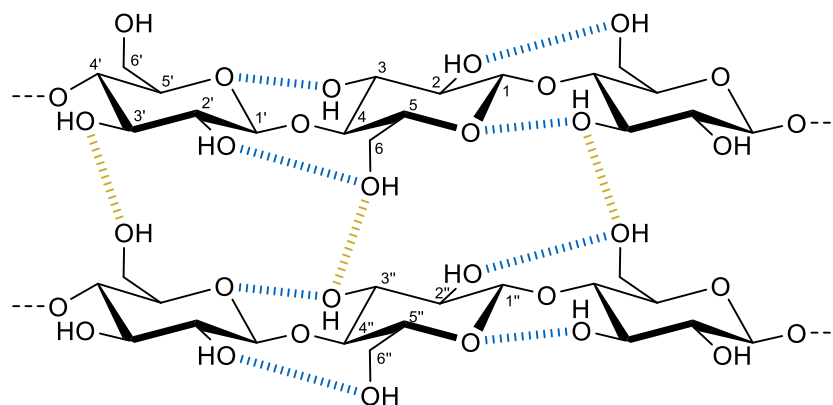
Figure 5: Intra- (=) and intermolecular (=) hydrogen bond network in a cellulose I sheet.

Native cellulose (cellulose I) occurs in two crystalline modifications, I_α and I_β, which coexist in arbitrary segments, and also within the same microfibril (*55, 78, 79*). The I_α-to-I_β ratio depends on cellulose's origin (*80*). While the single-chain triclinic space group (I_α) is the more dominant modification in bacterial cellulose and cellulose from algae, higher plants and tunicates predominantly form the double-chain monoclinic I_β modification of cellulose (*59, 60*). Cellulose I is thermodynamically metastable and can be converted to three other non-native cellulose polymorphs, namely II, III_I, and III_{II} (*81*). A schematic representation of unit cells is shown in Figure 6. Cellulose II is irreversibly formed by mercerization, when cellulose I is treated with sodium hydroxide, or by regeneration of cellulose from solution (*82*). Both processes lead to reorganization of the hydrogen bond pattern inside cellulose crystals. In contrast to cellulose I, polarity of adjacent chains in cellulose II is anti-parallel, with reducing ends present at both ends of the elementary fibril (*83, 84*). Due to chain rearrangement, cellulose II forms a three-dimensional hydrogen bond network (*85*). Celluloses III_I and III_{II} are reversibly formed from celluloses I and II, respectively, through treatment with supercritical ammonia or diamines (*86–88*), and subsequent evaporation of ammonia (*89–92*). In cellulose III modification, hydrogen bonds also occur between crystal sheets (*93*). Heat-treated cellulose III in glycerol has long been considered the cellulose IV polymorph (*94*); however, it has been found that it is only a distorted form of cellulose I_β (*95, 96*). Structural differences between cellulose polymorphs are reflected in their differing physicochemical properties; for example, surface hydration and orientation of cellulose crystals influences enzyme binding. Therefore, enzymatic hydrolysis is accelerated, when cellulose I is converted to celluloses II and III (*97, 98*). Furthermore, configuration of the hydrogen bond network and London dispersion forces determine cellulose accessibility to reactants (*75*). Additionally, cellulose I_β has the highest elastic modulus, among cellulose polymorphs (*99, 100*), which is estimated to be 110–173 GPa in axial direction of ideal crystals (*101*).
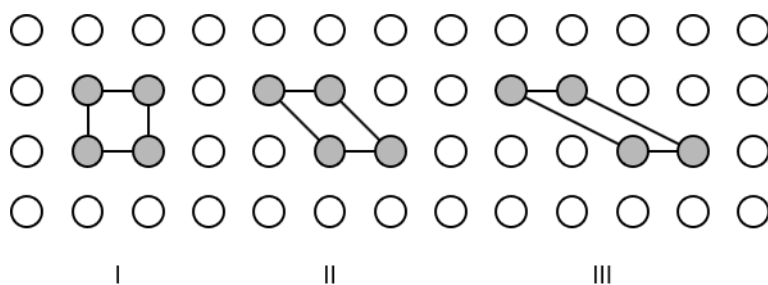
Figure 6: Schematic of primary unit cells of cellulose I, II, and III, according to Elias (*102*).

Hydrogen bonds and hydrophobic interactions not only play a significant role in crystalline cellulose formation, but also in its solubility in polar and nonpolar solvents (*103*). Cellulose is a rather polar molecule, having many hydroxy groups, and it features intrinsically good hydrogen bonding ability (*104*). However, while glucose is highly soluble in polar solvents, cellulose is insoluble in polar and most organic solvents. It has been hypothesized that the hydrogen bond network and hydrophobic intermolecular interactions result in significant amphiphilic or hydrophobic behavior, considering cellulose's different crystal faces (*104*). Increasing solubility by any chemical modification of cellulose, which alters the bond network structure and, thus, affects crystallinity, substantiated this hypothesis (*105*). To date, development of solvents for cellulose has been performed empirically. Nevertheless, there is scientific consensus that amphiphilic systems—such as ionic liquids, and systems with extreme pH levels, which lead to ionization of cellulose—are favorable approaches for efficient cellulose dissolution (*77*).

2.1.2. Cellulose biosynthesis

Cellulose synthesis and its assembly to elementary fibrils and microfibrils has been observed in various biological organisms, such as higher plants, bacteria, algae, and tunicates (Figure 7) (*23, 24, 106, 107*). In nature, cellulose occurs primarily in lignocellulosic materials, with wood as major source (*81*). In wood, cellulose is formed at the extracellular matrix by terminal cellulose synthase complexes (TCs) from glucose, which is previously produced by photosynthesis (*108, 109*). Morphology of elementary fibrils is determined by TC arrangement (*110*), which is characteristic for each organism, and varies from 3 to 15 nm in diameter (*111*). Largest fibrillar diameters have been found in tunicates and algae, with diameters of up to 15 nm. Each elementary fibril is composed of several hundred parallelly arranged cellulose chains (*110, 112*). Single elementary fibrils of higher plants are composed of 18 cellulose chains, which are arranged in diamond-shaped pattern and they have a diameter of 3 nm (*113*). However, average chain number per elementary fibril is usually overestimated due to their tendency for lateral aggregation without crystalline continuity. In most plants, fibrillar aggregation is promoted by lignin and hemicelluloses, which are, aside of cellulose, incorporated into cell walls, to form a microfiber composite (*114*). Lignin is a crosslinked phenolic polymer, which provides stiffness to cell walls. Hemicelluloses are mixtures of mostly branched polysaccharides, which provide an interface to cellulose and lignin (*115, 116*). Aggregated bundles of elementary fibrils in woody plants can have diameters of 10–20 nm (*117*).
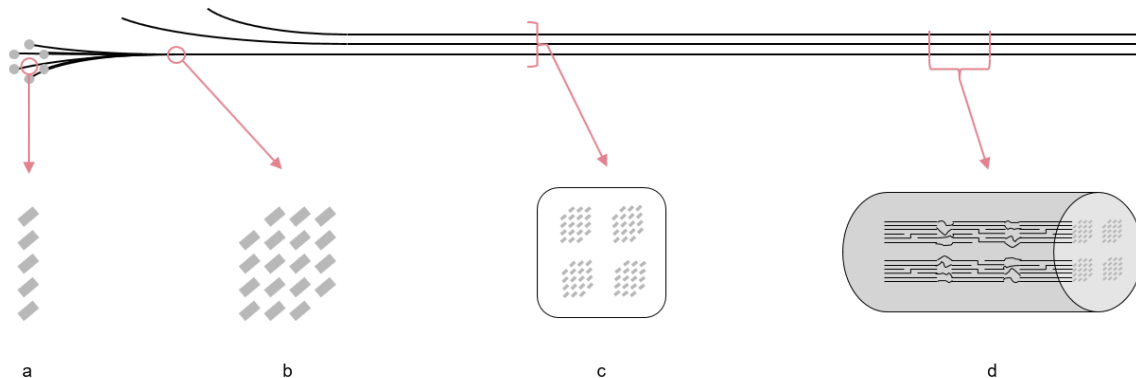
Figure 7: Schematic of cellulose fibril composition in wood, adopted from Moon et al. (*101*). (a) Cellulose sheets form from TCs. Each rectangle represents a cellulose chain, in cross-sectional view. (b) Sheets assemble to elementary fibrils, which are consolidated to microfibrils. These are schematically shown in (c) cross-sectional view and (d) longitudinal view.

Elementary fibril length depends on cellulose source and ranges from 1000–6000 AGUs for cellulose from plants; and they can be as long as 8000 AGUs for bacterial and algal cellulose (*118*). While celluloses in bacterial and algal cell walls show crystalline coherence along elementary fibrils (*119*), celluloses from higher plants have disordered regions, which coexist in each fibril cross-section (*79, 120–122*). It has been hypothesized that surface and intracrystalline hemicelluloses disturb the bond network inside elementary fibrils and, thus, their axial coherence (*117, 123*). Disordered regions either are of amorphous character, or they contain para-crystalline fringed fibrils with varying crystalline dimensions (*124*). Degree of crystallinity of native celluloses varies between 40% and 70% for botanical celluloses; and it can be as high as 80% for bacterial and algal celluloses (*82*). Due to its low solubility in most media, at least the initial phase of chemical cellulose processing often involves heterogeneous reactions. Reaction rate and degree of conversion of such reactions depends on availability of hydroxy groups at AGUs. This accessibility is governed by supramolecular structure, fibrillar arrangement, and cellulose's inner surface availability (*120, 125*).

2.1.3. Cellulose isolation

Comminution of feedstock usually precedes chemical isolation of cellulose from biomass, and it aims at complete or partial removal of matrix materials in multiple sequential or combined steps. Purity and average chain length of resulting fibrils can be controlled by respective process parameters, which also depend on the material's source. Cellulose from wood is mainly isolated by chemical digestion, to remove most of lignin and hemicelluloses, followed by bleaching, to eliminate residual lignin (*23*). By adding an acidic or alkaline pretreatment to remove other residuals, similar process conditions can be applied to isolated cellulose from other plants (*126, 127*). However, disordered regions of cellulose fibrils are also attacked by chemical treatment and, hence, fibrillar length may be reduced by more than 80% (*118*). In contrast, chemical isolation of cellulose from bacterial cellulose, algae, and tunicates has only minor impact on final fibrillar length, due to their almost defect-free structure. In tunicates and algae, wall matrix materials are usually chemically dissolved by acidic or alkaline pretreatments. Then, almost pure cellulose is isolated from tunicates, algae, and bacterial cellulose by single or repeated acidic or alkaline treatments, analogously to bleaching, which is applied similarly to treatment of wood cellulose (*128–133*).

2.1.4. Cellulose derivatives

Traditionally, cellulose from wood and plants is used for papermaking and, in its intact botanical form, as construction material and natural textile fibers (*23*). Today, cellulose converted to energy and biofuels makes up almost half of harvested biomass (*98, 134*). Furthermore, regarding its abundancy and capacity to participate in diverse chemical reactions, cellulose is a beneficial platform for advanced materials development. Specific cellulose properties for advanced materials can be targeted by chemical derivatization. Such reactions may be performed in either homogeneous or heterogeneous phase, or the phases change during processing (*135*). In total, three hydroxy groups per AGU are potentially available for derivatization. However, reactions with the primary hydroxy group are thermodynamically preferred, and limited solubility of supramolecular cellulose structure in common solvents further reduces reactive sites' accessibility (*82*). Utilization of dipolar aprotic solvents, and co-solvents in combination with salts and ionic liquids, could almost completely eliminate effects of the supramolecular structure, to enable homogeneous derivatization (*125, 136, 137*). To date, however, such processes have not been transferred to technical scales, mainly due to economic and ecologic concerns toward involved solvents (*135, 137, 138*). Derivatization of cellulose in heterogeneous reactions has recently gained scientific attention, due to its use for manufacturing of CNMs with the aim to enhance isolation efficiency. Furthermore, CNM functionalization has been applied to change surface hydrophobicity, for improved dispersibility in specific solvents and advanced materials (*139*). A comprehensive list of surface modifications of cellulose is shown in Table A8. Reaction mechanisms involved in CNM functionalization are analogous to cellulose derivatization reactions in homogeneous and heterogeneous processes: they involve either imparting of ionic surface charges, hydrophobization, or polymer grafting (*101, 139, 140*).

2.1.5. Cellulose nanomaterials

Nowadays, cellulose's hierarchical structure is exploited in numerous applications, which span from molecular scale to macroscale. Molecular cellulose derivatives, such as cellulose acetate, microscale cellulose fibers for paper and packaging, and macroscale cellulose particles from wood are broadly used in engineering applications for industrial and consumer products (*141*). CNMs, and AdMs based on them, are anticipated to fill the gap that remains on the nano- and mesoscale, between molecular cellulose and individual cellulose fibers. CNMs' structure-property relationship, particularly based on intrinsic chemical and physical properties, in combination with their nanoscale dimensions, makes them high-performance building blocks for development of sustainable AdMs. Due to numerous combinations of cellulose source, manufacturing methods, and derivatization techniques, CNM classification based on the structure-property relationship is the most reasonable approach. In this regard, a published standard exists to define CNMs (*1*), which is derived from ISO/TS 80004-1 (*142*). A hierarchical summary of the standard is shown in Figure 8.
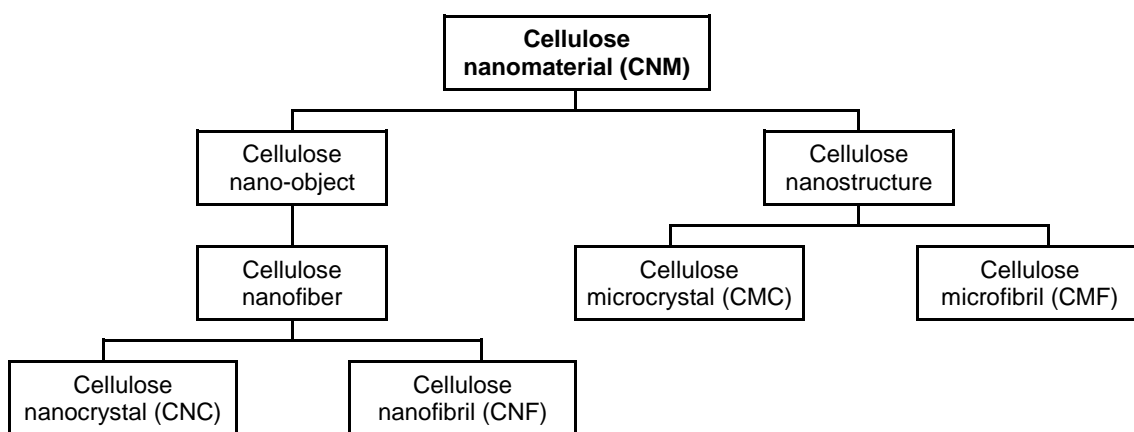
Figure 8: CNM classification based on structure; nomenclature and abbreviations according to ISO/TS 20477 (*1*).

CNMs are isolated from cellulose fibers by chemical or mechanical treatment, or by a combination of both, and can be sub-divided into nano-objects and nanostructures (Table 1). Discrete cellulose nano-objects, namely nanocrystals and nanofibrils, with at least one external nanoscale dimension, are produced under severe chemical or mechanical conditions (*143*). Cellulose nanocrystals are commonly isolated by heterogeneous acid-catalyzed hydrolysis at high acid concentrations, yielding individual nanoparticles, which are composed of at least one single elementary fibril. Acid hydrolysis rate in disordered regions is higher, compared to crystalline regions. Therefore, nanoparticles with high crystallinity result from such a process (*144, 145*). Cellulose nanofibrils (CNFs) are isolated by mechanical delamination with or without chemical pretreatment, yielding particles, which are composed of one or more elementary fibrils and form stretched aggregates. Chemical pretreatment can be applied to achieve more efficient isolation, and to alter particle properties (*146*). Cellulose nanostructures, namely microcrystals and microfibrils, are produced under milder chemical or mechanical conditions, compared to cellulose nano-objects. Hence, they are composed of inter-related parts, of which at least one part has nano-object features.

Table 1: Comparison of CNM composition and structure on multiple levels, according to ISO/TS 20477 (*1*).

	CNC	CNF	CMC	CMF
Number of elementary fibrils	≥ 1	≥ 1	Multiple	Multiple
Standard manufacturing method	Chemical	Mechanical + chemical	Chemical	Mechanical
Particle structure				
Longitudinal splits	No	Yes	Yes	Yes
Particle entanglement	No	Yes	Yes	Yes
Network-like structures	No	Yes	Yes	Yes
Phase composition				
Crystalline	Yes	Yes	Yes	Yes
Para-crystalline	Yes	Yes	Yes	Yes
Amorphous	No	Yes	No	Yes

Cellulose microcrystals (CMCs) are agglomerates of multiple elementary fibrils. They are isolated through heterogeneous acid-catalyzed hydrolysis with dilute mineral acids. Cellulose microfibrils (CMFs) are produced by mechanical refinement of cellulose, yielding multiple aggregates of elementary fibrils. It has been reported that both chemical and mechanical processing of CNMs can be enhanced, or partially replaced, by enzymatic treatment (*35, 147*).

Based on processing conditions, CNMs have different degrees of splitting, entanglement, and network formation. Dimensional placement of CNMs is shown in Figure 9. Intrinsic fibrous cellulose structure facilitates top-down production of nano-objects and nanostructures with high aspect ratio (*143*). Both CNCs and CNFs have minimum cross-sectional diameters, d, of 3 nm, corresponding to a single elementary fibril. Maximum cross-sectional diameter is 50 nm for CNCs, and 100 nm for CNFs. While CNCs have aspect ratios between 5 and 50, CNFs' length-to-diameter ratio is ≥ 10. The multifibrillar character of cellulose nanostructures is reflected in CMFs' cross-sectional diameter of 20–100 nm, and microscale particle dimensions for CMCs. CMFs have aspect ratios between 25 and 100, whereas CMCs are spherical, or rod-shaped agglomerates of elementary fibrils with aspect ratios ≤ 20.
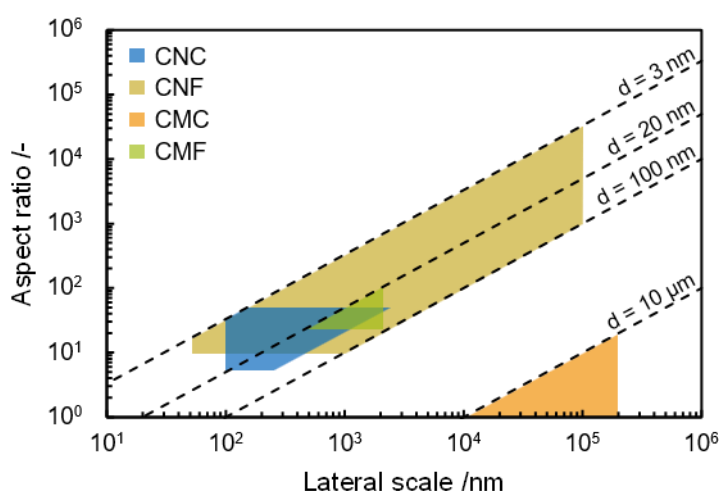
Figure 9: Comparison of CNMs' lateral scale versus their aspect ratio, derived from ISO/TS 20477 (*1*).

In conclusion, CNM properties result from intrinsic cellulose properties, which include low weight, high strength, thermal stability, thermal conductivity, optical transparency, nontoxicity, and biodegradability. Furthermore, helical structure of crystalline cellulose induces chirality and enables spontaneous particle self-assembly in liquid crystalline suspensions and in solid state. High surface area and active surface facilitate effective derivatization of CNMs. In combination with high surface area, high aspect ratio and dimensional stability of CNMs induce low oxygen permeability and particular rheological behavior (*148*). Therefore, potential high-volume industrial applications of CNMs are envisaged as reinforcing filler in nanocomposites, gas barrier in packaging, and rheology modifier in food applications. Potential low-volume applications include utilization of CNMs in medicine, cosmetics, and pharmaceuticals in implants, and as carrier in drug delivery. Based on their electrical and photonic properties, applications of CNMs in electronics, photovoltaics, and photonic films are conceivable.

Comprehensive reviews have summarized properties and potential applications of CNMs (*139, 2, 3, 149–154*) and, in particular, CNCs (*39, 42, 155–158*). Structure-related properties of CNMs are summarized in Table 2. Due to high crystallinity, high individualization, and high surface area, these properties are most pronounced in CNCs. In contrast, structure of other CNMs mitigate some properties in whole or in part (*27*).

Table 2: Properties of cellulose nanomaterials, adapted from Hamad (*27*). Only CNCs have the full set of properties, while structure of other CNMs (Table 1) mitigates some properties.

Dimensional properties	Mechanical properties	Physical-chemical properties
− High aspect ratio	− High stress resistance	− Active surface
− High surface area	− High elastic modulus	− Self-assembly
		− Chirality
		− Photonic properties
		− Electromagnetic properties
		− Piezoelectric properties

2.2. Cellulose nanocrystals

2.2.1. General considerations of CNC production

Product properties of particulate materials, including cellulose nanocrystals, depend on their chemical composition and dispersity (*159, 160*). Since CNCs can be isolated from numerous natural and, thereby, differently structured cellulose sources, process parameters need to be adjusted to the processed material's composition. It has been agreed that CNC performance in advanced materials can be mainly evaluated in terms of PSD, crystallinity, and surface charge (*39*). In this regard, processes for production of rod-shaped CNCs aim at particles with diameters of 3 to 50 nm, and aspect ratio of 5 to 50 (section 2.1.5). CNCs' crystallinity index is higher, compared to the cellulose source material, and their colloidal stability, induced by their surface charge, enables uniform dispersions for targetable performance.

The following sections, 2.2.2 to 2.2.6, address CNC production and processing. CNC production involves cellulose isolation from source material during upstream processing (section 2.2.2). Thereby, the goal is complete removal of other biomass from cellulose, while fibrillar length is preferably unaffected. CNCs are subsequently isolated by chemical treatment of purified cellulose. This is mainly done by acid-catalyzed heterogeneous hydrolysis with H_2SO_4 (*144, 145, 161–164*). Furthermore, CNCs have been isolated by oxidative degradation (*165*), biological degradation (*166*) and hydrolytic decomposition with other dilute and concentrated acids (*167–169*). An overview on alternative pathways for CNC isolation, which find attention in academic research and industry, can be viewed in Table A9 and Table A10, respectively. Further discussion in this work focuses on CNC isolation through hydrolysis of cellulose with H_2SO_4, as it is the method of choice in this work, and it is the most used production route in academia and industry to date (section 2.2.3). CNC isolation is followed by a series of chemical and mechanical unit operations, to separate product from reactant solution during downstream processing (section 2.2.4). Improved process design for CNC production requires knowledge on the structure-property and the process-structure function. This has been reported for unit operations during upstream processing (*170*), CNC isolation

(*171–181*), and downstream processing (*171, 173*) (section 2.2.5). Post-processing procedures aim at CNC drying and subsequent redispersion, and their compatibilization with different media and matrices (section 2.2.6).

2.2.2. Upstream processing of CNC production

Due to their large natural availability, lignocellulosic sources, such as wood, cotton, or grasses, are most commonly used for CNC production (*39, 81*). This is in accord with the anticipation of industrial-scale CNC production as an extension to existing pulp and paper industry, where logistical infrastructure would be already in place (*30*). Active pilot plants for CNC production can be viewed in Table A10. They are usually operated with softwood and hardwood pulps, woody and agricultural residues, as well as purer cellulose, such as dissolving pulp and cotton. However, where ecozones favor different compositions of flora over lignocellulosic plants, CNCs can be produced from other sources as well. These involve agricultural waste, algae, animals, and bacterial cellulose. Most commercial CNC production routes have been stated to be feedstock-agnostic (*39*). However, large-scale use of cellulose sources, other than lignocellulosic biomass, is retained and requires further process development (*37*). A comprehensive overview on different cellulose sources available for CNC isolation is given in Table A9. Further cellulose sources for CNC production are summarized in comprehensive review articles (*38, 101, 139, 182*).

General procedure for cellulose isolation from biomass is briefly outlined in section 2.1.3. While most research on CNCs and their commercial production starts from preprocessed and purified cellulose, some groups started development of CNC isolation procedures from, so far, unexploited feedstock. Comminution of biomass to increase cellulose accessibility commonly forgoes any chemical treatment. Severity of chemical treatment, as well as sequence of involved unit operations must be adjusted to structure and composition of each cellulose source. Unit operations involved in upstream processing are extraction, digestion, and bleaching. Extraction is used for dewaxing and removal of inorganic compounds. Hemicelluloses, lignin, and inorganic impurities are removed by alkaline (NaOH; KOH) or acidic (HCl) digestion, or by a combination of both. Throughout extraction, process parameters must be chosen to avoid mercerization by structural reorganization (section 2.1.1). In addition, extracted cellulose for CNC production is usually heavily bleached with chlorine compounds (NaOCl; $NaClO_2$) in an alkaline buffer solution, or with chlorine-free oxidative reactants (H_2O_2) to remove residual lignin. An overview on different processing strategies is illustrated in Table 3. When less severe bleaching conditions are applied, cellulose's fibrillar length may remain unchanged (*30*).

The most applied route for cellulose isolation involves comminution, followed by digestion, and subsequent bleaching (D_{II}). Some cellulose sources have not been pre-processed due to their initially high purity (Table A9), but the CNC product was bleached afterwards (*183*). Surveyed literature indicated no preference for source-specific isolation strategies. On the lab-scale, bleaching has usually been done with $NaClO_2$. However, for low environmental impact in the scope of an LCA, and for matching with industrial standard, bleaching with H_2O_2 or ClO_2^- should be favored (*30*).

Table 3: Upstream processing strategies for cellulose isolation from biomass for CNC production.

Process	Unit operations	References
E_I	Comminuted cellulose → Extraction → Digestion → Bleaching	(*184–189*)
E_{II}	Digestion	(*190–192*)
E_{III}	Extraction	(*193, 194*)
D_I	Digestion	(*55, 185, 195–197*)
D_{II}	Bleaching	(*175, 198–215*)
D_{III}	Digestion	(*216–221*)
D_{IV}	Extraction	(*222*)

2.2.3. CNC isolation

Chemical cellulose depolymerization and related conversion kinetics to glucose have been extensively studied for its utilization for biofuels and bio-based chemicals (*223*). The mainly applied route via acid-catalyzed hydrolysis involves the degradation reaction of β-1,4-glycosidic linkage between two consecutive AGUs. The dominant pathway of acid-catalyzed cellulose hydrolysis involves three steps, which are illustrated in Figure 10 (*224–227*).
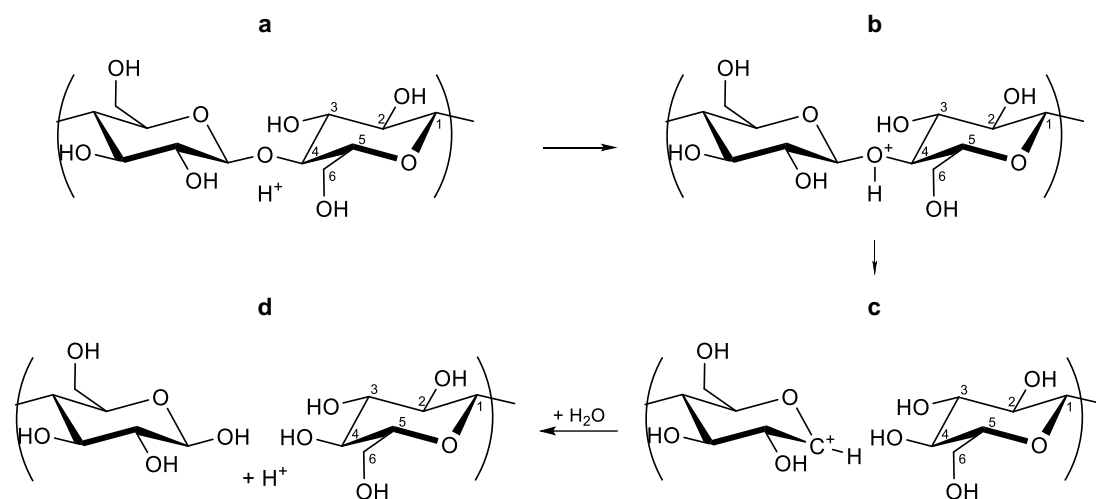
Figure 10: Dominant pathway of acid-catalyzed hydrolysis of cellulose, adopted from Fengel and Wegener (*224*).

First, a proton of the catalyzing acid interacts with the glycosidic linkage (a), yielding a conjugate acid (b). Subsequently, the C-O bond of the glycosidic linkage is cleaved at the C_1 or the C_4 atom, and an intermediate cyclic carbonium cation is formed (c). The cation initiates addition of a water molecule, resulting in a stable product and release of

a proton (d). Alternatively, protonation may also occur at the ring oxygen, which results in formation of a non-cyclic carbonium cation (*224*). This process is governed by kind, strength, and concentration of acid; as well as temperature, pressure, and pH, under which the process is operated (*224*).

Starting from native cellulose, acid-catalyzed hydrolysis is a heterogeneous reaction. Therefore, it is not only controlled by reaction conditions, but also by physical structure of elementary fibrils on the molecular level (*228, 229*). While upstream processing increases overall accessibility of cellulose to the reaction medium, ability to isolate cellulose nanocrystals from cellulose is enabled by proton penetration rate of differently ordered cellulose fractions (*224*). Mann and Marrinan found that deuteration of hydroxy groups occurred rapidly in disordered regions of cellulose, whereas deuteration was slow in ordered regions (*230–232*). Consequently, protons can penetrate disordered regions at a similar rate within fibrils and at the surface, while ordered regions are only laterally accessible to protons, progressing from the surface. It is believed that this effect is caused—besides the intrafibrillar bond network—by hydrophobic interaction of crystalline cellulose sheets, which induce formation of a dense H_2O layer in the interface's proximity (*233*).
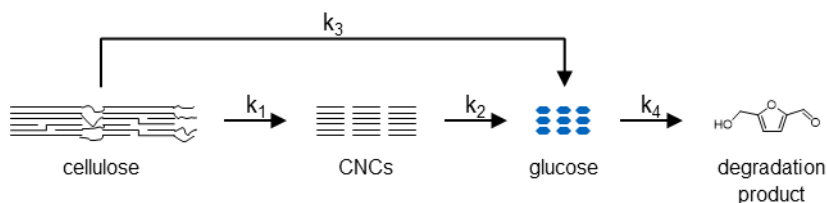
Figure 11: Reaction pathways of acid-catalyzed cellulose hydrolysis for CNC production, adapted from Wang et al. (*177*).

The reaction pathways involved in acid-catalyzed cellulose hydrolysis is shown in Figure 11. k_1 is the dominant pathway and represents hydrolysis of disordered fractions of native cellulose to CNCs (*177, 234*). Concurrently, disordered cellulose, which is less incorporated into elementary fibrils, is directly hydrolyzed to glucose (k_3). Hydrolysis kinetics of the ordered cellulose fraction to glucose (k_2), and decomposition of glucose (k_4) to furfural and 5-hydroxylmethfurfural, follow more severe reaction conditions (*177, 235*). Further hydrolysis of CNCs, following pathway k_2, is rate-determined by oligosaccharide formation. Therefore, it is 2 to 30 times slower than hydrolysis of disordered cellulose (*177, 223*). Albeit cellulose hydrolysis is mostly governed by heterogeneous reactions, global kinetics can be described by pseudo-homogeneous first-order laws (*235–237*). Rate constants, k_i, and reaction temperature, T_R, are linked by an Arrhenius equation, which additionally account for acid concentration effects, c_{acid} (*177, 223, 225, 238*):

$$\ln k_i = \ln k_{i0} - \frac{E_A}{RT_R} + a \ln c_{acid}. \tag{2.1}$$

k_{i0}; E_A; R; and a are pre-exponential factor, activation energy, universal gas constant, and reaction order with respect to acid concentration, respectively.

In the 1940s, first CNC production has been reported by Nickerson and Habrle, in their research series on "Hydrolysis and Catalytic Oxidation of Cellulose Materials" (*228, 234, 239–242*). They investigated decomposition of cellulose to glucose, along pathway $k_1 \rightarrow k_2$, and established the corresponding process-structure relationship. CNCs' lateral size,

which remain after acid-catalyzed hydrolysis with boiling 2.5 N HCl and H_2SO_4, were estimated to be in the same range, as it has been determined by powder X-ray diffraction (PXRD) (*144, 243*). Shortly afterwards, Rånby and Ribi showed stable colloidal suspensions of CNCs, isolated through sulfuric acid-catalyzed hydrolysis (*145, 161–164*). To this effect, sulfuric acid reacts with cellulose's surface hydroxy groups concurrently to hydrolysis, to form sulfate half-esters (*244–247*). Introduction of multivalent sulfate anions brings in negative surface charges, which induce electrostatic particle repulsion. Associated reaction mechanism is shown in Figure 12. There are three hydroxy groups per two AGUs, pointing away from crystals' surface: one at C_2, C_3, and C_6, respectively. Therefore, ignoring hydroxy groups at C_1 and C_4 at opposite chain ends, maximal overall possible degree of sulfation is 1.5. It is suggested that reactivity of surface hydroxy groups in heterogeneous reactions varies, and follows order $C_2 > C_6 > C_3$ (*248, 249*). Thus, CNCs with degree of sulfation > 1 are unlikely (*140*). To date, location of sulfate groups on CNC surfaces is not satisfactorily determined (*250*). Nevertheless, CNCs' bulk lattice structure is preserved during sulfation (*145, 163*). This suggests that the pseudo-homogeneous reaction mechanism proceeds laterally from the CNC surface.
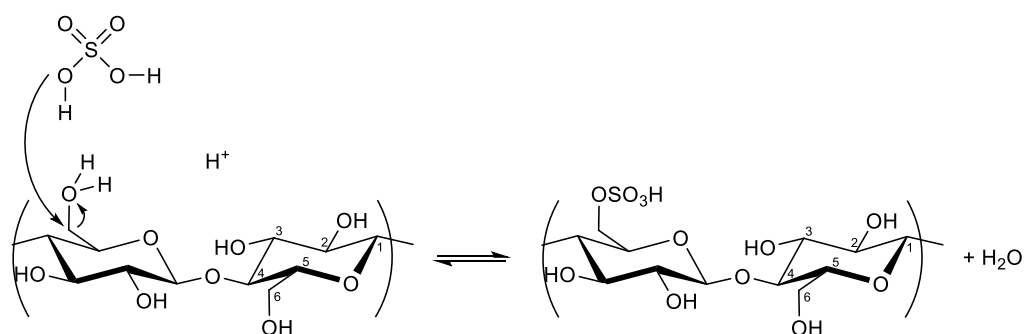
Figure 12: Cellulose esterification by sulfuric acid at the C_6 hydroxy group, according to Vanderfleet and Cranston (*39*).

2.2.4. Downstream processing of CNC production

When the desired extent of hydrolysis is reached, hydrolysis and concurrent sulfation are terminated (*39*). High ionic strength of the reactant solution, which at this point contains CNCs, acid, and byproducts, causes CNC agglomeration (*251, 252*). At this stage, different series of unit operations are implementable, to separate CNCs from reactant solution and form stable colloidal suspensions. An overview on different methods is given in Table 4. L_I represents the primarily used laboratory-scale approach via sedimentation and filtration (*253*). First, the reactant solution is diluted with cold water to particle concentrations below the gel point. Concentrations of excess acid and byproducts are then reduced by repeated centrifugation and rinsing, which is optionally preceded by gravity settling, until peptization of CNCs occurs. Subsequently, residual acid and byproducts are removed by either dialysis or a series of diafiltration (DF) and ultrafiltration (UF) steps (*30, 254, 255*). Ions and oligomers, which are trapped in the particles' solvation shell, can be removed through ion-exchange resin treatment (*253, 256, 257*). Colloidal CNC suspensions in the resulting protonated form are reportedly long-term stable (*258*); however, surface sulfate esters are strongly acidic in their protonated form, which causes autocatalytic depolymerization and chain degradation (*247, 259, 260*). Therefore, if long-term storage is intended, it has been recommended to keep product storage temperature low; and exchange counterions of ester groups with

inert cations, for which mostly a sodium base is added (H⁺ → Na⁺) (*253, 257, 260*). Furthermore, CNCs tend to form lateral agglomerates and clusters of multiple CNCs, due to strong interparticle hydrogen bonds (*254, 261*). Therefore, mechanical treatment, such as ultrasound-assisted homogenization (ultrasonication), is needed to individualize CNCs (*262–265*). Eventually, incompletely hydrolyzed cellulosic residues (CSR) and aggregates are removed from the product by filtration or centrifugation.

Table 4: Unit operations involved in downstream processing, ensuing CNC isolation. To date, methods L_I and L_II are implemented on laboratory scale, while C_I and C_II have been reported in the scope of commercial environments.

Process	Unit operations					References
	Solid-liquid separation	*Chemical post-treatment*	*Solid-liquid separation*	*Mechanical post-treatment*	*Solid-liquid separation*	
	CNCs in reactant solution					
L_I	Sedimentation		Dialysis or DF→UF	Ultrasonication	Sedimentation	(*253*)
L_II		Neutralization	Sedimentation	Ultrasonication	Sedimentation	(*252, 266, 267*)
C_I		Bleaching and neutralization			Sedimentation and UF → DF → CF → UF	(*258*)
C_II	Sedimentation	Bleaching and neutralization			CF → DF → UF	(*268*)

In scale-up scenarios, solid-liquid separation steps involve neutralization of remaining acid before (L_II) or after centrifugation (C_I, C_II), to decrease water usage and reduce reactor volume (*252, 258, 266–268*). Furthermore, neutralization—followed by sedimentation—supersedes time-intensive dialysis or filtration and, therefore, contributes to an overall rapid production process of colloidally stable CNCs (*252*). Industrial-scale CNC production usually starts from less pure pulps and agricultural residues as cellulose source (Table A10). Bleaching is then postponed from upstream to downstream processing. Additionally, dialysis is replaced by membrane filtration in commercial production plants; involving candle filtration (CF), UF, and DF, which are further used to adjust final suspension concentration (*30*).

2.2.5. Process improvement for sulfated CNCs

State-of-the-art processes for production of colloidally stable, sulfated CNCs are still based on the principle of Rånby and Ribi; and use hydrolysis and sulfation with H_2SO_4, which is followed by peptization after liquid-solid separation (*145, 161–164*). Since then, process parameters have been improved in many ways, aiming at exploitation of different cellulose sources, control over disperse particle properties, and efficient process design (*269*). Generally, high acid concentrations are preferred for rapid CNC isolation (*270*). Furthermore, cellulose's degree of sulfation and, thus, colloidal stability of CNCs, is

predominantly controlled by acid concentration (*244*). In this context, Mukherjee and Woods determined the concentration range of 8.7–10.1 M H_2SO_4 for CNC isolation in modern production processes (*271*). They monitored extent of hydrolysis at varying acid concentrations with X-ray diffraction (XRD); and found that acid concentrations above 10.1 M H_2SO_4 result in partial recrystallization of cellulose I to cellulose II. CNCs produced under more severe reaction conditions show high enzymatic digestibility, which suggests structural degradation; and rapid decomposition complicates process control, which has been complementarily reported elsewhere (*177, 270*). Maximum H_2SO_4 concentration for isolation of crystalline cellulose is 12 M, when it further depolymerizes to oligomeric and monomeric sugars (*177, 272*).[c] In contrast, low reaction severity, at sulfuric acid concentrations below 8.7 M, effects only gradual removal of hemicellulose-cellulose linkages and insufficient cellulose degradation in amorphous regions, yielding CNCs with low crystallinity index. Reaction severity of acid-catalyzed cellulose hydrolysis has been approximated by Arrhenius temperature behavior (*273*). Based on the severity factor concept of Chum et al. (*273*), Wang et al. (*177*) introduced a combined severity factor, which accounts for degree of hydrolyzable cellulose, with regard to sulfuric acid concentration and reaction temperature. They concluded a preferred acid concentration range of 8.7–10.1 M H_2SO_4 for CNC isolation, which is in conformity with the study of Mukherjee and Woods (*271*). In addition, their kinetic study outlined a temperature range of 50–60 °C, in which pathway k_1 is dominant. Further empirical studies on CNC isolation established a broader temperature range of 40–70 °C, and hydrolysis times of 40–120 min; both dependent on cellulose source, as well as reactor scale and design (*171, 177, 254, 262, 274*).

Acid concentration, reaction temperature, and reaction time—all within the given ranges—, among other parameters, are revisited as explanatory variables in statistical designs of experiments (DoEs), addressing their effect on selected response variables, regarding the process-structure relationship. Explanatory variables are process conditions, which are applied during upstream processing, such as cellulase concentration, c_{enz}, for enzymatic pretreatment and mechano-chemical pretreatment time, t_{mc}. Acid concentration, c_{acid}, reaction temperature, T_R, reaction time, t_R, and pulp-to-acid mass ratio, m_c/m_a, are explanatory variables for acid-catalyzed CNC isolation. Ultrasonication time, t_{US}, has been varied during downstream processing. Response variables are directly measurable properties, such as particle size—in terms of length, L, and diameter, d—, crystallinity index, CrI, and colloidal stability, regarding the surface sulfate group density, ρ_S. Furthermore, properties, such as hydrodynamic apparent particle size, $z\text{-}avg$, zeta potential, ζ, critical concentration for liquid crystalline phase separation, c_{crit}, and suspension viscosity, η, at given particle concentration, are qualitatively characterizable measures for particle size, suspension stability, and product performance. Since extraction yield, Y, determines economic feasibility of industrial CNC production, it has been assessed, along with mass conversion ratio, m_P/m_B, of product mass, m_P, and mass of byproduct, m_B. An overview on studies, which comprehensively addressed process improvement of CNC production, is given in Table 5 in chronological

---

[c] Molar concentration of 2.5 N H_2SO_4 corresponds to a mass fraction of 11.5 wt.%. The operating window determined by Mukherjee and Woods (*271*) corresponds to a mass fraction of 58–64 wt.%. Reportedly, degradation of crystalline cellulose occurs at 72 wt.% (*272*). Molar concentration of pure sulfuric acid is 18.7 M.

order. Respectively chosen DoEs indicate authors' objectives. Blocking designs have been applied to determine significance of selected explanatory variables, and to screen out important variables. In contrast, response surface designs' purpose, such as fractional factorial, full factorial, central composite, and quadratic designs, was to search for improved or optimal process conditions and processes' weak points, and to increase process robustness against non-controllable variables. An overview on different DoEs can be found in literature (*275–278*). Beyond works listed in Table 5, other groups carried out less comprehensive studies on process improvement of CNC production (*279–283*).

Table 5: Studies addressing process improvement for CNC production, utilizing statistical DoEs. References are listed in chronological order.

DoE	Cellulose source	Catalyst	Response variables	Explanatory variables	Reference
Block	Cotton	H_2SO_4	$Y; L; \rho_S; c_{crit}$	$t_R; T_R; t_{US}$	(*171*)
Block	Softwood pulp*; hardwood pulp*	H_2SO_4	$L; d; \rho_S; c_{crit}$	$t_R; m_c/m_a$	(*172*)
Fractional factorial	CMC	H_2SO_4	$Y; L$	$c_{acid}; t_R; T_R; m_c/m_a; t_{US}$	(*173*)
Block	Softwood pulp*	H_2SO_4	$Y; L; \rho_S; \eta$	$c_{acid}; T_R$	(*174*)
Block	Kenaf bast fibers	H_2SO_4	$Y; L; d; CrI$	t_R	(*175*)
Central composite	Hardwood pulp*	H_2SO_4	$Y; \rho_S$	$c_{acid}; t_R; T_R$	(*176*)
Central composite	Hardwood pulp*	H_2SO_4	$Y; m_P/m_B$	$c_{acid}; t_R; T_R$	(*177*)
Central composite	Hardwood pulp*	H_2SO_4	$Y; L; d; \rho_S; CrI$	$c_{acid}; t_R; T_R$	(*178*)
Block	Softwood pulp*; CMC	H_2SO_4, H_3PO_4	$z\text{-}avg; \rho_S; CrI$	T_R	(*179*)
Full factorial	Cotton	H_2SO_4	$Y; z\text{-}avg; \rho_S$	$c_{enz}; t_R; T_R$	(*284*)
Central composite	Softwood pulp*	H_2SO_4	$Y; \rho_S$	$c_{acid}; t_R; T_R$	(*181*)
Full factorial	Cotton	H_3PO_4	$L; \rho_S; \zeta$	$c_{acid}; t_R; T_R$	(*180*)
Quadratic	Bamboo pulp*	$H_3PW_{12}O_{40}$	Y	$c_{acid}; t_R; t_{mc}$	(*170*)

Pulps, as cellulose source, were obtained in their bleached form.

Even with the use of statistical DoEs, abundance of explanatory variables complicates all-encompassing description of the complete CNC production process. Hence, majority of authors started their studies on process improvement from preprocessed cellulose, such as CMC, ashless cotton, and bleached pulps, and directed their focus on effects of process conditions during CNC isolation. During this unit operation, reaction severity has been identified as dominant factor, which determines CNC properties. Comprehensively, it has been found that both degree of hydrolysis and degree of sulfation increase with reaction severity (*177*). Reaction time had a minor effect, except in early stage of hydrolysis. Equal product properties have been obtained through protocols following similar process conditions, starting from the same cellulose source (*37*). Since no universally defined CNC target properties have been reported, results from statistical approaches have limited transferability. However, basic process-structure relationship can be derived from such works.

Looking at the entirety of literature on CNC production, process development has mainly focused on technical feasibility of CNC extraction from different cellulose sources (*269*). Process conditions during CNC isolation were within abovementioned ranges, and

commonly implemented protocols were mostly derived from the work of Bondeson et al. (*173*). Remarkably often, information on process development for new cellulose sources, as well as information on structure and composition was absent from method description; or documented incompletely. Same applies for process conditions during upstream and downstream processing. Only secondary, such works aimed at CNCs with high aspect ratio, higher crystallinity index than the starting material, and good colloidal stability. However, these properties are also dependent on cellulose structure and, thus, co-determine mechanical and physical-chemical product properties, such as mechanical strength, self-assembly, and rheological behavior (Table 2); and, therefore, CNC performance in advanced materials. Furthermore, extraction yield and process time were rarely covered in general literature on CNC production (*39*).

Reportedly, scale-up of sulfuric acid-catalyzed hydrolysis to produce CNCs—from laboratory scale to industrial scale—does not require significant changes, up to an approximate daily production volume of 10 t (*30, 285*). At this scale, mainly mixing-related issues must be addressed. Beyond this scale, switching from batch to continuous processing allows shorter set-up times and improved control over reaction conditions. Only recently, the first continuous process, involving sulfuric acid-catalyzed hydrolysis for CNC production, has been reported (*39, 286, 287*). Furthermore, substantial attention has been given to CNC preparation concepts, involving approaches not based on sulfuric acid-catalyzed hydrolysis, over the past years (*269*). To that effect, chemical resistance of crystalline cellulose has also been found for oxidative degradation (*165*), biological degradation (*166*) and hydrolytic decomposition with other acids at varying concentration (*167–170, 179, 180*).

2.2.6. CNC target properties

CNC performance in advanced materials is predominantly governed by particle size, crystallinity index, and colloidal stability (*39*). These properties are determined by process conditions during CNC isolation and cellulose structure, which in turn is set by cellulose source and cellulose isolation process. An overview on interdependent properties of sulfated CNCs is shown in Figure 13 and Table 6. Commonly, effects of individual explanatory variables on CNC properties have been assessed by empirical screening and DoE approaches, as it is outlined in section 2.2.5.

Regarding CNC dimensions and morphology, high aspect ratios promote particle assembly in liquid crystalline phases and formation of percolated networks. Furthermore, increasing surface area with decreasing particle size originates high surface activity for chemical reactions and sorption processes. In addition, high aspect ratio, along with high surface area-to-volume ratio, facilitates interfacial effects, in terms of emulsion stabilization and force transmission in nanocomposites. Crystallinity index indicates extent of hydrolysis and is primarily linked to CNCs' mechanical properties. CNCs' colloidal stability, against agglomeration and sedimentation, is governed by their surface chemistry. Colloidal suspensions of sulfated CNCs are stabilized by electrostatic particle repulsion, which is induced by negatively charged sulfate groups. High colloidal stability provides uniform product properties, along with consistent performance, and it determines suspension viscosity. Furthermore, post-processing conditions and product shelf life strongly depend on colloidal stability.

Cellulose isolation → CNC isolation → Particle length → Size/aspect ratio
Cellulose source → Cellulose structure → Particle diameter → Surface area
Surface chemistry → Colloidal stability
Crystallinity index
Particle concentration → Chirality
Ionic strength → Self-assembly
Rheology
Photonic properties
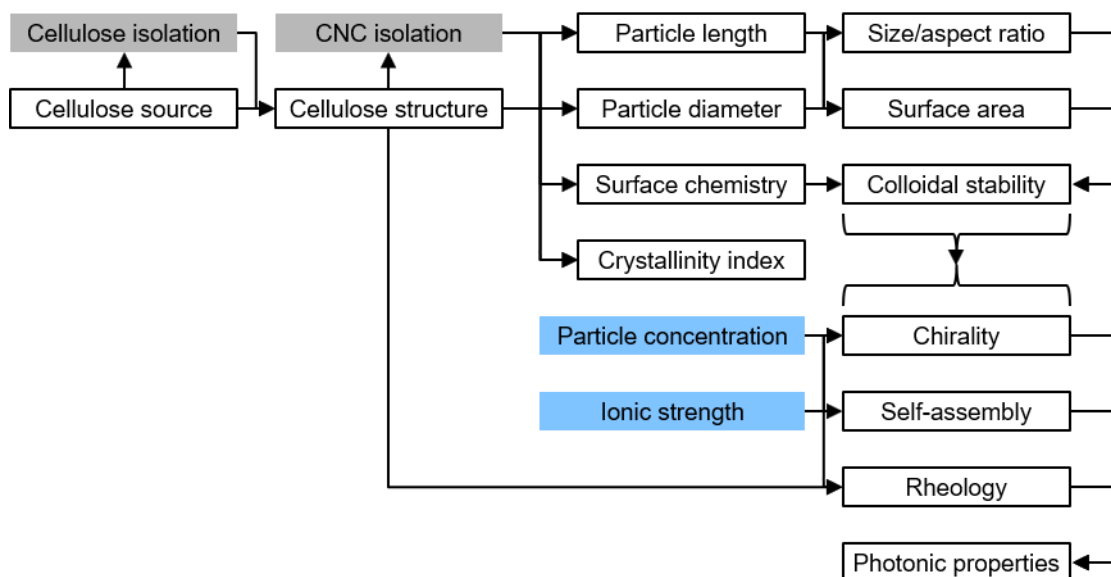
Figure 13: Dependence of disperse properties of colloidal CNCs on cellulose source, as well as structure and process conditions. Unit operations and external factors are shaded in grey and blue, respectively. Visualized interrelationship was compiled from references in running text.

Table 6: Qualitative dependence of application-related CNC properties on cellulose source and intrinsic CNC properties, taken from references in running text.

	Cellulose structure	Size/ aspect ratio	Crystallinity index	Surface area	Surface chemistry
Biocompatibility	x	x			x
Mechanical strength	x	x	x		
Surface activity	x			x	x
Hydrophilicity				x	x
Thermal stability	x		x	x	x
Piezoelectric properties		x	x		x
Electromagnetic properties		x	x		x

In the context of numerous cellulose sources, from which CNCs are produced under varying process conditions, only nomenclature, morphology, and dimensions are standardized (section 2.1.5) (*1, 142, 264*). ISO/TS 20477 (*1*) defines CNCs as rod-shaped nano-objects of predominantly crystalline and paracrystalline structure. Additional standards outline protocols for assessing CNC crystallinity index and colloidal stability (*45, 48*). However, none of these standards quantifies minimum CrI of CNCs to be considered nanocrystalline or specifies independently measured properties to assess their colloidal stability. This coincides with difficulties to concurrently tailor multiple CNC properties, due to their complex interdependence. Thus, authors mainly focused on assessing CNC performance in specific use cases, along with extraction yield of the applied process. In the following, works listed in Table A9 are screened for particle size, crystallinity index, and extraction yield. Furthermore, colloidal stability is discussed, to conclude a general view on the structure-property function of fundamental CNC properties.

Particle size. With regard to particle size, structure of cellulose source and its accessibility are most decisive factors (*269*). A qualitative excerpt on lateral dimensions of CNCs from different cellulose sources is shown in Figure 14 (a). All authors applied similar process conditions during CNC isolation. However, a wide spread of particle lengths, between 28 nm and 10 µm, has been reported. Botanical cellulose sources, such as wood, plants and grasses, cotton, and agricultural wastes, yield comparably short CNCs, whereas faunal celluloses and celluloses from prokaryotes yield longer CNCs. Quantitative meta-analysis of data was unrewarding because cellulose isolation protocols were not consistent throughout literature, and information on method development was mostly absent. All considered works aimed at chemical purity of cellulose source, which, however, was then infrequently evaluated, and potential effects of upstream processing on fibrillar length and cellulose structure were disregarded. Nevertheless, upstream processing under real conditions cannot remove all non-cellulosic compounds from complex biomasses. Residual hemicelluloses are source-specific and affect cellulose accessibility during acid-catalyzed hydrolysis. Therefore, a reaction pathway parallel to cellulose hydrolysis must be considered, which involves hydrolysis of hemicelluloses to hemicellulosic sugars; and further degradation products, complementarily to the reaction pathways shown in Figure 11 (*177*). Furthermore, downstream processing and product handling are differently implemented throughout literature, which reduces comparability level of CNC lengths from different cellulose sources. Same applies for CNC diameters, which depend on cellulose source and process conditions. CNC diameters of 3–10 nm have been reported for botanical cellulose sources (*171, 197, 288–290*), and higher diameters of 10–20 nm have been reported for CNCs from faunal celluloses and celluloses from prokaryotes (*185, 288, 291, 292*). After isolation, CNCs are usually present as lateral agglomerates of multiple particles (*261, 288*). CNCs can be individualized by ultrasonication during downstream processing (*264, 293, 294*). However, assessing true CNC diameters is often disregarded in literature, because of their low dimensions and inevitable agglomeration during sample preparation for electron microscopy (EM) or atomic force microscopy (AFM) (*42, 295, 293*).
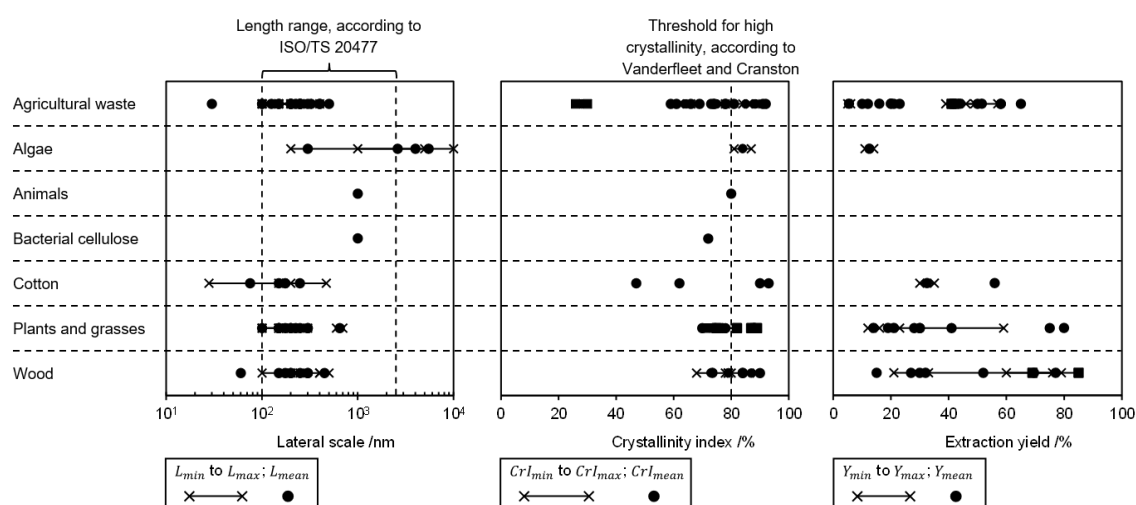
Figure 14: Qualitative visualization of (a) lateral dimensions and (b) crystallinity index of CNCs, as well as (c) CNC extraction yield from different cellulose sources. Data is extracted from references compiled in Table A9, which are abstracted from Vanderfleet's and Cranston's review (*39*). Process conditions for CNC isolation were similar throughout all studies. The graphs, however, only allow qualitative comparison of attributes, since both upstream and downstream processing were non-uniform, and no differentiation has been made between individual measurement methods, which were applied by the respective authors.

Crystallinity index. Degree of crystallinity of cellulose and CNCs is expressed as crystallinity index, which represents dry mass ratio of crystalline substance in a sample (*296–298*). Native celluloses of botanical origin have a CrI of 40%–70%; whereas CrI of bacterial and algal celluloses can be as high as 80% (*82*). No minimum CrI is defined for CNCs to be considered as crystalline material. However, a CrI of CNCs of ≥ 80% has been suggested to be considered as highly crystalline (*39*). Qualitative representation of CrI of CNCs from different cellulose sources is shown in Figure 14 (b), which ignores pre-treatment of source material and overlooks respective measurement methods. High crystallinity indexes have been reported for CNCs from all cellulose sources, where average CrI of faunal, bacterial, and algal celluloses was higher, compared to CrI of CNCs from botanical cellulose. However, CNCs' CrI was not deductible from cellulose source only. Achievable CrI is presumably limited by presence of disordered cellulose fractions in CNCs' interior, which are protected from hydrolytic attack (*250*). Furthermore, upstream processing can affect cellulose structure in terms of crystalline modification and structural organization and, therefore, co-determines the product's CrI. Similar to dimensional assessment of CNCs, quantitative comparison of different studies is expendable, due to inconsistent cellulose isolation protocols.

Colloidal stability. Native cellulose crystals are structurally anisotropic and show three lateral crystal faces (section 2.1.1). While two of these display hydrophilic hydroxy groups, the crystal plane orthogonal to cellulose sheets displays mostly C-H bonds (*288, 299, 300*). Therefore, it has lower surface free energy, resulting in lower hydrophilicity than other surfaces, which constitutes overall amphiphilic nature of cellulose crystals. During sulfation, negatively charged monovalent sulfate half-esters are introduced to CNC surfaces at hydroxy groups at C_2, C_3, and C_6 (section 2.2.3). Note that these surface functional groups undergo slow autocatalyzed de-sulfation at ambient conditions (*260*). Sulfate group density depends on CNC structure and process conditions during CNC isolation (*168, 171, 196, 244*). Sulfated CNCs are considered polar nanoparticles, due to inability to disperse them in nonpolar solvents and polymer matrices (*27, 301*). However, negative surface charges facilitate electrostatic stabilization of CNCs in highly dielectric solvents and polar matrices (*174*). Electrostatic interaction distance is defined as Debye length, κ^{-1}, which depends on dielectric constant, ε_{sol}, salt concentration, c_{salt}, and respective ion valence, z (*302*). Long-range electrostatic repulsive particle interactions are opposed by attractive London dispersion forces, which are of short range on the molecular level. However, their additive nature expands their range, and interaction distance, H, between two attracted bodies shifts from H^{-6} for molecules to H^{-1} for cylindrical particles (*303*). Particle interactions in dispersions, comprising uniform particles—where repulsive electrostatic and attractive London forces predominate—are described by the theory of Derjaguin, Landau, Verwey, and Overbeek (DLVO) (*304, 305*). Their theory has been further adapted to orthogonally approaching cylindrical particles (*306–308*). Transferring the essence of these models, colloidal stability in CNC suspensions results from complex interactions of numerous independent variables. Leaving aside solvent properties and focusing on particle fraction only, repulsive forces in CNC suspensions are mostly governed by particle size, concentration, and distance, as well as temperature and surface potential; whereas attractive forces are governed by particle size, particle distance, and the Hamaker constant (*308, 309*). Nevertheless, comprehensive models only facilitate qualitative description of monovalent systems.

Thus, quantitative measured values for CNCs' colloidal stability are surface charge density (*257*) and zeta potential (*42, 310*). CNCs' surface charge ranges between 100–350 mmol kg^{-1} and strongly depends on cellulose structure and process conditions during CNC isolation. Similarly, corresponding zeta potentials are in the range between –20 and –50 mV, which constitutes a range between incipient agglomeration and good stability (*42, 253*). Determination of both measured values strongly depends on measurement set-up. However, measurement parameters are mostly absent in literature, or results have been acquired by non-uniform methodologies. Thus, only limited comparability is given between different published studies. Furthermore, downstream processing strongly affects quantification of surface charges (*254, 256, 257, 311*); ions trapped in CNCs' solvation shells and accumulated oligosaccharides at CNC surfaces interfere with electrostatic repulsive forces (*179*).

Furthermore, recent studies accounted for additional contributions of CNCs' anisotropic structure to their colloidal stability. Affinity of CNCs to numerous solvents and polymer systems has been empirically mapped to establish the structure-property relationship, based on Hansen solubility parameters (*312–314*). Additional stabilization mechanisms were then proposed, based on solvation-induced interactions (*315, 316*).

Extraction yield. Extraction yield, Y, of CNCs from native cellulose is defined as CNC-to-cellulose mass ratio, m_{CNC}/m_c. Both masses are gravimetrically determined in dry state, before and after CNC production. Therefore, m_{CNC} is not specific for CNCs, but it involves all unevaporated species in the product. A qualitative excerpt on extraction yields from different cellulose sources is shown in Figure 14 (c), where yields of up to 85% for wood cellulose have been reported. Broad range of reported extraction yields originates from different cellulose sources and non-uniform processing conditions, across different protocols. Furthermore, methodological descriptions on yield acquisition is missing from most reported studies. Isolation yield of crystalline cellulose is limited by crystalline fraction of the cellulose source, which is 40%–70% for botanical celluloses; and it can be as high as 80% for bacterial and algal celluloses (*82*). Therefore, higher yields indicate lower product CrI and presumably lower reaction severity during CNC isolation. Revisiting the severity concept (section 2.2.3), particle size, degree of sulfation, and isolation yield must be considered during process development. Y is governed by competing reactions k_1 and k_2, as function of reaction severity (*177*). While cellulose depolymerizes under low-severity conditions, high-severity conditions cause further degradation of crystalline cellulose and, hence, isolation yield decreases. Y cannot be improved independent of CNC properties. Thus, process improvement becomes a trade-off of product properties and isolation yield. Therefore, Wang et al. (*176*) suggested process improvement not toward maximizing CNC isolation yield, but to focus on recovery of incompletely hydrolyzed cellulosic residues for subsequent CNF production, aiming at minimal cellulose loss and, thereby, an overall economic process.

2.2.7. CNC post-processing

After downstream processing, aqueous suspensions of sulfated CNCs are referred to as never dried CNCs. Ideally, such suspensions are agglomerate-free and contain individual CNCs with uniform properties, to facilitate predictable performance in advanced materials. While CNC processing in advanced materials is mostly started from never dried state, dry CNCs are favored for easier storage, transportation, and handling

(*317*). However, fully protonated CNCs are prone to agglomeration and only partially redispersible. Furthermore, never dried CNCs show ab initio agglomeration, due to strong interparticle hydrogen bonds (*261*). Thus, more uniform properties of never dried and redispersed CNCs have been achieved by individualization or fractionation (*261, 318*). Due to their hydrophilicity, sulfated CNCs are only poorly dispersible in nonpolar media. Here, surface modification facilitates control of both particle-particle and particle-matrix interaction, by adding functional groups to CNC surfaces (*101*). Methods for post-processing of sulfated CNCs are briefly discussed in the following.

Drying and redispersion. Dry CNC nanostructures with different degrees of agglomeration are achievable by solvent evaporation, lyophilization, or supercritical drying in batch processes, or by continuous spray drying (*319*). During drying, sulfated CNCs undergo interparticle attraction, which is promoted by hydrogen bonds between hydroxy groups at CNC surfaces. CNC agglomeration is irreversible or, at best, partially reversible (*320, 321*). In this regard, both solvent evaporation and lyophilization induce compact CNC structures, which compromise effective redispersion. In contrast to solvent evaporation, lyophilization produces less aggregated CNCs (*322, 323*). Here, CNCs form ordered structures along growing ice crystals during the initial freezing step (*324, 325*). Agglomeration occurs during subsequent water sublimation at elevated temperatures. Water vapor penetrates the nanocrystalline structure; and induces structural alteration and agglomeration, by forming interparticle hydrogen bonds (*322, 326*). Supercritical drying of CNCs involves liquid CO_2, which exhibits compressibility similar to a gas, and dissolution of solutes similar to a liquid. Diffusivity of supercritical CO_2 enables solvent extraction, while chemical reactions and structural alterations of CNCs are inhibited (*327*). However, CNCs form highly networked agglomerates during this process, which are difficult to redisperse (*322*). Other than presented batch methods, continuous character of spray drying allows high volumetric throughput and produces free flowing CNC granules with diameters from less than 1 µm up to above 10 µm (*328, 329*). Particle size and morphology mainly depend on operating conditions, such as flow rate, temperature, and nozzle size; and suspension properties, such as particle concentration and particle size (*322, 330*). It has been shown that spray-dried CNCs have good redispersibility and, therefore, superior performance in nanocomposites, compared to CNCs from other drying techniques (*328*).

Commonly, never dried sulfated CNCs only show limited redispersibility after drying (*263*). Nevertheless, agglomeration without any additives or chemical modification before drying is partially reversible, when residual moisture content above 4 wt.% is retained (*329*). Furthermore, redispersibility of fully dried CNCs increases, when protons—as counterions to sulfate half-ester groups—are replaced through neutralization with hydroxides or carbonates (*45, 263, 329*); or by using appropriate ion-exchange resins (*256*). The most commonly available form of sulfated CNCs—the sodium form—is produced by neutralization with NaOH or Na_2CO_3; and it has similar disperse properties to original CNC suspensions, after mild mechanical treatment to individualize CNCs (*45, 263, 329*). In addition, neutralized CNCs have lower propensity for autocatalyzed de-sulfation at ambient conditions (*260*).

Individualization and fractionation. Generally, individualization of dried CNCs is performed through ultrasonication as mild mechanical treatment, which is, furthermore, utilizable to tailor suspension properties (*171, 262, 264, 329*). Similarly, never dried CNCs tend to form lateral agglomerates and clusters of multiple nanocrystals, due to strong interparticle hydrogen bonds (*254, 261*). Parallelly oriented CNCs in lateral agglomerates are only partially individualizable, because energy input, required for individualization, exceeds binding energy of the C-C bond (*328*). In this regard, the preliminary technical specification ISO/CD TS 23151 (*264*) suggests to select energy input during ultrasonication as a compromise between de-agglomeration and sample damage. However, depolymerization of CNCs requires application of high-frequency ultrasound (*331*). To date, application of high-frequency ultrasound to CNCs has not been reported in literature. In addition, relevant literature suggests that no sample damage occurs in the form of de-sulfation, when temperature is kept constant, just above 0 °C, during ultrasonication (*171*). It is widely accepted that energy input of ~2000 J g^{-1} CNC is sufficient to disperse agglomerated CNCs (*171, 329*), while effects of ultrasonication are permanent and cumulative (*329, 332*). It has been reported that ultrasonication only results in insignificant increase of CNC surface group density (*171*). Regarding particle size, applied ultrasound power finds expression in decreasing apparent size with increasing energy input, while absolute energy input and treatment time are secondary (*171, 254, 293, 294, 333*). Note in this context that most literature indicated only duration of ultrasonication; while no information is reported on power, energy input, or equipment for treatment, to reproduce any of the omitted variables.

While ultrasonication facilitates CNC cluster dispersion and, therefore, PSD narrowing, sulfated CNCs are inherently polydisperse in size, due to non-uniform length of crystalline domains, as well as uneven accessibility for acid-catalyzed hydrolysis. CNCs with narrow PSD are beneficial for studying their structure-property (*318*) and property-performance relationship (*261*); and for assessing nanotoxicity (*334, 335*). In this regard, differential centrifugation enables CNC partitioning in different length fractions as function of relative centrifugal force, while length distribution of each fraction becomes narrower (*336*). In addition, CNCs with initially broad PSD can be fractionated by multi-stage separation with layered filter membranes (*337*), or by phase separation in liquid crystalline state (*291, 318*). Furthermore, asymmetrical flow field-flow fractionation, coupled with multi-angle light scattering detection, facilitates controlled fractionation of polydisperse CNCs, and provides quantitative insight into their state of agglomeration (*261, 265, 338*). While chemical composition and crystalline modification remain constant among differently sized CNC fractions, their physical-chemical properties and self-assembly properties diverge (*291, 318, 337*). It is hypothesized that uniformly sized CNCs, with similar physical-chemical properties, show homogeneous accessibility for surface derivatization and, thereby, provide improved processability in advanced materials, over non-uniformly sized CNCs (*337*).

Surface modification. CNC surface modification mainly aims at modulating surface free energy (SFE) to improve interfacial compatibility of CNCs, with nonpolar media and hydrophobic polymer matrices (*140, 339, 340*). SFE of cellulose and CNCs is related to the Hamaker constant via London dispersion forces, and hydrogen bonding follows principles of the Lewis acid-base concept (*341*). Sulfate half-ester groups and hydroxy groups at sulfated CNCs' surfaces promote high SFE, which induces hydrophilic

behavior. However, CNC dispersibility in nonpolar media and polymer matrices requires low SFE (*157, 184, 342, 339*). In this regard, surface modification via physisorption is based on electrostatic interactions, between CNC surface and surfactants or polyelectrolytes; but migration of physically adsorbed species may occur, when sorption equilibrium is disturbed by external factors (*343, 344*). In contrast, chemical derivatization of CNC surface introduces covalently bonded functional groups. Both small molecules and macromolecules can be semi-irreversibly attached to CNCs (*345*); detachment of functional groups depends on activation energy of respective bonds. While all chemical cellulose derivatization techniques are principally applicable to CNCs (Table A8), surface modification based on oxidation (*346*), carbamation (*347, 348*), etherification (*349, 350*), and esterification have most commonly been reported. Among these, esterification is the method of choice for CNC surface modification, due to its simplicity and versatility (*140, 345*). Quantitative assessment of literature regarding different esterification methods—in terms of reaction efficiency, final CNC structure, and performance—is not feasible, due to varying cellulose sources and reagents, differently implemented reaction pathways, and inconsistent characterization methods (*345*). Conclusively, chemical derivatization of CNCs must be carried out carefully to preserve CNC structure and crystalline modification, while irreversible agglomeration and aggregation decrements isolation yield (*157, 351, 352*).

2.2.8. Analytical methods for CNC characterization

Based on high aspect ratio, size polydispersity, and proneness to agglomeration, robust protocols for reproducible CNC characterization are currently under development (*293, 353*). To date, efforts on standardized analytical methods have been documented in technical reports (*45, 48*), which are provided along with auxiliary specification sheets (*49*). In this context, the National Research Council of Canada (*354*) supplies certified reference materials in the form of spray-dried CNC powders (*355, 356*) and colloidal suspension (*357*) with uniform properties, and in-depth certificates of analysis. Such reference materials are actively used in process development, inter-laboratory metrology validation, and benchmarking of different cellulose sources (*253, 264, 358*). In the following, analytical methods for assessing CNC key properties—namely, particle size and aspect ratio, chemical composition, surface functional groups, and crystallinity index (*39, 42, 293*)—are briefly introduced.

Size. Length, diameter, and aspect ratio of CNCs are commonly determined by scanning electron microscopy (SEM) and transmission electron microscopy (TEM) (*185, 219, 288, 325, 359–361*). Both techniques require vacuum and, therefore, samples must be dried prior to analysis. Suitable CNC dispersion on substrates has been achieved by adding in dispersing agents, and subsequent solvent evaporation from dilute suspensions with CNC concentrations below 0.01 wt.% (*42*). Furthermore, preparation of so-called sub-monolayers—corresponding to partial CNC coverage—on atomically flat substrates as a preventive of lateral agglomeration, particle overlap, and drying patterns, enable CNC particle sizing by AFM (*295, 362*). However, while each of these techniques is actively used for CNC size analyses, nanoscale particle sizing is a method-defined parameter (*293*). Staining effects and tip convolution affect results of electron microscopy and AFM, respectively. Thereby, comparability of measurement results between each technique is limited (*295*). With regard to particle size and aspect ratio of dried CNCs, the technical

specification ISO/CD TS 23151 (*264*) describes method development, validation of measurement protocols, and assessment of uncertainties in an inter-laboratory comparison of TEM and AFM measurements. Furthermore, dynamic light scattering (DLS) is addressed for reproducible measurement of hydrodynamic apparent particle size, $z\text{-}avg$, of colloidal CNCs. $z\text{-}avg$ is calculated from scattered light intensity of particles undergoing Brownian motion, under the basic assumption that particles have a single, constant rate of diffusion (*363*). However, rod-shaped CNC morphology implies different translational diffusion constants parallel and perpendicular to the particle axis. Thus, DLS does not provide specific information on CNC length or diameter, but it facilitates semi-quantitative assessment of CNC agglomeration and, hence, colloidal stability (*253, 364, 365*). A more detailed determination of colloidal CNCs' state of aggregation is achieved by fractionation through asymmetrical flow field-flow fractionation, coupled with DLS or multiangle light scattering (MALS) (*261, 265, 338, 366, 367*). Furthermore, AF4-MALS makes quantitative information on particle size and morphology available (*261, 338*).

Chemical composition. Bulk chemical composition of CNCs, regarding stoichiometric ratio of carbon, hydrogen, and oxygen, is fixed to the chemical formula of cellulose. Compositional shift of elemental ratio, as well as other elements present in the sample can be detected, when functional groups are covalently bonded to CNC surfaces during sulfation or derivatization, or when physisorbed moieties are introduced during post-processing. In this context, elemental analysis of CNCs is mainly used to quantify surface modification and chemical purity of samples (*368–372*). Quantitative analysis of carbon linkages, which enables verification of chemical modification in relation to oxygen and carbon content, is facilitated by X-ray photoelectron spectroscopy and Auger electron spectroscopy (*373–375*). In addition, both techniques facilitate detection of binding energy shifts, depending on elements' binding state, which provides complementary information to verify bulk structure and kind of CNC surface modification. Furthermore, energy dispersive X-ray spectroscopy, in combination with SEM, is applied to quantify spatially resolved chemical composition of a beforehand visually identified surface (*376–378*). Similarly, secondary ion mass spectrometry enables laterally resolved quantification of chemical modification at CNC surfaces (*379–381*). Each technique allows at least qualitative detection of impurities and trace elements; however, they are mostly limited to heavier elements, or higher elemental concentrations. In this regard, atomic emission spectroscopy and mass spectroscopy, both paired with inductively coupled plasma, are also applicable to identify metallic or salt compounds in CNC samples (*382–384*).

Surface functional groups and colloidal stability. Functional groups on CNC surfaces are required to provide colloidally stable suspensions with reproducible properties (*293*). Quantification of surface functional groups, such as sulfate half-esters, is facilitated by elemental analysis, which detects respective sulfur content. However, other moieties, such as carboxyl groups, have no element that is distinct from CNCs' bulk chemical composition. In such cases, surface group density of both negatively and positively charged moieties can be determined by conductometric titration with alkaline or acidic titrants; premised that surface functional groups promote electrostatic stabilization (*45, 48, 256, 257, 385*). However, colloidal stability is not only linked with surface group density and, thus, surface charge density; but it is furthermore controlled by suspension

properties, such as pH, ionic strength, and temperature. In this regard, zeta potential (ζ)—which corresponds to electric potential in the interfacial double layer surrounding CNCs—can be evaluated from electrophoretic particle mobility, and it provides a direct measure of colloidal stability (*45, 48*).

Solid state properties and crystallinity index. Quantifying solid state properties and crystallinity index of CNCs enables understanding of their basic structure to improve CNC isolation, and to achieve efficient surface modification without altering bulk structure. Commonly, X-ray diffraction is used to estimate CNCs' CrI (*386, 387*); but Raman spectroscopy is suitable as well (*250, 388, 389*). Particular information on contributions of CNCs' surface structure and atomic structure, including polymorphs, is accessible via solid-state nuclear magnetic resonance (*79, 390, 391*).

Further state-of-the-art techniques for comprehensive CNC characterization, along with existing challenges, have been presented in extensive reviews by Foster et al. (*42*) and Jakubek et al. (*293*). In addition, general-purpose measurement techniques and standardized protocols facilitate assessment of CNC performance in advanced materials. Exemplarily, these involve estimation of mechanical properties in nanocomposites (*392, 393*), gas barrier properties in polymeric films (*394, 395*), rheological properties in suspensions and emulsions (*396*); as well as environmental, health, and safety practices for MNMs in general (*46, 47*).

3. Actionable goals and methods

3.1. Integration of actionable goals

Chapter 1 of this thesis presents global incentives for green and affordable technologies, which prompt academic research on sustainable advanced materials and processes. Consequently, scientific interest in cellulose-based and nanoscale materials, involving CNMs and CNCs, has rapidly expanded over the last decades (*3, 36, 397*). The number of patents that cite CNCs has similarly increased, which implies strong industrial desire for bringing CNC-based products onto the market (*29, 398*). Concurrently, numerous market reports and guides for end users have forecasted potential use cases of CNCs (*36, 39*), which are categorially outlined in Table 7. Since CNCs form stable colloidal suspensions in water, applications in aqueous and hydrophilic environments, such as emulsions and gels, are key research areas. Furthermore, structure and properties of CNCs—in terms of high aspect ratio and distinct mechanical properties—make them a prominent reinforcing filler in polymer nanocomposites. Contemporary efforts to predict and control CNCs' properties and performance via the process-structure-property relationship are presented in chapter 2 of this thesis, along with challenges and limits of existing methods. Additionally, characterization techniques for deeper understanding of CNC morphology, stability, and particle-particle interactions are shown.

Table 7: Importance of CNC properties for performance in advanced materials, qualitatively rated by relevance: + slightly important, ++ moderately important, +++ highly important. Ratings were adapted from Vanderfleet and Cranston (*39*).

Property	Effect of production route	Importance			
		Biomedical devices	Nanocomposites	Rheology modifiers	Emulsions and foams
Surface chemistry	High	+++	+	-	-
Surface charge density	High	++	-	+	+++
Colloidal stability in high ionic strength media	Medium	+	-	++	+
Aspect ratio	Medium	-	+++	+++	++
Thermal stability	Medium	-	++	+	-
Dispersibility (non-aggregated CNCs)	Low	++	++	-	+
Crystallinity	Low	-	+++	-	-

Despite broad academic and industrial interest in CNCs, advanced materials based on CNCs have yet to bridge the gap from laboratory to the commodity market (*30, 31, 34, 40, 41, 44, 50, 399*). Regardless of application, production of individualized and well-dispersed CNCs in stable suspension is critical, because agglomeration defeats nanoscale effects, reduces surface area, and increases percolation threshold. Consequently, development of CNC-based advanced materials necessitates thorough understanding of mechanisms involved in particle agglomeration and, furthermore, tools for particle individualization. However, while scientific literature on CNCs presents various use cases, along with CNC processing, reports largely lack consistency and completeness. Hence, protocols are due to be adjusted to specific applications; and shift toward knowledge-driven process development is imperative. In this context, the work in this thesis represents an effort toward deeper understanding of agglomeration and

individualization of CNCs, by characterizing them in their native never dried state. Beyond that, effects of processing conditions on CNC performance in polymer nanocomposites are addressed, which emphasizes their added value in actual use cases for packaging materials with improved barrier and mechanical properties.

3.2. Methods

Experiments within the works presented in this thesis are designed with the aim to characterize CNCs, and elucidate impacts of particular unit operations on particle size distribution and colloidal stability. Moreover, CNC properties are specifically modified, and CNC performance in barrier coatings and nanocomposites is assessed to demonstrate added value in advanced materials. Therefore, pre-processed cotton cellulose (α-cellulose or cotton linters) is used for CNC isolation through sulfuric acid-catalyzed hydrolysis, while process design follows the principles, which are introduced in section 2.2.3. Product separation (section 2.2.4) is performed via route L_I or L_{II}, as it is shown in Table 4. CNC post-processing is performed in accordance with methods outlined in section 2.2.7. Primarily, conventional analytical methods, which are presented in section 2.2.8, are used to probe particle size and morphology, chemistry, as well as physical properties of CNCs (section 2.2.6). A significant portion of particle characterization—performed both process-accompanying and in the product—is employed off-line on aqueous CNC suspensions. Thereby applied analytical methods comprise optical (dynamic light scattering, electrophoretic light scattering, UV-Vis spectrometry, laser diffraction), chemical (conductometric titration), and physical (viscosimetry) measurement techniques; to determine particle size, colloidal stability, state of agglomeration, and processability. Complementarily, dried CNCs are characterized off-line by electron microscopy (transmission electron microscopy and scanning electron microscopy) to determine particle size and morphology. CNC isolation yield and salt content are quantified by gravimetric dry weight measurements, and ion content is also determined by ion chromatography. In addition, less commonly used analytical procedures are used to assess particle size distribution and colloidal stability of CNCs. Specifically, multiangle light scattering, UV spectrometry, and electrophoretic mobility measurements are coupled with (electrical) asymmetrical flow field-flow fractionation to determine particle size and shape, as well as colloidal stability. This approach is highly modular and precise, which facilitates detailed CNC characterization in their native never dried state. CNC performance in barrier coatings depends on suspension spreadability on polymer substrates and CNC adhesion after drying. Therefore, film coating is accompanied by surface tension measurements and pinhole testing of polymer substrates to assess their compatibility with hydrophilic CNCs and ab initio permeability. Subsequently, coating quality and barrier performance are characterized by optical (reflected-light microscopy, scanning electron microscopy, UV-Vis spectrometry) and physical (oxygen permeability, water vapor permeability) methods. Regarding their mechanical reinforcing effect in nanocomposites, CNC performance is determined by dynamic mechanical testing.

Design of experiments and applied analytical methods vary among individual studies in this thesis. The following figures 15–19 show processing protocols, which are used to achieve the thesis objectives (section 1.3). Thereby applied unit operations in downstream processing and CNC processing (left and center-left columns), according to sections 2.2.3, 2.2.4, and 2.2.7, are accompanied by analytical methods (center-right columns), which are presented along with their respective purpose (right columns). In the center-left columns, black-framed boxes represent unit operations, and boxes shaded in gray represent products and intermediate products. Detailed description of used materials and methods, as well as experimental results and discussion of the results, is presented in chapter 4.

(I) Develop efficient downstream processing strategy, based on CNC agglomeration behavior

The first part of **Paper I** (section 4.1) aims at understanding CNC agglomeration behavior in the presence of sulfates. Thereby, sulfated CNCs are isolated from cotton cellulose and surface sulfate groups are neutralized by counterion exchange with monovalent or divalent cations (Figure 15). Subsequently, secondary sulfates corresponding to the neutralizing cation are added in different concentration to determine CNC agglomeration behavior as function of ionic strength. CNC suspensions are characterized off-line by optical, chemical, and physical methods.
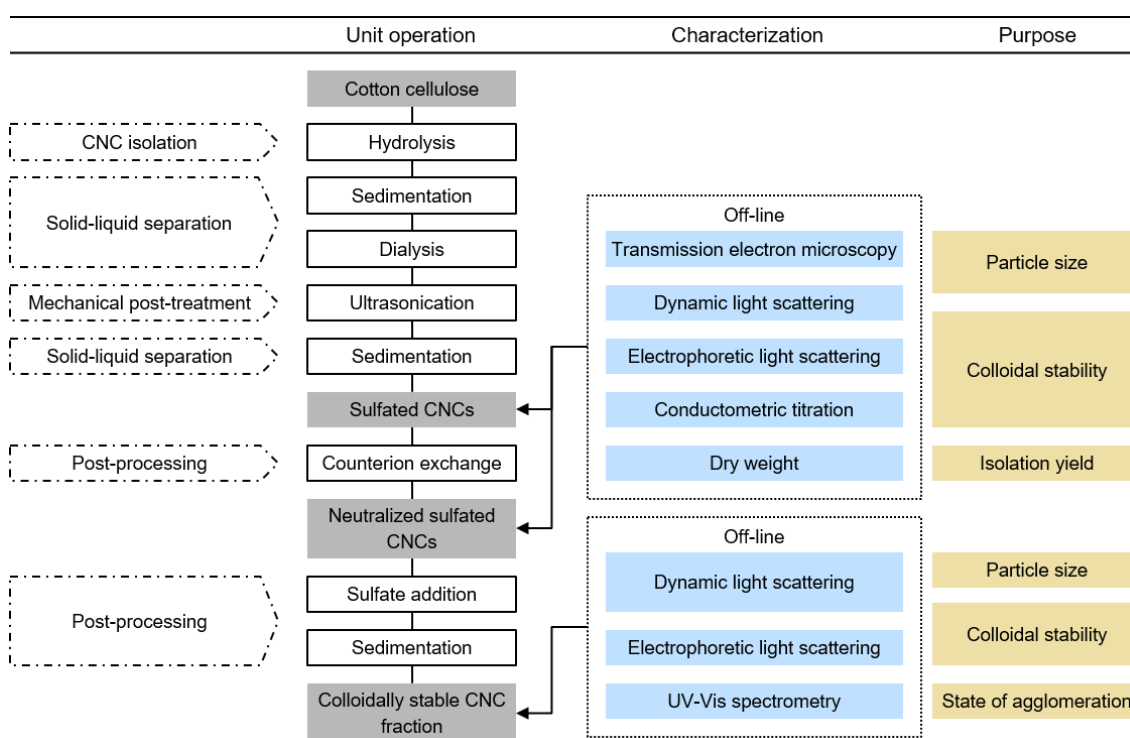

Figure 15: CNC agglomeration behavior in the presence of secondary sulfates was determined on sulfated CNCs from cotton cellulose, which were isolated via route L$_I$ (Table 4). Detailed methodology and results are shown in **Paper I** (section 4.1).

In the second part of **Paper I** (section 4.1), findings on CNC agglomeration are applied to design downstream processing at low reactant consumption. For this purpose, neutralized reactant solutions are repeatedly sedimented to reduce salt content, until peptization occurs (Figure 16). CNC suspensions are characterized off-line by optical, chemical, and physical methods.
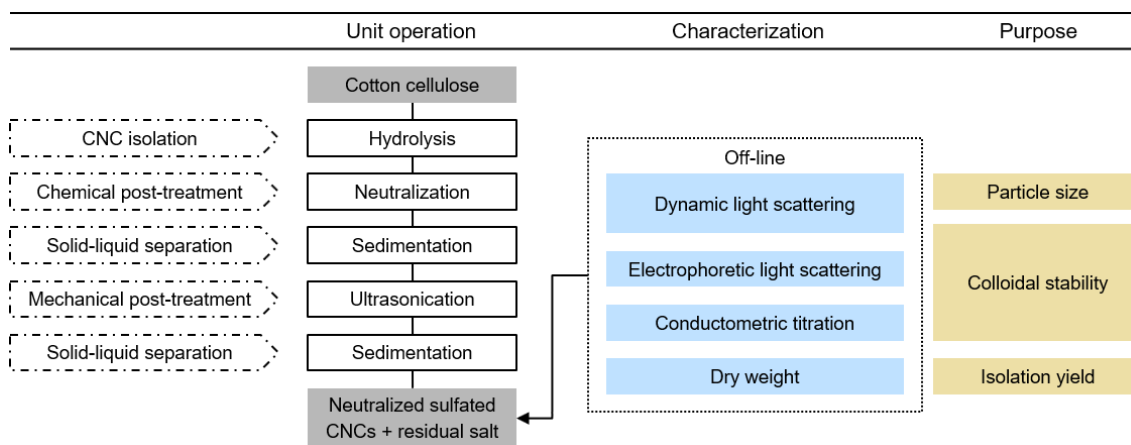
Figure 16: CNC agglomeration behavior in the presence of secondary sulfates was utilized for process design, conforming to route L$_{II}$ (Table 4). Detailed methodology and results are shown in **Paper I** (section 4.1).

(II) Thoroughly characterize effects of ultrasonication on CNC suspension properties

In **Paper II** (section 4.2), CNCs are individualized by incremental ultrasound treatment and subsequently separated by (electrical) asymmetrical flow field-flow fractionation (Figure 17). Short-term and long-term effects of ultrasonication on particle size distribution and stability of CNC suspensions are analyzed on-line and off-line, by optical and chemical methods.
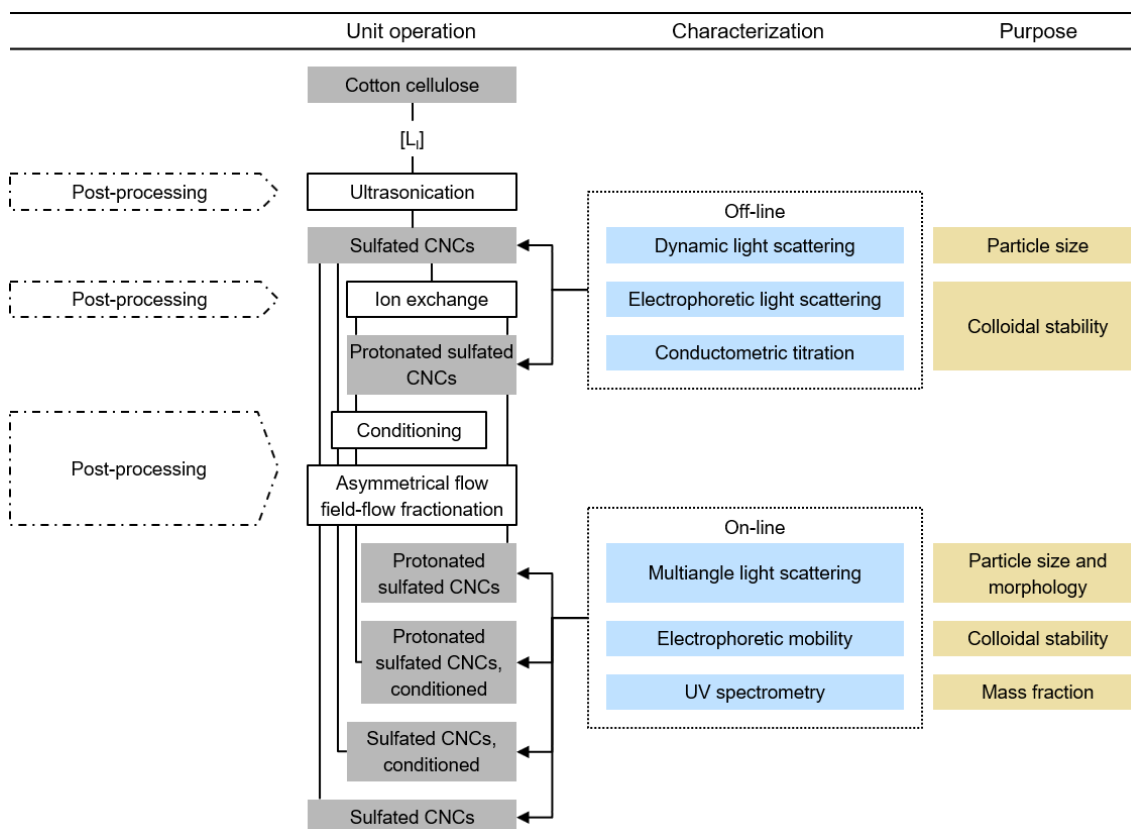

Figure 17: Effect of ultrasound treatment on CNC particle size distribution and suspension stability were determined on sulfated CNCs, which were isolated from cotton cellulose via route L$_I$ (Table 4), through multi-detector AF4. Detailed methodology and results are shown in **Paper II** (section 4.2).

(III) Demonstrate CNC performance in advanced materials

In the first part of **Paper III** (section 4.3), CNCs are produced by sulfuric acid-catalyzed hydrolysis and neutralization, as outlined in the second part of **Paper I**. Subsequently, polymer films are pre-treated and coated with CNC suspensions, which contain residual salt from neutralization (Figure 18). CNC processing, coating, and CNC performance in barrier coatings is analyzed off-line by optical, chemical, and physical methods.
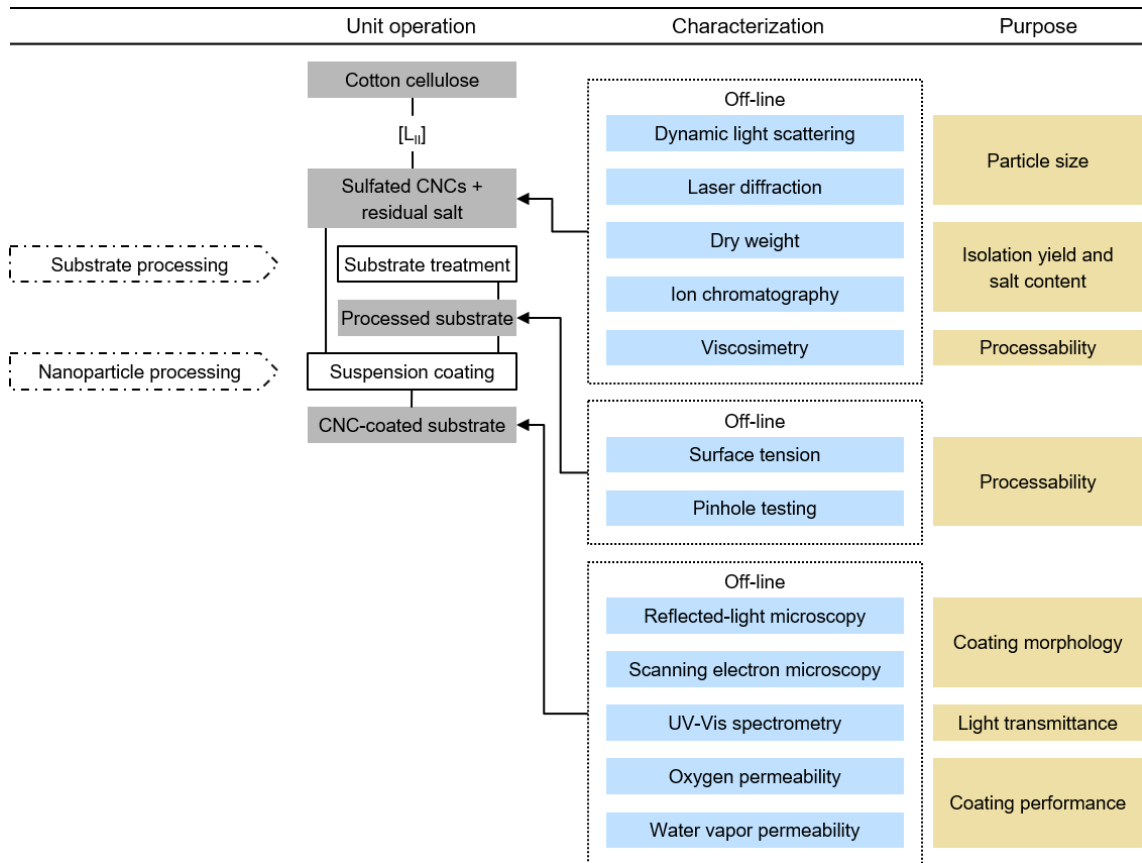

Figure 18: CNCs were isolated from cotton cellulose via route L_{II} (Table 4) and coated onto polymer substrates, to improve the substrates' barrier performance. Detailed methodology and results are shown in **Paper III** (section 4.3).

In the second part of **Paper III** and in **Paper IV** (section 4.4), CNCs are produced by sulfuric acid-catalyzed hydrolysis and neutralization, as outlined in the second part of **Paper I**. Subsequently, starch-based nanocomposites are produced, which contain CNCs and residual salt from neutralization (Figure 19). Suspension properties and CNC performance in nanocomposites are determined off-line by optical and physical methods.
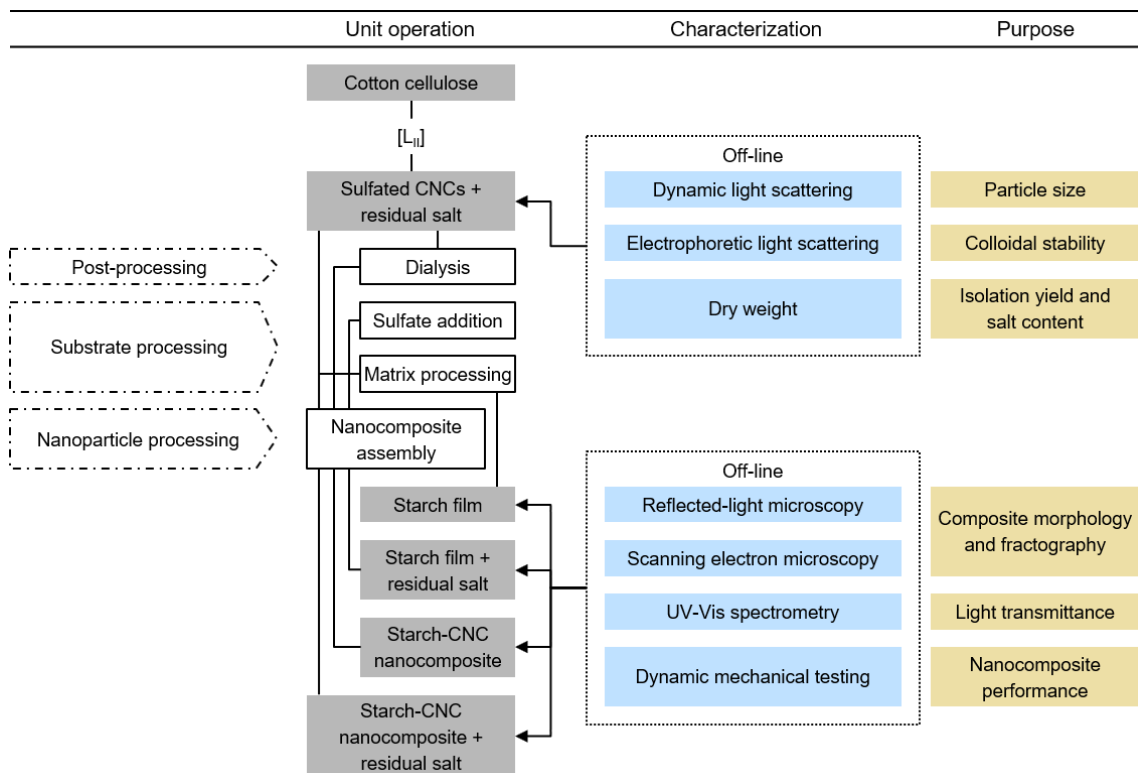

Figure 19: CNCs were isolated from cotton cellulose via route L_{II} (Table 4) and dispersed in a hydrophilic starch matrix, to improve the polymer's mechanical performance. Detailed methodology and results are shown in **Paper III** (section 4.3) and **Paper IV** (section 4.4).

4. Results

4.1. Agglomeration of cellulose nanocrystals: the effect of secondary sulfates and their use in product separation

Summary. State-of-the-art processes for CNC isolation use sulfuric acid to catalyze hydrolysis of amorphous cellulose. Concurrently, negatively charged sulfate half-esters are introduced to remaining cellulose nanocrystals' surfaces (*145, 162–164*). Colloidally stable CNC suspensions are then produced by dialysis or reverse osmosis; to separate nanoparticles from the reactant solution, which also contains residual acid and byproducts. These techniques implicate high water consumption and large reactor design, as well as long processing time (*253, 258, 268*). Since surface functional groups of purified CNCs are fully protonated (*R*-OSO$_3$H), they are prone to autocatalytic de-sulfation at high particle concentrations; and they have a propensity for semi-irreversible agglomeration during drying (*260, 329*). Thus, protonated CNCs are commonly counterion-exchanged with NaOH or Na$_2$CO$_3$ to improve shelf-life, and to facilitate redispersion after drying (*263, 269, 329*). Furthermore, neutralization of ionic residues with said ionic compounds is required in scale-up scenarios, where particularly sulfates remain in the product after filtration (*258*). Formed sulfate salt impacts CNC suspensions' colloidal stability and, thereby, their performance in advanced materials (*263*). Notably—while several works address colloidal stability of CNCs in the presence of chlorides with varying counterions (*251*)—, studies on colloidal CNCs' properties in the presence of sulfates are absent in literature.

In this context, this work aimed at investigating salt-induced CNC agglomeration in the presence of secondary sulfates. Protonated CNCs, with mean particle length of 120 nm, were produced through sulfuric acid-catalyzed hydrolysis of ashless cotton cellulose. Subsequently, (NH$_4$)$_2$SO$_4$, K$_2$SO$_4$, Na$_2$SO$_4$, and CaSO$_4$ were added in different concentrations, and the number fraction of colloidally stable CNCs at each concentration was monitored via UV-Vis spectroscopy. Each salt promoted different critical agglomeration concentration (CAC), which corresponds to the highest salt concentration without particle agglomeration. Similarly, critical peptization concentration (CPC), which is the minimal salt concentration at which all CNCs are agglomerated, is salt-specific. Both CAC and CPC followed the sequence K$^+$ < Na$^+$ < NH$_4^+$ < Ca^{2+}. Differing effects of each salt on CNC agglomeration behavior was not only attributable to electrostatic charge screening, but it could be tentatively explained by the law of matching affinities (*251, 400*). Soft cations, in terms of charge density (NH$_4^+$ and Ca^{2+}), triggered CNC agglomeration with soft sulfate groups already at lower salt concentrations. Colloidal stability, in terms of zeta potential, was then determined at salt concentrations between CAC and CPC. After initial absolute zeta potential increase, when about half of CNCs remained colloidally stable, it decreased to –30 to –20 mV toward CPC, indicating poor colloidal stability. Presence of clusters at all salt concentrations between CAC and CPC was substantiated by DLS. This study showed that CNCs have similar agglomeration behavior in the presence of sulfates, as in the presence of chlorides.

In the second part of the study, salt-specific CAC and CPC were used to design a neutralization-based downstream process, aiming at low water consumption. After CNC isolation, the reactant solution was neutralized with alkaline solutions of NH_4OH, KOH, NaOH, and $Ca(OH)_2$. Respectively identified stability ranges between CAC and CPC in the first part of this study were then used for salt removal in successive centrifugation and dilution steps, while dialysis or reverse osmosis was omitted. It was found that CAC and CPC are independent of CNC concentration and, therefore, this process can be further improved toward lower reactant consumption. Produced CNCs were colloidally stable and had similar properties to fully protonated CNCs. While economic feasibility of CNC production mainly aims at increasing yield during hydrolytic isolation of CNCs (*39, 178*), the proposed process design represents a further approach for lower reactant consumption, and more compact reactor design.

Author's contributions. The author was lead scientist in all parts of this work and conceptualized the study. He designed experiments together with DA. He conducted or supervised all data acquisition and performed most laboratory work. He performed most of the data evaluation. DA performed preparatory laboratory work and measured part of UV-Vis data. SD contributed SEM images and evaluated particle length distribution. HB supervised the research. All authors contributed to the discussion and interpretation of results. The manuscript was written by the author and discussed with HB, and all authors read and approved the final manuscript.

ORIGINAL RESEARCH

Agglomeration of cellulose nanocrystals: the effect of secondary sulfates and their use in product separation

Christoph Metzger · David Auber · Stephan Dähnhardt-Pfeiffer · Heiko Briesen

Abstract This study was aimed at the development of a better understanding of the agglomeration behavior of sulfated cellulose nanocrystals (CNCs) in the presence of sulfates with monovalent (NH_4^+, K^+, Na^+) and divalent (Ca^{2+}) cations, and to demonstrate their potential in simple and efficient product separation. Protonated CNCs were counterion-exchanged and their ionic strength was increased by adding sulfates of the respective cation to trigger agglomeration. The critical concentrations of agglomeration (CAC) and peptization (CPC) were determined. We found that the agglomeration behavior of CNCs could be attributed to matching affinities between the cations and the sulfate half-ester groups on the CNC surfaces. Based on these findings, a facile and efficient downstream process was designed to separate CNCs from neutralized reactant solutions using CAC and CPC. This method provides colloidally stable CNCs at high yield provided by centrifugation. When salt concentrations in the product are maintained below the CAC, as prepared CNCs from neutralized reactant solutions might be used in hydrogels and emulsions.

Keywords Cellulose nanocrystals · Agglomeration · Peptization · Colloidal behavior · UV–Vis · Separation efficiency

C. Metzger (✉) · D. Auber · H. Briesen
Chair of Process Systems Engineering, TUM School of Life Sciences Weihenstephan, Technical University of Munich, Munich, Germany
e-mail: christoph.metzger@tum.de

S. Dähnhardt-Pfeiffer
Microscopy Services Dähnhardt GmbH, Plambeckskamp 2, 24220 Flintbek, Germany

Introduction

Cellulose nanocrystals (CNCs) are nanorods with widths ranging from 3 to 50 nm and aspect ratios from 5 to 50 (ISO 2017b). They have received an increasing amount of attention from academia and industry alike due to their straightforward production and their remarkable physical and chemical properties, which make them high-performance building blocks for a wide range of potential commercial applications (Cowie et al. 2014; Thomas et al. 2018; Dufresne 2019). CNCs are commonly produced by sulfuric acid-catalyzed hydrolysis of purified cellulosic feedstock extracted from botanical sources, tunicates, or bacteria (Habibi et al. 2010; Sacui et al. 2014), although numerous extraction methods exist (Trache et al. 2017). Hydrolytic cleavage of glycosidic linkages and further breakdown of cellulose to glucose and

oligosaccharides, as well as conversion to 5-(hydroxymethyl)furfural preferably occurs in the amorphous domains of cellulose (Sun et al. 2016), leaving CNCs with higher acid resistance as the product. The morphology and yield of CNCs for a process are mainly determined by processing temperature, time, and the cellulose source (Beck-Candanedo et al. 2005; Dong et al. 2016). Concurrent with the hydrolysis, sulfate half-esters (R–O–SO$_3^-$) are grafted onto some of the hydroxy sites of the CNCs. The number density of surface sulfate groups can be controlled by acid concentration and the acid-to-cellulose ratio (Dong et al. 2016; Abitbol et al. 2018). The electric surface charge governs electrostatic interparticle repulsion forces and thus the colloidal stability of CNCs in polar media. CNCs produced by sulfuric acid-catalyzed hydrolysis usually contain between 240 and 330 mmol of sulfate per kg of CNCs (Dong et al. 1996; Araki et al. 1999).

Never-dried CNC colloids and counterion-exchanged CNCs (H$^+$ → Na$^+$) are commonly used for subsequent processing, as well as to produce new materials incorporating CNCs. Thus, a significant effort has been made to understand and to tune their colloidal stability. Several works have addressed the effect of electrolytes and ionic species on the agglomeration and gelation behavior of colloidal CNCs (Dong et al. 1996; Dong and Gray 1997; Boluk et al. 2011; Shafiei-Sabet et al. 2014; Cherhal et al. 2015; Peddireddy et al. 2016; Phan-Xuan et al. 2016; Bertsch et al. 2017; Mikhailov et al. 2017; Wu et al. 2017, 2019; Liu et al. 2018; Moud et al. 2018, 2019; Qi et al. 2019). All of the aforementioned studies focused on agglomeration of sulfated CNCs induced by chlorides, with inorganic counterions of varying valence. Studies have shown that the critical agglomeration concentration (CAC) of a volume of an electrolyte is in the range of tens of mM and decreases to a few mM with increasing valence of the counterion, roughly following the Schulze-Hardy rule (Phan-Xuan et al. 2016).

Agglomeration of CNCs also plays a role in downstream processing when CNCs are separated from the reactant solution that also contains sulfuric acid, the previously mentioned byproducts formed by hydrolysis, and incompletely hydrolyzed cellulosic residues. However, the unit operations involved have received only little attention. Hydrolysis of cellulose in a solution volume is usually quenched by adding a ten-fold amount of water (Trache et al. 2017). CNCs are then present in an agglomerated state due to the prevalently high ionic strength and cannot form a stable colloid. This agglomeration facilitates the removal of any excess ions and soluble reaction products by repeated washing by centrifugation and decanting of the supernatant, and subsequent redispersion in fresh water. In the presence of only sulfate anions, the critical peptization concentration (CPC) is approached at about 100 mM sulfuric acid when peptization of the CNCs occurs, recognizable by an accruing cloudiness of the supernatant. Subsequent washing steps at ionic strengths below the CPC would imply a loss of colloidally stable product fractions in the discarded supernatant. Thus, any further purification of the intermediate product involves low-efficiency techniques such as dialysis or reverse osmosis, or it requires special apparatus, for example for diafiltration or electrodialysis (Rudie 2017).

In scale-up scenarios, CNC production may involve neutralization of the remaining acid with caustic soda after centrifugation (Reiner and Rudie 2013; Assis et al. 2017). Alternatively, the reactant solution can be neutralized with mono- or divalent hydroxides or metal oxides at an arbitrary step in downstream processing (Müller and Briesen 2017, Metzger et al. 2018). By analogy with product separation from diluted reactant solutions, ionic residues must be thoroughly removed from neutralized reactant solutions to obtain a colloidally stable product.

To date, studies of salt-induced agglomeration of CNCs have only addressed the use of chlorides to control the product properties, while the roles of salt and ionic residues during product separation have received no attention to our knowledge. In this study, we hypothesize that CNCs will show similar agglomeration behavior in the presence of sulfates as they do with chlorides. We therefore presume that it is not only ionic strength but also the type of cation that contributes to the colloidal stability of CNCs. Because the separation efficiency by centrifugation is directly related to colloidal stability, we assumed that the introduction of cations during neutralization of the intermediate product affects the CPC. Therefore, neutralization can be used to reduce the effort to purify the product.

The colloidal stability of sulfated CNCs in the presence of the secondary sulfates (NH_4)$_2SO_4$, K_2SO_4, Na_2SO_4, and $CaSO_4$ was investigated in this work by a

fast and easy-to-use spectrophotometric method. The results were applied to design an efficient purification process based on the CAC and the CPC during centrifugation, yielding colloidally stable CNCs. The results are of particular interest for the sustainable production of CNCs with low resource requirements in downstream processing steps.

Materials and methods

Chemicals

Whatman ashless filter aids (cotton α-cellulose) were purchased from Sigma-Aldrich (Taufkirchen, Germany). Calcium hydroxide ($Ca(OH)_2$, 96%), sulfuric acid (H_2SO_4, 96%), potassium hydroxide (KOH, 85%), ammonium hydroxide (NH_4OH, 25%), and sodium hydroxide (NaOH, 99%) were used for preparing and processing CNCs and were purchased from Carl Roth (Karlsruhe, Germany). Poly-L-lysine (0.1% (aq), Ted Pella, Redding, CA, USA), ethanol (70%, Carl Roth, Karlsruhe, Germany), and uranyl acetate (SERVA, Heidelberg, Germany) were used for transmission electron microscopy. Sodium chloride (NaCl, 99.5%) and sodium hydroxide (NaOH (aq), 2 mM), required for conductometric titration, were purchased from Carl Roth. All chemicals were used in their as-received state. Ultrapure (type 1) water (H_2O) with a resistivity of 18.2 MΩ cm (Milli-Q Direct 8 system, Merck Chemicals, Schwalbach, Germany) was used to prepare solutions for all experiments.

Preparation and processing of CNCs

Aqueous colloidal suspensions of sulfated CNCs were prepared by heterogeneous hydrolysis of oven-dried (105 °C, 30 min) cellulose with sulfuric acid, based on the method of Cranston and Gray (2006). The bound water content of the cellulosic feedstock after drying was determined to be 4.5 wt% by Karl Fischer titration, and was considered when calculating the weighed portions of the educts. Sulfuric acid, 96 wt% was diluted to 64.2 wt% with water and pre-heated to 45 °C. Cellulose was added in at a mass-mixing ratio of 10 $m_{H_2SO_4} m_{cellulose}^{-1}$ with the weighed portions of sulfuric acid, $m_{H_2SO_4}$, and cellulose, $m_{cellulose}$, and stirred constantly for 45 min.

The agglomeration behavior of CNCs in the presence of secondary sulfates was studied in CNCs which were separated by centrifugation and dialysis (route A), as commonly reported in literature. The neutralization-based separation of CNCs by centrifugation (route B) was conducted to demonstrate the applicability of the results from route A. Both routes were implemented in this work as illustrated in the flowcharts in Fig. 1. A detailed description of the unit operations involved in both routes, as well as further treatment of the CNCs prior to subsequent analyses, is given in the following sections.

Route A: Product separation from diluted reactant solutions

After hydrolysis, the reactant solution was quenched by tenfold dilution with regard to the effective initial acid concentration (64 → 6.4 wt%) with 4 °C water. Excess acid and soluble byproducts were decanted after leaving the precipitate to settle overnight. The resultant cloudy suspension was washed by twofold centrifugation for 15 min at 4500 × g (Centrifuge 5804 R, Eppendorf, Hamburg, Germany), decanting, and further dilution with water. The precipitate was then dialyzed in regenerated cellulose tubes with a molecular weight cutoff of 12—14 kDa (ZelluTrans/ROTH T3, Carl Roth, Karlsruhe, Germany) against running water with a volumetric flow of 0.5 L h^{-1} in a 7 L vessel to remove the remaining acid and soluble byproducts. Dialysis was stopped when the waste water had a conductivity ≤ 30 μS cm^{-1} after equilibration for 6 h. Agglomerated CNCs were disagglomerated by sonication with a homogenizer (Sonopuls HD 3400 with the sonotrode VS 70 T, Bandelin, Berlin, Germany) at an energy input of 5 kJ g^{-1} cellulose and an amplitude setting of 30% in an ice bath. In accordance with Beck et al. (2011), no breakage of covalent cellulose-sulfate half-ester bonds—and thus no release of sulfate ions—was assumed due to sonication. Incompletely hydrolyzed solid cellulosic residues were then removed by centrifugation for 15 min at 4500 × g. Any further treatment with ion-exchange resins was omitted due to the extensive dialysis (Abitbol et al. 2013). The final dispersion of never-dried protonated CNCs, denoted as H-CNC, was stored at 4 °C until further use.

To study salt-induced agglomeration, H-CNCs were first neutralized as separate samples by the
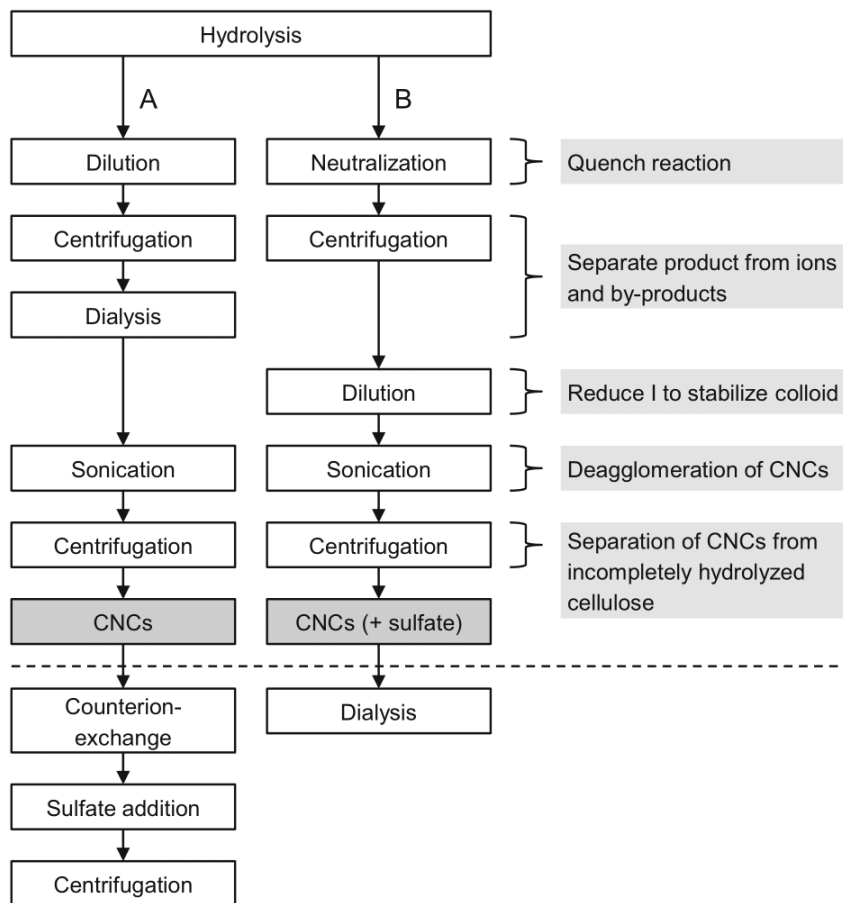
Fig. 1 Downstream processes for the purification of CNCs by centrifugation/dialysis (**a**) and neutralization/centrifugation (**b**). Further sample treatments for studying the agglomeration behavior and for determining the dispersion properties of the CNCs are presented below the dashed line

addition of the respective base until a stable pH of 7 was reached. The samples were named in accordance with the respectively exchanged counterion NH_4^+, K^+, Na^+, or Ca^{2+} (Table 1). Then, the CAC, at which agglomeration is initially observed, and the CPC, at which all CNCs are agglomerated, were empirically determined using a binary search approach. For this approach, the ionic strengths, I, of aliquots of each

Table 1 Nomenclature of CNCs by the respective counterions and properties of the associated secondary sulfates

Sample	Counterion	Associated sulfate salt	Salt solubility[a] /g L^{-1}
H-CNC	H^+		
NH_4-CNC	NH_4^+	$(NH_4)_2SO_4$	754
K-CNC	K^+	K_2SO_4	111
Na-CNC	Na^+	Na_2SO_4	170
Ca-CNC	1/2 Ca^{2+}	$CaSO_4$	2

[a]At 20 °C; data retrieved from the GESTIS substance database: gestis-en.itrust.de

sample were adjusted by adding aqueous solutions of the secondary sulfate. In accordance with the literature (Cherhal et al. 2015), agglomeration at higher salt concentrations occurred instantly for all salts and was visible to the unaided eye. Destabilized CNCs would settle out over time (Cherhal et al. 2015), but the fraction of colloidally stable CNCs, φ_s, was separated by centrifugation for 15 min at 4500 × g and optical absorbance was used to quantify φ_s. The ionic strength of each sample was then adjusted in 15 steps from the CAC to the CPC. The salt solutions had been previously prepared by mixing the respective bases with sulfuric acid. The CNC concentration was kept constant at 1 wt% throughout the experiments.

Route B: Product separation from neutralized reactant solutions

Partial quantities from the same batch that was used to produce the H-CNCs were separated after hydrolysis and the reaction was stopped by incremental neutralization with NH_4OH, KOH, NaOH, or $Ca(OH)_2$ to an excess of 15% of the initial sulfuric acid. For this operation, the reactant solutions were transferred to an ice bath to compensate for the neutralization enthalpy and were incrementally neutralized with their respective ice-cold base solutions. The concentration of bases with mono- and divalent cations was 1.25 M and 0.65 M, respectively. The intermediate products with monovalent cations were then washed by centrifugation for 15 min at 4500 × g, decanted to remove the supernatant, and successively redispersed in fresh water to remove excess ions and soluble byproducts from the hydrolyzed product. Each sample was then neutralized to a pH of 7 with its respective base. In the $CaSO_4$ sample, the salt concentration exceeded its maximum solubility. Enough water and base were added to fall below the CAC after the first washing step. The pellet, including precipitated $CaSO_4$ and entrained CNCs, was discarded. All samples were subsequently diluted to a salt concentration of 1.1 CPC and centrifuged again. The supernatant was decanted and the precipitate was diluted to 0.9 CAC using water. Similar to route A, all samples were eventually sonicated, centrifuged again, and stored at 4 °C until further use. Quantities of each sample were dialyzed to compare their dispersion properties to CNCs from route A.

Instrument measurements

All measurements were performed at least in triplicate and are presented with the 95% confidence interval of the mean. The uncertainty of quantities depending on multiple variables is driven by the propagation of error.

Conductometric titration

The content of the protonated sulfate half-esters (R-OSO_3H) of the CNCs was determined by conductometric titration (Konduktometer 703 with the electrode sensor SE 204, Knick, Berlin, Germany) at 23 °C, based on the method proposed by Beck et al. (2015). 5 mL of a 1 wt% CNC dispersion was diluted into 80 mL of water. 1 mL of 0.1 M NaCl (aq) was added to elevate the conductivity to a measurable level. 2 mM NaOH (aq) was used as titrant in 0.2 mL increments under constant stirring. Stable conductivity readings were recorded 30—60 s after each addition.

The volume-corrected conductivity values were plotted against the added volume of NaOH. The equivalence volume of NaOH needed, and thus the number of accessible sulfate groups, was calculated from the intersection of the least squares regression lines of the two linear branches ($R^2 \approx 1$) of the titration curve.

The conductivity of the waste water was also measured during dialysis (see Supporting Information).

Dry weight and yield calculations

The concentrations of dry constituents at different stages of production were calculated from the mass quotient of an aliquot before water evaporation, m_{wet}, and after water evaporation, m_{dry}, by lyophilization (2–4 LSCplus, Christ, Osterode am Harz, Germany). Acidic aliquots were neutralized to a pH of 7 by titration against NaOH before water evaporation, and the weight of the formed salt, m_{salt}, was considered in order to calculate the concentration of the cellulosic fraction. The cellulosic fraction of a sample of weight, m_{sample}, was then extrapolated from the aliquot's concentration. The yield refers to $m_{cellulose}$, considering the overall mass balance and losses of individual

unit operations. The yield, Y, of cellulosic solid residues after centrifugation is:

$$Y = \frac{m_{dry} - m_{salt}}{m_{wet}} \cdot \frac{m_{sample}}{m_{cellulose}} \qquad (1)$$

The cellulose-to-CNC conversion rate was calculated from the ratio of the dry mass after dialysis and the dry mass after dialysis, sonication, and centrifugation.

Concentration adjustments were performed by diluting the stock dispersions with the respective amount of water.

Dynamic and electrophoretic light scattering

The hydrodynamic apparent particle size of dispersed CNCs was measured by dynamic light scattering (DLS) using a Zetasizer Nano ZSP (Malvern Instruments, Worcestershire, UK) equipped with a red laser (633 nm) under a backscatter detection angle of 173°. The harmonic intensity-weighted average particle diameter (z-avg) and the polydispersity index (PdI) from the cumulants analysis were obtained according to ISO 22412 (2017a) for 0.025 wt% CNC dispersions after equilibration for 30 min at 25 °C in disposable polystyrene cuvettes.

The ζ potential is derived from the electrophoretic mobility of the CNCs, which was determined from electrophoretic light scattering (ELS) with the same instrument as above. 0.25 wt% CNC dispersions were analyzed after equilibration for 30 min at 25 °C in folded capillary cells (DTS1070). Smoluchowski behavior with $f(\kappa a) = 1.5$ was assumed for Henry's function, where κ was the Debye length and a the particle radius.

Transmission electron microscopy

Pioloform-coated copper grids (G2440C) from Plano (Wetzlar, Germany) were incubated with 0.1% poly-L-lysine at 23 °C for 30 min, rinsed with water, and dried under dust-free atmosphere. Never-dried CNCs were diluted with H_2O to a concentration of 0.025 wt% and homogenized in a low-intensity ultrasonic bath for 10 min before droplets of the suspension were applied to the grids with a pipette. After 20 min, the grids were rinsed with water and left for drying. Negative staining of the CNCs was performed with a saturated ethanolic uranyl acetate solution. Excess

liquid was removed and the samples were dried again. Transmission electron microscopy (TEM) images were acquired with a Philips CM10 instrument, coupled with a CCD camera (IDS, Obersulm, Germany), at an acceleration voltage of 80 kV. Particle length L was evaluated from 66 randomly chosen, individual particles using ImageJ (Rasband 2018).

UV–Vis spectrophotometry

Cellulose has no conjugated or unsaturated bonds. Hence, the optical absorption of transmitted light in the forward direction (180°) is 0 and the absorbance is governed by scattering only. For non-absorbing particles, the specific absorbance A at infinite dilution of colloidally stable CNCs, $c_{CNC} \rightarrow 0$, is

$$\left(\frac{A}{c_{CNC}}\right)_0 = k\lambda^{-n} \qquad (2)$$

with the scattering coefficient k, the wavelength λ, and the wavelength exponent n (Heller et al. 1962). k is a function of a and the relative refractive indices of the particles μ_2 and the dispersant μ_1. n is a function of a and can be derived from the slope of $\ln\left(Ac_{CNC}^{-1}\right)$ versus $\ln \lambda$.

For non-spherical particles, the scattering cross sections and therefore the equivalent radii a_{eq} can be represented by the radii of spheres with equivalent volume-to-surface-area ratios (Grenfell and Warren 1999). The size parameter

$$x = \frac{2\pi a_{eq}}{\lambda} \qquad (3)$$

of the CNCs being not significantly smaller than 1 over the scanned wavelength range indicates Mie scattering, while Rayleigh scattering can be ignored. This was confirmed on absorbance spectra with a_{eq} derived from TEM data and wavelength-dependent refractive index data of cellulose from Sultanova et al. (2009), modeled with MiePlot (Laven 2018).

Thus, a linear relationship between the specific absorbance of a sample and the respective CNC concentration is observed. UV–Vis spectrophotometry is therefore suitable for the determination of the concentration of non-spherical colloidal CNCs with similar equivalent radii by using a comparison library of spectra of known CNC concentrations. A change of a_{eq}—for example induced by agglomeration, a change

in polydispersity, or the use of particles of different dimensions—would manifest in a change of n. This establishes a validity criterion for the applicability of the library to the measurement data, but also limits its applicability for the determination of CNC concentration to particles of similar sizes only. The evaluation of the validity of measurement is shown in the Supplementary Information.

A library of the UV–Vis absorbance spectra was set up, consisting of 18 individual samples of H-CNCs with defined concentrations between 0 and 1 wt%. Aliquots of 1 mL were transferred to quartz glass cuvettes with an optical path length of 10 mm and spectra were recorded with a Specord 50 Plus spectrophotometer (Analytik Jena, Jena, Germany) in the wavelength range from 200 to 500 nm. The CNC concentration of an arbitrary, water-dispersed sample could then be calculated from Eq. (2), for a sample concentration that is in the same concentration range as the library.

Results and discussion

H-CNCs from diluted reactant solution

H-CNCs were produced by sulfuric acid-catalyzed hydrolysis of cellulose according to route A. A CPC of 115 mM SO_4^{2-} of CNCs in the presence of residual sulfuric acid was empirically determined in a binary search. The yield of cellulosic solid residues after centrifugation was $46.2 \pm 0.6\%$.

Further purification of the product was achieved by using dialysis. The conductivity of the waste water decayed exponentially to 30 μS cm^{-1} after 166 h and the exchange of 83 L of water (see Supporting Information). CNCs were separated from incompletely hydrolyzed solid cellulosic residues by centrifugation subsequent to dialysis and sonication. The overall yield for cellulose-to-CNC conversion was $33.9 \pm 0.5\%$.

Figure 2a is a representative TEM image of H-CNCs. The number-weighted particle length distribution of H-CNCs ranged from 70 to 230 nm with a mean particle length L_{mean} of 120 nm (Fig. 2b). Particle width W was estimated to be ≤ 10 nm for the particles, yielding an aspect ratio of ≤ 25 for all H-CNCs. The mean hydrodynamic apparent particle diameter of H-CNCs was 198 ± 4 nm.

Overestimation of the particle size by DLS in relation to the more accurate TEM evaluation can be explained by the presence of a minor fraction of strongly scattering larger particles (Jakubek et al. 2018). The PdI of 0.21 ± 0.02 suggests moderate polydispersity, in accordance with the TEM images.

The ζ potential of the H-CNCs was -47.5 ± 5.4 mV and had a distribution width $\Delta\zeta$ of 7.8 ± 1.2 mV. A sulfate half-ester content of 238 ± 5 mmol kg^{-1} was determined by conductometric titration. Table 2 summarizes the results from cellulose hydrolysis and the most relevant properties of H-CNCs. The data is in accordance with literature values (Bondeson et al. 2006; Reid et al. 2017).

Salt-induced agglomeration of CNCs

Cation-specific agglomeration of CNCs by the addition of sulfate salts

Colloidally stable CNCs in the presence of salts form self-similar clusters as a function of the salt concentration (Cherhal et al. 2015; Phan-Xuan et al. 2016; Moud et al. 2018). Therefore, controlling the ionic species and the salt concentration provides control over colloidal stability and thus the agglomeration of CNCs.

Colloidal stability of counterion-exchanged CNCs was not impeded by minor salt additions, so the number fraction of colloidally stable CNCs remained constant until the salt concentration exceeded the CAC. As can be observed from Fig. 3a, the concentration of colloidally stable CNCs indeed did decline at salt concentrations above the CAC. The evolution of agglomeration with increasing salt concentration for every sulfate salt followed canonical colloidal behavior (Gregory 1976). Above the CPC, all CNCs were agglomerated and could be sedimented by centrifugation, leaving no colloidally stable CNCs in the supernatant. Both CAC and CPC follow the sequence $K^+ < Na^+ < NH_4^+ < Ca^{2+}$.

All monovalent salts have similar interval widths of $\Delta CxC = CPC$—CAC, and a comparatively narrower one for the salt with a divalent cation (Table 3). Each salt has a different CAC and CPC with regard to its ionic strength and therefore agglomeration cannot be explained by the screening of electrostatic surface charge alone (Fig. 3b). Monovalent cations do not follow Hofmeister's lyotropic series $NH_4^+ < K^+$
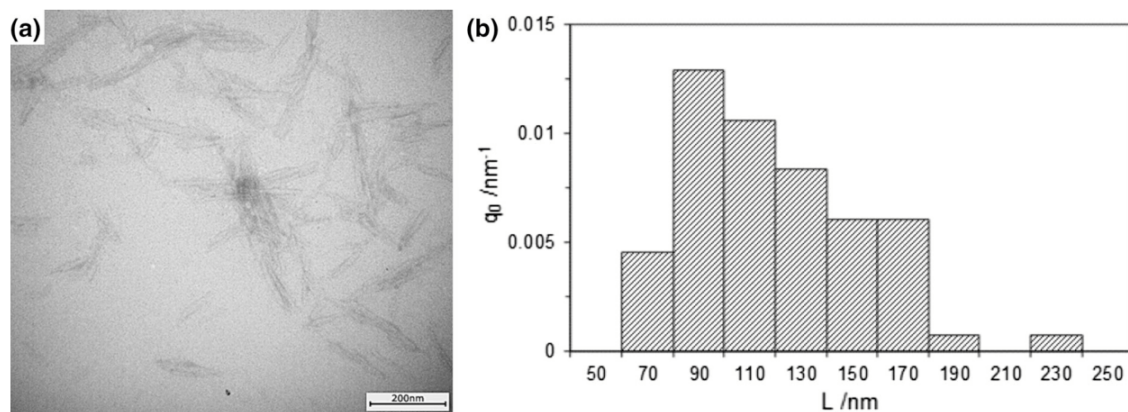
Fig. 2 TEM image of negatively stained H-CNCs (**a**) and number-weighted length distribution from 66 particles (**b**)

Table 2 Summary of hydrolysis and dispersion properties of H-CNCs

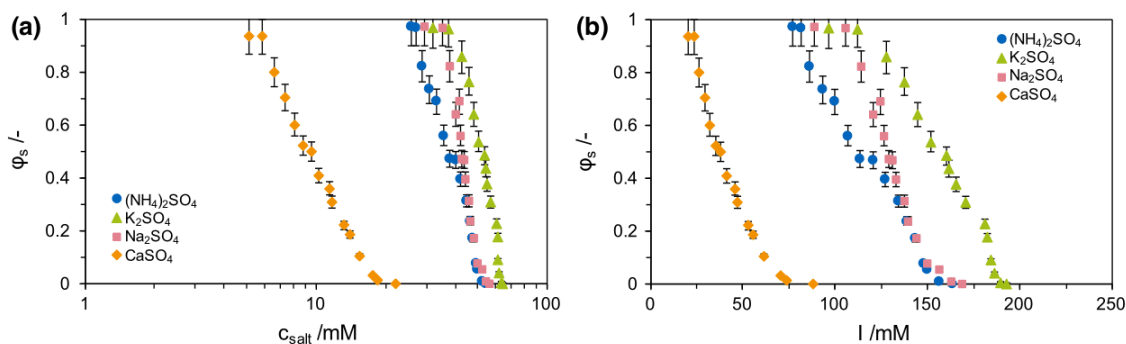| Yield (solids) (%)	Yield (CNCs) (%)	L (TEM) (Nm)	z-avg (nm)	ζ (mV)	c (R-OSO$_3^-$) (mmol kg^{-1})
46.2 ± 0.6	33.9 ± 0.5	70–230	198 ± 4	-47.5 ± 5.4	238 ± 5

Fig. 3 Concentration of colloidally stable CNCs, φ_s, as a function of salt concentration c_{salt} (**a**) and ionic strength I (**b**) for mono- and divalent secondary sulfates in separate aliquots having the same initial CNC concentration

Table 3 Critical concentrations and ionic strengths for agglomeration and peptization of CNCs in the presence of mono- and divalent secondary sulfates

Counterion	CAC			CPC			ΔCxC		
	c (mM)	I (mM)	$m_{salt}\ m_{CNC}^{-1}$ (mg g^{-1})	c (mM)	I (mM)	$m_{salt}\ m_{CNC}^{-1}$ (mg g^{-1})	c (mM)	I (mM)	$m_{salt}\ m_{CNC}^{-1}$ (mg g^{-1})
NH$_4^+$	27	82	360	52	157	690	25	75	330
K$^+$	37	112	650	63	189	1100	26	77	450
Na$^+$	35	106	50	56	169	800	21	63	750
Ca^{2+}	6	24	8	18	73	250	12	50	242

< Na^+ (Hofmeister 1888). Furthermore, there is a marked difference in the agglomeration behavior of CNCs in the presence of a sulfate with a divalent cation with regards to its ionic strength. A tentative explanation of the deviation from DLVO theory of CNCs in the presence of salts has been proposed by Phan-Xuan et al. (2016). The differing magnitude of the impact of salts on the agglomeration of CNCs could be explained by the law of matching affinities (Vlachy et al. 2009). Soft cations in terms of charge density—such as NH_4^+ and Ca^{2+}—trigger earlier agglomeration of CNCs electrostatically stabilized by soft sulfate half-ester groups. The strong effect of Ca^{2+} on agglomeration could furthermore be induced by more intense clustering of CNCs in the presence of divalent salts, or could be initiated due to cross-linking of CNCs by multivalent cations (Wu et al. 2017; Moud et al. 2019).

Colloidal stability at different salt concentrations

Figure 4a shows the evolution of the ζ potential of CNCs in the presence of sulfate salts with different cations between CAC and CPC. Adding a salt to sulfated CNCs promotes the screening of electrostatic charges and gel formation by particle agglomeration (Peddireddy et al. 2016; Moud et al. 2018). Thus, colloidal stability at the CAC was inferior to H-CNCs, manifesting in lower absolute ζ potentials in the presence of the sulfates. Soft cations showed an effect on colloidal stability at lower ionic strengths. The addition of sulfate salts in concentrations slightly above the CAC led to the precipitation of unstable clusters, which were sedimented by centrifugation and removed from the aliquots, as well as an increase in the absolute ζ potential of the colloidally stable particle fraction. The evolution of the ζ potential between CAC and CPC showed similar trends for all sulfates with increasing salt concentration; first, colloidal stability increased with increasing ionic strength, but
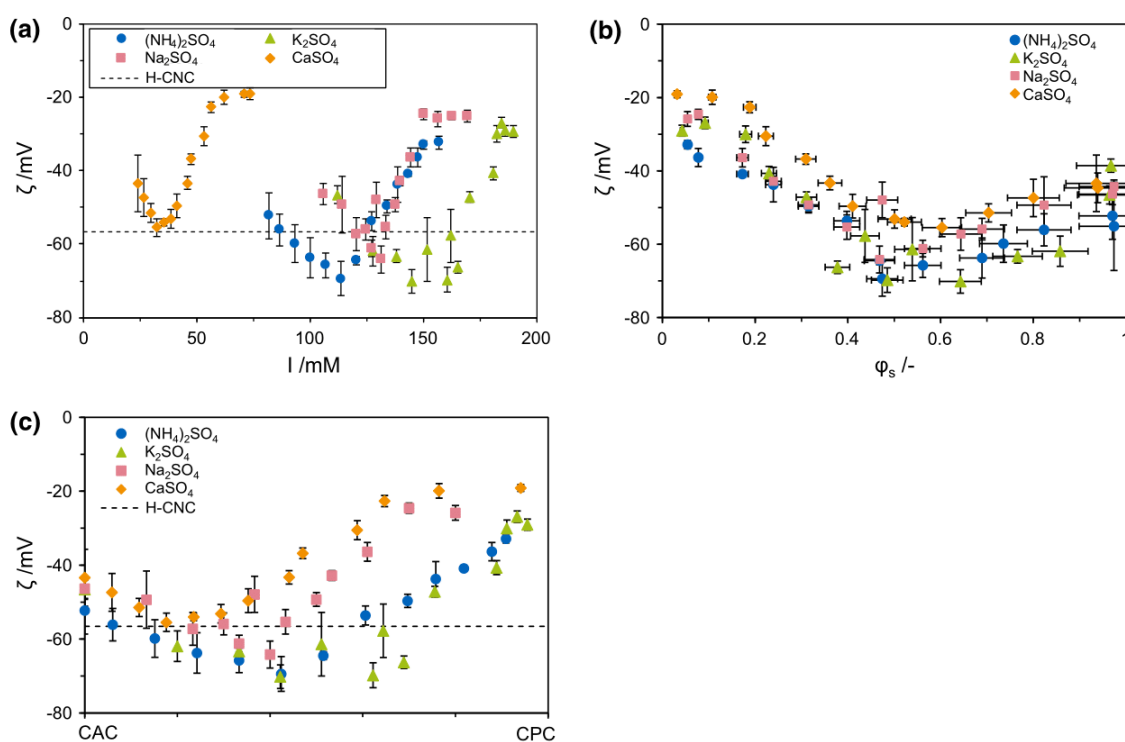

Fig. 4 Zeta potential of colloidally stable CNCs in the presence of mono- and divalent secondary sulfates as a function of ionic strength (**a**), as a function of the fraction of colloidally stable CNCs φ_s (**b**), and as normalized between CAC and CPC (**c**)

then decreased to $|-20|$–$|-30|$ mV towards the CPC (Fig. 4b, c). The highest absolute ζ potential for every salt was observed at $\varphi_s \approx 0.5$.

It must be noted that the stable CNC fraction was very small toward the CPC (compare to Fig. 3a, b). Considering the loss of CNCs, adding salts between the CAC and the CPC could enable fractionation of CNCs by their colloidal stability (see Supporting Information).

Figure 5 shows the hydrodynamic particle diameter of CNCs between CAC and CPC in the presence of sulfates having different cations. Increasing ionic strength has led to an overall higher z-avg compared to that of H-CNCs. This might be caused by the formation of denser clusters and elongated agglomerates due to an increasing number of contact points per particle (Moud et al. 2018). However, in our study, no correlation of hydrodynamic particle diameter and salt concentration or ζ potential was found. This result suggested that a weak cluster network with similar colloidal structures independent of the salt concentration, which has been observed by Moud et al. (2018) in CNCs in the presence of sodium chloride.

Efficiency of separation of CNCs from neutralized reactant solutions

The use of secondary sulfates for efficient CNC product separation by using the CAC and the CPC is demonstrated. For this purpose, the hydrolysis process was stopped by neutralizing the reactant solution with NH_4OH, KOH, $NaOH$, and $Ca(OH)_2$. Washing steps were designed according to the CAC and the CPC, determined on H-CNCs (route B).
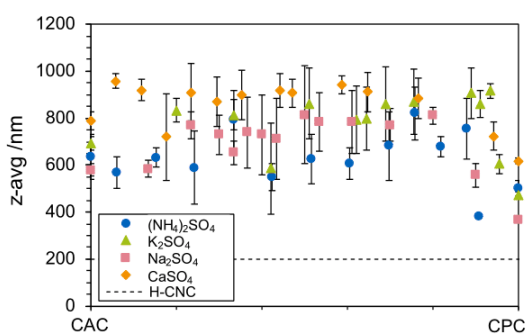

Fig. 5 Hydrodynamic apparent particle size (z-avg) of colloidally stable CNCs in the presence of mono- and divalent secondary sulfates, normalized between CAC and CPC

Salt solubility (Table 1), ionic strength at the CPC, and ΔCxC determine the amount of water required during product separation (see Supporting Information). Accordingly, the final CNC concentration was highest for sulfates with monovalent cations (Table 4). Since the agglomeration behavior of CNCs does not depend on particle concentration (Phan-Xuan et al. 2016), the parameter that must be considered is the ionic strength at the CAC of the final CNC dispersion. Thus, by concentrating the intermediate sample, the method demonstrated here allows for higher final CNC concentrations and the salt-to-CNC ratio can be further reduced, yielding higher product purity.

Figure 6 shows the yield and colloidal properties of H-CNCs compared to CNCs produced by route B using different base solutions for neutralization. To assess the colloidal properties under equivalent conditions, CNCs produced by route B were thoroughly dialyzed.

The yield of cellulose-to-CNC conversion was similar for each separation procedure involving sulfates with monovalent cations. The slightly lower yields of CNCs that were obtained from route B than for the production of H-CNCs were attributed to product loss during manual sample handling. The significantly lower yield for neutralization with $Ca(OH)_2$ was attributed to the loss of intermediate product with the precipitated salt. About 13% fewer sulfate half-ester groups per unit weight of CNCs were available for neutralized CNCs compared to H-CNCs. Thus, it was not possible to remove all counterions by dialysis; further deionization could be achieved by using a strong acid exchange resin (Abitbol et al. 2013). The lower concentration of accessible sulfate half-ester groups, in conjunction with the slightly greater hydrodynamic diameter, indicated the

Table 4 Concentration of colloidally stable CNCs in the product after neutralization and centrifugation, as well as the salt concentration, normalized to the relative salt-to-CNC mass ratio and the ionic strength

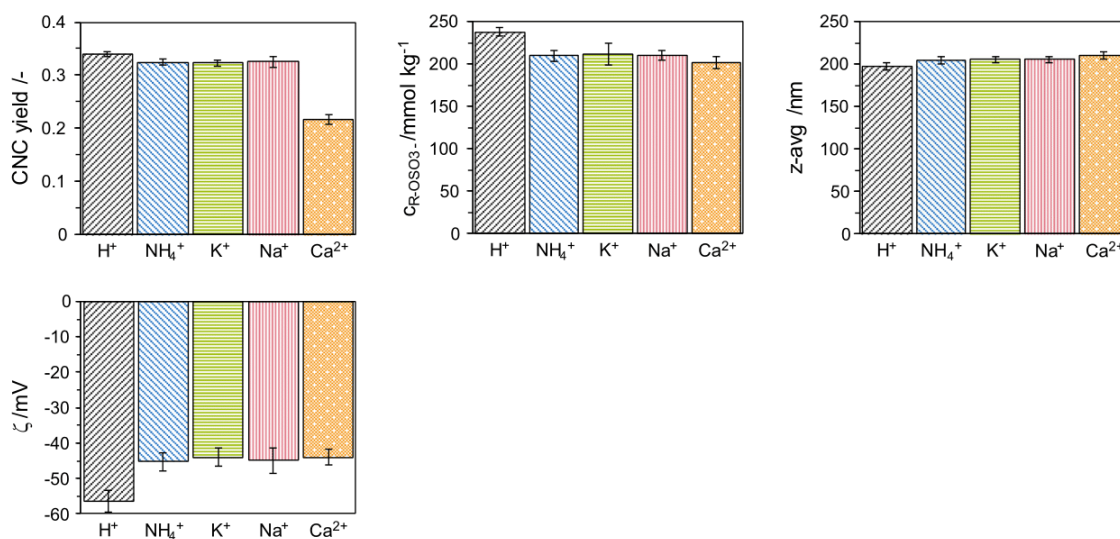| Counterion	c_{CNC} /wt%	$m_{salt}\, m_{CNC}^{-1}$ /g g^{-1}	I /mM
NH_4^+	1.675 ± 0.026	0.193 ± 0.003	18
K^+	2.525 ± 0.045	0.233 ± 0.004	25
Na^+	2.254 ± 0.074	0.201 ± 0.007	13
Ca^{2+}	0.661 ± 0.026	0.111 ± 0.004	4

Fig. 6 Yield and dispersion properties of H-CNCs in comparison to CNCs from neutralized and centrifuged reactant solutions

presence of CNC agglomerates which were not entirely broken up by sonication. Lower colloidal stability of CNCs as compared to H-CNCs was also reflected in the lower absolute ζ potential of CNCs from neutralized reactant solutions.

Conclusions and outlook

The agglomeration behavior of cellulose nanocrystals extracted from ashless cotton cellulose was studied in the presence of four secondary sulfates with mono- and divalent cations from Groups 1 and 2 of the periodic table. An increase of ionic strength led to progressively greater agglomeration between the CAC and the CPC. Colloidal stability of CNCs was observed at salt concentrations below the CAC. No stable colloids formed at salt concentrations above the CPC. Both CAC and CPC varied among the different types of mono- and divalent cations. Therefore, agglomeration behavior is not attributable to electro-static charge screening only and can be attributed to cluster formation and matching affinities. This result corroborates the hypothesis of similar agglomeration behavior of CNCs in the presence of sulfates as with that in the presence of chlorides. CAC and CPC were identified for each sulfate, and were applied in designing a neutralization-based downstream process.

Peptization of CNCs at decreasing ionic strengths limits the applicability of centrifugation for product separation after hydrolysis and dilution. Therefore, the CPC was shifted by introducing cations during neutralization of the reactant solution with NH_4OH, KOH, NaOH, and $Ca(OH)_2$. Using both the CAC and the CPC for salt removal by successive centrifugation and dilution steps facilitated efficient separation of CNCs. The validity of the CAC and the CPC at higher CNC concentrations proves their independence of the CNC concentration. Thus, the process can be further improved to demand lower water consumption as well as lower consumption of other educts by first quench-ing the reaction with water, and then neutralizing the remaining acid after the first centrifugation.

When the added base formed a highly soluble sulfate salt, product yields were equal to those achieved for CNCs separated by dialysis. Any salt remaining in the product from neutralized solutions affected the dispersion properties of the CNCs; however, stable colloids were obtained. Reduction of the salt-to-cellulose ratio during centrifugation would enable lower salt concentrations in the product, by scaling the cellulosic portion. But dialyzing neutral-ized intermediate products did not result in fully protonated CNCs, and further purification might be accomplished through the use of ion-exchange resins. When ionic traces in the product are negligible for its use case, our process reduces the need for additional

effort in product purification, since most sulfates are benign.

Knowledge about the CAC and the CPC could be used for fractionating CNCs by their colloidal stability. In the original never-dried state, the salt concentration can be adjusted to control the hydrogel structure. Last, intrinsically present counterions and salts promote redispersibility of dried CNCs and the stability of pickering emulsions (Beck et al. 2012; Missoum et al. 2012; Liu et al. 2018).

Authors' contributions CM and DA conceptualized and designed the study. Material preparation, data collection, and analysis were performed by CM, DA, and SDP. HB supervised the research. All authors contributed to the discussion and interpretation of results. The first draft of the manuscript was written by CM, and all authors reviewed and edited the successive versions of the manuscript. All authors read and approved the final manuscript.

Data Availability The authors confirm that the data supporting the conclusions of this article are included within the article and its supplementary materials.

Compliance with ethical standards

Conflict of interest The authors declare that they have no conflict of interest.

References

Abitbol T, Kloser E, Gray DG (2013) Estimation of the surface sulfur content of cellulose nanocrystals prepared by sulfuric acid hydrolysis. Cellulose 20(2):785–794

Abitbol T, Kam D, Levi-Kalisman Y, Gray DG, Shoseyov O (2018) Surface charge influence on the phase separation and viscosity of cellulose nanocrystals. Langmuir 34(13):3925–3933

Araki J, Wada M, Kuga S, Okano T (1999) Influence of surface charge on viscosity behavior of cellulose microcrystal suspension. J Wood Sci 45(3):258–261

de Assis CA, Houtman C, Phillips R, Bilek EM, Rojas OJ, Pal L, Peresin MS, Jameel H, Gonzalez R (2017) Conversion economics of forest biomaterials: risk and financial analysis of CNC manufacturing. Biofuels Bioprod Bioref 11(4):682–700

Beck S, Bouchard J, Berry R (2011) Controlling the reflection wavelength of iridescent solid films of nanocrystalline cellulose. Biomacromol 12(1):167–172

Beck S, Bouchard J, Berry R (2012) Dispersibility in water of dried nanocrystalline cellulose. Biomacromol 13(5):1486–1494

Beck S, Méthot M, Bouchard J (2015) General procedure for determining cellulose nanocrystal sulfate half-ester content by conductometric titration. Cellulose 22(1):101–116

Beck-Candanedo S, Roman M, Gray DG (2005) Effect of reaction conditions on the properties and behavior of wood cellulose nanocrystal suspensions. Biomacromol 6(2):1048–1054

Bertsch P, Isabettini S, Fischer P (2017) Ion-induced hydrogel formation and nematic ordering of nanocrystalline cellulose suspensions. Biomacromol 18(12):4060–4066

Boluk Y, Lahiji R, Zhao L, McDermott MT (2011) Suspension viscosities and shape parameter of cellulose nanocrystals (CNC). Colloid Surf Physicochem Eng Aspects 377(1–3):297–303

Bondeson D, Mathew A, Oksman K (2006) Optimization of the isolation of nanocrystals from microcrystalline cellulose by acid hydrolysis. Cellulose 13(2):171–180

Cherhal F, Cousin F, Capron I (2015) Influence of charge density and ionic strength on the aggregation process of cellulose nanocrystals in aqueous suspension, as revealed by small-angle neutron scattering. Langmuir 31(20):5596–5602

Cowie J, Bilek EM, Wegner TH, Shatkin JA (2014) Market projections of cellulose nanomaterial-enabled products—part 2: volume estimates. TAPPI J 13(6):57–69

Cranston ED, Gray DG (2006) Morphological and optical characterization of polyelectrolyte multilayers incorporating nanocrystalline cellulose. Biomacromol 7(9):2522–2530

Dong XM, Gray DG (1997) Effect of counterions on ordered phase formation in suspensions of charged rodlike cellulose crystallites. Langmuir 13(8):2404–2409

Dong XM, Kimura T, Revol J-F, Gray DG (1996) Effects of ionic strength on the isotropic−chiral nematic phase transition of suspensions of cellulose crystallites. Langmuir 12(8):2076–2082

Dong S, Bortner MJ, Roman M (2016) Analysis of the sulfuric acid hydrolysis of wood pulp for cellulose nanocrystal

production: a central composite design study. Industrial Crops Prod 93:76–87

Dufresne A (2019) Nanocellulose processing properties and potential applications. Curr Forestry Rep 5(2):76–89

Gregory J (1976) The effect of cationic polymers on the colloidal stability of latex particles. J Colloid Interface Sci 55(1):35–44

Grenfell TC, Warren SG (1999) Representation of a nonspherical ice particle by a collection of independent spheres for scattering and absorption of radiation. J Geophys Res 104(D24):31697–31709

Habibi Y, Lucia LA, Rojas OJ (2010) Cellulose nanocrystals: chemistry, self-assembly, and applications. Chem Rev 110(6):3479–3500

Heller W, Bhatnagar HL, Nakagaki M (1962) Theoretical investigations on the light scattering of spheres. XIII. The ''wavelength exponent'' of differential turbidity spectra. J Chem Phys, 36(5):1163–1170

Hofmeister F (1888) Zur Lehre von der Wirkung der Salze. Archiv f experiment Pathol u Pharmakol 24(4–5):247–260

ISO (2017a) ISO 22412:2017-Particle size analysis—Dynamic light scattering (DLS), 2017-02. International Organization for Standardization, Geneva, Switzerland. https://www.iso.org/standard/65410.html

ISO (2017b) ISO/TS 20477:2017-Nanotechnologies-standard terms and their definition for cellulose nanomaterial, 2017-10. International Organization for Standardization, Geneva, Switzerland. https://www.iso.org/standard/68153.html

Jakubek ZJ, Chen M, Couillard M, Leng T, Liu L, Zou S, Baxa U, Clogston JD, Hamad WY, Johnston LJ (2018) Characterization challenges for a cellulose nanocrystal reference material: dispersion and particle size distributions. J Nanopart Res, 20(4)

Laven P (2018) MiePlot 4.6-https://www.philiplaven.com/mieplot.htm

Liu L, Hu Z, Sui X, Guo J, Cranston ED, Mao Z (2018) Effect of counterion choice on the stability of cellulose nanocrystal pickering emulsions. Ind Eng Chem Res 57(21):7169–7180

Metzger C, Sanahuja S, Behrends L, Sängerlaub S, Lindner M, Briesen H (2018) Efficiently extracted cellulose nanocrystals and starch nanoparticles and techno-functional properties of films made thereof. Coatings 8(4):142

Mikhailov VI, Torlopov MA, Martakov IS, Krivoshapkin PV (2017) Stability of nanocrystalline cellulose in aqueous KCl solutions. Colloid J 79(2):226–233

Missoum K, Bras J, Belgacem MN (2012) Water redispersible dried nanofibrillated cellulose by adding sodium chloride. Biomacromol 13(12):4118–4125

Moud AA, Arjmand M, Yan N, Nezhad AS, Hejazi SH (2018) Colloidal behavior of cellulose nanocrystals in presence of sodium chloride. ChemistrySelect 3(17):4969–4978

Moud AA, Arjmand M, Liu J, Yang Y, Sanati-Nezhad A, Hejazi SH (2019) Cellulose nanocrystal structure in the presence of salts. Cellulose 26:9387–9401

Müller V, Briesen H (2017) Nanocrystalline cellulose, its preparation and uses of such nanocrystalline cellulose. U.S. Patent 20170306056 A1

Peddireddy KR, Capron I, Nicolai T, Benyahia L (2016) Gelation kinetics and network structure of cellulose nanocrystals in aqueous solution. Biomacromol 17(10):3298–3304

Phan-Xuan T, Thuresson A, Skepö M, Labrador A, Bordes R, Matic A (2016) Aggregation behavior of aqueous cellulose nanocrystals: the effect of inorganic salts. Cellulose 23(6):3653–3663

Qi W, Yu J, Zhang Z, Xu HN (2019) Effect of pH on the aggregation behavior of cellulose nanocrystals in aqueous medium. Mater Res Express 6(12):125078

Rasband W (2018) ImageJ 1.52h - https://imagej.nih.gov/ij/. NIH

Reid MS, Villalobos M, Cranston ED (2017) Benchmarking cellulose nanocrystals: from the laboratory to industrial production. Langmuir 33(7):1583–1598

Reiner RS, Rudie AW (2013) Process scale-up of cellulose nanocrystal production to 25 kg per batch at the Forest Products Laboratory. In: Postek MT, Moon RJ, Rudie AW, Bilodeau M (eds) Production and applications of cellulose nanomaterials. TAPPI Press, Peachtree Corners, GA, USA, pp 21–24

Rudie A (2017) Commercialization of cellulose nanofibril (CNF) and cellulose nanocrystal (CNC): pathway and challenges. In: Kargarzadeh H, Ahmad I, Thomas S, Dufresne A (eds) Handbook of nanocellulose and cellulose nanocomposites, vol 1. Wiley-VCH. Weinheim, Germany, pp 761–797

Sacui IA, Nieuwendaal RC, Burnett DJ, Stranick SJ, Jorfi M, Weder C, Foster EJ, Olsson RT, Gilman JW (2014) Comparison of the properties of cellulose nanocrystals and cellulose nanofibrils isolated from bacteria, tunicate, and wood processed using acid, enzymatic, mechanical, and oxidative methods. ACS Appl Mater Interfaces 6(9):6127–6138

Shafiei-Sabet S, Hamad WY, Hatzikiriakos SG (2014) Ionic strength effects on the microstructure and shear rheology of cellulose nanocrystal suspensions. Cellulose 21(5):3347–3359

Sultanova N, Kasarova S, Nikolov I (2009) Dispersion properties of optical polymers. Acta Phys Pol A 116(4):585–587

Sun Y, Liu P, Liu Z (2016) Catalytic conversion of carbohydrates to 5-hydroxymethylfurfural from the waste liquid of acid hydrolysis NCC. Carbohydrate Polym 142:177–182

Thomas B, Raj MC, Athira KB, Rubiyah MH, Joy J, Moores A, Drisko GL, Sanchez C (2018) Nanocellulose, a versatile green platform: from biosources to materials and their applications. Chem Rev 118(24):11575–11625. https://doi.org/10.1021/acs.chemrev.7b00627

Trache D, Hussin MH, Haafiz MKM, Thakur VK (2017) Recent progress in cellulose nanocrystals: sources and production. Nanoscale 9(5):1763–1786

Vlachy N, Jagoda-Cwiklik B, Vácha R, Touraud D, Jungwirth P, Kunz W (2009) Hofmeister series and specific interactions of charged headgroups with aqueous ions. Adv Colloid Interface Sci 146(1–2):42–47

Wu Q, Li X, Fu S, Li Q, Wang S (2017) Estimation of aspect ratio of cellulose nanocrystals by viscosity measurement: influence of surface charge density and NaCl concentration. Cellulose 24(8):3255–3264

Wu Q, Li X, Li Q, Wang S, Luo Y (2019) Estimation of aspect ratio of cellulose nanocrystals by viscosity measurement: influence of aspect ratio distribution and ionic strength. Polymers 11(5):781

Supporting Information

Agglomeration of Cellulose Nanocrystals: The Effect of Secondary Sulfates and Their Use in Product Separation

Christoph Metzger,[1,†] David Auber,[1] Stephan Dähnhardt-Pfeiffer,[2] Heiko Briesen[1]

[1]*Technical University of Munich, Germany, TUM School of Life Sciences Weihenstephan, Chair of Process Systems Engineering*

[2]*Microscopy Services Dähnhardt GmbH, Plambeckskamp 2, 24220 Flintbek, Germany*

[†]+49 8161 71-5383

[1]+49 8161 71-4510

[†]christoph.metzger@tum.de

[†]http://svt.wzw.tum.de/

1

Karl Fischer titration

The water content of cellulose was determined by volumetric Karl Fischer titration (TitroLine KF, Xylem Analytics, Weilheim, Germany). All chemicals were purchased from Carl Roth (Karlsruhe, Germany). The iodine titrant (Roti®hydroquant C5; 5 mg H_2O mL^{-1}, free of pyridine) was determined with the water standard (Roti®hydroquant; 10 mg H_2O g^{-1}). Methanol (Roti®hydroquant D; dry) and formamide (99.5%) were used as solvent in a volume ratio of 1.5 : 1. About 0.3 g of cellulose was added to the solvent. The titration was started when the sample was completely dissolved. The solvent was exchanged after each measurement.

Concentration determination by UV-Vis spectrophotometry – validity of approach

UV-Vis spectra of H-CNCs of different concentrations

A stock solution of 1 wt.% H-CNCs was prepared and UV-Vis absorbance spectra between 0 and 1 wt.% were recorded in the λ range of 200 to 500 nm (see **Fig. S1a**). Linearity of $A(\lambda,c)$ vs. c was best between 229 and 476 nm ($R^2 \geq 0.99$). Thus, data evaluation was done in the λ range between 250 and 450 nm. The mean absolute error of the library was 0.9% and 0.5% for CNC concentrations > 0.1 wt.%. The mean wavelength exponent n of all spectra was 3.354 ± 0.012 and the mean scattering coefficient k was 0.151 ± 0.008.

For H-CNCs, a slight decrease of k was observed from $k_{c \to 0} = 0.167 \pm 0.010$ with a rate of -0.044 ± 0.003 g_{CNC}^{-1}. The concentration-dependent change of k might be induced by the increasing probability of multiple scattering with increasing particle concentration. However, the error introduced to the evaluation was negligible.
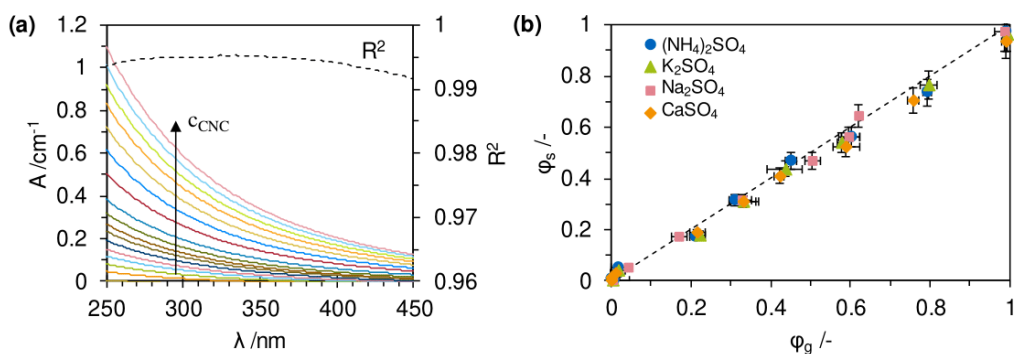
2

Fig. S1 Absorbance spectra of H-CNCs between 0 and 1 wt.% (a) and correlation of spectroscopically and gravimetrically determined CNC concentration (b)

UV-Vis spectra of CNCs in the presence of salts

In the presence of salt, the wavelength coefficient increased slightly for all investigated salts (see **Fig. S2**). Towards high ionic strengths, n increased strongly, which might indicate cluster growth.
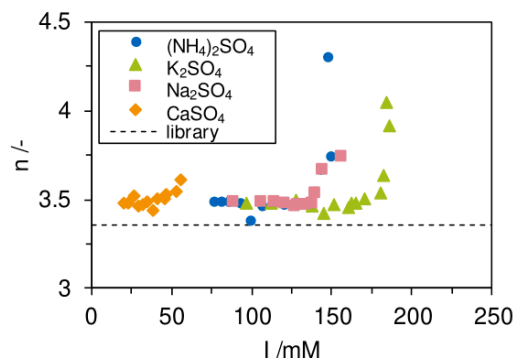
Fig. S2 Wavelength coefficients of CNCs in the presence of different salts and varying salt concentrations

The validity of the determination of CNC concentration was checked by correlating the mass fraction of CNCs derived from the spectra library φ_s and the gravimetrically determined mass fraction of the respective aliquot φ_g (see **Fig. S1**b). The data was in good agreement and therefore the spectra library is seen as suitable to determine the concentration of colloidally stable CNCs in the presence of salts.

Particle size distributions with a_{eq}, recalculated from L_{mean} and a reasonable range of values for W (5 - 20 nm) as well as the mean hydrodynamic apparent particle diameter, were set up to model the respective absorbance spectra. No interparticle interaction and equal probability of all orientational scattering states of the particles was assumed. Resulting wavelength exponents of $n \approx 4$ indicated

3

an underestimation of the actual scattering area or the polydispersity of the CNCs. Thus, information from ex-situ TEM or DLS are not suitable to model the actual absorbance profile of scattering of CNCs. One-dimensional absorbance data furthermore cannot be used for the conclusion of geometrical information of CNCs without additional boundary conditions that cannot be reasonably assumed and therefore other methods must be used, for example small-angle neutron scattering (Mohraz et al. 2004, Cherhal et al. 2015).

UV-Vis absorbance spectra are suitable to comparably detect changes of the size distribution of a particulate system, but not to deduce the origin, type, or extent of change. It must be taken into consideration that a change of n – for example by particle growth or agglomeration – also affects turbidity-based determinations of concentration, albeit deviations may be minor.

Water consumption

Dialysis

The conductivity of the wastewater during dialysis of H-CNCs decayed exponentially to 30 µS cm^{-1} after 166 h and the exchange of 83 L of water (see **Fig. S3**).
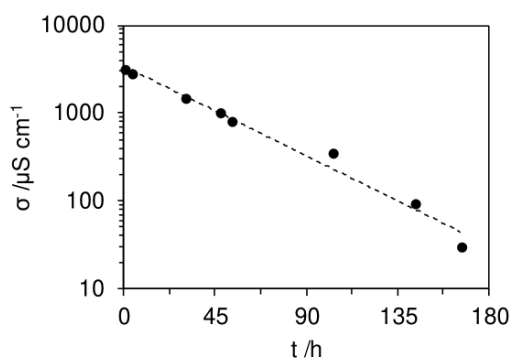
Fig. S3 Water consumption during dialysis of H-CNCs

Comparison of water consumption during downstream processing

The non-optimized production processes of H-CNCs, NH$_4$-CNCs, K-CNCs, Na-CNCs and Ca-CNCs were evaluated (see **Fig. S4**). It must be noted that while the water consumption of quenching and centrifugation for H-CNCs is more or less fixed, the water consumption of the neutralized products can vary strongly depending on the point of neutralization (for example after hydrolysis or after first

4

centrifugation) and the choice of counterion, resulting in secondary sulfates of varying solubility. However, the water consumption for any purification strategy is strongly dependent on the cellulose-to-CNC conversion ratio and will be in the range of several hundred to thousand g of H_2O per produced g of CNCs. Extensive dialysis brings the water consumption up to several tens of kg of H_2O per produced g of CNC. Thus, improving water consumption or recycling waste water from dialysis is worth considering.
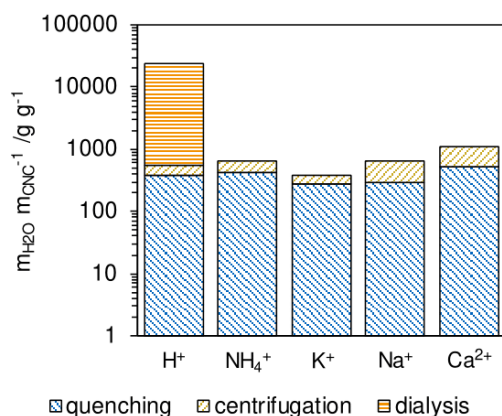
Fig. S4 Water consumption of unit operations per gram of CNC produced

References

Cherhal F, Cousin F, Capron I (2015) Influence of charge density and ionic strength on the aggregation process of cellulose nanocrystals in aqueous suspension, as revealed by small-angle neutron scattering. Langmuir 31(20):5596–5602

Mohraz A, Moler DB, Ziff RM, Solomon MJ (2004) Effect of monomer geometry on the fractal structure of colloidal rod aggregates. Physical review letters 92(15):155503

5

4.2. Effect of ultrasonication on the size distribution and stability of cellulose nanocrystals in suspension: an asymmetrical flow field-flow fractionation study

Summary. Numerous systematic studies aim at improvement of process conditions during CNC isolation from cotton or wood, to tailor their properties and performance in advanced materials (*171–179, 181, 284*). Along with hydrolysis conditions, downstream processing and, particularly, ultrasonication further impacts colloidal CNCs' properties (*171, 173, 253*). Commonly, energy input of 2 kJ g^{-1} CNC is considered to be sufficient for dispersion of agglomerated CNCs (*171, 329*). CNC individualization by ultrasonication results in de-agglomeration and, thus, higher available surface area, narrower particle size distribution, and decrease of hydrodynamic apparent particle size, with increasing energy input (*171, 254, 293, 295, 333*). Consequently, ultrasonication improves reproducibility of CNC derivatization during post-processing (*401*), and enables control over CNC performance in advanced materials (*332, 333, 402*). While effects of ultrasonication on CNC properties are apparent from their performance, quantification of their state of agglomeration is challenging. DLS is applicable to determine hydrodynamic particle size; however, $z\text{-}avg$ is averaged over the full particle collective and fails to factor in particle morphology. In this regard, Guan et al. (*366*) established AF4, coupled with MALS, for fractionation and subsequent quantitative analysis of full CNC particle size distributions. Chen et al. (*261*) determined CNCs' state of agglomeration from AF4-MALS and found that clustered CNCs are still present, when samples were ultrasonicated at 5 kJ g^{-1} CNC beforehand.

The objective of this work was targeted breakage of agglomerated CNCs by ultrasonication at energy inputs of up to 40 kJ g^{-1} CNC and subsequent estimation of particle size distribution and stability through multi-detector AF4. CNCs were isolated from ashless cotton cellulose through sulfuric acid-catalyzed hydrolysis, separated from reactant solution by dialysis. Eventually, cellulosic solid residues were removed by centrifugation. Ultrasound was incrementally applied and aliquots at increasing energy input were taken from suspension. Each aliquot was split, and one half was successively treated with mixed bed ion-exchange resin and strong acid cation ion-exchange resin to remove potentially released ions from CNC solvation shells. Suspension properties were determined by AF4-MALS, DLS, electrophoretic light scattering (ELS), and conductometric titration. All samples were then stored in a benign environment for six months, to evaluate stability of ultrasonicated CNC suspensions.

It was found that that mean particle length decreased logarithmically with increasing ultrasound energy input. Concurrently, particle length distribution shifted to shorter lengths, and narrowing of length distribution was observed. Furthermore, shorter CNCs had higher shape factors and, hence, lower diameters at similar length. Therefore, ultrasonication facilitated CNC individualization by dispersing both laterally and axially agglomerated clusters. Simultaneously, suspensions' electrical conductivity increased with increasing ultrasound energy input. This effect was attributed to faster diffusion of smaller particles and exposure of particle surface, which was trapped in clusters prior to de-agglomeration. No release of ionic species from solvation shells or de-sulfation was detected. Colloidal stability was not affected by ultrasonication. Long-term impact of

ultrasonication on colloidal CNCs' stability was evaluated after six months, using the same experimental set-up. It was found that effects of ultrasonication on mean particle length and nanostructure morphology were more lasting for high ultrasound energy densities, while CNCs treated at low energy inputs formed lateral agglomerates over the course of six months.

Results of this work are of particular interest, regarding ongoing standardization of CNC production and characterization. Furthermore, commercialization efforts require CNCs with narrow particle size distribution and, hence, predictive and uniform properties. Multi-detector AF4 facilitated quantification of properties of full particle collectives in their native, colloidal state, which, therefore, emphasizes its capacity for on-line characterization during CNC production.

Author's contributions. The author had a leading role in this work. He conceptualized the study and conducted or supervised most data acquisition and experiments. The author prepared all samples and designed the separation strategy. RD performed AF4. RD acquired MALS and UV spectroscopy data and supported the author with the interpretation of results. HB and FM supervised the research. The author wrote the manuscript and discussed the results with all authors.

Acknowledged contributions. Alexandra Zandt, Jan Stotz, and Johannes Zuber performed part of CNC production and conductometric titrations.

ORIGINAL RESEARCH

Effect of ultrasonication on the size distribution and stability of cellulose nanocrystals in suspension: an asymmetrical flow field-flow fractionation study

Christoph Metzger (ORCID) · **Roland Drexel** · **Florian Meier** (ORCID) · **Heiko Briesen** (ORCID)

Abstract Cellulose nanocrystals (CNCs) are bio-based building blocks for sustainable advanced materials with prospective applications in polymer composites, emulsions, electronics, sensors, and biomedical devices. However, their high surface area-to-volume ratio promotes agglomeration, which restrains their performance in size-driven applications, thereby hindering commercial CNC utilization. In this regard, ultrasonication is commonly applied to disperse CNCs in colloidal suspensions; however, ultrasonication methodology is not yet standardized and knowledge of the effects of ultrasound treatments on CNC size distribution is scarce. The major goals of this study were attributed to targeted breakage of CNC agglomerates and clusters by ultrasound. The evolution of particle size distribution and potential desulfation by ultrasonication as well as the long-term stability of ultrasonicated CNC suspensions were investigated. Colloidal suspensions of sulfated CNCs were isolated from cotton α-cellulose. Effects of ultrasonication on particle size distribution were determined by asymmetrical flow field-flow fractionation (AF4) coupled with on-line multi-angle light scattering and ultraviolet spectroscopy. These results were complemented with off-line dynamic light scattering. High ultrasound energy densities facilitated cumulative dispersion of CNC clusters. Consequently, the mean rod length decreased logarithmically from 178.1 nm at an ultrasound energy input of 2 kJ g^{-1} CNC to 141.7 nm (− 20%) at 40 kJ g^{-1} CNC. Likewise, the hydrodynamic diameter of the particle collective decreased logarithmically from 94.5 to 73.5 nm (− 22%) in the same processing window. While the rod length, below which 95 wt% of the CNCs were found, decreased from 306.5 to 231.8 nm (− 24%) from 2 to 40 kJ g^{-1} CNC, the shape factor of the main particle fraction ranged from 1.0 to 1.1, which indicated a decreasing number of dimers and clusters in the particle collective. In summary, progressing ultrasonication caused a shift of the particle length distribution to shorter particle lengths and simultaneously induced narrowing of the distribution. The suspension's electrical conductivity concurrently increased, which has been attributed to faster diffusion of smaller particles and exposure of previously obscured surface charges. Colloidal stability, investigated through electrical AF4 and electrophoretic light scattering, was not affected by

C. Metzger (✉) · H. Briesen
TUM School of Life Sciences Weihenstephan, Chair of Process Systems Engineering, Technical University of Munich, Freising, Germany
e-mail: christoph.metzger@tum.de
URL: http://svt.wzw.tum.de/

R. Drexel · F. Meier
Postnova Analytics GmbH, Rankinestr. 1, 86899 Landsberg am Lech, Germany

Ⓐ Springer

ultrasonication and, therefore, indicates no de-sulfation by the applied ultrasound treatment. Occurrence of minor CNC agglomeration at low ultrasound energy densities over the course of 6 months suggest the effect was not unmitigatedly permanent.

Keywords Cellulose nanocrystals (CNCs) · Ultrasound · Ultrasonication · Asymmetrical flow field-flow fractionation (AF4) · Electrical asymmetrical flow field flow fractionation (EAF4) · Particle size distribution (PSD) · Colloidal stability

Introduction

Cellulose nanocrystals (CNCs) have attracted substantial attention in academia and industry over the past decade. They are considered, through extensive review, to be renewable, biodegradable, and non-toxic high-performance building blocks for numerous potential commercial applications (Habibi et al. 2010; Moon et al. 2011; Abitbol et al. 2016; Vanderfleet and Cranston 2020). CNCs were initially isolated by Nickerson and Habrle (1947) and Rånby and Ribi (1950) from cotton cellulose via acid-catalyzed heterogeneous hydrolysis. Over the years, numerous manufacturing methods were developed (Brinchi et al. 2013; Jonoobi et al. 2015; Reid et al. 2017; Trache et al. 2017) and a number of natural cellulose sources have been successfully employed (Trache et al. 2017). To date, however, both academia and industry have focused on isolation of CNCs via acid-catalyzed hydrolysis of cotton or wood. The mostly crystalline nanoparticles that remain after heterogeneous hydrolysis—the CNCs—can be approximated as cylindrical, semi-crystalline rods with diameters ranging between 3 and 50 nm and aspect ratios of 5 to 50 (Souza Lima et al. 2003, ISO 2017b, Lin et al. 2019). Besides chain cleavage, hydrolysis of cellulose with sulfuric acid facilitates sulfation by esterification of some of the hydroxy sites of CNCs (R-OSO$_3^-$). The introduced electrical surface charge promotes colloidal stability in polar media due to electrostatic interparticle repulsion.

When the desired extent of hydrolysis of cellulose is approached during CNC production, the reactant solution—now containing CNCs, acid, and byproducts—is quenched with water. Its high ionic strength causes agglomeration of CNCs (Phan-Xuan et al. 2016; Metzger et al. 2020). Peptization and the formation of a stable colloidal suspension is achieved by separating CNCs from acid and byproducts via sedimentation and filtration (Marchessault et al. 1961; Rudie 2017; Gicquel et al. 2019). Purified suspensions are considered long-term stable, however, CNCs tend to form lateral agglomerates and clusters of multiple nanocrystals due to strong interparticle hydrogen bonds (Marchessault et al. 1961; Chen et al. 2020). Further mechanical treatment, such as ultrasonication, is therefore needed to individualize the nanoparticles (Revol et al. 1994; Dong et al. 1998; ISO 2018a). The apparent particle size decreases with increasing energy input as a result of ultrasound treatment (Marchessault et al. 1961; Dong et al. 1998; Jakubek et al. 2018; Mazloumi et al. 2018; Shojaeiarani et al. 2020). For example, Brinkmann et al. (2016) observed a bi-exponential decrease of hydrodynamic apparent particle diameter with increasing ultrasound energy. The applied power (transferred energy per unit time) predominates the effect on particle size rather than absolute energy input or treatment time (Beuguel et al. 2018; Shojaeiarani et al. 2020). The overall impact of ultrasound treatment on particle size distribution (PSD) is assumed to be permanent and cumulative when there is no change of state; for example, through precipitation or drying (Beck et al. 2011, 2012). Typically, brief ultrasonication at an energy density, e_{US}, of $\sim$ 2 kJ g^{-1} CNC is sufficient to disperse agglomerated CNCs (Dong et al. 1998; Beck et al. 2012). However, a more recent study suggests that an e_{US} of 10 kJ g^{-1} CNC is required to disperse CNCs without any remaining large agglomerates (Beuguel et al. 2018).

To the best of our knowledge, no studies have reported treatment of CNCs with high-frequency ultrasound. In this respect, note that high-frequency ultrasound irradiation of cellulose in water can cause homolytic fission of water and subsequent radical depolymerization of cellulose by scission of glycosidic bonds and by delamination due to hydrogen bond cleavage (Haouache et al. 2020). In contrast, low-frequency ultrasonic laboratory baths are not sufficiently powerful to individualize CNCs (Beck et al. 2012). On a related note, Beck et al. (2011) showed that the use of conventional ultrasound homogenizers with a frequency of 20 kHz and a power of up to 130 W facilitates CNC individualization. These

process parameters reportedly do not cause breakage of covalent bonds between CNCs and sulfate half-esters—provided that thermal energy, converted from ultrasound energy, is dissipated during the treatment. The reaction rate of autocatalyzed de-sulfation by proton counterions associated with sulfate half-esters significantly increases with temperature (Dong and Gray 1997; Jiang et al. 2010; Beck and Bouchard 2014). In this regard, however, Dong et al. (1998) observed only an insignificant increase of sulfate half-ester density on CNC surfaces when temperature was maintained constant, just above 0 °C, during ultrasonication. This increase could be attributed to the gained free surface through particle individualization (Girard et al. 2021). Girard et al. (2021) further noted that geometric and volumetric effects during ultrasonication must be considered and suggested an ultrasonication protocol for improved dispersion efficiency based on a numerical approach.

Common methods for determining CNC size and morphology—or for monitoring changes in PSD—are dynamic light scattering (DLS), atomic force microscopy (AFM), and transmission electron microscopy (TEM) (Foster et al. 2018). These methods are usually performed off-line and come with considerable limitations. Particle sizing by DLS is performed under the assumption that the sample comprises particles having a single, constant rate of diffusion. Rod-like nanoparticles like CNCs, however, have different translational diffusion constants parallel and perpendicular to the particle axis (Souza Lima et al. 2003). Thus, the hydrodynamic apparent particle size obtained from DLS cannot be directly correlated to actual particle size. Furthermore, as an intensity-based method, DLS results may be dominated by the presence of agglomerates and particle clusters (Chen et al. 2020). Regardless, DLS is an established semi-quantitative method for analyzing dispersed, rod-like CNCs (Fraschini et al. 2014; Foster et al. 2018). Imaging techniques, such as AFM and TEM, enable the full quantitative description of CNC size and morphology. However, both techniques are preparatorily challenging and require sufficiently large data sets to adequately describe PSD (Jakubek et al. 2018; Campano et al. 2021). Native size and morphology of CNCs in a liquid suspension may significantly differ from the dry CNCs required for AFM and TEM (Guan et al. 2012). Furthermore, TEM imaging commonly involves negative staining of CNCs with uranyl acetate, which

favors lateral particle agglomeration and generates radioactive waste (Kaushik et al. 2014). Jakubek et al. (2018) therefore suggested the use of asymmetrical flow field-flow fractionation (AF4) for the analysis of a full distribution of dispersed CNCs (Supporting Information, Fig. S1). Among the field-flow fractionation techniques, which are subdivided by the applied separation force, AF4 is the most prominent sub-technique (Contado 2017; Drexel et al. 2020a, b).

Guan et al. (2012) were the first to apply AF4 in combination with multi-angle light scattering (MALS) to investigate the separation of CNCs. They established a rod-like form factor and found that the length distribution of CNCs calculated from MALS data agrees well with the length from TEM analyses of early eluting fractions. Espinosa et al. (2017) and Ruiz-Palomero et al. (2017) used AF4-MALS for qualitative detection of CNCs and correlated their results with DLS. While Espinosa et al. (2017) demonstrated the ability to display small particle fractions that were not resolvable with DLS, Ruiz-Palomero et al. (2017) used AF4-MALS for detecting CNCs extracted from consumer goods. More recently, Mukherjee and Hackley (2018) focused on the improvement of AF4, in combination with MALS and differential refractometry (dRI), for size-based separation and on-line characterization of CNCs. However, their calculated mean rod length of 146 nm differed from reported mean lengths of the same CNC sample calculated from TEM images (87 nm) and AFM images (76 nm) by Jakubek et al. (2018). In this regard, Chen et al. (2020) focused on surface imaging analysis of single CNC fractions previously separated and analyzed using multi-detector AF4. While early eluting fractions contained mostly individual CNCs, they predominantly detected clustered CNCs at higher retention times—even though the suspension was ultrasonicated at 5 kJ g^{-1} CNC beforehand.

Thus far, only a handful of studies have applied AF4 to CNCs. These are summarized in Supporting Information, Table S1 and validate multi-detector AF4 for semi-quantitative and quantitative analysis of CNC suspensions. It is reported that, even in ultrasonicated and stable CNC suspensions, a considerable particle fraction exists in the agglomerated state, which implies a broad PSD. However, a narrow PSD of CNCs facilitates better dispersibility and reinforcement capacity in polymer matrices (Chen et al. 2020;

Shojaeiarani et al. 2020), promotes tailoring of self-assembly properties in the liquid crystalline phase and in chiral nematic films (Dong et al. 1998; Beck et al. 2011; Gicquel et al. 2019), and enables control over the viscosity of CNC suspensions (Shafiei-Sabet et al. 2012; Beuguel et al. 2018; Gicquel et al. 2019). Furthermore, a narrower PSD may be useful in nanotoxicological studies (Roman 2015; Shatkin and Kim 2015) and for in-line detection of CNCs and monitoring their PSD in complex environments (Foster et al. 2018).

The aforementioned studies on the impact of ultrasonication on CNC suspensions showed that the ultrasound treatment facilitates dispersion of clusters and narrowing of the PSD. However, while assessing their state of agglomeration with DLS, AFM, and TEM is qualitatively feasible, this comes with above-mentioned shortcomings. In this context, our primary objective was the targeted dispersion of CNC clusters by ultrasonication and the investigation of its impact on the full distribution of species via multi-detector AF4 and off-line techniques. Anticipated effects of ultrasonication on colloidal CNCs are summarized in Fig. 1.

Our hypotheses were based on reported literature that (1) ultrasonication induces breakage of agglomerates and clusters. An increase of the applied ultrasound energy density is generally associated with a cumulative reduction of cluster size and, thus, a decrease of mean particle size (Fig. 1a). This may go unnoticed with commonly applied off-line imaging techniques, such as AFM and TEM, because laterally cohering CNCs may fabricate similar particle lengths and diameters compared to individual particles in the initial suspension. Therefore, it does not necessarily significantly change the apparent PSD of a sample (Jakubek et al. 2018). However, surface charges obscured inside the clusters contribute to the net charge after ultrasonication (Girard et al. 2021). Moreover, (2) CNC ultrasonication in water may induce the release of charged moieties from the bound-water surface layer of CNCs (Fig. 1b) (Bouchard et al. 2016; Beuguel et al. 2018). In this context, Beck et al. (2011) and Bouchard et al. (2016) attributed the effect of ultrasonication on rheological and self-assembly properties of CNC suspensions mainly to a change of electrostatic particle interactions. No de-sulfation has been reported during ultrasonication of sulfated, Na^+-exchanged CNCs at room temperature and ultrasound

energy density of 10 kJ g^{-1} CNC (Beuguel et al. 2018). We, however, investigated the effect of ultrasonication on protonated CNCs for which autocatalyzed de-sulfation has already been reported at low temperatures (Fig. 1c) (Jiang et al. 2010; Beck and Bouchard 2014). Samples were, therefore, kept at 2 °C during all ultrasonication experiments to mitigate potential de-sulfation; nevertheless, ultrasound induces cavitation and local temperature peaks occur. Furthermore, (3) deagglomeration by ultrasonication is permanent and cumulative when there is no change of state (Beck et al. 2011, 2012).

Expanded understanding of the impact of ultrasonication on CNC suspensions provides potential for tailoring the PSD of CNCs through breakage of particle clusters. This is also emphasized by the ongoing development of technical specification ISO/TC 229—PWI 23151 (ISO 2018a), which addresses ultrasound-assisted deagglomeration of redispersed sulfated CNCs.

Materials and methods

Materials

Whatman ashless filter aids (cotton α-cellulose) were purchased from Sigma-Aldrich (Taufkirchen, Germany). Sulfuric acid (H_2SO_4, 96%) was used for preparing CNCs and was purchased from Carl Roth (Karlsruhe, Germany). The isolation of CNCs was performed under nitrogen atmosphere (N_2, 99.8%, Linde, Pullach, Germany). Sodium chloride (NaCl, 99.5%) and sodium hydroxide (NaOH (aq), 2 mM), required for conductometric titration, were purchased from Carl Roth. Protonated strong acid cation ion-exchange resin (SAC; Dowex Marathon C) and Amberlite MB6113 H^+ OH^- mixed bed ion-exchange resin (MB) were purchased from Sigma-Aldrich and thoroughly rinsed with water before use. Syringe filters with hydrophilic polyethersulfone (PES) membranes and a pore size of 0.45 μm (CHROMAFIL Xtra PES) and hydrophilic glass fiber membranes with a pore size of 1 μm (CHROMAFIL Xtra GF) were purchased from Macherey–Nagel (Düren, Germany) and used for filtration of CNC suspensions. Sodium chloride (NaCl, 99.5%, Avantor Performance Materials, Gliwice, Poland) was diluted to 1 mM and used as the eluent in AF4 for CNC fractionation. All eluents
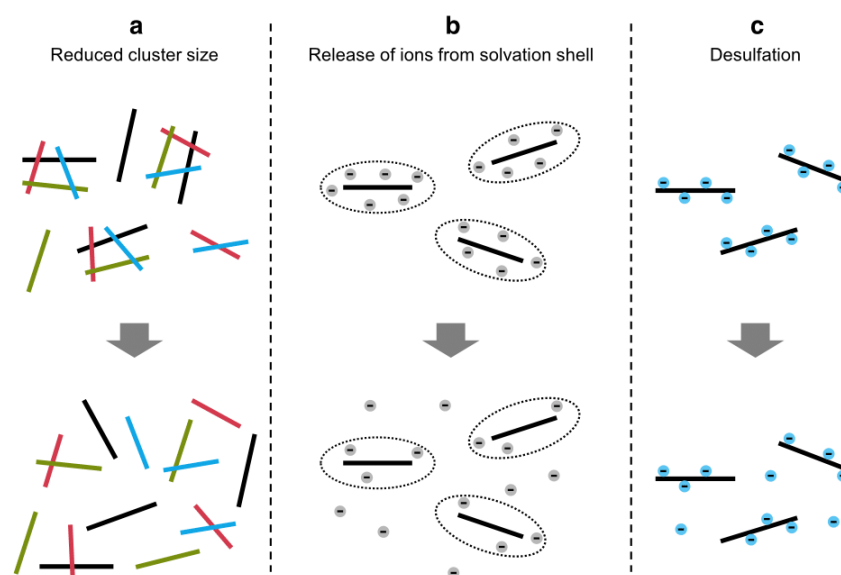
Fig. 1 Effects potentially involved in the ultrasound treatment of colloidal CNCs

were filtered by vacuum using a membrane filter with a pore size of 0.1 μm (Durapore, Merck, Tullagreen, Ireland).

All chemicals were used in their as-received state. Ultrapure (type 1) water (H_2O) with a resistivity of 18.2 MΩ cm (Milli-Q Direct 8 system, Merck Chemicals, Schwalbach, Germany) was used to prepare solutions for all experiments.

Preparation of CNCs

Colloidal suspensions of sulfated CNCs were prepared through the heterogeneous hydrolysis of cellulose with sulfuric acid, based on the method of Cranston and Gray (2006) and Metzger et al. (2020). Cotton cellulose was dried at 105 °C for 30 min to remove adsorbed water. Meanwhile, 96 wt% sulfuric acid was diluted to 64.2 wt% with water and pre-heated to 45 °C in a stirred tank reactor equipped with an anchor-type stirrer (Atlas, Syrris, Royston, UK). The dried cellulose was then added in at a mass-mixing ratio of 10 $m_{H_2SO_4} m_{cellulose}^{-1}$ with the weighed portions of sulfuric acid, $m_{H_2SO_4}$, and cellulose, $m_{cellulose}$; the reactant solution was stirred constantly at 200 rpm under nitrogen atmosphere. The reaction was quenched by ten-fold dilution with 4 °C water after

45 min and stirring was continued at 12 °C for 30 min.

Excess acid and soluble byproducts were decanted, after leaving the precipitate to settle overnight. The resultant cloudy suspension was washed by two-fold centrifugation for 15 min at a relative centrifugal force of 4250 × g (Centrifuge 5910 R, Eppendorf, Hamburg, Germany), followed by decanting and further dilution with water. The precipitate was filled into regenerated cellulose tubes with a molecular weight cutoff of 12–14 kDa (ZelluTrans/ROTH T3, Carl Roth, Karlsruhe, Germany) and remaining acid and soluble byproducts were removed by dialysis against running water (0.5 L h^{-1}) at 23 °C in a 7 L glass reactor for 10 days. Agglomerates were broken via ultrasonication using a homogenizer (Sonopuls HD 3400 with the sonotrode VS 70 T, Bandelin, Berlin, Germany) at a specific energy of 2 kJ g^{-1} cellulose and a power of 33.3 W in a cooled secondary glass container at 2 °C. Incompletely hydrolyzed solid cellulosic residues were then removed by centrifugation for 15 min at 4250 × g. The final stock suspension of never dried sulfated and protonated CNCs was stored in a sealed container at 4 °C until further use.

Ultrasound treatment of CNCs

The CNC stock suspension was diluted to a particle concentration of 1 wt%. The abovementioned homogenizer was used for ultrasound treatment and the probe was adjusted according to ISO/CD TS 23151 (2018a) to ensure minimal bubbling and aerosoling. The suspension was placed in a temperature-controlled secondary glass container at 2 °C. The sample temperature was constantly monitored and treatment was paused when the temperature exceeded 4 °C. The ultrasound power was set to 33.3 W. Aliquots were extracted from the stock suspension at seven prespecified energy inputs and the remaining suspension was further treated until an energy input of 40 kJ g^{-1} CNC was reached (Supporting Information, Table S2).

Removal of ionic species by ion-exchange resins

Ultrasonicated aliquots were split and one respective half was stored at 4 °C. Ionic species were then removed from the other halves by successive batch treatments with MB followed by SAC as suggested by Abitbol et al. (2013). Resins were added in at a resin-to-CNC mass ratio of eight and the aliquots were continuously stirred for 24 h. After each treatment, the aliquots were rinsed with water over a sieve and filtered with 0.45 μm syringe filters before they were stored at 4 °C. No loss of CNCs was assumed by using microporous resins (Beck et al. 2015).

CNC morphology

Chen et al. (2020) separated sulfated, Na^+-exchanged CNCs from softwood pulp with AF4 and classified them, with the help of imaging techniques, as singles, dimers, and clusters. They predominantly detected singles and dimers in early eluting fractions and the relative proportion of clusters in the particle collective increased toward later fractions. Herein, we assume that sulfated, protonated CNCs from cotton are composed of similar nano-objects and nanostructures and refer to them according to the illustration in Fig. 2.

Sample naming

CNC suspensions are named here by the applied ultrasound energy density. For example: CNC-2 for an input of 2 kJ g^{-1} CNC and CNC-40 for 40 kJ g^{-1}
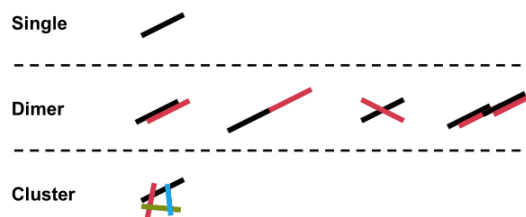
Fig. 2 Classification of CNCs, based on the work of Chen et al. (2020)

CNC. Aliquots treated with ion-exchange resins are further denoted with a postposed "R". For example: CNC-2-R for CNC-2 treated with ion-exchange resin.

Fractionation of CNCs by AF4

Size-based fractionation of colloidal CNCs was performed at 25 °C using an AF4 system (AF2000) equipped with an autosampler (PN5300) and a channel thermostat (PN4020). All experiments were monitored using on-line coupled MALS and ultraviolet spectroscopy (UV) detectors. The CNC suspensions were filtered with 1 μm syringe filters and then diluted to 0.04 wt%. Sample volumes of 20 μL were injected using 1 mM NaCl as the eluent. The applied separation parameters are shown in Table 1.

The planar separation channel (Supporting Information, Fig. S1) had a tip-to-tip length of 277 mm and was equipped with a Mylar spacer with a thickness of 350 μm and a regenerated cellulose (RC) membrane with a molecular weight cutoff of 10 kDa. Using the slot outlet option of the AF4 channel (PN1650), the eluting channel flow was split into a detector flow with a CNC-enriched fraction at a flow rate of 0.30 mL min^{-1} and a particle-free eluent fraction at a flow rate of 0.20 mL min^{-1}, which was discarded. All instruments and consumables in this section that were not mentioned in earlier sections were provided by Postnova Analytics GmbH (Landsberg am Lech, Germany).

Instrument measurements

Preliminary evaluations of CNC suspensions separated with AF4 showed high repeatability and reproducibility in accordance with the guidelines of ISO/TS 21362 (ISO 2018b). Thus, fractionation and related measurements were replicated twice. All other

Table 1 Separation parameters for AF4

Step	Flow type and rate (mL min^{-1})		Duration (min)	Mode
General	Detector flow	0.30		
	Slot flow	0.20		
Focusing and injection	Injection flow	0.20	6	
	Cross flow	1.00		
	Focus flow	1.30		
Transition			0.5	
Elution 1	Cross flow	1.00	2	Constant
Elution 2	Cross flow	1.00	40	Power decay (exponent 0.2)
Elution 3	Cross flow	0.10	40	Constant
Rinse	Rinse flow	0.50	15	

measurements were performed at least in triplicate and are presented with the 95% confidence interval of the mean.

Optical measurements

Multi-angle light scattering The scattered light intensity of fractionated CNCs was detected under 19 active angles ranging from 12° to 156° with an on-line coupled MALS detector PN3621 (Postnova) at a wavelength of 532 nm and a cell temperature of 35 °C. The angular-dependent scattering intensity function, $P(\theta)$, is given by

$$P(\theta) = \frac{2}{qL} \text{Si}(qL) - \left(\frac{\sin \frac{qL}{2}}{\frac{qL}{2}} \right)^2, \tag{1}$$

with scattering angle, θ; rod length, L; scattering vector, $q = 4\pi n_0 \sin\left(\frac{\theta}{2}\right)/\lambda$; and sine integral function, $\text{Si}(qL)$ (van de Hulst [1958]). q includes the refractive index of the eluent, n_0, and the incidental wavelength, λ. All data were normalized with respect to the signal at an angle of 90°. Standard polystyrene beads with a nominal size of 60 nm (NIST [2021]) were fractionated and used to normalize detectors at different angles with respect to 90° to the radius of gyration, r_g, as a function of retention time by considering the angular-dependent spherical scattering intensity function $P(\theta)$ (Supporting Information, Fig. S2). In accordance with Mukherjee and Hackley ([2018]), a rod model was best suited for fitting MALS data of fractionated CNCs. Consequently, the relationship of r_g and L for thin rigid rods with a high L-d ratio, where d is the particle

diameter, can be approximated as (Stepto et al. [2015]; Mukherjee and Hackley [2018]):

$$r_g^2 = \frac{L^2}{12} \quad \text{for } d \ll L \tag{2}$$

The evaluation of r_g was performed using the NovaMALS software (Postnova Analytics GmbH [2020c]). In addition, the hydrodynamic radius, r_h, which depends on the translational diffusion coefficient of the CNCs, was derived from AF4 conditions, such as cross flow rate, channel thickness, and channel flow rate (Wahlund and Giddings [1987]; Litzen and Wahlund [1991]). The effective channel height was determined from the retention times of fractionated standard polystyrene beads, with a nominal diameter of 60 nm (NIST [2021]). r_h as a function of retention time was evaluated using the NovaAnalysis software (Postnova Analytics GmbH 2020a).

Ultraviolet spectroscopy An UV detector (PN3211, Postnova) was coupled on-line with AF4 and absorbance was recorded at a wavelength of 254 nm. The analyte recovery, *Rec*, was evaluated from the peak area of the eluted sample, A_S, and the peak area of the sample measured in absence of any separation field, A_D, according to ISO/TS 21362 (ISO [2018b]):

$$Rec(\%) = \frac{A_S}{A_D} \cdot 100\%. \tag{3}$$

Zeta potential (ζ) EAF4 (EAF2000, Postnova) was used to determine the size-resolved electrophoretic mobility and zeta potential (ζ) of colloidal CNCs on-line. The same fractionation parameters as those for the size-based fractionation experiment with AF4

were applied (Table 1). Here, however, an amphiphilic RC membrane (Postnova) with a molecular weight cutoff of 10 kDa was used. The cross flow was superimposed with an electrical field (PN2410), which was controlled with the NovaFFF software (Postnova Analytics GmbH 2020b). EAF4 data were evaluated with the NovaAnalysis software (Postnova Analytics GmbH 2020a).

Off-line zeta potential measurements were performed with a Zetasizer Nano ZSP (Malvern Instruments, Worcestershire, UK) in folded capillary cells (DTS1070). CNC dispersions at a concentration of 0.25 wt% were analyzed after equilibration for 30 min at 25 °C.

For both on-line and off-line measurements ζ is calculated from the electrophoretic mobility assuming Smoluchowski behavior with $f(\kappa r) = 1.5$ for Henry's function, where κ is the Debye length and r the particle radius (Smoluchowski 1906).

Dynamic light scattering The hydrodynamic apparent particle diameter, d_h, was determined off-line from DLS using a Zetasizer Nano ZSP under a backscatter detection angle of 173°. d_h and the dispersity, Đ, from cumulants analysis was obtained according to ISO 22412 (ISO 2017a) for 0.04 wt% CNC suspensions after equilibration for 3 min at 25 °C in disposable polystyrene cuvettes (Stepto 2009).

Conductometric titration

The surface sulfate half-ester concentration, c_S, of colloidal CNCs was determined by conductometric titration, as suggested by Beck et al. (2015). For the electrical conductivity measurements, 5 mL of a 1 wt% CNC dispersion was diluted into 80 mL of water. To elevate the electrical conductivity, σ, to a measurable level, 1 mL of 0.1 M NaCl (aq) was added. The titrant used was 2 mM NaOH (aq) in 0.2 mL increments under constant stirring. Stable conductivity readings (Konduktometer 703 with the electrode sensor SE 204, Knick, Berlin, Germany) were recorded 30–60 s after each addition and plotted against the amount of NaOH added. The equivalent amount of NaOH, and, thus, the concentration of accessible sulfate half-ester groups of the CNCs, was calculated from the intersect of the least squares regression lines of the two linear branches ($R^2 \approx 1$) of

the conductivity curve. All measurements were performed at 25 °C.

Results and discussion

Size distributions of ultrasonicated CNCs

Effect of ultrasonication on size distribution

Suspensions of 1 wt% colloidal CNCs were ultrasonicated with increasing energy densities ranging from 2 to 40 kJ g^{-1} CNC. Each sample was then size fractionated by AF4. The fractograms in Fig. 3a show MALS intensities at 90° (solid lines) along with the radii of gyration of three selected samples (filled points). As shown in Fig. 3b, the UV absorbance signals were slightly left-shifted in regard to the MALS scattering intensity. All intensity distributions followed lognormal behavior, in accordance with the AF4 separation pattern, and had peaks, I_{max}, at $t_R(I_{max})$. $t_R(I_{max})$ shifted to shorter retention times with increasing ultrasound energy density, which is equivalent to a shift to smaller particle sizes. Concurrent narrowing of the MALS scattering intensity implied narrowing of the CNC size distribution. Simultaneously, an exponential decrease of I_{max} with increasing ultrasound energy was observed (Supporting Information, Fig. S3) and the mass-weighted particle concentration, derived from the UV signal, decreased by 25 wt% from CNC-2 to CNC-40. As all samples were branched off from the same stock solution with constant CNC concentration, the origin of the apparent mass loss is ambiguous. Throughout all AF4 experiments, the initial void peak remained at a constant and insignificant level. Similarly, no significant field-off peak was observed during rinsing when cross flow was zero, which therefore indicated inconsiderable agglomeration during fractionation. Simultaneously, recoveries of 84–92% were achieved for all samples while no dependence of Rec on e_{US} was observable. Hence, only marginal particle adsorption to or diffusion through the membrane occurred and good separation performance was achieved, in accordance with ISO/TS 21362 (ISO 2018b). No sedimentation was observed for all samples over the course of 1 month and in contrast to UV spectroscopy, conformable count rates during off-line DLS measurements implied no sample loss. The apparent mass loss
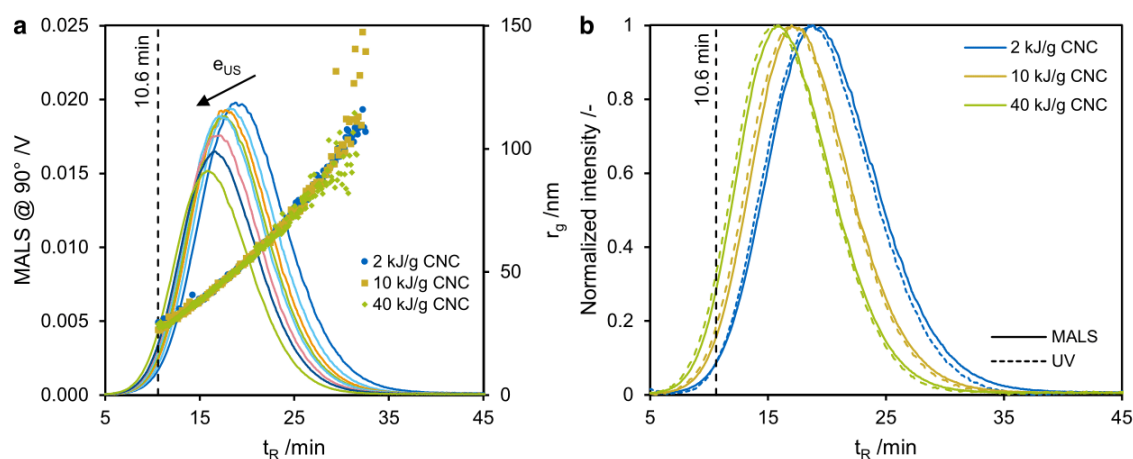
Fig. 3 Fractograms of CNC suspensions ultrasonicated at different energy densities ranging from 2 to 40 kJ g^{-1} CNC. **a** MALS scattering intensity distributions and radii of gyration are represented by solid lines and filled points, respectively. Radii of gyration are displayed for retention times higher than 10.6 min (dashed vertical lines). **b** UV absorbance signal (dashed lines) are slightly left-shifted with regard to the MALS scattering intensity

with increasing ultrasound energy input revealed by the UV detector may result from an additional size and shape-dependent scattering contribution of rod-like CNCs and irregularly shaped clusters to the overall UV absorbance signal (van de Hulst 1958). This may lead to overestimation of the overall CNC concentration and, hence, UV spectroscopy is not suited to evaluate the mass balance at varying ultrasound energy input. Consequently, the comparability of incremental size fractions decreases with increasing retention time and quantification is only feasible for early eluting fractions, wherein singles and dimers predominate (Chen et al. 2020).

Figure 4a shows the shift of $t_R(I_{max})$, as well as the narrowing of MALS intensity distributions, with regard to their full widths at half maximum, *FWHM*, in response to increasing ultrasound energy density. Both had a linear interrelationship (Fig. 4b) and could be individually approximated logarithmically.

Equivalent to the MALS peak shift in Fig. 4a, r_g at $t_R(I_{max})$ and the associated decrease of rod lengths with more extensive ultrasonication followed logarithmic laws. A decrease in $r_g(I_{max})$, from 51.4 ± 0.5 to 40.9 ± 0.2 nm (− 20%), was observed from CNC-2 to CNC-40, and L decreased conformably, from 178.1 ± 1.7 to 141.7 ± 0.7 nm (Fig. 5). In the same interval, the mean hydrodynamic apparent diameter of the full particle collective, determined by off-line DLS, decreased from 94.5 ± 0.3 to 73.5 ± 0.4 nm

(− 22%). No statistically significant trend was found for Đ, which ranged between moderate values of 0.155 ± 0.014 and 0.174 ± 0.013 for all samples (ISO 2017a).

It is recognizable from Fig. 3 that in all CNC suspensions notable sample fractions were eluted at retention times earlier than 10.6 min, which, therefore, had an r_g below 25 nm. The share of this particular fraction, $\varphi_{<10.6min}$, of the cumulative particle mass was quantified from the UV absorbance signal (Fig. 3b); it increased from 1.0 ± 0.3 to 5.3 ± 0.1 wt% from CNC-2 to CNC-40, following a power law (Fig. 6a). Consequently, extensive ultrasonication caused progressive dispersion of dimers and clusters and the amount of CNCs with lengths < 87 nm increased. It is unclear whether this fraction was only comprised of individual CNCs. Reported mean particle lengths of CNCs from cotton α-cellulose are typically in the range of 100–250 nm and may vary with hydrolysis severity (Araki et al. 2001; Beck-Candanedo et al. 2005; Wang et al. 2012; Boluk and Danumah 2014). Other groups who have analyzed size-fractionated CNC suspensions by MALS in combination with imaging techniques have also not identified particle fractions with lengths < 80 nm (Guan et al. 2012; Mukherjee and Hackley 2018; Chen et al. 2020). However, all of those studies have only applied a maximal ultrasound density of 5 kJ g^{-1} CNC. Therefore, extensive ultrasonication may induce
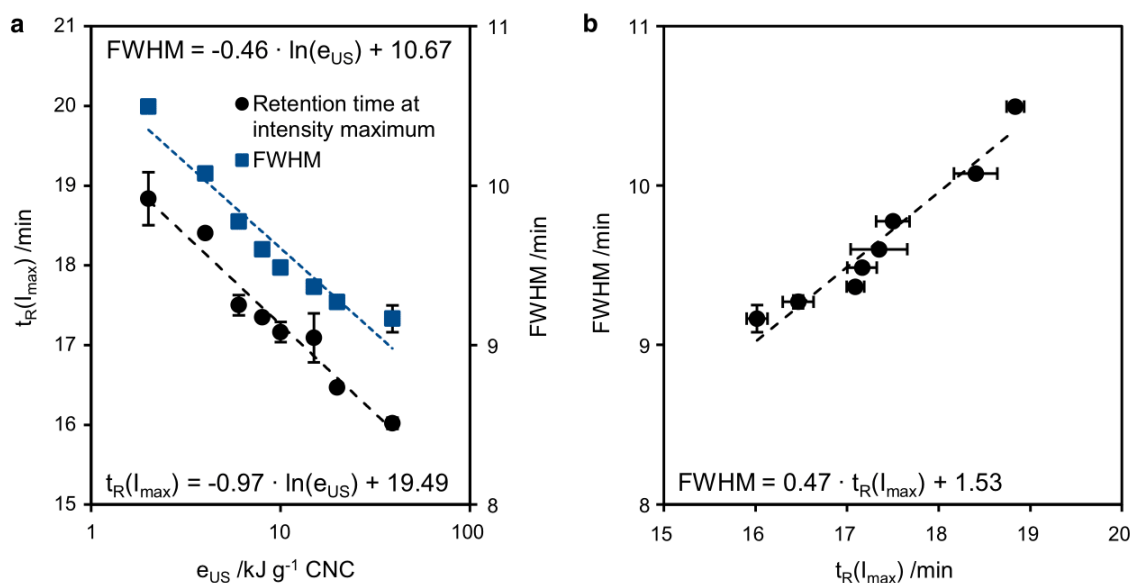
Fig. 4 **a** Evolution of peak maximum (left vertical axis) and *FWHM* (right vertical axis) of the MALS signal as a function of ultrasonication energy density and **b** the respective relationship of *FWHM* and peak maximum
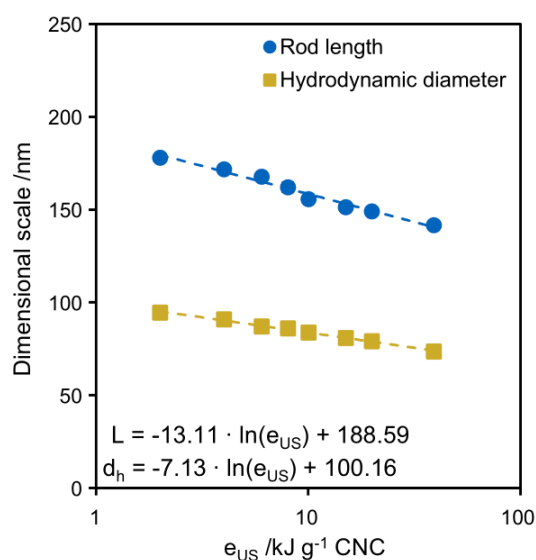

Fig. 5 Rod length L at I_{max}, from AF4-MALS, and hydrodynamic diameter d_h, from off-line DLS, decrease logarithmically with increasing ultrasound energy. r_g and L at I_{max} are linearly proportional, according to Eq. (2)

a progressing release of not fully immobilized oligosaccharides that were previously trapped in the solvation shells of the particles (Bouchard et al. 2016)

or debris from formerly fringed polymer chains that seceded from the bulk particles (Kontturi 2018). Furthermore, acid-catalyzed hydrolysis of cellulose in combination with ultrasonication reportedly enables the production of spherical cellulose nano-objects with diameters down to 10 nm (Wang et al. 2007, 2008; Zianor Azrina et al. 2017). Thus, cavitation-induced temperature increase may have induced progressing autocatalysis during ultrasonication of protonated CNCs, facilitating their disintegration into spherical fragments with radii of gyration < 25 nm.

Dispersion of clusters

The concurrently observed dispersion of large clusters further manifested narrowing of PSD. The rod length, below which 95 wt% of the CNCs were found, decreased from 306.5 ± 7.3 to 231.8 ± 0.0 nm $(- 24\%)$ from CNC-2 to CNC-40 (Fig. 6b). The concurrent change in shape of clusters was quantifiable by the shape factor, which is represented by the ratio of the radius of gyration and the hydrodynamic radius, $r_g r_h^{-1}$, that is shown in Fig. 7. The mass-related large portion of CNCs with lengths of 130–270 nm had shape factors ranging from 1.0 to 1.1, which increased toward shorter lengths. This substantiates
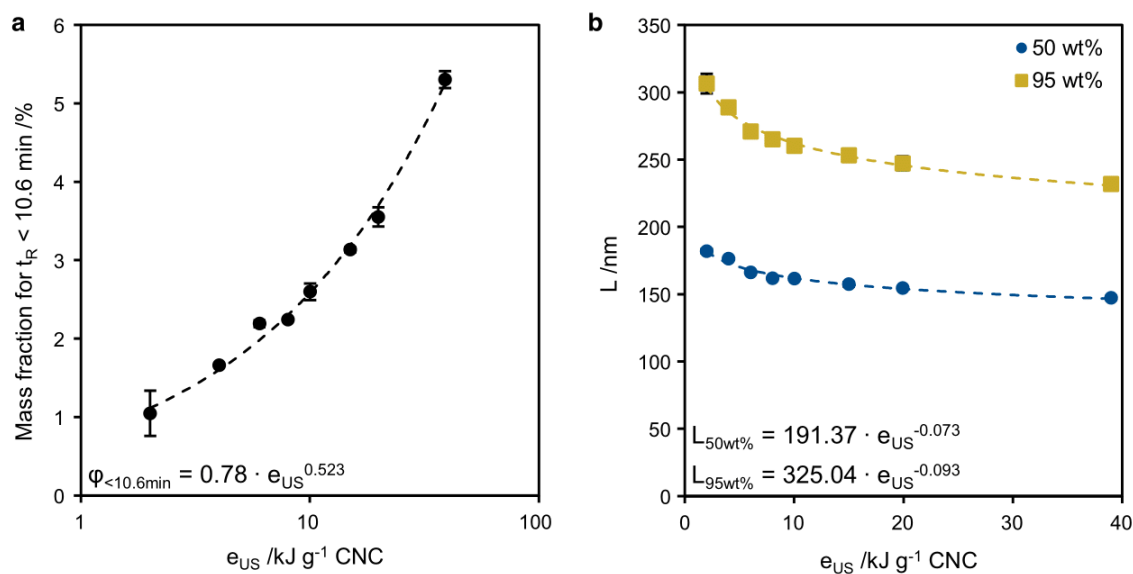
Fig. 6 **a** Cumulative mass fraction at retention times < 10.6 min, derived from UV signal, and **b** rod lengths when 50 wt% and 95 wt% of CNCs are shorter than this value
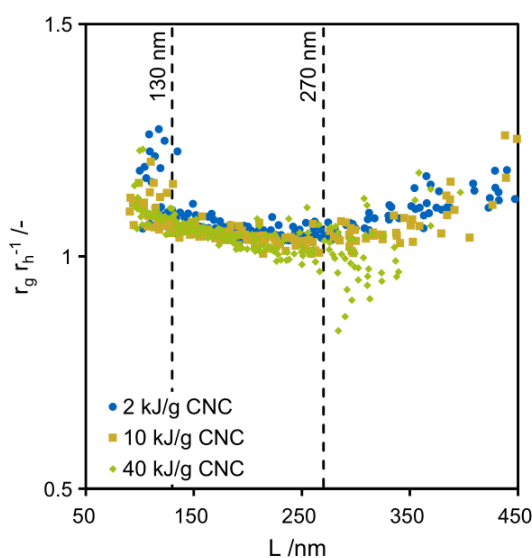

Fig. 7 The shape factor of CNC suspensions as a function of rod length

ratio and, consequently, the shape factor increases.[1] The shape factors of the fractions outside of this length range were notably increased. With reference to the MALS scattering intensity and the UV absorbance signal, note that these particular fractions only represented < 4 wt% of each particle collective. Complementary to the decrease of the shape factor with increasing particle length ranging between 130 and 270 nm, a minor shift toward lower shape factors was observed with increasing ultrasound energy input. The notable decrease of the shape factor for CNC-40 at rod lengths > 270 nm only constituted 1 wt% of the particle collective.

The overall shift of the CNC lengths with increasing ultrasound energy density, toward smaller values, and the concurrent narrowing of the PSD is shown in the cumulative mass-weighted length distribution plot in Fig. 8a. Equally, the rod length at I_{max} decreased, which is shown in Fig. 8b for arbitrary particle diameters along with the size-related definition of CNCs, according to ISO/TS 20477 (ISO 2017b).[2] The

the observation of Chen et al. (2020) that the number of dimers and clusters decreases toward shorter retention times, which increases the effective L-d

---

[1] $r_g r_h^1$ of rod-like nanostructures is ~ 2, while hard and soft spheres have shape factors of 0.778 and 0.977, respectively (Brewer and Striegel 2009).

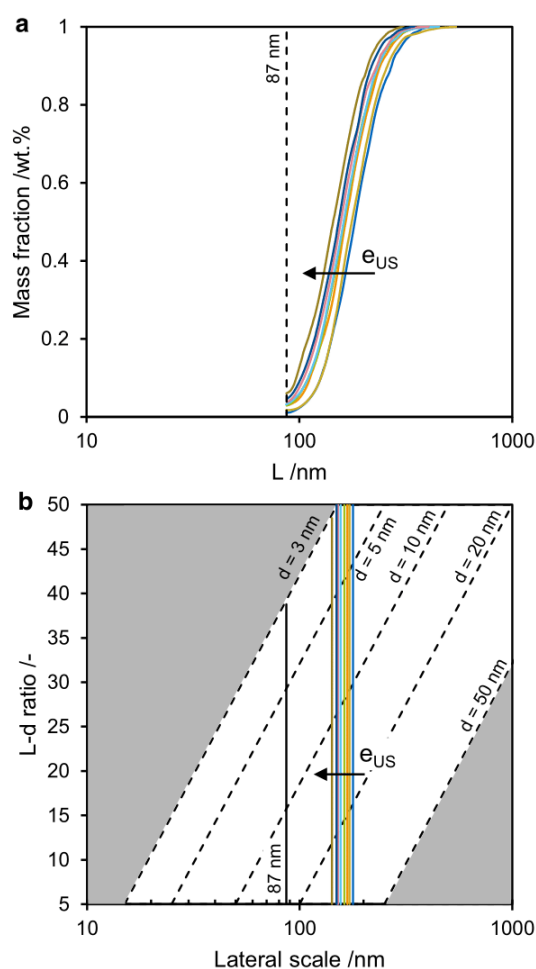[2] CNCs are defined as individual nano-objects with a diameter of 3–50 nm and a L-d ratio of 5–50.

Fig. 8 a Cumulative mass-weighted length distribution of CNCs at different ultrasonication energy densities and **b** rod lengths at I_{max}. The diagrams comprise the confinements of CNCs, according to ISO/TS 20477 (2017b), which describes them as nano-objects with diameters of 3–50 nm (dashed lines) and aspect ratios of 5–50 (vertical axis)

resolution limit of our set-up (87 nm) is indicated by the vertical solid line in the figure. Provided that singles are infrangible, the dispersion of dimers can occur laterally, axially, or in a mixed form, depending on the arrangement of the nanostructure (Fig. 2). When laterally agglomerated dimers are dispersed the length is merely altered, whereas the diameter remains consistent when axially agglomerated dimers are dispersed. Figuratively translated to Fig. 8b, dispersion of laterally agglomerated dimers causes a vertical upward shift—the diameter decreases and the L-d ratio

increases. In contrast, dispersion of axially agglomerated dimers induces a diagonal downshift parallel to the dashed lines, which represent the particle diameter—length and L-d ratio decrease. Similar considerations are applicable to the dispersion of clusters that have intrinsically higher L-d ratios than dimers (Fig. 7).

In summary, extensive ultrasonication of CNC suspensions caused a progressive shift of the length distribution to shorter particle lengths and a concurrent narrowing of the distribution. Shorter CNCs had higher shape factors and, hence, lower diameters at similar length. Ultrasonication therefore facilitated CNC individualization by dispersing laterally and potentially present axially agglomerated nanostructures. Note that laterally agglomerated CNCs may not be perfectly congruent and, hence, a single deagglomeration event can cause a decrease of both particle length and particle diameter at the same time. Analogously, Beck et al. (2012), Beuguel et al. (2018), and Shojaeiarani et al. (2020) found that ultrasound treatment of CNC suspensions induces concurrent decrease of mean particle size and narrowing of particle size distribution, which then involves a reduction of the L-d ratio.

Surface charge and colloidal stability
of ultrasonicated CNCs

Conductivity of CNC suspensions and surface charge density of CNCs

The electrical conductivity of the CNC stock suspension was measured in parallel to its incremental ultrasonication. The sample CNC-2 had a conductivity of $190.2 \pm 0.2 \, \mu S \, cm^{-1}$. The conductivity increased, following a power law, to $254.8 \pm 0.9 \, \mu S \, cm^{-1}$ (34%) for CNC-40 (Fig. 9a). The background conductivity of water was $0.07 \pm 0.01 \, \mu S \, cm^{-1}$. An increase of σ with increasing ultrasound energy density may have been attributed to the elevated diffusion coefficient of smaller particles and, in accordance with Fig. 1, the contribution of previously obscured surface charges in clusters, charged moieties that were released from the solvation shells of the particles, and potentially detached sulfate half-esters due to de-sulfation. For further insight into the origin of the increased electrical conductivity, each aliquot was treated with ion-exchange resins to scavenge free ions from the
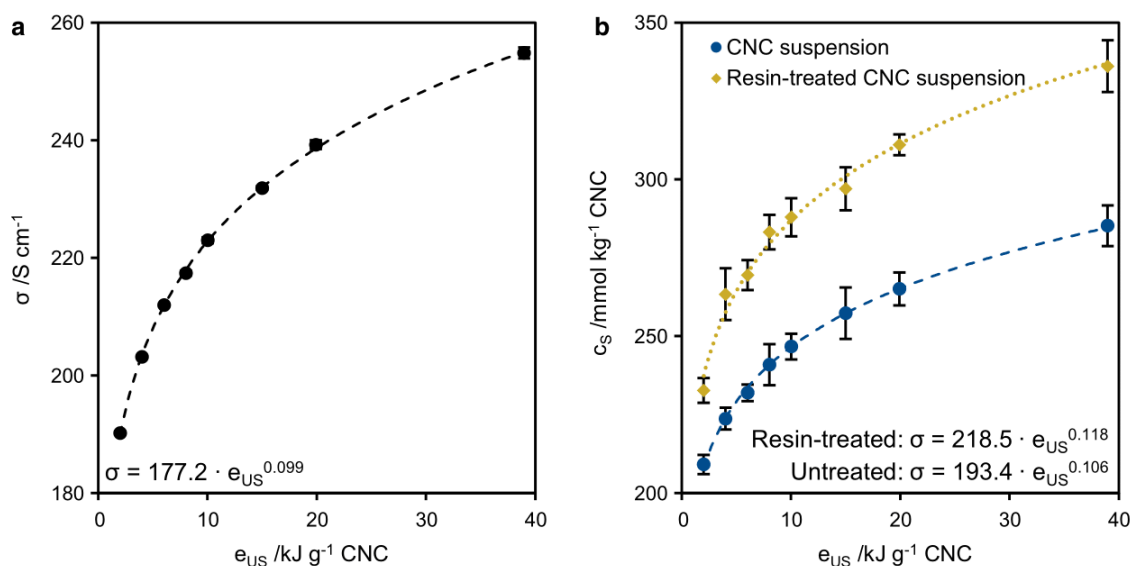
Fig. 9 a Electrical conductivity of 1 wt% CNC at different stages of ultrasound treatment and **b** the corresponding surface sulfate charge of colloidal CNCs, along with ion-exchange resin-treated CNC suspensions at equal stages of ultrasonication

suspensions. Subsequently, the sulfate half-ester density of all samples was determined by conductometric titration (Fig. 9b). With increasing ultrasound energy density, an increase of the apparent sulfate half-ester density with power-law behavior, from 209 ± 3 mmol kg^{-1} CNC for CNC-2 to 285 ± 7 mmol kg^{-1} CNC for CNC-40 (36%), was observed. In the same interval, c_S increased from 233 ± 4 mmol kg^{-1} CNC to 336 ± 8 mmol kg^{-1} CNC (44%) for ion-exchange resin-treated CNC suspensions. The mean apparent sulfate half-ester density of resin-treated suspensions was elevated overall by $16 \pm 2\%$ compared to untreated suspensions. All measured values were in the range of commonly reported surface group densities for sulfated CNCs from cotton α-cellulose, ranging from 80 to 350 mmol kg^{-1} CNC (Abitbol et al. 2013; Cherhal et al. 2015; Reid et al. 2017).

Each resin-treated CNC suspension was then separated with AF4 and analyzed by MALS and UV under equal measurement conditions as those for non-treated suspensions discussed earlier. No loss of sample mass was observed and congruent particle length distributions of non-treated and resin-treated CNC suspensions at each stage of ultrasonication implied that no adsorption of CNCs to the ion-exchange resin occurred (Supporting Information,

Fig. S4). Furthermore, the hydrodynamic particle radius remained constant and, therefore, the shape factors were unaltered. In accordance with Abitbol et al. (2013) and Beck et al. (2015), it was concluded that the treatment of suspensions with ion-exchange resins promoted protonation of CNCs. Concurrently, constant hydrodynamic CNC properties suggested that no release of ionic species from the solvation shell or the particle surface occurred. Thus, the increase of both the electrical conductivity of the suspension and the increase of the apparent sulfate half-ester density with increasing ultrasound energy density was attributable to faster diffusion of smaller particles and exposure of surface charges, which were previously obscured in clusters (Girard et al. 2021).

Colloidal stability

Anionic surface sulfate groups on CNCs provide colloidal stability in aqueous suspensions by electrostatic particle repulsion. Their concentration is an important parameter for the manufacture of advanced materials with predictable and homogeneous properties. However, the concentration of surface sulfate half-esters provides no insight into colloidal stability and, instead, zeta potential measurements are employed (Foster et al. 2018). Herein, neither

ultrasonication nor treatment with ion-exchange resins had significant effect on colloidal stability in terms of the zeta potential. The zeta potentials of CNCs treated with 2 and 40 kJ g^{-1} CNC, determined by ELS for the full particle collective and by EAF4 at I_{max}, are shown in Table 2. All values were in the common range of -50 to -20 mV of sulfated CNCs (Foster et al. 2018). The elevated zeta potential of CNC-40-R was in the same stability regime as the other samples and all values indicated moderate colloidal stability (Kumar and Dixit 2017).

Stability of ultrasonicated CNC suspensions

All samples were hermetically sealed in glass vials and then conditioned at 4 °C under exclusion of light for 6 months. AF4-MALS-UV was subsequently applied to determine the long-term stability of ultrasonicated CNC suspensions. A comparison of the cumulative mass-weighted length distributions of colloidal CNCs, before and after conditioning, is shown in Fig. 10 for different extents of ultrasonication. Overall, no significant change of particle length distribution was observed. The mass-weighted particle fractions with lengths < 87 nm changed by ± 1 wt% (Supporting Information, Fig. S5) after 6 months and L at I_{max} shifted to larger values by less than 2% for all samples. Concurrently, marginal broadening of the PSD, in terms of the *FWHM*, was noticeable. Figure 11 shows the related shape factors before and after conditioning. Generally, all samples exhibited lower shape factors after 6 months while the decline of $r_g r_h^{-1}$ was mitigated with increasing ultrasound energy density. In accordance with literature, CNCs are inferred to be susceptible to lateral agglomeration (Chen et al. 2020); however, extensive ultrasonication provided improved long-term stability.

Conclusions and outlook

This work presents, in detail, the effect of ultrasonication on the size distribution of colloidal CNCs from cotton α-cellulose in aqueous suspensions. We applied AF4 with on-line coupled MALS and UV to analyze the particle dimensions in their native colloidal state. Furthermore, conductometric titration, EAF4, and ELS were applied to assess the surface charge density and the colloidal stability of ultrasonicated CNCs.

The results confirm that ultrasonication causes a decrease of mean particle length, along with a narrowing of particle length distribution. Increasing shape factors at shorter particle lengths indicate ultrasound-induced dispersion of dimers and clusters. The process conditions applied during ultrasound treatment did not cause liberation of ionic species from solvation shells of the particles and no de-sulfation was detected. Nevertheless, ultrasonication elevated the apparent sulfate half-ester density, which was attributed to a higher surface area by dispersion of clusters. Concurrently, colloidal stability remained constant throughout the experimental series. The stability of ultrasonicated CNC suspensions was assessed after conditioning the particles for 6 months in a benign environment. The impact of ultrasonication on PSD was found to be more lasting for high ultrasound energy densities, whereas CNCs ultrasonicated at low energy inputs form lateral agglomerates over the course of 6 months.

Ongoing endeavors directed at the commercialization of CNCs require comprehension and standardization of unit operations during CNC processing, as well as the implementation of consistent, reliable, and accurate characterization methods. In this context, our work addressed targeted ultrasonication of CNC suspensions to facilitate production of colloidally stable CNCs with narrow PSD and, thus, predictive and uniform properties. In addition, multi-detector

Table 2 Zeta potential of colloidal CNCs ultrasonicated at 2 and 40 kJ g^{-1} CNC

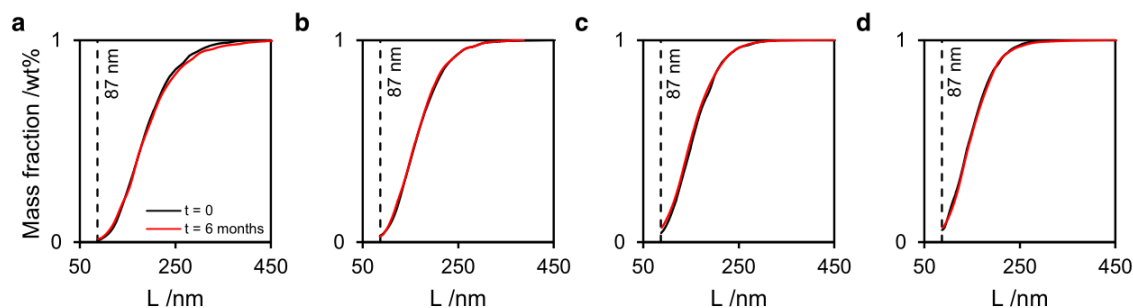|	2 kJ g^{-1} CNC		40 kJ g^{-1} CNC
	ζ from ELS (off-line) (mV)	ζ at I_{max} from EAF4 (on-line) (mV)	
Untreated	-31.4 ± 1.8	-29.1 ± 4.9	-27.5 ± 5.1
Resin-treated	-35.8 ± 2.7	-27.1 ± 4.9	-36.8 ± 2.8

Fig. 10 Comparison of the cumulative mass-weighted length distributions of colloidal CNCs ultrasonicated at energy densities of **a** 2 kJ g^{-1} CNC, **b** 10 kJ g^{-1} CNC, **c** 20 kJ g^{-1} CNC, and **d** 40 kJ g^{-1} CNC before and after storage for 6 months
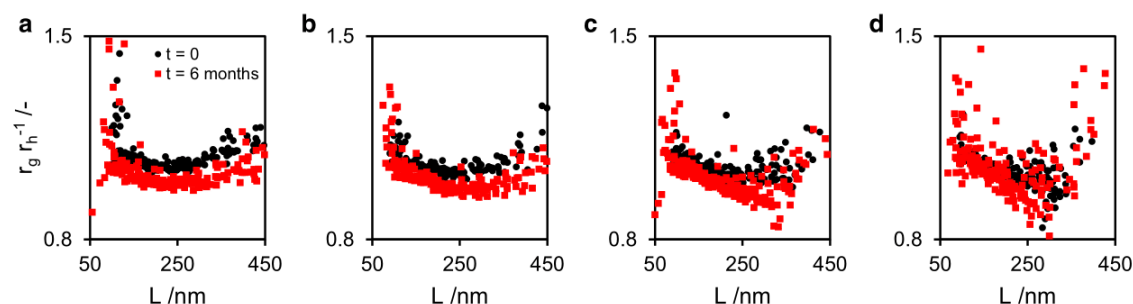

Fig. 11 Comparison of the shape factors of colloidal CNCs ultrasonicated at energy densities of **a** 2 kJ g^{-1} CNC, **b** 10 kJ g^{-1} CNC, **c** 20 kJ g^{-1} CNC, and **d** 40 kJ g^{-1} CNC before and after storage for 6 months

AF4 enables qualitative and quantitative characterization of CNCs in their native state.

Future work on ultrasonication of CNC suspension should address the combined effect of further process conditions—such as particle concentration, frequency, and amplitude—on size, colloidal stability, and the crystallinity index of CNCs. While our work suggests that no morphological degradation of CNCs occurs, Shojaeiarani et al. (2020) reported a notable decrease of crystallinity index by extensive ultrasonication. Therefore, investigating the structural impact of ultrasound treatment on CNCs is necessary to facilitate its targeted adaption to their required performance in advanced materials. Issues raised by our work that require further investigation involve size-related characterization of particle fractions with radii of gyration $r_g < 25$ nm via imaging techniques and the evaluation of agglomeration kinetics of protonated CNCs at different extents of ultrasonication.

Supporting Information

Validation of AF4 set-up, evolution of maximal MALS intensity, effect of CNC treatment with ion-exchange resins, and fractograms after CNC conditioning for 6 months.

References

Abitbol T, Kloser E, Gray DG (2013) Estimation of the surface sulfur content of cellulose nanocrystals prepared by sulfuric acid hydrolysis. Cellulose 20(2):785–794. https://doi.org/10.1007/s10570-013-9871-0

Abitbol T, Rivkin A, Cao Y, Nevo Y, Abraham E, Ben-Shalom T, Lapidot S, Shoseyov O (2016) Nanocellulose, a tiny fiber with huge applications. Curr Opin Biotechnol 39:76–88. https://doi.org/10.1016/j.copbio.2016.01.002

Araki J, Wada M, Kuga S (2001) Steric stabilization of a cellulose microcrystal suspension by poly(ethylene glycol) grafting. Langmuir 17(1):21–27. https://doi.org/10.1021/la001070m

Beck S, Bouchard J (2014) Auto-catalyzed acidic desulfation of cellulose nanocrystals. Nord Pulp Pap Res J 29(1):6–14. https://doi.org/10.3183/npprj-2014-29-01-p006-014

Beck S, Bouchard J, Berry R (2011) Controlling the reflection wavelength of iridescent solid films of nanocrystalline cellulose. Biomacromol 12(1):167–172. https://doi.org/10.1021/bm1010905

Beck S, Bouchard J, Berry R (2012) Dispersibility in water of dried nanocrystalline cellulose. Biomacromol 13(5):1486–1494. https://doi.org/10.1021/bm300191k

Beck S, Méthot M, Bouchard J (2015) General procedure for determining cellulose nanocrystal sulfate half-ester content by conductometric titration. Cellulose 22(1):101–116. https://doi.org/10.1007/s10570-014-0513-y

Beck-Candanedo S, Roman M, Gray DG (2005) Effect of reaction conditions on the properties and behavior of wood

cellulose nanocrystal suspensions. Biomacromol 6(2):1048–1054. https://doi.org/10.1021/bm049300p

Beuguel Q, Tavares JR, Carreau PJ, Heuzey M-C (2018) Ultrasonication of spray- and freeze-dried cellulose nanocrystals in water. J Colloid Interface Sci 516:23–33. https://doi.org/10.1016/j.jcis.2018.01.035

Boluk Y, Danumah C (2014) Analysis of cellulose nanocrystal rod lengths by dynamic light scattering and electron microscopy. J Nanoparticle Res. https://doi.org/10.1007/s11051-013-2174-4

Bouchard J, Méthot M, Fraschini C, Beck S (2016) Effect of oligosaccharide deposition on the surface of cellulose nanocrystals as a function of acid hydrolysis temperature. Cellulose 23(6):3555–3567. https://doi.org/10.1007/s10570-016-1036-5

Brewer AK, Striegel AM (2009) Particle size characterization by quadruple-detector hydrodynamic chromatography. Anal Bioanal Chem 393(1):295–302. https://doi.org/10.1007/s00216-008-2319-y

Brinchi L, Cotana F, Fortunati E, Kenny JM (2013) Production of nanocrystalline cellulose from lignocellulosic biomass: technology and applications. Carbohydr Polym 94(1):154–169. https://doi.org/10.1016/j.carbpol.2013.01.033

Brinkmann A, Chen M, Couillard M, Jakubek ZJ, Leng T, Johnston LJ (2016) Correlating cellulose nanocrystal particle size and surface area. Langmuir 32(24):6105–6114. https://doi.org/10.1021/acs.langmuir.6b01376

Campano C, Lopez-Exposito P, Gonzalez-Aguilera L, Blanco Á, Negro C (2021) In-depth characterization of the aggregation state of cellulose nanocrystals through analysis of transmission electron microscopy images. Carbohydr Polym 254:117271. https://doi.org/10.1016/j.carbpol.2020.117271

Chen M, Parot J, Mukherjee A, Couillard M, Zou S, Hackley VA, Johnston LJ (2020) Characterization of size and aggregation for cellulose nanocrystal dispersions separated by asymmetrical-flow field-flow fractionation. Cellulose 27(4):2015–2028. https://doi.org/10.1007/s10570-019-02909-9

Cherhal F, Cousin F, Capron I (2015) Influence of charge density and ionic strength on the aggregation process of cellulose nanocrystals in aqueous suspension, as revealed by small-angle neutron scattering. Langmuir 31(20):5596–5602. https://doi.org/10.1021/acs.langmuir.5b00851

Contado C (2017) Field flow fractionation techniques to explore the "nano-world." Anal Bioanal Chem 409(10):2501–2518. https://doi.org/10.1007/s00216-017-0180-6

Cranston ED, Gray DG (2006) Morphological and optical characterization of polyelectrolyte multilayers incorporating nanocrystalline cellulose. Biomacromol 7(9):2522–2530. https://doi.org/10.1021/bm0602886

de Souza Lima MM, Wong JT, Paillet M, Borsali R, Pecora R (2003) Translational and rotational dynamics of rodlike cellulose whiskers. Langmuir 19(1):24–29. https://doi.org/10.1021/la020475z

Dong XM, Gray DG (1997) Effect of counterions on ordered phase formation in suspensions of charged rodlike

cellulose crystallites. Langmuir 13(8):2404–2409. https://doi.org/10.1021/LA960724H

Dong XM, Revol J-F, Gray DG (1998) Effect of microcrystallite preparation conditions on the formation of colloid crystals of cellulose. Cellulose 5(1):19–32. https://doi.org/10.1023/A:1009260511939

Drexel R, Siupa A, Carnell-Morris P, Carboni M, Sullivan J, Meier F (2020a) Fast and purification-free characterization of bio-nanoparticles in biological media by electrical asymmetrical flow field-flow fractionation hyphenated with multi-angle light scattering and nanoparticle tracking analysis detection. Molecules. https://doi.org/10.3390/molecules25204703

Drexel R, Sogne V, Dinkel M, Meier F, Klein T (2020b) Asymmetrical flow field-flow fractionation for sizing of gold nanoparticles in suspension. J vis Exp. https://doi.org/10.3791/61757

Espinosa E, Sánchez R, Otero R, Domínguez-Robles J, Rodríguez A (2017) A comparative study of the suitability of different cereal straws for lignocellulose nanofibers isolation. Int J Biol Macromol 103:990–999. https://doi.org/10.1016/j.ijbiomac.2017.05.156

Foster EJ, Moon RJ, Agarwal UP, Bortner MJ, Bras J, Camarero-Espinosa S, Chan KJ, Clift MJD, Cranston ED, Eichhorn SJ, Fox DM, Hamad WY, Heux L, Jean B, Korey M, Nieh W, Ong KJ, Reid MS, Renneckar S, Roberts R, Shatkin JA, Simonsen J, Stinson-Bagby K, Wanasekara N, Youngblood J (2018) Current characterization methods for cellulose nanomaterials. Chem Soc Rev 47(8):2609–2679. https://doi.org/10.1039/c6cs00895j

Fraschini C, Chauve G, Le Berre J-F, Ellis S, Méthot M, O'Connor B, Bouchard J (2014) Critical discussion of light scattering and microscopy techniques for CNC particle sizing. Nord Pulp Pap Res J 29(1):31–40. https://doi.org/10.3183/npprj-2014-29-01-p031-040

Gicquel E, Bras J, Rey C, Putaux J-L, Pignon F, Jean B, Martin C (2019) Impact of sonication on the rheological and colloidal properties of highly concentrated cellulose nanocrystal suspensions. Cellulose 26(13–14):7619–7634. https://doi.org/10.1007/s10570-019-02622-7

Girard M, Vidal D, Bertrand F, Tavares JR, Heuzey M-C (2021) Evidence-based guidelines for the ultrasonic dispersion of cellulose nanocrystals. Ultrason Sonochem 71:105378. https://doi.org/10.1016/j.ultsonch.2020.105378

Guan X, Cueto R, Russo P, Qi Y, Wu Q (2012) Asymmetric flow field-flow fractionation with multiangle light scattering detection for characterization of cellulose nanocrystals. Biomacromol 13(9):2671–2679

Habibi Y, Lucia LA, Rojas OJ (2010) Cellulose nanocrystals: chemistry, self-assembly, and applications. Chem Rev 110(6):3479–3500. https://doi.org/10.1021/cr900339w

Haouache S, Karam A, Chave T, Clarhaut J, Amaniampong PN, Garcia Fernandez JM, de Oliveira Vigier K, Capron I, Jérôme F (2020) Selective radical depolymerization of cellulose to glucose induced by high frequency ultrasound. Chem Sci 11(10):2664–2669. https://doi.org/10.1039/D0SC00020E

ISO (2017a) ISO 22412:2017: particle size analysis—dynamic light scattering (DLS), 2017–02. International Organization for Standardization, Geneva, Switzerland

ISO (2017b) ISO/TS 20477:2017: nanotechnologies—standard terms and their definition for cellulose nanomaterial. 2017–10. International Organization for Standardization, Geneva, Switzerland

ISO (2018a) ISO/CD TS 23151: nanotechnologies—particle size distribution for cellulose nanocrystals (under development). International Organization for Standardization, Geneva, Switzerland

ISO (2018b) ISO/TS 21362:2018: nanotechnologies—analysis of nanoobjects using asymmetrical-flow and centrifugal field-flow fractionation. International Organization for Standardization, Geneva, Switzerland

Jakubek ZJ, Chen M, Couillard M, Leng T, Liu L, Zou S, Baxa U, Clogston JD, Hamad WY, Johnston LJ (2018) Characterization challenges for a cellulose nanocrystal reference material: dispersion and particle size distributions. J Nanoparticle Res. https://doi.org/10.1007/s11051-018-4194-6

Jiang F, Esker AR, Roman M (2010) Acid-catalyzed and solvolytic desulfation of H2SO4-hydrolyzed cellulose nanocrystals. Langmuir 26(23):17919–17925. https://doi.org/10.1021/la1028405

Jonoobi M, Oladi R, Davoudpour Y, Oksman K, Dufresne A, Hamzeh Y, Davoodi R (2015) Different preparation methods and properties of nanostructured cellulose from various natural resources and residues: a review. Cellulose 22(2):935–969. https://doi.org/10.1007/s10570-015-0551-0

Kaushik M, Chen WC, van Ven TGM, de Moores A (2014) An improved methodology for imaging cellulose nanocrystals by transmission electron microscopy. Nord Pulp Pap Res J 29(1):77–84. https://doi.org/10.3183/npprj-2014-29-01-p077-084

Kontturi E (2018) Supramolecular aspects of native cellulose: fringed-fibrillar model, leveling-off degree of polymerization and production of cellulose nanocrystals. In: Potthast A, Hell J, Rosenau T (eds) Cellulose science and technology: chemistry, analysis, and applications. Wiley, Hoboken, pp 263–276

Kumar A, Dixit CK (2017) Methods for characterization of nanoparticles. In: Nimesh S, Chandra R, Gupta N (eds) Advances in nanomedicine for the delivery of therapeutic nucleic acids. Elsevier Science, Kent, pp 43–58

Lin K-H, Hu D, Sugimoto T, Chang F-C, Kobayashi M, Enomae T (2019) An analysis on the electrophoretic mobility of cellulose nanocrystals as thin cylinders: relaxation and end effect. RSC Adv 9(58):34032–34038. https://doi.org/10.1039/c9ra05156b

Litzen A, Wahlund KG (1991) Zone broadening and dilution in rectangular and trapezoidal asymmetrical flow field-flow fractionation channels. Anal Chem 63(10):1001–1007. https://doi.org/10.1021/ac00010a013

Marchessault R, Morehead F, Koch M (1961) Some hydrodynamic properties of neutral suspensions of cellulose crystallites as related to size and shape. J Colloid Sci 16(4):327–344. https://doi.org/10.1016/0095-8522(61)90033-2

Mazloumi M, Johnston LJ, Jakubek ZJ (2018) Dispersion, stability and size measurements for cellulose nanocrystals by static multiple light scattering. Cellulose

25(10):5751–5768. https://doi.org/10.1007/s10570-018-1961-6

Metzger C, Auber D, Dähnhardt-Pfeiffer S, Briesen H (2020) Agglomeration of cellulose nanocrystals: the effect of secondary sulfates and their use in product separation. Cellulose. https://doi.org/10.1007/s10570-020-03476-0

Moon RJ, Martini A, Nairn J, Simonsen J, Youngblood J (2011) Cellulose nanomaterials review: structure, properties and nanocomposites. Chem Soc Rev 40(7):3941–3994. https://doi.org/10.1039/c0cs00108b

Mukherjee A, Hackley VA (2018) Separation and characterization of cellulose nanocrystals by multi-detector asymmetrical-flow field-flow fractionation. Analyst 143(3):731–740. https://doi.org/10.1039/c7an01739a

Nickerson RF, Habrle JA (1947) Cellulose intercrystalline structure. Ind Eng Chem 39(11):1507–1512. https://doi.org/10.1021/ie50455a024

NIST (2021) SRM 1964: Polystyrene Spheres (Nominal Diameter 60 nm)

Phan-Xuan T, Thuresson A, Skepö M, Labrador A, Bordes R, Matic A (2016) Aggregation behavior of aqueous cellulose nanocrystals: the effect of inorganic salts. Cellulose 23(6):3653–3663. https://doi.org/10.1007/s10570-016-1080-1

Postnova Analytics GmbH (2020a) NovaAnalysis (2007). https://www.postnova.com/

Postnova Analytics GmbH (2020b) NovaFFF (2.1.0.5). https://www.postnova.com/

Postnova Analytics GmbH (2020c) NovaMALS (1.5.0.8). https://www.postnova.com/

Rånby BG, Ribi E (1950) Ueber den Feinbau der Zellulose (Ultrastructure of cellulose). Experientia 6(1):12–14. https://doi.org/10.1007/BF02154044

Reid MS, Villalobos M, Cranston ED (2017) Benchmarking cellulose nanocrystals: from the laboratory to industrial production. Langmuir 33(7):1583–1598. https://doi.org/10.1021/acs.langmuir.6b03765

Revol J-F, Godbout L, Dong X-M, Gray DG, Chanzy H, Maret G (1994) Chiral nematic suspensions of cellulose crystallites; phase separation and magnetic field orientation. Liq Cryst 16(1):127–134. https://doi.org/10.1080/02678299408036525

Roman M (2015) Toxicity of Cellulose Nanocrystals: A Review. Ind Biotechnol 11(1):25–33. https://doi.org/10.1089/ind.2014.0024

Rudie A (2017) Commercialization of cellulose nanofibril (CNF) and cellulose nanocrystal (CNC): pathway and challenges. In: Kargarzadeh H, Ahmad I, Thomas S, Dufresne A (eds) Handbook of nanocellulose and cellulose nanocomposites, vol 1. Wiley-VCH. Weinheim, Germany, pp 761–797

Ruiz-Palomero C, Laura Soriano M, Valcárcel M (2017) Detection of nanocellulose in commercial products and its size characterization using asymmetric flow field-flow fractionation. Microchim Acta 184(4):1069–1076. https://doi.org/10.1007/s00604-017-2106-6

Shafiei-Sabet S, Hamad WY, Hatzikiriakos SG (2012) Rheology of nanocrystalline cellulose aqueous suspensions. Langmuir 28(49):17124–17133. https://doi.org/10.1021/la303380v

Shatkin JA, Kim B (2015) Cellulose nanomaterials: life cycle risk assessment, and environmental health and safety roadmap. Environ Sci Nano 2(5):477–499. https://doi.org/10.1039/C5EN00059A

Shojaeiarani J, Bajwa D, Holt G (2020) Sonication amplitude and processing time influence the cellulose nanocrystals morphology and dispersion. Nanocomposites 6(1):41–46. https://doi.org/10.1080/20550324.2019.1710974

Stepto R, Chang T, Kratochvíl P, Hess M, Horie K, Sato T, Vohlídal J (2015) Definitions of terms relating to individual macromolecules, macromolecular assemblies, polymer solutions, and amorphous bulk polymers (IUPAC Recommendations 2014). Pure Appl Chem 87(1):71–120. https://doi.org/10.1515/pac-2013-0201

Stepto RFT (2009) Dispersity in polymer science (IUPAC Recommendations 2009). Pure Appl Chem 81(2):351–353. https://doi.org/10.1351/PAC-REC-08-05-02

Trache D, Hussin MH, Haafiz MKM, Thakur VK (2017) Recent progress in cellulose nanocrystals: sources and production. Nanoscale 9(5):1763–1786. https://doi.org/10.1039/c6nr09494e

van de Hulst HC (1958) Light scattering by small particles. Q J R Meteorol Soc 84(360):198–199. https://doi.org/10.1002/qj.49708436025

Vanderfleet OM, Cranston ED (2020) Production routes to tailor the performance of cellulose nanocrystals. Nat Rev Mater. https://doi.org/10.1038/s41578-020-00239-y

von Smoluchowski M (1906) Zur kinetischen Theorie der Brownschen Molekularbewegung und der Suspensionen. Ann Phys 326(14):756–780. https://doi.org/10.1002/andp.19063261405

Wahlund KG, Giddings JC (1987) Properties of an asymmetrical flow field-flow fractionation channel having one permeable wall. Anal Chem 59(9):1332–1339. https://doi.org/10.1021/ac00136a016

Wang N, Ding E, Cheng R (2007) Thermal degradation behaviors of spherical cellulose nanocrystals with sulfate groups. Polymer 48(12):3486–3493. https://doi.org/10.1016/j.polymer.2007.03.062

Wang N, Ding E, Cheng R (2008) Preparation and liquid crystalline properties of spherical cellulose nanocrystals. Langmuir 24(1):5–8. https://doi.org/10.1021/la702923w

Wang QQ, Zhu JY, Reiner RS, Verrill SP, Baxa U, McNeil SE (2012) Approaching zero cellulose loss in cellulose nanocrystal (CNC) production: recovery and characterization of cellulosic solid residues (CSR) and CNC. Cellulose 19(6):2033–2047. https://doi.org/10.1007/s10570-012-9765-6

Zianor Azrina ZA, Beg MDH, Rosli MY, Ramli R, Junadi N, Alam AKMM (2017) Spherical nanocrystalline cellulose (NCC) from oil palm empty fruit bunch pulp via ultrasound assisted hydrolysis. Carbohydr Polym 162:115–120. https://doi.org/10.1016/j.carbpol.2017.01.035

Effect of ultrasonication on the size distribution and stability of cellulose nanocrystals in suspension: an asymmetrical flow field-flow fractionation study

Christoph Metzger,[1,†] Roland Drexel,[2] Florian Meier,[2] Heiko Briesen[1]

[1]*Technical University of Munich, Germany, TUM School of Life Sciences Weihenstephan, Chair of Process Systems Engineering*

[2]*Postnova Analytics GmbH, Rankinestr. 1, 86899 Landsberg am Lech, Germany*

[†]+49 8161 71-5383

[1]+49 8161 71-4510

[†]christoph.metzger@tum.de

[1]http://svt.wzw.tum.de/

ORCID iDs: Christoph Metzger (0000-0003-1582-8305); Florian Meier (0000-0003-1395-4877); Heiko Briesen (0000-0001-7725-5907)

1

Operating principle of asymmetrical flow field-flow fractionation

Separation in asymmetrical flow field-flow fractionation (AF4) occurs in a thin, ribbon-like channel where the channel bottom (accumulation wall) is equipped with a semi-permeable ultrafiltration membrane that withholds sample constituents while simultaneously allowing cross flow to pass through. Cross flow is applied perpendicularly to the parabolic channel flow, thereby counteracting the diffusion of sample constituents. In an equilibrium state of forces, smaller sample constituents are located further away from the accumulation wall, compared to larger constituents. They are thus transported in faster streamlines of the channel flow, eluting earlier than larger constituents. Consequently, the retention time of the constituents is directly correlated with their diffusion coefficient, which is convertible to hydrodynamic size using the Stokes-Einstein equation (Schimpf et al. 2000). A further development of AF4 is electrical AF4 (EAF4) where the cross flow is superimposed with an electrical field to facilitate separation based on both size and electrophoretic mobility (**Fig. S1**) (Drexel et al. 2020).
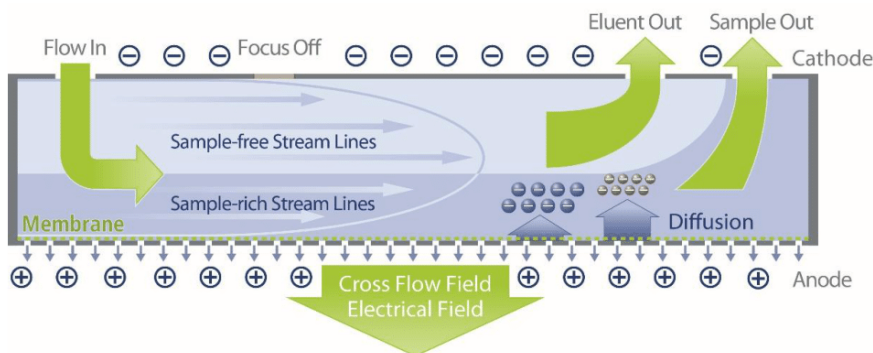
Fig. S1: Longitudinal section of an EAF4 channel (reprinted with permission of Postnova Analytics GmbH)

Literature survey of multi-detector AF4 on cellulose nanocrystal suspensions

Table S1: Summary of studies on multi-detector AF4 for analysis and fractionation of cellulose nanocrystals (CNCs)

Cellulose source	CNC initial state and surface	Detection	Offline validation	Objectives[♦]	Reference
Microcrystalline cellulose (Avicel), cotton fabric	Never dried, sulfated	MALS, DLS, dRI	TEM	PSD of CNCs – effect of cellulose source and processing; correlated with TEM results	Guan et al. (2012)
Cereal straws (wheat, corn, barley, oat)	Never dried, TEMPO-oxidized	MALS, dRI	DLS	(Qualitative) PSD of polydisperse CNCs	Espinosa et al. (2017)
Microcrystalline cellulose (Avicel)	Never dried, TEMPO-oxidized	MALS, dRI	DLS	Qualitative detection of CNCs in consumer products	Ruiz-Palomero et al. (2017)
Softwood pulp; CNCs supplied by National Research Council, Canada	Spray dried, sulfated, Na$^+$-exchanged	MALS, DLS, dRI	DLS, TEM	Semi-preparatory CNC fractionation via AF4 for narrow PSDs	Mukherjee and Hackley (2018)
Softwood pulp; CNCs supplied by CelluForce Inc., Windsor, QC, Canada	Spray dried, sulfated, Na$^+$-exchanged	MALS, DLS, dRI	AFM, DLS, TEM	Fractionation of polydisperse CNCs—facilitated microscopy, correlated PSD, and agglomeration level with TEM results	Chen et al. (2020)

[♦]Related to purpose of AF4.

3

Ultrasonication of CNC suspension

$$e_{US} = \frac{ultrasound\ power \cdot treatment\ time}{CNC\ mass} \qquad \text{(S1)}$$

Table S2: Process parameters during incremental ultrasonication of CNC suspension

Sample name	CNC-2	CNC-4	CNC-6	CNC-8	CNC-10	CNC-15	CNC-20	CNC-40
Suspension mass /g	243.35	213.32	183.66	153.88	124.05	94.35	64.51	34.70
CNC mass /g	2.43	2.13	1.83	1.54	1.24	0.94	0.64	0.35
Energy input /kJ	4.90	9.13	12.82	15.89	18.36	23.05	26.21	32.81
Treatment time /s	146	274	385	477	551	692	787	985
Targeted e_{US} /kJ g^{-1} CNC	2.00	4.00	6.00	8.00	10.00	15.00	20.00	40.00
Actual e_{US} /kJ g^{-1} CNC	2.01	4.01	6.02	8.02	10.02	14.99	19.91	38.98

4

Fractionation of CNCs by AF4

Validity of the set-up
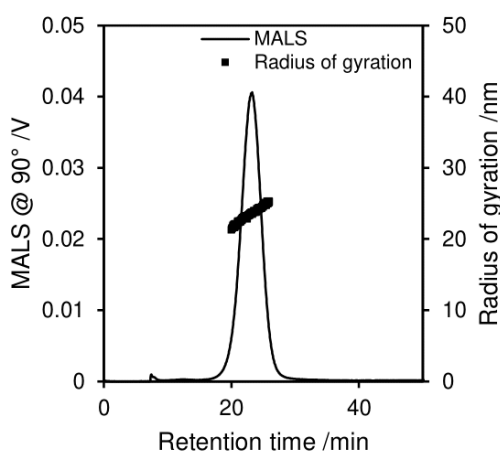
Fig. S2: Fractogram of standard polystyrene beads with a nominal diameter of 60 nm (NIST 2021). r_g was evaluated with the NovaMALS software (Postnova Analytics GmbH 2020)

Our set-up enabled an accurate determination of particles with a $r_g \geq 25$ nm that eluted at net retention times, $t_R, \geq 10.6$ min (**Fig. S2**). Provided that the applied rod model is valid over the full distribution (Mukherjee and Hackley 2018) and CNCs have a L-d ratio of 5–50 (ISO 2017), a r_g of 25 nm corresponds to particles with a rod length of 87 nm and a minimal L-d ratio of 5 limits them to particle diameters below 17 nm. Notably, single elementary cellulose fibrils of plantal sources have diameters in the range of 3 nm (Kubicki et al. 2018) and reported crystallite dimensions of single CNCs from cotton are in the range from 5–10 nm (Dong et al. 1998, Beck-Candanedo et al. 2005). Accordingly, single CNCs with a length of 87 nm and diameters of 3, 5, or 10 nm have respective L-d ratios of 29, 17, or 9. Likewise, minimal evaluable rod lengths of 95 nm (Guan et al. 2012), 101 nm (Mukherjee and Hackley 2018), and 104 nm (Chen et al. 2020) have been reported for the application of AF4-MALS on colloidal CNCs. Shorter rod lengths determined by AF4-MALS have been reported by Ruiz-Palomero et al. (2017) and Espinosa et al. (2017); however, these values are either not unequivocally attributable to CNCs or methodically not inducible, respectively.

5

Evolution of maximal multi-angle light scattering intensity
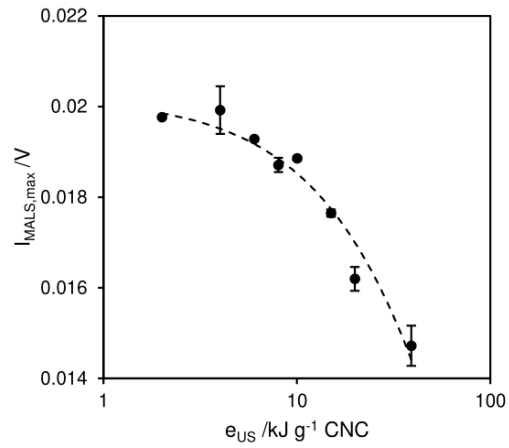
Fig. S3: Maximal intensity of the 90° signal decreases exponentially with increasing ultrasound energy density

Effect of CNC treatment with ion-exchange resins
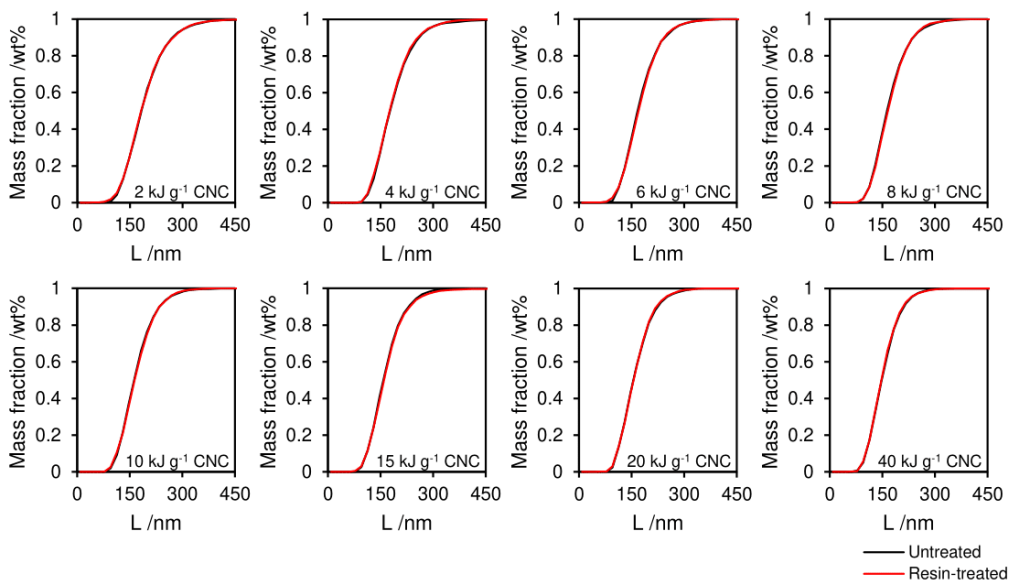
Fig. S4: Particle size distributions of colloidal CNCs before (black) and after (red) treatment with ion-exchange resins at each energy input

6

Fractograms after CNC conditioning for six months
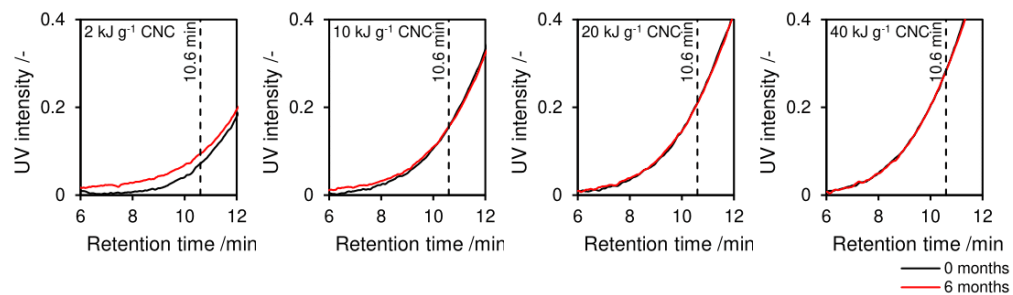
Fig. S5: Normalized UV absorbance signals before (black) and after (red) conditioning of CNC suspensions for six months

7

References

Beck-Candanedo S, Roman M, Gray DG (2005) Effect of reaction conditions on the properties and behavior of wood cellulose nanocrystal suspensions. Biomacromolecules 6(2):1048–1054. https://doi.org/10.1021/bm049300p

Chen M, Parot J, Mukherjee A, Couillard M, Zou S, Hackley VA, Johnston LJ (2020) Characterization of size and aggregation for cellulose nanocrystal dispersions separated by asymmetrical-flow field-flow fractionation. Cellulose 27(4):2015–2028. https://doi.org/10.1007/s10570-019-02909-9

Dong XM, Revol J-F, Gray DG (1998) Effect of microcrystallite preparation conditions on the formation of colloid crystals of cellulose. Cellulose 5(1):19–32. https://doi.org/10.1023/A:1009260511939

Drexel R, Siupa A, Carnell-Morris P, Carboni M, Sullivan J, Meier F (2020) Fast and Purification-Free Characterization of Bio-Nanoparticles in Biological Media by Electrical Asymmetrical Flow Field-Flow Fractionation Hyphenated with Multi-Angle Light Scattering and Nanoparticle Tracking Analysis Detection. Molecules 25(20). https://doi.org/10.3390/molecules25204703

Espinosa E, Sánchez R, Otero R, Domínguez-Robles J, Rodríguez A (2017) A comparative study of the suitability of different cereal straws for lignocellulose nanofibers isolation. International journal of biological macromolecules 103:990–999. https://doi.org/10.1016/j.ijbiomac.2017.05.156

Guan X, Cueto R, Russo P, Qi Y, Wu Q (2012) Asymmetric flow field-flow fractionation with multiangle light scattering detection for characterization of cellulose nanocrystals. Biomacromolecules 13(9):2671–2679

ISO (2017) ISO/TS 20477:2017 - Nanotechnologies — Standard terms and their definition for cellulose nanomaterial. 2017-10. International Organization for Standardization, Geneva, Switzerland

Kubicki JD, Yang H, Sawada D, O'Neill H, Oehme D, Cosgrove D (2018) The Shape of Native Plant Cellulose Microfibrils. Scientific reports 8(1):13983. https://doi.org/10.1038/s41598-018-32211-w

Mukherjee A, Hackley VA (2018) Separation and characterization of cellulose nanocrystals by multi-detector asymmetrical-flow field-flow fractionation. The Analyst 143(3):731–740. https://doi.org/10.1039/c7an01739a

NIST (2021) SRM 1964 - Polystyrene Spheres (Nominal Diameter 60 nm)

Postnova Analytics GmbH (2020) NovaMALS (1.5.0.8) - https://www.postnova.com/

Ruiz-Palomero C, Laura Soriano M, Valcárcel M (2017) Detection of nanocellulose in commercial products and its size characterization using asymmetric flow field-flow fractionation. Microchimica Acta 184(4):1069–1076. https://doi.org/10.1007/s00604-017-2106-6

Schimpf ME, Caldwell K, Giddings JC (eds) (2000) Field-flow fractionation handbook. Wiley-Interscience, New York, Chichester

8

4.3. Efficiently extracted cellulose nanocrystals and starch nanoparticles and techno-functional properties of films made thereof

Summary. Fossil-based polymers are still indispensable in packaging applications, due to their low weight, high performance, and low cost, in combination with good processability. They meet packaging materials' requirements for good barrier properties against oxygen and water vapor, good mechanical performance, and high transparency (*403*). However, while synthetic polymers are designed for performance and durability, most packaging materials are used for less than a week only (*404*). Furthermore, they show limited degradability and recyclability, which causes large amounts of waste. In contrast, biodegradable polymers, such as poly(lactic acid) (PLA), are derived from renewable resources; and they can be integrated into a sustainable circular economy (*405*). Nevertheless, PLA's high gas permeability limits its range of applications. In this context, CNC barrier films can be applied onto PLA to reduce oxygen transmission rate of composite films (*406*). During drying, CNCs form a complex dense network with increased tortuosity, which increases diffusion path within the film (*407*). Furthermore, CNCs' crystalline structure contributes to improved barrier properties of such films (*408, 409*).

Primary objective of this study was performance assessment of CNC coatings from saline CNC suspensions in gas barrier films. CNCs were isolated from cotton linters, following the protocol in **Paper I**, and stable particle suspensions contained residual Na_2SO_4. Compatibilization of hydrophobic PLA and hydrophilic CNCs was achieved by air plasma treatment of polymeric substrates to elevate their interfacial tension (*410*). Then, CNC coatings with thickness of 2.6 µm were applied to a PLA film of 26.8 µm thickness using a blade. CNC coatings were microscopically inhomogeneous due to particle agglomeration during solvent evaporation, but light transmittance was only reduced by 10%, compared to bare PLA. CNC coatings reduced oxygen permeability of PLA of 515 cm^3 m^{-2} d^{-1} bar^{-1} by 75% to 130 cm^3 m^{-2} d^{-1} bar^{-1}, at a relative humidity of 50%. No improvement of water vapor barrier of coated PLA was found. For comparison, starch nanoplatelets (SNPs) were isolated from corn starch by a similar protocol, involving acid-catalyzed hydrolysis and subsequent neutralization. SNP coatings on PLA showed lower light transmittance, compared to CNC coatings; but they resulted in similar improvement of oxygen permeability when coated onto PLA. Hereby, it was shown that neutralization-based isolation of CNCs and SNPs yields colloidally stable nanoparticles, which facilitate good oxygen barrier properties on PLA. Therefore, such nanoparticle suspensions are suitable for production of sustainable packaging materials with good application properties. Furthermore, it was attempted to coat paper substrates with both CNCs and SNPs. However, the substrate's high porosity resulted in pitted coatings, and no improvement of barrier properties was achieved.

Secondary objective of this study was performance assessment of CNCs as reinforcing filler in nanocomposites. CNC-based polymeric nanocomposites are one of the most

studied fields in academic research on CNCs (*411*). In this work, CNC and SNP suspensions, containing residual Na_2SO_4, were incorporated into hydrophilic starch matrices by solution casting at different concentrations, to estimate reinforcing effects as function of nanoparticle loading. However, no significant effect of nanoparticle loading on mechanical properties was found. It was assumed that both segregation of the filler from the matrix during drying and the measurement set-up compromised accurate determination of mechanical properties.

Author's contributions. The author had a leading role in this work. He planned and coordinated the workflow, performed or supervised all data acquisition, and performed data analysis, as well as interpretation. SSa designed and conducted groundwork for the coating strategy and performed preliminary analyses on barrier properties. LB carried out most of the experiments. ML and SSä supported the author with data evaluation and interpretation. HB supervised the research. The author wrote the manuscript and discussed all results with HB.

Efficiently Extracted Cellulose Nanocrystals and Starch Nanoparticles and Techno-Functional Properties of Films Made Thereof

Christoph Metzger [1] [ID]**, Solange Sanahuja [1], Lisa Behrends [1], Sven Sängerlaub [2,3], Martina Lindner [2,3] and Heiko Briesen [1,*]**

[1]   Chair of Process Systems Engineering, TUM School of Life Sciences Weihenstephan, Technical University of Munich, Gregor-Mendel-Str. 4, 85354 Freising, Germany; christoph.metzger@tum.de (C.M.); solange.sanahuja@tum.de (S.S.); lisa.behrends@tum.de (L.B.)

[2]   Chair of Food Packaging Technology, Technical University of Munich, TUM School of Life Sciences Weihenstephan, Weihenstephaner Steig 22, 85354 Freising, Germany; sven.saengerlaub@ivv.fraunhofer.de (S.S.); martina.lindner@ivv.fraunhofer.de (M.L.)

[3]   Fraunhofer Institute for Process Engineering and Packaging IVV, Giggenhauser Str. 35, 85354 Freising, Germany

*   Correspondence: briesen@wzw.tum.de; Tel.: +49-8161-71-3272

Abstract: Cellulose nanocrystals (CNC) and starch nanoparticles (SNP) have remarkable physical and mechanical characteristics. These properties particularly facilitate their application as high-performance components of bio-based packaging films as alternatives to fossil-based counterparts. This study demonstrates a time-efficient and resource-saving extraction process of CNC and SNP by sulfuric acid hydrolysis and neutralization. The yields of the hydrolyzed products were 41.4% (CNC) and 32.2% (SNP) after hydrolysis times of 3 h and 120 h, respectively. The nanoparticle dispersions were wet-coated onto poly(lactic acid) (PLA) and paper substrates and were incorporated into starch films. No purification or functionalization of the nanoparticles was performed prior to their application. Techno-functional properties such as the permeability of oxygen and water vapor were determined. The oxygen permeability of 5–9 cm^3 (STP) 100 µm m^{-2} d^{-1} bar^{-1} at 50% relative humidity and 23 °C on PLA makes the coatings suitable as oxygen barriers. The method used for the extraction of CNC and SNP contributes to the economic production of these nanomaterials. Further improvements, e.g., lower ion concentration and narrower particle size distribution, to achieve reproducible techno-functional properties are tangible.

Keywords: cellulose nanocrystals (CNC); starch nanoparticles (SNP); biopolymers; packaging; barrier films; nanomaterials; nanocomposites; bio-coatings; oxygen barrier; water vapor barrier

1. Introduction

Films and coatings made of cellulose nanocrystals (CNC) and starch nanoparticles (SNP) have considerable potential for application in sustainable and bio-based packaging materials [1–10]. Their techno-functional properties can supplement the limited gas barrier properties and the mechanical properties of renewable biopolymers such as poly(lactic acid) (PLA), paper and starch [11–15]. PLA is synthesized from fermented carbohydrates [16,17]. It is used in the packaging industry due to its thermal properties manifesting in good processing characteristics, its chemical and UV resistance, and its biodegradability [18–20]. However, the oxygen and water vapor permeability of PLA necessitates barrier enhancement for oxygen and water vapor sensitive packaging goods [21–23]. Pant et al. [24] reported an oxygen permeability of PLA of 153 (STP) 100 µm m^{-2} d^{-1} at 23 °C and 50% relative

humidity and a water vapor transmission rate of 58 g (STP) 100 μm m^{-2} d^{-1} at 23 °C at a gradient in relative humidity of 85→0%. Similarly, the application of fiber-based packaging materials, such as paper, is restricted due to high sensitivity to moisture accompanied by poor barrier properties [25,26]. Starch can be converted into a continuous polymeric phase and is therefore processable using extrusion technology developed to produce fossil-based polymer packaging. The use of starch is nevertheless just as well limited due to its hydrophilic nature leading to moisture sensitivity that is compromising the dimensional stability and mechanical properties [27]. The techno-functional properties of these three materials can be enhanced by the introduction of CNC and SNP in the form of coatings or fillers in nanocomposites. Both CNC and SNP facilitate tailored physical and mechanical properties enabling the manufacturing of bio-based packaging materials to substitute or complement conventional, fossil-based polymers. Due to their presumably low environmental, health, and safety risks, packaging applications for fast moving consumer goods are conceivable [28].

However, the large-scale production of CNC and SNP is presently unattractive. Sulfuric acid hydrolysis is the commonly used method to extract CNC and SNP from suitable biopolymeric feed stocks [29,30]. Separating the hydrolyzed product from the acidic reaction solution is laborious and comprises a high consumption of resources and high material costs; usually applied strategies involve dilution with a large amount of water and quenching, sedimentation, and eventually centrifugation in combination with ultrafiltration or dialysis for purification [30]. In contrast, Müller et al. [31] suggested an efficient approach based on the neutralization of the acid. Flocculation of the nanoparticles is induced in the presence of cations at high ionic strengths. The salt concentration is subsequently reduced by centrifugation until the ion concentration level for peptization is reached. Hereby, a high yield of hydrolyzed product is achievable at an overall low net process time and low consumption of resources and materials.

Manufacturing limitations due to the nanoparticles' intrinsic physical properties further impede their application in coatings on substrates and as a filler in nanocomposites. These difficulties arise from the limited interfacial adhesion of the hydrophilic nanoparticles and the hydrophobic polymers, moisture absorption, and agglomeration issues. Several studies addressed the application of CNC and SNP in biopolymeric packaging materials [2,6–10,27,30,32–35]. Techno-functional properties such as gas permeability, mechanical properties, and thermal stability were adjusted by modifying the nanoparticles' surface chemistry. If further functionalization of the nanoparticles is desired, the use of non-green chemicals and additional time is required [36].

The aim of the present study was (i) to demonstrate a time-efficient and resource-saving post-processing method to produce CNC and SNP. The qualification of the nanomaterials as (ii) barrier coatings on flat substrates and (iii) as filler in nanocomposites was evaluated. The study tested several hypotheses (h). We tested whether (h1) stable dispersions of CNC and SNP are producible by the presented method and (h2) the nanoparticles lower the gas permeability of PLA and paper substrates and (h3) improve the water vapor permeability and the mechanical properties of solution-cast starch films. Good spreadability of the nanoparticles on the substrate materials and their miscibility in hydrophilic starch films are the necessary preconditions to achieve improved techno-functional properties.

2. Materials and Methods

2.1. Materials

2.1.1. Materials for Nanoparticle Processing

Cotton linters (water content 4 wt %) were purchased from Buch-Kunst-Papier (St. Ingbert Rentrisch, Germany). Corn starch (water content 15 wt %), sodium azide (99%), and sodium hydroxide (99%) were purchased from Carl Roth (Karlsruhe, Germany). Sulfuric acid (95%) was obtained from VWR (Ismaning, Germany). All chemicals were used as received. Ultrapure (type 1) water with a resistivity

of 18.2 MΩ cm (Milli-Q Direct 8 system, Merck Chemicals, Schwalbach, Germany) was used for all experiments.

2.1.2. Substrate Materials

Poly(lactic acid) films (2002D, NatureWorks LLC, Minnetonka, MN, USA) with a thickness of 25 μm were provided by Fraunhofer IVV (Freising, Germany). Material properties of 2002D were determined by other groups: Murphy et al. [37] report a melting temperature T_m of 154 °C and a glass transition temperature T_g of 55 °C as well as a D-lactide content of 4% and a molecular weight M_W of 194,000 g mol^{-1}. Ge et al. [38] report values of T_m of 168.2 °C, T_g of 58.6 °C, a D-lactide content of 4%, a L-lactide content of 96% and a M_W of 121,400 g mol^{-1}. Mihai et al. [39] report semi-crystallinity of 2002D.

Paper sheets (Metalkote Evolution, Ahlstrom-Munksjö Group, Stockholm, Sweden) with a grammage of 65 g m^{-2} were also provided by Fraunhofer IVV (Freising, Germany). Untreated (bare) substrates were tested as reference materials.

2.1.3. Cast Films

Corn starch (water content 15 wt %) and glycerol (water content 14 wt %) were purchased from Carl Roth (Karlsruhe, Germany). Pure starch-glycerol films without nanofillers were tested as reference material.

2.1.4. Karl Fischer Titration

Formamide (99.5 wt %), iodine solution (Roti$^®$hydroquant C5; 5 mg H_2O mL^{-1}, free of pyridine), methanol (Roti$^®$hydroquant D; dry), and a water standard (Roti$^®$hydroquant; 10 mg H_2O g^{-1}) were purchased from Carl Roth (Karlsruhe, Germany).

2.1.5. Pinhole Testing

Pinholes were determined with peanut oil containing Sudan Red III (Merck, Darmstadt, Germany) in a concentration of 1 part per thousand.

2.2. Nanoparticle Preparation

CNC were prepared by sulfuric acid hydrolysis and subsequent basic neutralization. The procedure was derived from the method described by Müller et al. [31]. 2 mol of sulfuric acid (64 wt %) was added to cut cotton linters in a mass ratio of 15:1 and transferred to a heated water bath at 50 °C. The raw cellulose was hydrolyzed for 3 h under vigorous stirring. Following hydrolysis, the reaction solution was diluted to 54 wt % H_2SO_4 to decrease the viscosity and then decanted to 3 mol of sodium hydroxide (7 mol kg^{-1}) in a cooled water bath. After homogenization for 15 min, the CNC were separated from the reaction solution by consecutive centrifugation steps until a pH of ~2 was reached. Excess ions were removed from the hydrolyzed product by decantation of the supernatant after each washing step and successive redispersion with H_2O. Eventually, the dispersion was ultrasonicated (8 kJ g^{-1} CNC) with a homogenizer (Sonoplus HD 3400 with the sonotrode VS 70 T, Bandelin, Berlin, Germany) and stored at 6 °C until further use.

The hydrolysis conditions to produce SNP was derived from the method demonstrated by Angellier et al. [40]. 1 mol of sulfuric acid (18 wt %) was added to corn starch in a mass ratio of 7:1 and then hydrolyzed for 120 h at 40 °C. Subsequently, the reaction mixture was decanted to 1.5 mol of sodium hydroxide (5 mol kg^{-1}) for neutralization. Similar to the extraction of CNC, SNP were separated from the salt solution by consecutive precipitation and redispersion until the pH stabilized at ~2.7. After ultrasonication, 0.01 g sodium azide L^{-1} was added as an antimicrobial agent before storing the product at 6 °C.

2.3. Coating of PLA and Paper

The coating strategy of the nanoparticle dispersions onto polymer substrates was empirically developed for CNC dispersions. Qualitative parameters were considered regarding the application of a nanoparticle dispersion onto a flat substrate and the subsequent drying process. PLA was corona-treated (Corona Station, Softal, Hamburg, Germany) at 400 W and 5 m min^{-1} to increase the surface energy with the aim to achieve good spreadability of the aqueous coatings on the substrate surface [41]. For paper this pretreatment was not necessary. The effect of viscosity of the coating medium was investigated for CNC dispersions with concentrations of $3 \leq c \leq 8$ wt %. It was found that with increasing concentration and hence increasing viscosity, contraction of the wet film could be fully avoided. The dynamic viscosity of a dispersion with 6 wt % of CNC was >2000 Pa s at a shear rate of 0.01 s^{-1} and decreased exponentially to 0.05 Pa s at 1000 s^{-1}.

The concentration of the nanoparticle dispersions was adjusted in a rotary evaporator (Rotavapor R-100, Büchi, Flawil, Switzerland) at 40 °C and 70 mbar to ~63 g kg^{-1} and ~73 g kg^{-1} of hydrolyzed product for cellulose and starch, respectively. The dispersions were applied onto the substrates with a semi-automatic coating unit (CUF5, Sumet Systems, Denklingen, Germany).

The interplay of blade velocities v of $5 \leq v \leq 60$ mm s^{-1} and wet film thicknesses d of $10 \leq d \leq 100$ μm was tested. At $v = 10$ mm s^{-1} and $d \approx 51$ μm under a normal load of 40 N, the coatings showed no macroscopic cracks or delamination on both PLA and paper. The same parameters led to conformable coatings using SNP dispersions on both substrates.

Drying was tested for temperatures of $40 \leq T \leq 60$ °C for PLA and $40 \leq T \leq 120$ °C for paper. The drying time was $1 \leq t \leq 10$ min. Drying at high temperatures and within narrow time spans led to contraction of the coating medium and eventually delamination of the coating layer on PLA. Furthermore, high temperature for extended time spans bears the risk of denaturation of plastic substrates and desulfation of the nanoparticles [42]. Eventually, a temperature of 40 °C for 10 min was chosen for PLA. Paper was dried at 70 °C for 3 min to avoid wrinkling [43]. To avoid possible pinholes in the coating layer on the paper substrate due to its surface roughness it was coated and dried two times with the same parameters.

2.4. Cast Film Preparation

The starch-glycerol and nanocomposite films were prepared by solution casting according to the method of Alves et al. [33]. Precursor solutions of the nanocomposite films with the total mass m_{total} had a water content c_{aq} of 97 wt %. Five different nanoparticle concentrations $0 \leq c_{\text{NP}} \leq 9$ wt % were added as well as glycerol as plasticizer with a concentration c_{gly} of 30 wt %, both relative to the weighed portion of starch m_{starch}. The weighed portions of chemicals were calculated according to Equation (1), considering the mass of water added $m_{\text{H}_2\text{O}}$, corrected for the water content of the other components.

$$m_{\text{total}} = \left(1 + c_{\text{gly}} + c_{\text{NP}}\right) m_{\text{starch}} + c_{\text{aq}} m_{\text{H}_2\text{O}} \tag{1}$$

Starch was added to preheated water with a temperature of 70 °C in a water bath and stirred for 1 h to allow plastification. Glycerol and nanoparticles were then added and stirring was continued for 20 min to allow plasticization and mixing of the composite. A dry film thickness of 50 μm was targeted. Before casting in polystyrene Petri dishes (Greiner Bio-One, distributed by VWR, Ismaning, Germany), the filmogenic solutions were homogenized in an ultrasonic bath for 3 min. Excess water was evaporated from the dishes overnight in a climatic chamber (ICH 110, Memmert, Schwabach, Germany) at 40 °C and a relative humidity (r.h.) of 47%. The films were then peeled off from the Petri dish and turned upside down for double-sided drying overnight.

2.5. Instrument Measurements

If applicable, all measurements were performed at least in triplicate and are presented with the 95% confidence interval of the mean. The uncertainty of quantities depending on multiple variables is

given by the propagation of error. For the determination of the oxygen permeability, the mean value of two measurements is given with the minimum and the maximum value.

2.5.1. Particle Size and Viscosity

The hydrodynamic apparent particle size of the nanoparticle dispersions was measured by dynamic light scattering (DLS) using a Zetasizer Nano ZSP (Malvern Instruments, Worcestershire, UK). Aliquots were filtered with syringe filters with a hydrophilic PES membrane and a pore size of 1 μm (Chromafil PES, Macherey-Nagel, Düren, Germany). The harmonic intensity averaged particle diameter (*z*-average) and the polydispersity index (PdI) from the cumulants analysis were obtained for 0.025 wt % nanoparticle dispersions after equilibration for 30 min at 25 °C.

The volume-weighed particle size of residual microparticles was measured using a HELOS/KR laser diffraction particle size analyzer with a QUIXEL wet dispersion system (Sympatec, Clausthal-Zellerfeld, Germany) at 23 °C and an optical concentration of 10%. The balanced mean size $x_{1,3}$ and the *span* were evaluated according to Equations (2) and (3) as

$$x_{1,3} = \int_{x_{\min}}^{x_{\max}} x q_3(x) dx \text{ and} \tag{2}$$

$$span = \frac{x_{90} - x_{10}}{x_{50}}. \tag{3}$$

Here, $x_{\min}$ and $x_{\max}$ are the smallest and the largest particle size, x is the class midpoint and $q_3(x)$ is the volume-weighted particle size distribution. x_{10}, x_{50} and x_{90} are the particle sizes corresponding to 10%, 50% and 90% of the cumulative undersize distribution, respectively.

The viscosity of the concentrated CNC dispersion was determined using a Physica MCR 501 rheometer (Anton Paar, Graz, Austria) at 25 °C with a cone-plate geometry. Shear flow curves were measured in the range from 0.01 to 1000 s^{-1}.

2.5.2. Dry Mass, Ion Chromatography and Yield

The mass of nanoparticles m_{np} in the product was determined gravimetrically in combination with ion chromatography and calculated according to Equation (4):

$$m_{np} = m_{dry} - m_{wet} \sum_{i=0}^{n} \frac{\gamma_{IC,i} V_{IC}}{m_{IC}}. \tag{4}$$

About 2 g of wet product m_{wet} were freeze-dried (2–4 LSCplus, Christ, Osterode am Harz, Germany) and the dried product was weighed again to obtain m_{dry}. Ion chromatography (820 IC Separation Center, Metrohm, Herisau, Switzerland) was performed on aliquots with a mass m_{IC} of about 0.1 g, diluted in H_2O with a volume V_{IC} of 50 mL. The mass concentration $\gamma_{IC,i}$ of cations (Metrosep C 4—150/4.0 column) and anions (Metrosep A Supp 4—250/4.0 column) was obtained. The yield Y is the quotient of the initially provided mass of the feed stock m_{raw} and m_{np}.

2.5.3. Optical Properties of Dispersions, Coatings, and Cast Films

Optical microscopy was performed on a polarized light microscope (BX51-P, Olympus, Hamburg, Germany) equipped with a camera (XC50, Olympus, Hamburg, Germany) for the qualitative analysis of the coatings and the cast films.

Scanning electron microscopy (SEM) was carried out on a JEOL JSM-IT100 (Akishima, Japan) with a secondary electron detector and an acceleration voltage of 3–5 kV. The nanoparticle dispersions were freeze-dried beforehand and mounted on conductive carbon tape.

The optical absorbance A of dispersions and transparent films was measured using a Specord 50 Plus Spectrophotometer (Analytik Jena, Jena, Germany). The absorbance at a wavelength λ is

proportional to the extinction coefficient $\varepsilon(\lambda)$, the concentration c and the optical path length d, according to the Beer-Lambert law (Equation (5)).

$$A = \varepsilon(\lambda)cd \tag{5}$$

2.5.4. Physical Properties

Water Content

The water content of the raw materials was determined by volumetric Karl Fischer titration (TitroLine KF, Xylem Analytics, Weilheim, Germany). The iodine titrant was determined with the water standard. Methanol and formamide were used as solvent in a ratio of 1.5:1. About 0.3 g of the sample was added to the solvent. The titration was started when the sample was completely dissolved. The solvent was exchanged after each measurement. The water content of the raw materials was considered regarding the calculation of the mass ratios for the preparation of nanoparticles and cast films.

Surface Tension

The surface tension of untreated and corona-treated PLA was evaluated with test ink pens (Arcotest, Mönsheim, Germany). The pens are filled with an ink of defined surface tension. The ink is applied with the pens to the substrate surface. If the line of ink does not separate into drops after at least 2 s, the surface energy of the substrate is the same or higher than the surface tension of the fluid. Then, the pen with a higher surface tension is applied until a separation of the line of fluid into drops is observed.

Pinhole Testing

The grease resistance of the coated films was measured using an internal method from Fraunhofer IVV [44]. A test area of 25 cm^2 of the film surface was covered with a fleece—for constant and sufficient covering—and saturated with a solution of colored peanut oil. No further weight was applied. After 24 h at 23 °C and 50% r.h., the fleece and oil residues were removed, and the stained area was characterized by digital image evaluation. At least four specimens were characterized. No pinholes are present, when no fatty spots on the back of the sample are detected.

Thickness

The film thickness was measured mechanically (Precision Thickness Gauge FT3, Rhopoint Instruments, East Sussex, UK) on 5 evenly distributed measuring points. The coating thickness $d_{laminate}$ was calculated from the thickness of a coated film and the same substrate without a coating $d_{substrate}$.

Oxygen and Water Vapor Permeability

Prior to the measurements, all samples were stored at 23 °C and 50% r.h. All tests were conducted at the Fraunhofer IVV, where these methods are accredited.

The reciprocal gas permeability of coated substrates $Q_{laminate}$ is the sum of the reciprocals of the gas permeability of the substrate $Q_{substrate}$ and the coating $Q_{coating}$ (Equation (6)). The oxygen permeability (*OP*) of the coating $OP_{coating}$ is calculated from the oxygen transmission rate (*OTR*) of the coating $OTR_{coating}$ and the respective coating thickness $d_{coating}$. The *OTR* was measured according to DIN 53380-3 [45] with an automatic high barrier oxygen transmission rate system (OX-TRAN 2/21, MOCON, Minneapolis, MN, USA). A humidity of 50% r.h. and a temperature of 23 °C was applied. With reference to the standard conditions (STP, 273 K; 1013 hPa), $OP_{coating}$ is given in cm^3

(STP) μm m^{-2} d^{-1} bar^{-1} according to Equation (7) [46]. The normalization to a thickness of 100 μm as $OP\ Q_{100}$ in cm^3 (STP) 100 μm m^{-2} d^{-1} bar^{-1} is reasonable.

$$\frac{1}{Q_{\text{laminate}}} = \frac{1}{Q_{\text{substrate}}} + \frac{1}{Q_{\text{coating}}} \tag{6}$$

$$OP_{\text{coating}} = OTR_{\text{coating}} \times d_{\text{coating}} \tag{7}$$

The water vapor transmission rate *WVTR* of coated polymer substrates and cast films was measured gravimetrically using the cup method described in the DIN 53122-1 [47]. Films with an exposed area A of 50.3 cm^2 for coated polymer films and 44.2 cm^2 for cast films with a thickness d were used. The bottom of the cup was filled with anhydrous silica gel. The initial weight of the sealed measuring cells was determined, and they were transferred to a desiccator containing a saturated KOH solution to maintain a humidity of 85% r.h. at 23 °C. The samples were weighed 5 times within a timeframe t of 144 h until the weight gain Δm over a time increment Δt was constant. Transmission rates of the coated films are calculated according to Equation (8). The transmission rate of the pure coating is determined by Equation (6). Films of different thicknesses can be compared via the water vapor permeability *WVP* in g (STP) μm m^{-2} d^{-1} as calculated by Equation (9) and after further normalization to a thickness of 100 μm (g (STP) 100 μm m^{-2} d^{-1}).

$$WVTR = \frac{\Delta m}{\Delta t A} \tag{8}$$

$$WVP = WVTR \times d \tag{9}$$

Mechanical Testing

Uniaxial tensile tests were carried out on a zwickiLine Z2.5 (Zwick, Ulm, Germany) testing machine as described in the DIN EN ISO 527-3 [48]. The samples were cut in dimensions of 100 mm × 20 mm. After a preload of 0.1 N, a constant extension rate of 25 mm min^{-1} was applied. The ultimate tensile strength σ_{UTS} and the elongation at break ε_{f} were read from the stress-strain curve σ vs. ε. Young's modulus E was evaluated according to Hooke's law from the linear-elastic relationship in the initial region of the stress-strain curve (Equation (10)):

$$E = \frac{\sigma}{\varepsilon} \tag{10}$$

2.6. Experiment Plan

All tests carried out for nanoparticle dispersions, coatings and cast films are summarized in Table 1.

Table 1. Overview of all measurement methods applied on nanoparticle dispersions, coatings and cast films.

Material	Dry Mass	DLS	Ion Concentration	Viscosity	Surface Tension	Pinhole Test	Thickness	OTR	WVTR	Mechanical Testing	SEM
Dispersions											
CNC	x	x	x	x							x
SNP	x	x	x								x
Coatings											
PLA					x		x	x	x		x
PLA-CNC							x	x	x		x
PLA-SNP							x	x	x		x
Paper							x				x
Paper-CNC						x	x				x
Paper-SNP						x	x				x
Cast Films											
Starch							x		x	x	x
Starch-CNC							x		x	x	x
Starch-SNP							x		x	x	x

3. Results

3.1. Properties of Dispersions

3.1.1. Product Concentration and Ion Content

The yield was measured gravimetrically. The gross yield of nanoparticles was corrected for the ion mass, determined by ion chromatography. Sulfuric acid hydrolysis followed by basic neutralization and successive centrifugation led to a gross yield of 41.4 ± 0.8 wt % of CNC from cotton linters. A gross yield of 32.2 ± 0.7 wt % of SNP was achieved from corn starch.

Redundant H_2O and excess ions were mostly removed during precipitation and redispersion. The relative nanoparticle concentrations in the hydrolyzed products were 53.6 ± 1.0 g kg^{-1} of product and 125.2 ± 2.6 g kg^{-1} of product for cellulose and starch, respectively. The concentration of Na$^+$ of 4.3 ± 0.1 mmol g^{-1} of CNC and 1.0 ± 0.3 mmol g^{-1} of SNP, and the concentration of SO$_4{}^{2-}$ of 2.3 ± 0.1 mmol g^{-1} of CNC and 0.6 ± 0.0 mmol g^{-1} of SNP, respectively, indicate an excess of free sulfate ions in both hydrolyzed products. This finding is confirmed by the acidic pH of 2.07 and 2.71 after centrifugation for CNC and SNP, respectively. No other ions were detected, pointing at the purity of the raw materials. Thereby, more than 99.8% of the ionic residuals were removed during the washing step.

3.1.2. Particle Size

Both cellulose and starch feed stocks had a bimodal particle size distribution with a volume-weighted mean equivalent diameter of 50.1 ± 0.4 µm and 7.7 ± 0.0 µm, respectively, while the spans were 5.16 ± 0.1 µm and 1.1 ± 0.0 µm. After the sulfuric acid treatment, microscale hydrolyzed residues or agglomerates due to high salt concentrations with a diameter of 7.4 ± 0.1 µm and 4.3 ± 0.0 µm for cellulose and starch, respectively, were still present. The spans corresponding to the mean diameters were 2.7 ± 0.1 µm and 1.9 ± 0.0 µm, respectively.

The apparent mean size of the nanoparticles was 113.4 ± 0.6 nm for cellulose and 248.7 ± 15.7 nm for starch. Accordingly, the polydispersity indices were 0.225 ± 0.007 and 0.369 ± 0.015. Thus, both nanoscale and microscale particles coexist in the hydrolyzed product [49]. An overview of the dispersion properties and the nanoparticle sizes of CNC and SNP is given in Table 2.

Table 2. Properties of nanoparticle dispersions as prepared from cotton linters and corn starch.

Product Property	Cellulose Product	Starch Product
yield/wt %	41.4 ± 0.8	32.2 ± 0.7
hydrolyzed product g kg^{-1} product	53.6 ± 1.0	125.2 ± 2.6
Na$^+$ mmol g^{-1} polysaccharide	4.3 ± 0.1	1.0 ± 0.3
SO$_4{}^{2-}$ mmol g^{-1} polysaccharide	2.3 ± 0.1	0.6 ± 0.0
apparent nanoparticle size by DLS/nm	113.4 ± 0.6	248.7 ± 15.7

3.1.3. Microscopy

Macro- and microscopically, no phase separation was detected in the concentrated nanoparticle dispersions after 16 weeks at 23 °C. The morphology of the raw materials is shown in Figure 1a,b. Cotton linters have a fibrillar structure, whereas corn starch has a granular shape. Sulfuric acid primarily degrades amorphous regions of the polysaccharides. Upon freeze-drying, agglomeration of nanoparticles promoted by the presence of residual salt occurs (Figure 1c,d). Additionally, microscale hydrolyzed residues with a high aspect ratio can be found in both products.
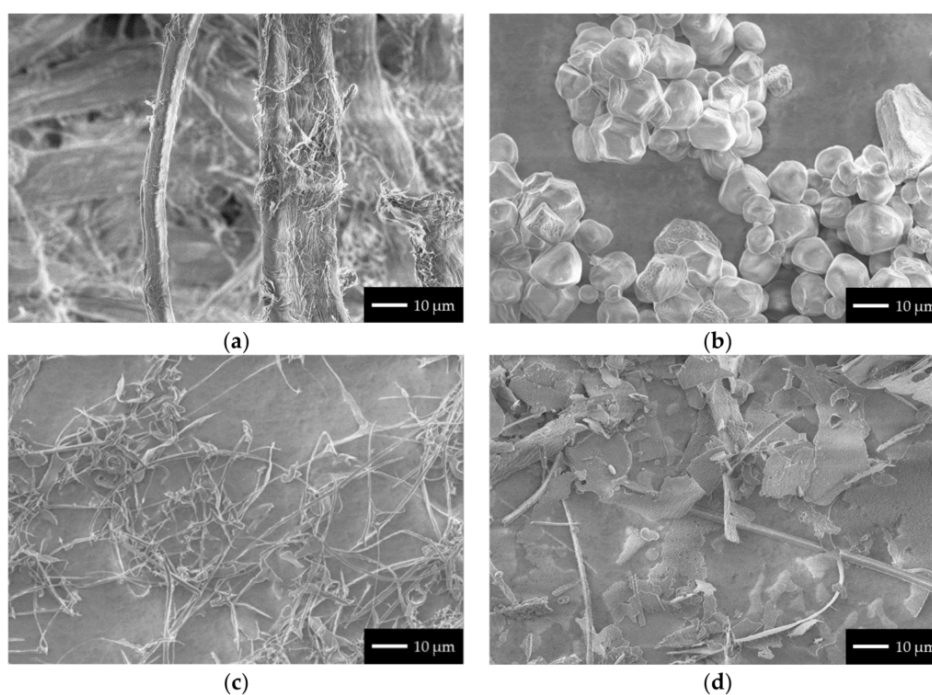
Figure 1. SEM images of (**a**) cotton linters, and (**b**) corn starch and the freeze-dried hydrolyzed products from (**c**) cotton linters, and (**d**) corn starch after hydrolysis and neutralization.

3.2. Properties of Nanoparticle Coatings

3.2.1. Surface Tension

Bare and untreated PLA had a surface tension of <34 mN m^{-1}, which is slightly below reported values (36–38 mN m^{-1} [50]). Corona-treating the substrate elevated the surface tension to 42 mN m^{-1}.

3.2.2. Dry Coating Thickness and Nanoparticle Loading

PLA and paper had thicknesses of 26.8 ± 0.1 μm and 62.5 ± 2.9 μm, respectively. Considering the concentration and the density of both the nanoparticles of 1.5 g cm^{-3} and Na$_2$SO$_4$ of 2.7 g cm^{-3}, the thickness of a single coated layer for a wet film thickness of 51 μm was estimated to be 2.5 μm for CNC and 2.7 μm for SNP. The actual coating thicknesses on PLA were 2.6 ± 0.8 μm for CNC and 5.9 ± 0.9 μm for SNP. Paper substrates were double-coated with both CNC and SNP, resulting in thicknesses of 9.5 ± 0.4 μm and 12.0 ± 1.0 μm, respectively.

The nanoparticle loading was calculated from the ratio of the mass of nanoparticles in the product m_{np} and the dry mass m_{dry} and was 75.6 ± 1.7 wt % in the CNC coating and 92.2 ± 2.6 wt % in the SNP coating.

3.2.3. Surface and Optical Properties

Coating PLA with CNC did not yield a uniform film (Figure 2a). Hydrolyzed residues and agglomerates were randomly distributed over the substrate surface. Hydrolyzed residues and agglomerates were found for SNP coatings as well, accompanied by fine fissures in the coating layer (Figure 2b).
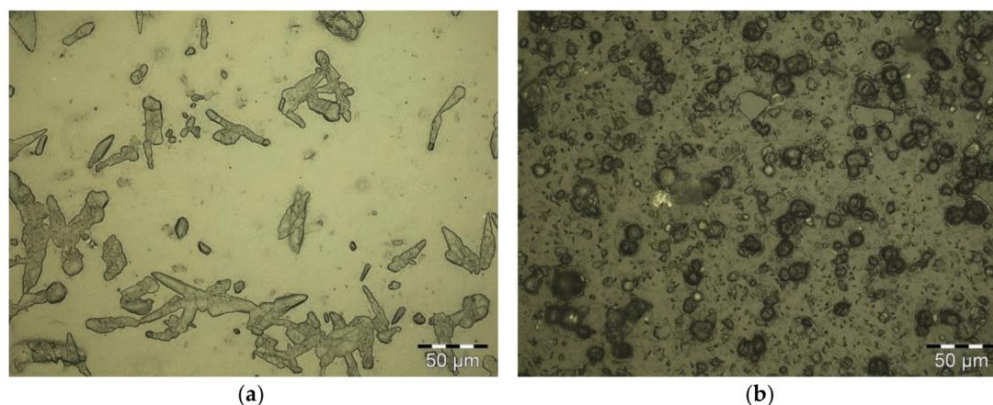
Figure 2. PLA coated with (**a**) CNC and (**b**) SNP in reflected bright-field microscopy.

The top side of the paper substrate was microscopically uniform (Figure 3a). The subjacent fibrous structure was visible via reflected light microscopy. While the top side appeared microscopically dense, the back side of the paper substrate showed pores with diameters in the micrometer range. Coating paper with CNC (Figure 3b) and SNP (Figure 3c) involved the deposition of hydrolyzed residues and agglomerates onto the surface, similar to the coatings on PLA. SEM imaging of the coated paper substrate shows the irregular surface topography caused by these residues (Figure 3e,f). Double-coating paper with SNP caused a more distinct topography.
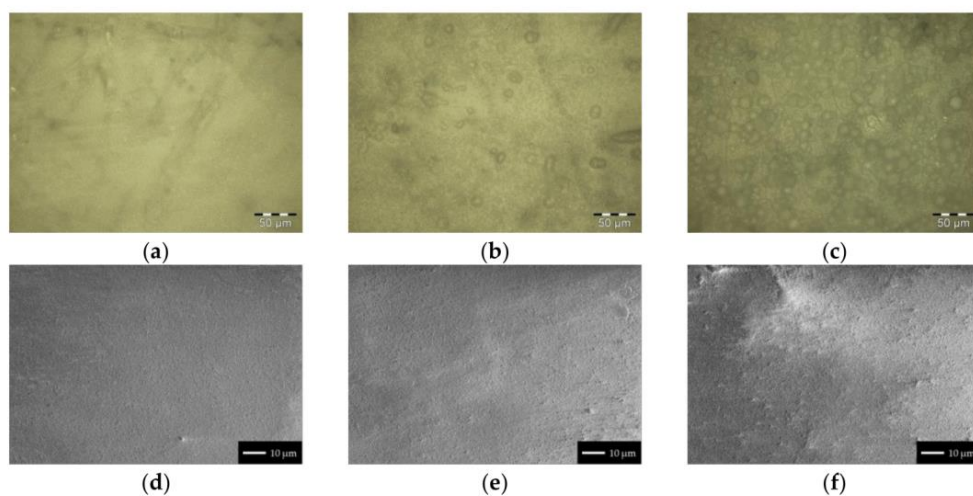
Figure 3. Paper (**a**,**d**) coated with CNC (**b**,**e**) or SNP (**c**,**f**) via reflected bright-field microscopy (**a**–**c**) and by secondary electron imaging via SEM (**d**–**f**).

The light transmittance of bare PLA of 91.4% ± 1.3% at a wavelength of 550 nm was reduced by the application of nanoparticle coatings. The CNC coating reduced the absolute light transmittance by 10.3% ± 1.6%, whereas SNP reduced the absolute light transmittance by 34.2% ± 1.7%.

3.2.4. Barrier Properties

Coating PLA with a single layer of CNC decreased the OP from 514.6 ± 3.8 cm^3 (STP) m^{-2} d^{-1} bar^{-1} to 129.7 ± 8.7 cm^3 (STP) m^{-2} d^{-1} bar^{-1} at 50% r.h. (74.8%) (Figure 4a). A decrease to an OP of 110.1 ± 14.2 cm^3 (STP) m^{-2} d^{-1} bar^{-1} (78.6%) was observed for a single coating layer of SNP. Considering the coating thickness, the *OP* Q_{100} of 4.7 ± 0.4 cm^3 (STP) 100 μm m^{-2} d^{-1} bar^{-1} and

8.5 $\pm$ 1.4 cm^3 (STP) 100 μm m^{-2} d^{-1} bar^{-1} for CNC and SNP resulted, emphasizing the noticeable barrier performance of CNC against oxygen compared to SNP (Figure 4b).

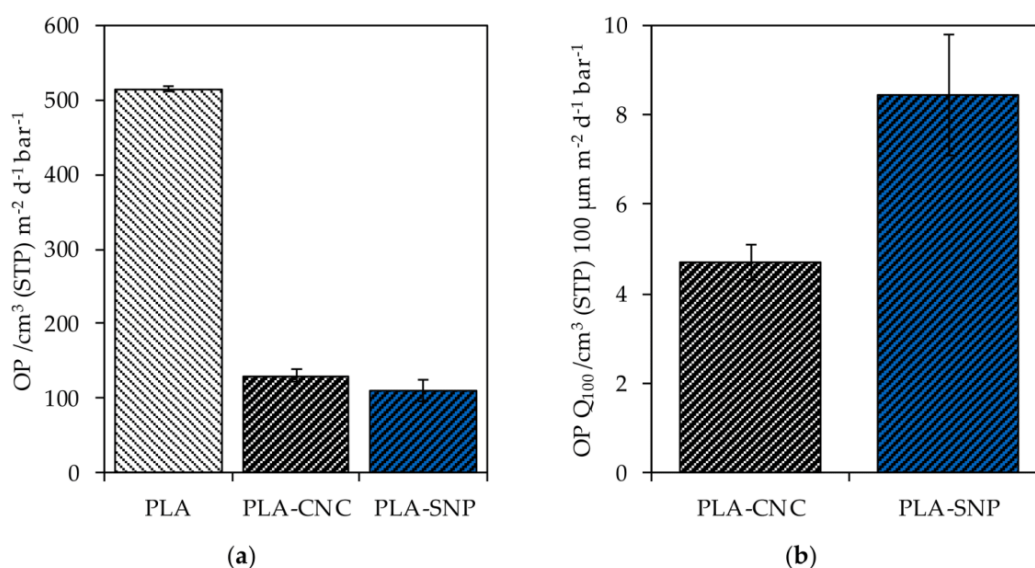**Figure 4.** (**a**) The measured OTR of bare PLA and PLA substrate coated with CNC and SNP; (**b**) the normalized OTR to a layer thickness of 100 μm (*OTR Q*$_{100}$).

The nanoparticle coatings did not improve the water vapor barrier of coated PLA. The *WVP Q*$_{100}$ of bare PLA substrate of 76.1 $\pm$ 3.1 g (STP) 100 μm m^{-2} d^{-1} remained almost constant for a coating with CNC (80.3 $\pm$ 4.6 g (STP) 100 μm m^{-2} d^{-1}; 85$\rightarrow$0% r.h.) and SNP (81.4 $\pm$ 1.8 g (STP) 100 μm m^{-2} d^{-1}; 85$\rightarrow$0% r.h.). The slight increase is explicable by water adsorption due to the hygroscopic character of both the coatings and the substrate in combination with the gravimetric measurement method.

Paper substrates double-coated with either CNC or SNP did not pass the pinhole test and were therefore excluded from the determination of barrier properties.

3.3. Properties of Cast Films

CNC and SNP were incorporated in hydrophilic starch matrices at different concentrations c_{filler} by solution casting. The target thickness was 50 μm. All experiments were repeated at least five times.

3.3.1. Microscopy and Optical Properties

Plastification at 70 °C for 1 h did not completely degrade the granular structure of corn starch. Swelling induced an increase of the grain size in the pure starch-glycerol film and ghost remnants were recognizable [51] (Figure 5a). Accordingly, the film surface displays the topography of the shells of the native starch granules (Figure 5d). Adding CNC (Figure 5b,e) or SNP (Figure 5c,f) in concentrations of $0 \leq c \leq 9$ wt % did not alter the microstructure of the film. Agglomerates or microscale residues from the hydrolyzed cellulose product were visible in both reflected bright-field microscopy and via SEM imaging. The visible accumulation suggests their segregation from the starch matrix during drying. Due to the similar appearance of the SNP and the starch matrix, no hydrolyzed starch residues were recognizable in these nanocomposites.
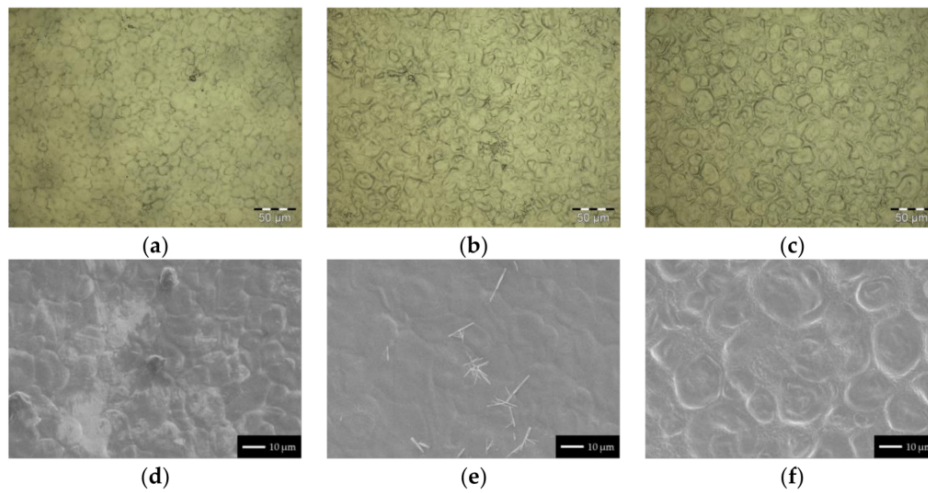
Figure 5.   Pure starch-glycerol film (**a,d**), starch-CNC nanocomposite (**b,e**), and starch-SNP nanocomposite (**c,f**). The shown nanocomposites had a filler content of 3 wt %. (**a–c**) Reflected bright-field microscopy and (**d–f**) secondary electron imaging (SEM).

The light transmittance of a starch-glycerol film T_{starch} with a thickness d of 50 μm was $83.5 \pm 2.1\%$ ($13.38 \times 10^{-3} \pm 2.3 \times 10^{-3}$ μm^{-1}) at 550 nm. For better comparability, the light transmittance T was normalized with respect to d. The addition of CNC and SNP reduced the light transmittance with increasing nanoparticle concentration $c_{nanoparticles}$ (Figure 6a). This effect was more pronounced for the addition of SNP. Accordingly, the extinction coefficient ε decreased with increasing filler content and was overall higher for SNP nanocomposites (Figure 6b). The high uncertainties prevalent at low $c_{nanoparticles}$ arose from the strong relative weighting of variable film thicknesses.
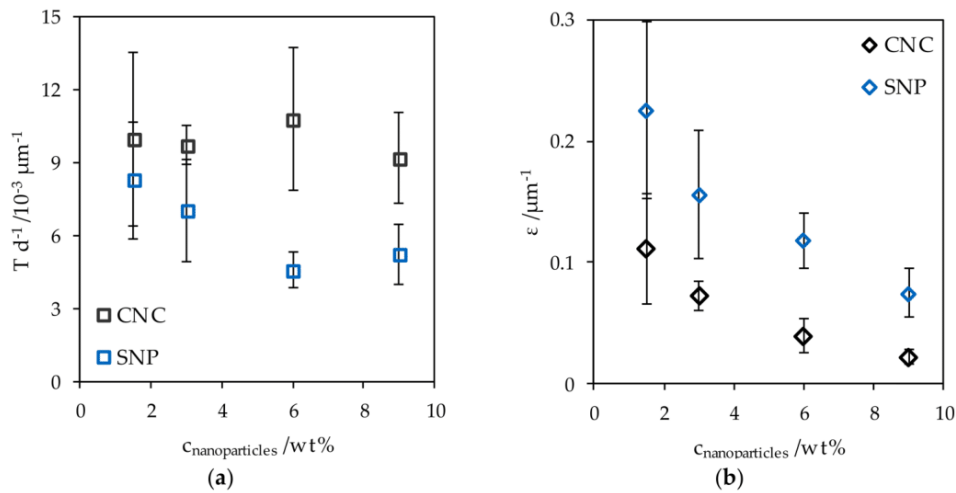
Figure 6. (**a**) The normalized transmittance of CNC and SNP nanocomposites and (**b**) the extinction coefficient at different nanoparticle concentrations.

3.3.2. Barrier Properties

A slight improvement of the *WVP* Q_{100} of cast starch-glycerol films was achieved by adding CNC or SNP (Table 3). However, all measured values lie within the 95% confidence interval of the *WVP* Q_{100} of 47.3 ± 20.6 g (STP) 100 μm m^{-2} d^{-1} (85→0% r.h.) of the pure starch-glycerol film.

Table 3. Normalized water vapor permeability of starch nanocomposites with different amounts of CNC or SNP.

Amount of Filler/wt %	*WVP* Q_{100}/g (STP) 100 μm m^{-2} d^{-1}	
	CNC	SNP
0.0	47.3 ± 20.6	–
1.5	40.3 ± 16.9	51.2 ± 15.7
3.0	43.6 ± 17.6	41.5 ± 14.5
6.0	45.4 ± 13.2	49.9 ± 12.4
9.0	43.7 ± 12.0	34.2 ± 16.8

3.3.3. Mechanical Properties

The ultimate tensile strength σ_{UTS} of the starch-glycerol films was 4.1 ± 2.1 MPa, Young's modulus E was 0.7 ± 0.4 MPa and the fracture strain ε_f was $23.7\% \pm 13.9\%$. The mechanical properties were changed by adding CNC and SNP, however, all measured values of nanocomposites lie within the 95% confidence interval of the values of starch-glycerol films (Figure 7). Although all samples were prepared with high diligence, the notch sensitivity of the organic composites caused the high uncertainties of the measured mechanical properties.

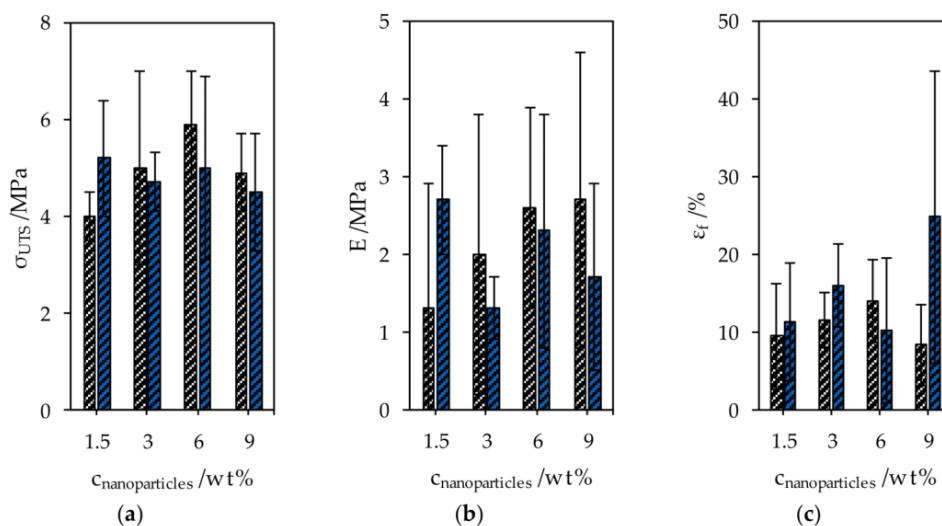**Figure 7.** Mechanical properties of CNC and SNP nanocomposites. (**a**) The ultimate tensile strength, (**b**) Young's modulus, and (**c**) the elongation at break.

4. Discussion

4.1. Nanoparticle Dispersions

The extraction of nanoparticles from cotton linters and corn starch was performed by sulfuric acid hydrolysis followed by neutralization with sodium hydroxide. To reduce the amount of hydrolyzed cellulose residues in the CNC product, a comparably long hydrolysis time of 3 h was chosen. The achieved gross yield was still >40 wt %. Exemplarily, other studies addressing the extraction of CNC from cotton linters reported gross yields of 52.7 wt % after 45 min at 45 °C (64 wt % H_2SO_4, 1:17.5 g mL^{-1}) [52] and 54.4 wt % after 5 min at 45 °C (60 wt % H_2SO_4, 1:20 g mL^{-1}) [53]. Similar short hydrolysis times in combination with the here presented extraction method could facilitate a distinctly higher gross yield. To evaluate the degree of conversion of the raw cellulose to CNC and soluble residues, X-ray diffraction measurements could complement the process evaluation

by giving information about the product crystallinity. Analogously, the gross yield of SNP from corn starch of 32.2 ± 0.7 wt % is comparably high (15% after 120 h at 40 °C and 25 wt % H_2SO_4 [54]).

The desired high ionic strength during washing enables flocculation of the nanoparticles. Therefore, a separation from the reaction solution is possible. The precipitation-redispersion mechanism enabled the removal of more than 99.8% of the ionic residues. Consequently, the nanoparticle dispersions showed no macroscopic phase separation over several weeks at 23 °C. Nevertheless, the presence of ions in the dispersions is expected to promote the formation of agglomerates [55,56] effecting larger apparent particle sizes. The actual particle size could be detected by atomic force microscopy and transmission electron microscopy.

A scale-up scenario regarding process time and the consumption of chemicals (Table 4) is derived from the applied process parameters and compared to a scaling approach documented by Reiner et al. [57]. Both approaches are normalized to a CNC product mass of 1 kg based on the respective yield. The rate-determining step of our approach is the hydrolysis time of 3 h. Further steps, comprising neutralization, washing, and homogenization, require only 1 h with the used equipment. Thus, the net process time is 4 h per batch. Reiner et al. used kraft pulp as feed stock and stopped the hydrolysis after 1.5 h by dilution and subsequent neutralization with NaOH. The unit operation times are given as 8 h for hydrolysis and neutralization, 24–48 h for gravity settling and initial purification and 24 h for filtration. The CNC produced by the overall faster process presented in this work has a higher residual ion content, but a markedly lower overall water consumption (75%) and facilitates a more compact reactor volume.

Table 4. Comparison of the masses of chemicals required to extract 1 kg of CNC from raw cellulose, based on the neutralization of sulfuric acid.

Chemical	Applied Parameters	Reiner et al. [57]
	m/kg	m/kg
raw cellulose	2.4	2.0
sulfuric acid, 64 wt %	37.2	18.5
hypochlorite	–	0.003
sodium hydroxide	14.6	9.8
water	196.3	800.0

Analogously, 1 kg of SNP is produced from 3.1 kg corn starch converted with 26.3 kg H_2SO_4 (18 wt %). Neutralization and washing require 81.2 kg H_2O. Complete neutralization is achieved by adding 16.9 kg NaOH. Due to the protracted hydrolysis, the net process time is 121 h per batch.

4.2. Nanoparticle Coatings

PLA needed to be corona-treated prior to the application of aqueous nanoparticle dispersions onto the hydrophobic substrate by blade-coating of the coating medium without contraction. High nanoparticle concentrations and therefore increased viscosities further facilitated good spreadability of the nanoparticle dispersions on the substrates. In particular, the presence of ions induced the gel-like character of the CNC dispersion [58]. The dry coating thicknesses of both CNC and SNP coatings exceeded the targeted values on PLA. It was assumed that in both cases, non-dense layers formed on the substrate surface due to agglomeration and the presence of microparticles. Furthermore, the hydration of the salt residues as well as water absorption of the hygroscopic nanoparticles must be factored in. Same applies for the coatings on paper. The intrinsically less smooth surface of paper was assumed to additionally contribute to the deviating dry coating thicknesses. For both CNC and SNP coatings, hydrolyzed residues as well as agglomerates accumulated on the coated substrates and thereby reduced the optical transmittance of the films.

The observed effect of lower oxygen permeation of CNC and SNP coatings can be attributed to the size and the structural organization of the nanoparticles in the coating layer. The structural

organization influences the diffusion path length of gas molecules in the film [59]. No improvement regarding the water vapor permeation was found. The intrinsic hydrophobicity of the nanoparticles in conjunction with the hygroscopic effect of the ionic residues is assumed to particularly impair the water vapor barrier properties. Microscopic cracks were found in starch coatings on PLA indicating embrittlement during solvent evaporation. Gentler drying conditions are not viewed as expedient. Instead, the addition of plasticizers may facilitate the prevention of cracks and lead to improved techno-functional properties [60].

Since the application of a double coating layer onto paper did not yield pinhole-free substrates, paper was excluded from further analyses. Alternatively to blade-coating, impregnating paper by dip-coating may lead to a pinhole-free substrate [5], however, accompanied by a higher expenditure of nanoparticles.

Results from other studies addressing the oxygen permeability of CNC coatings and cast films are shown in Table 5. A strong impact of the r.h., the substrate material and the nanoparticles themselves is recognizable. The *OP* Q_{100} at 50% r.h. of coatings in the present study were in the same range as plasticized nanocellulose films. However, compared to other approaches, the *OP* Q_{100} at 50% r.h. was up to 2 orders of magnitude higher. It was concluded that narrowing the particle size distributions of CNC and SNP by removing aggregates may be the decisive factor to further reduce the oxygen permeability of the nanoparticle coatings on polymer substrates.

Table 5. Comparison of oxygen permeabilities of coatings of CNC and SNP with results from other studies.

Barrier Film	r.h./%	$T/^\circ$C	*OP* Q_{100}/cm^3 (STP) 100 µm m^{-2} d^{-1} bar^{-1}	Ref.
CNC; 2.6 µm on PLA substrate	50	23	4.7 ± 0.4	this study
SNP; 5.9 µm on PLA substrate	50	23	8.5 ± 1.4	
CNC, 1.5 µm on				
PET substrate			0.02	
OPP substrate	0	23	0.37	[2]
OPA substrate			0.003	
TEMPO-oxidized cellulose, 1.5 µm on				
PET substrate (50 µm)	0	23	0.0006–0.0046	
PLA substrate (25 µm)			0.0009–0.003	[61]
PET substrate (50 µm)	50	23	0.0225–0.09	
PLA substrate (25 µm)			0.38–0.96	
Nanocellulose film	0	23	<0.01	
	50		0.3	
Nanocellulose film (plasticized)	0	23	0.03	[62]
	50		17	
Nanocellulose film (heat-treated)	0	23	<0.01	
	50		0.02	

4.3. Cast Films

Solvated and swollen starch granules formed the microstructure of the cast films. In CNC nanocomposites the agglomerates and hydrolyzed residues segregated from the starch-glycerol matrix. Similar behavior was assumed from the techno-functional properties of SNP nanocomposites. No improvement was determined regarding the WVP and the mechanical properties of CNC and SNP nanocomposites. Both types of nanoparticles may have a low percolation threshold in the starch-glycerol film. Thus, a negligible increase of the tortuosity and hindered force transmission in the polymer matrix resulted [59,63]. Agglomerates are considered as potential predetermined breaking points during applied mechanical stress. The reduced relative light transmittance and extinction coefficient with increasing CNC and SNP loading in the nanocomposites indicated increasing light scattering on nanoparticles and agglomerates.

Prolonged mixing at elevated temperature may have led to desulfation of the nanoparticles and promoted agglomeration [64]. Reducing mixing time and temperature in the polymer precursor as well as the addition of surfactants [32] and the adjustment of the surface energy by altering the ionic strength of the nanoparticle dispersions is considered beneficial.

5. Conclusions

The restricted efficiency of the extraction of CNC and SNP is one main limiting factor for the effective competition with already established additives for packaging materials [65]. While fossil-based polymers for packaging are still far ahead regarding economic competitiveness and techno-functional properties, such as barrier and mechanical properties, the potential of CNC and SNP is evident. In favor of the reduction of the complexity of multi-layer films and towards more ecofriendly and sustainable packaging solutions, CNC and SNP are promising candidates to enhance bio-based polymers with intrinsically attenuated barrier and mechanical properties. In this regard, an efficient post-processing method contributing to an overall economic extraction process was applied in this paper along with two examples of application. The use of non-functionalized CNC and SNP as coatings and nanofillers is attractive regarding an overall fast and green process.

From this study, we conclude:

(h1) The neutralization-based approach for the extraction of CNC and SNP from biopolymeric feed stocks in combination with the applied post-processing method is time-efficient and resource-saving. With hydrolysis times of 3 h for cellulose and 120 h for starch, gross yields of 41.4% and 32.2%, respectively, were achieved. The nanoparticle dispersions showed long-term stability.

(h2) Reduced oxygen permeabilities were achieved with coatings of CNC and SNP on PLA. The barrier improvement of paper failed due to pinholes in the substrate.

(h3) No improvement of the WVP and the mechanical properties of cast starch-glycerol films incorporating CNC or SNP were found. It was deduced from the results that agglomeration of the nanoparticles during the cast film preparation and segregation of the filler from the matrix during drying compromised the techno-functional properties.

Further purification of the hydrolyzed products regarding ionic residues and agglomerates is suggested to improve the techno-functional properties of CNC and SNP applied in coatings and cast nanocomposite films.

Author Contributions: Christoph Metzger and Solange Sanahuja conceived and designed the experiments; Christoph Metzger and Lisa Behrends carried out the experiments; Christoph Metzger, Martina Lindner, Heiko Briesen, and Sven Sängerlaub analyzed the data and interpreted the results; Heiko Briesen, Sven Sängerlaub and Martina Lindner contributed reagents, materials and measurement equipment, and contributed to and edited the manuscript; Christoph Metzger wrote the manuscript.

Conflicts of Interest: The authors declare no conflict of interest. The funding sponsors had no role in the design of the study; in the collection, analyses, or interpretation of data; in the writing of the manuscript, and in the decision to publish the results.

References

1. LeCorre, D.; Dufresne, A.; Rueff, M.; Khelifi, B.; Bras, J. All starch nanocomposite coating for barrier material. *J. Appl. Polym. Sci.* **2014**, *131*, 39826. [CrossRef]

2. Li, F.; Biagioni, P.; Bollani, M.; Maccagnan, A.; Piergiovanni, L. Multi-functional coating of cellulose nanocrystals for flexible packaging applications. *Cellulose* **2013**, *20*, 2491–2504. [CrossRef]

3. Belbekhouche, S.; Bras, J.; Siqueira, G.; Chappey, C.; Lebrun, L.; Khelifi, B.; Marais, S.; Dufresne, A. Water sorption behavior and gas barrier properties of cellulose whiskers and microfibrils films. *Carbohydr. Polym.* **2011**, *83*, 1740–1748. [CrossRef]

4. Herrera, M.A.; Mathew, A.P.; Oksman, K. Gas permeability and selectivity of cellulose nanocrystals films (layers) deposited by spin coating. *Carbohydr. Polym.* **2014**, *112*, 494–501. [CrossRef] [PubMed]

5. Herrera, M.A.; Sirviö, J.A.; Mathew, A.P.; Oksman, K. Environmental friendly and sustainable gas barrier on porous materials. *Mater. Des.* **2016**, *93*, 19–25. [CrossRef]

6. Zheng, H.; Ai, F.; Chang, P.R.; Huang, J.; Dufresne, A. Structure and properties of starch nanocrystal-reinforced soy protein plastics. *Polym. Compos.* **2009**, *30*, 474–480. [CrossRef]

7. Angellier, H.; Molina-Boisseau, S.; Dufresne, A. Mechanical properties of waxy maize starch nanocrystal reinforced natural rubber. *Macromolecules* **2005**, *38*, 9161–9170. [CrossRef]

8. Pei, A.; Malho, J.-M.; Ruokolainen, J.; Zhou, Q.; Berglund, L.A. Strong nanocomposite reinforcement effects in polyurethane elastomer with low volume fraction of cellulose nanocrystals. *Macromolecules* **2011**, *44*, 4422–4427. [CrossRef]

9. Khan, A.; Khan, R.A.; Salmieri, S.; Le Tien, C.; Riedl, B.; Bouchard, J.; Chauve, G.; Tan, V.; Kamal, M.R.; Lacroix, M. Mechanical and barrier properties of nanocrystalline cellulose reinforced chitosan based nanocomposite films. *Carbohydr. Polym.* **2012**, *90*, 1601–1608. [CrossRef] [PubMed]

10. Fortunati, E.; Peltzer, M.; Armentano, I.; Torre, L.; Jimenez, A.; Kenny, J.M. Effects of modified cellulose nanocrystals on the barrier and migration properties of PLA nano-biocomposites. *Carbohydr. Polym.* **2012**, *90*, 948–956. [CrossRef] [PubMed]

11. Thompson, R.C.; Moore, C.J.; Vom Saal, F.S.; Swan, S.H. Plastics, the environment and human health: Current consensus and future trends. *Philos. Trans. R. Soc. B Biol. Sci.* **2009**, *364*, 2153–2166. [CrossRef] [PubMed]

12. Miller, S.A. Sustainable polymers: Opportunities for the next decade. *ACS Macro Lett.* **2013**, *2*, 550–554. [CrossRef]

13. Davis, G.; Song, J.H. Biodegradable packaging based on raw materials from crops and their impact on waste management. *Ind. Crops Prod.* **2006**, *23*, 147–161. [CrossRef]

14. Niaounakis, M. *Biopolymers: Processing and Products*; Elsevier Science: Burlington, NJ, USA, 2015.

15. Markarian, J. Biopolymers present new market opportunities for additives in packaging. *Plast. Addit. Compd.* **2008**, *10*, 22–25. [CrossRef]

16. Vink, E.T.H.; Rábago, K.R.; Glassner, D.A.; Gruber, P.R. Applications of life cycle assessment to NatureWorks™ polylactide (PLA) production. *Polym. Degrad. Stab.* **2003**, *80*, 403–419. [CrossRef]

17. Carothers, W.H.; Dorough, G.L.; van Natta, F.J. Studies of polymerization and ring formation—X. The reversible polymerization of six-membered cyclic esters. *J. Am. Chem. Soc.* **1932**, *54*, 761–772. [CrossRef]

18. Lunt, J. Large-scale production, properties and commercial applications of polylactic acid polymers. *Polym. Degrad. Stab.* **1998**, *59*, 145–152. [CrossRef]

19. Gruber, P.; O'Brien, M. Polylactides "NatureWorks® PLA". In *Biopolymers Online*; Steinbüchel, A., Ed.; Wiley-VCH: Weinheim, Germany, 2005.

20. Auras, R.; Harte, B.; Selke, S. An overview of polylactides as packaging materials. *Macromol. Biosci.* **2004**, *4*, 835–864. [CrossRef] [PubMed]

21. Auras, R.; Harte, B.; Selke, S. Effect of water on the oxygen barrier properties of poly(ethylene terephthalate) and polylactide films. *J. Appl. Polym. Sci.* **2004**, *92*, 1790–1803. [CrossRef]

22. Chaiwong, C.; Rachtanapun, P.; Wongchaiya, P.; Auras, R.; Boonyawan, D. Effect of plasma treatment on hydrophobicity and barrier property of polylactic acid. *Surf. Coat. Technol.* **2010**, *204*, 2933–2939. [CrossRef]

23. Siracusa, V.; Blanco, I.; Romani, S.; Tylewicz, U.; Rocculi, P.; Rosa, M.D. Poly(lactic acid)-modified Films for food packaging application: Physical, mechanical, and barrier behavior. *J. Appl. Polym. Sci.* **2012**, *125*, 390–401. [CrossRef]

24. Pant, A.F.; Sängerlaub, S.; Müller, K. Gallic acid as an oxygen scavenger in bio-based multilayer packaging films. *Materials* **2017**, *10*, 11. [CrossRef] [PubMed]

25. Pan, Y.; Xiao, H.; Song, Z. Hydrophobic modification of cellulose fibres by cationic-modified polyacrylate latex with core-shell structure. *Cellulose* **2013**, *20*, 485–494. [CrossRef]

26. Miller, K.S.; Krochta, J.M. Oxygen and aroma barrier properties of edible films: A review. *Trends Food Sci. Technol.* **1997**, *8*, 228–237. [CrossRef]

27. Rhim, J.-W.; Park, H.-M.; Ha, C.-S. Bio-nanocomposites for food packaging applications. *Prog. Polym. Sci.* **2013**, *38*, 1629–1652. [CrossRef]

28. Roman, M. Toxicity of cellulose nanocrystals—A review. *Ind. Biotechnol.* **2015**, *11*, 25–33. [CrossRef]

29. Rånby, B.G.; Banderet, A.; Sillén, L.G. Aqueous colloidal solutions of cellulose micelles. *Acta Chem. Scand.* **1949**, *3*, 649–650. [CrossRef]

30. Habibi, Y.; Lucia, L.A.; Rojas, O.J. Cellulose nanocrystals: Chemistry, self-assembly, and applications. *Chem. Rev.* **2010**, *110*, 3479–3500. [CrossRef] [PubMed]

31. Müller, V.; Briesen, H. Nanocrystalline Cellulose, Its Preparation and Uses of Such Nanocrystalline Cellulose. U.S. Patent 20170306056 A1, 26 October 2017.

32. Kim, J.; Montero, G.; Habibi, Y.; Hinestroza, J.P.; Genzer, J.; Argyropoulos, D.S.; Rojas, O.J. Dispersion of cellulose crystallites by nonionic surfactants in a hydrophobic polymer matrix. *Polym. Eng. Sci.* **2009**, *49*, 2054–2061. [CrossRef]

33. Alves, J.S.; dos Reis, K.C.; Menezes, E.G.T.; Pereira, F.V.; Pereira, J. Effect of cellulose nanocrystals and gelatin in corn starch plasticized films. *Carbohydr. Polym.* **2015**, *115*, 215–222. [CrossRef] [PubMed]

34. Li, F.; Mascheroni, E.; Piergiovanni, L. The potential of nanocellulose in the packaging field: A review. *Packag. Technol. Sci.* **2015**, *28*, 475–508. [CrossRef]

35. Liu, H.; Brinson, L.C. Reinforcing efficiency of nanoparticles: A simple comparison for polymer nanocomposites. *Compos. Sci. Technol.* **2008**, *68*, 1502–1512. [CrossRef]

36. Habibi, Y. Key advances in the chemical modification of nanocelluloses. *Chem. Soc. Rev.* **2014**, *43*, 1519–1542. [CrossRef] [PubMed]

37. Murphy, S.H.; Marsh, J.J.; Kelly, C.A.; Leeke, G.A.; Jenkins, M.J. CO_2 assisted blending of poly(lactic acid) and poly(ε-caprolactone). *Eur. Polym. J.* **2017**, *88*, 34–43. [CrossRef]

38. Ge, H.; Yang, F.; Hao, Y.; Wu, G.; Zhang, H.; Dong, L. Thermal, mechanical, and rheological properties of plasticized poly(L-lactic acid). *J. Appl. Polym. Sci.* **2013**, *127*, 2832–2839. [CrossRef]

39. Mihai, M.; Huneault, M.A.; Favis, B.D. crystallinity development in cellular poly(lactic acid) in the presence of supercritical carbon dioxide. *J. Appl. Polym. Sci.* **2009**, *113*, 2920–2932. [CrossRef]

40. Angellier, H.; Choisnard, L.; Molina-Boisseau, S.; Ozil, P.; Dufresne, A. Optimization of the preparation of aqueous suspensions of waxy maize starch nanocrystals using a response surface methodology. *Biomacromolecules* **2004**, *5*, 1545–1551. [CrossRef] [PubMed]

41. Lindner, M.; Rodler, N.; Jesdinszki, M.; Schmid, M.; Sängerlaub, S. Surface energy of corona treated PP, PE and PET films, its alteration as function of storage time and the effect of various corona dosages on their bond strength after lamination. *J. Appl. Polym. Sci.* **2018**, *135*, 45842. [CrossRef]

42. Beck, S.; Bouchard, J. Auto-catalyzed acidic desulfation of cellulose nanocrystals. *Nord. Pulp Pap. Res. J.* **2014**, *29*, 6–14. [CrossRef]

43. Lindner, M. Factors affecting the hygroexpansion of paper. *J. Mater. Sci.* **2018**, *53*, 1–26. [CrossRef]

44. Jost, V.; Kobsik, K.; Schmid, M.; Noller, K. Influence of plasticiser on the barrier, mechanical and grease resistance properties of alginate cast films. *Carbohydr. Polym.* **2014**, *110*, 309–319. [CrossRef] [PubMed]

45. *DIN 53380-3 Testing of Plastics—Determination of Gas Transmission Rate—Part 3: Oxygen-Specific Carrier Gas Method for Testing of Plastic Films and Plastics Mouldings*; German National Standard: Berlin, Germany, 1998.

46. Langowski, H.-C. Permeation of gases and condensable substances through monolayer and multilayer structures. In *Plastic Packaging: Interactions with Food and Pharmaceuticals*, 2nd ed.; Piringer, O.G., Baner, A.L., Eds.; Wiley-VCH: Weinheim, Germany, 2008.

47. *DIN 53122-1 Testing of Plastics and Elastomer Films, Paper, Board and Other Sheet Materials—Determination of Water Vapour Transmission—Part 1: Gravimetric Method*; German National Standard: Berlin, Germany, 2001.

48. *DIN EN ISO 527-3 Plastics—Determination of Tensile Properties—Part 3: Test Conditions for Films and Sheets*; German National Standard: Berlin, Germany, 2012.

49. LeCorre, D.; Bras, J.; Dufresne, A. Evidence of micro- and nanoscaled particles during starch nanocrystals preparation and their isolation. *Biomacromolecules* **2011**, *12*, 3039–3046. [CrossRef] [PubMed]

50. Zirkel, L. PLA for thermoforming. *Bioplast. Mag.* **2012**, *7*, 18–20.

51. Zhang, B.; Dhital, S.; Flanagan, B.M.; Gidley, M.J. Mechanism for starch granule ghost formation deduced from structural and enzyme digestion properties. *J. Agric. Food Chem.* **2014**, *62*, 760–771. [CrossRef] [PubMed]

52. Mascheroni, E.; Rampazzo, R.; Ortenzi, M.A.; Piva, G.; Bonetti, S.; Piergiovanni, L. Comparison of cellulose nanocrystals obtained by sulfuric acid hydrolysis and ammonium persulfate, to be used as coating on flexible food-packaging materials. *Cellulose* **2016**, *23*, 779–793. [CrossRef]

53. Chang, C.-P.; Wang, I.-C.; Hung, K.-J.; Perng, Y.-S. Preparation and characterization of nanocrystalline cellulose by acid hydrolysis of cotton linter. *Taiwan J. For. Sci.* **2010**, *25*, 251–264.

54. LeCorre, D.; Bras, J.; Choisnard, L.; Dufresne, A. Optimization of the batch preparation of starch nanocrystals to reach daily time-scale. *Starch* **2012**, *64*, 489–496. [CrossRef]

55. Phan-Xuan, T.; Thuresson, A.; Skepö, M.; Labrador, A.; Bordes, R.; Matic, A. Aggregation behavior of aqueous cellulose nanocrystals: The effect of inorganic salts. *Cellulose* **2016**, *23*, 3653–3663. [CrossRef]

56. Cherhal, F.; Cousin, F.; Capron, I. Influence of charge density and ionic strength on the aggregation process of cellulose nanocrystals in aqueous suspension, as revealed by small-angle neutron scattering. *Langmuir* **2015**, *31*, 5596–5602. [CrossRef] [PubMed]

57. Reiner, R.S.; Rudie, A.W. Process scale-up of cellulose nanocrystal production to 25 kg per batch at the forest products laboratory. In *Production and Applications of Cellulose Nanomaterials*; Postek, M.T., Moon, R.J., Rudie, A.W., Bilodeau, M.A., Eds.; TAPPI Press: Peachtree Corners, GA, USA, 2013; pp. 21–24.

58. Xu, Y.; Atrens, A.D.; Stokes, J.R. Rheology and microstructure of aqueous suspensions of nanocrystalline cellulose rods. *J. Colloid Interface Sci.* **2017**, *496*, 130–140. [CrossRef] [PubMed]

59. Nielsen, L.E. Models for the permeability of filled polymer systems. *J. Macromol. Sci. Part A Chem.* **1967**, *1*, 929–942. [CrossRef]

60. Sanyang, M.L.; Sapuan, S.M.; Jawaid, M.; Ishak, M.R.; Sahari, J. Effect of plasticizer type and concentration on physical properties of biodegradable films based on sugar palm (arenga pinnata) starch for food packaging. *J. Food Sci. Technol.* **2016**, *53*, 326–336. [CrossRef] [PubMed]

61. Fukuzumi, H.; Saito, T.; Isogai, A. Influence of TEMPO-oxidized cellulose nanofibril length on film properties. *Carbohydr. Polym.* **2013**, *93*, 172–177. [CrossRef] [PubMed]

62. Vartiainen, J.; Kaljunen, T.; Kunnari, V.; Lahtinen, P.; Salminen, A.; Seppälä, J.; Tammelin, T. Nanocellulose films: Towards large scale and continuous production. In Proceedings of the 26th IAPRI Symposium on Packaging 2013, Espoo, Finland, 10–13 June 2013; Nissi, M.V., Ed.; VTT: Espoo, Finland, 2013; pp. 197–209.

63. Favier, V.; Dendievel, R.; Canova, G.; Cavaille, J.Y.; Gilormini, P. Simulation and modeling of three-dimensional percolating structures: Case of a latex matrix reinforced by a network of cellulose fibers. *Acta Mater.* **1997**, *45*, 1557–1565. [CrossRef]

64. Jiang, F.; Esker, A.R.; Roman, M. Acid-catalyzed and solvolytic desulfation of H_2SO_4-hydrolyzed cellulose nanocrystals. *Langmuir* **2010**, *26*, 17919–17925. [CrossRef] [PubMed]

65. Tang, X.Z.; Kumar, P.; Alavi, S.; Sandeep, K.P. Recent advances in biopolymers and biopolymer-based nanocomposites for food packaging materials. *Crit. Rev. Food Sci. Nutr.* **2012**, *52*, 426–442. [CrossRef] [PubMed]

4.4. Thermoplastic starch nanocomposites reinforced with cellulose nanocrystal suspensions containing residual salt from neutralization

Summary. This study aimed at improvement of mechanical properties of starch nanocomposites, by adding CNCs as a reinforcing filler. It followed the inconclusive evaluation of mechanical properties of CNC-starch nanocomposites in **Paper III**. The measurement set-up was revisited, and sample holders were identified to introduce an irregular stress profile to samples, causing sudden crack extension. Thus, a new sample holder was designed, following the guidelines of ISO 527-1 and 527-3 (*392, 393*). CNCs were isolated from ashless cotton cellulose through acid-catalyzed hydrolysis, and then neutralized. Product separation followed the protocol, which was presented in **Paper I**, involving incremental centrifugation and dilution, until a stable colloidal suspension formed. A product's portion was then dialyzed, to remove residual Na_2SO_4. Corn starch was plasticized, and four different experimental series were prepared: pure starch films; nanocomposite films containing CNCs and residual Na_2SO_4; nanocomposite films containing dialyzed CNCs; and starch films containing Na_2SO_4, where salt concentration matches residual salt concentration in respective nanocomposite film. Adjusted CNC concentration was 1–5 wt.%. It was found that an increase of nanoparticle loading resulted in an increase of elastic modulus, which corresponds to higher nanocomposite stiffness. Concurrently, nanocomposites' elasticity decreased with increasing CNC loading. No significant effect of residual salt on mechanical properties of starch films and CNC-starch nanocomposites was found. It was concluded that residual salt did not affect CNC dispersibility in the starch matrix at loadings ≤ 5 wt.%. Therefore, neutralization-based CNC isolation yields nanoparticles with good compatibility in hydrophilic polymeric matrices for tailored mechanical properties of advanced materials.

Author's contributions. The author had a leading role in this work. He planned and designed the experiments and conducted all experiments. He performed all data acquisition, evaluation, and interpretation. HB supervised the research. The author wrote the manuscript and discussed all results with HB.

Thermoplastic Starch Nanocomposites Reinforced with Cellulose Nanocrystal Suspensions Containing Residual Salt from Neutralization

Christoph Metzger* and Heiko Briesen*

Sulfuric acid-catalyzed hydrolysis of cellulose commonly isolates cellulose nanocrystals (CNCs). Neutralizing the reactant solution with sodium hydroxide facilitates efficient downstream processing, but residual salt remains in the product. This study examines the reinforcing effects of CNCs from suspensions that contain residual salt on the mechanical properties of thermoplastic starch nanocomposites. By reinforcing starch films with up to 5 wt% CNCs, stiffness and strength are improved by 118% and 79%, respectively, indicating a good dispersion of CNCs in the starch matrix. Compared to nanocomposites incorporating salt-free CNCs, the remaining salt has no significant impact on the material's mechanical performance. The results indicate great potential of CNCs containing residual salt as biobased, low-cost nanofiller in hydrophilic polymer matrices.

1. Introduction

Many polymeric materials for everyday's use in key application areas, such as packaging, health care, electronics, automotive, and aerospace, are derived from petroleum.[1–5] However, contemporary profuse consumption of petroleum and the lack of sustainable disposal possibilities introduce ecological concerns at petroleum-derived materials.[1,6,7] Consequently, increasing efforts have been made toward the development of biopolymeric materials with properties that are tailored to particular applications.[8–10] Biopolymers are produced from abundant resources, biodegradable and environmentally benign.[11,12] However, individual biopolymers cannot compete with or exceed the performance of well-advanced thermoplastics derived from petroleum. For example, polylactic acid's (PLA) toughness

C. Metzger, Prof. H. Briesen
TUM School of Life Sciences Weihenstephan
Chair of Process Systems Engineering
Technical University of Munich
Gregor-Mendel-Str. 4, 85354 Freising, Germany
E-mail: christoph.metzger@tum.de; briesen@wzw.tum.de

The ORCID identification number(s) for the author(s) of this article can be found under https://doi.org/10.1002/mame.202100161

is greater than that of polystyrene;[13] nevertheless, the mechanical properties of polyethylene terephthalate and polycarbonate are still superior to those of PLA.[14] Generally, biodegradable polymers from renewable resources, such as PLA, polyhydrodybutyrate, polycaprolactone, and polyhydroalkanoate, underperform regarding their mechanical and barrier properties.[1,15] Furthermore, natural biopolymers, such as starch, chitosan, and alginate, show fast degradation and deteriorating mechanical properties in humid environment due to their prevalently hydrophilic character.[7,16]

In nature, single materials' restraints are compensated for by forming composites, often with building blocks of nanoscale dimensions.[17] Modern manufactured materials in engineering applications benefit from the same principles: composites containing nanoscale building blocks, for example organic–inorganic nanocomposites from sol–gel chemistry or carbon black reinforced elastomers, were in use long before even being referred to as nanotechnology.[18] Since the mid-1990s, there has been a steady increase in published research addressing nanocomposites made from nanofillers dispersed in polymer matrices.[19] Conforming to this principle, blends of biopolymers and nanofillers yield materials with improved properties for specific use cases.[1,7,13,20] Depending on the nanofillers' inherent properties, they provide improved mechanical, barrier, and thermal properties to the nanocomposite.[21,22] Furthermore, nanocomposite properties are, among others, strongly dependent on the filler's composition, aspect ratio, and surface properties.[7,21,23–25] Increasing awareness of ecological problems has drawn attention to synthetic bionanocomposites with additional functionalities, such as biodegradability, biocompatibility, and renewability.[26–29] In this context, the low cost and wide availability of starch from several renewable resources make it an interesting candidate for biodegradable products in packaging,[30,31] which is reflected in the high number of original research articles and patents on the material.[19] However, there is only a limited number of applications because of the low mechanical strength of starch and starch films' high gas permeation.[32] Addition of nanofillers, such as silicates, carbon-based nanomaterials, or metal nanoparticles can improve the biopolymer's functional properties.[18] Moreover, nanofillers from biopolymers, such as cellulose nanocrystals (CNCs), chitin nanocrystals, or starch nanoplatelets, make composites fully biodegradable,

**ADVANCED
SCIENCE NEWS**

www.advancedsciencenews.com

**Macromolecular
Materials and Engineering**

www.mame-journal.de

offering great potential for food packaging.[17,18,26–29,32] In particular, CNCs' high axial elastic modulus, low density, and low-cost potential make them a promising candidate to improve the overall properties of starch-based nanocomposites.[33] For that purpose, the large number of hydroxy groups on the CNC surfaces promotes hydrophilicity and, therefore, good dispersibility in a hydrophilic starch matrix.[34–36] Hence, incorporation of CNCs in the starch matrix yields improved mechanical properties, which are promoted by good interfacial bonding, percolation network formation, and an increase of the system's crystallinity.[33,37–42] A concurrent increase of the glass transition temperature expands the useful temperature range of CNC-starch nanocomposites.[39,40,43–47] In addition, CNCs constrain swelling of starch and impede water diffusion through the nanocomposite.[39,46,48–51] Considering macroscopic stiffness and strength of low-modulus polymers, CNCs are typically added to starch at low mass fractions < 30 wt% to improve the nanocomposite's mechanical properties.[21,52] In this regard, it has been shown that volume fractions of about 1% already promote a continuous path of connected CNCs through the polymer matrix.[52] In contrast, CNC aggregation occurs at elevated mass fractions, which results in reduced matrix homogeneity and limited interfacial cohesion and, thus, decremented overall performance.[31,44]

CNC performance in nanocomposites strongly depends on the pathway used for their production as well as the cellulose source.[53] Commonly, CNCs are produced by the sulfuric acid-catalyzed hydrolysis of cellulosic feedstock, yielding rod-shaped particles with a diameter of 3–50 nm and an aspect ratio between 5 and 50.[54] Concurrent sulfation by grafting sulfate half-esters onto the CNCs induces a negative surface charge, resulting in stable colloidal suspensions in polar media.[55] This well-studied laboratory procedure has a high potential for the pilot- and industrial-scale top-down production of CNCs.[56,57] However, product separation from an acidic reactant solution necessitates low-efficiency techniques, such as dialysis or reverse osmosis.[58] Overall, a more energy- and resource-efficient production method is required to successfully commercialize CNCs.[59]

In this context, Metzger et al. designed an economic separation process to produce colloidally stable CNCs from neutralized reactant solutions.[60] After hydrolysis, the reactant solution is neutralized with a base, such as sodium hydroxide, to form a secondary sulfate (Na_2SO_4). Successive centrifugation steps remove excess ions and by-products until peptization occurs. Critical concentrations for agglomeration and peptization are independent of CNC mass fraction. Hence, the amount of salt in the product can be controlled by adjusting the amount of water added before and after each washing step.[60,61] Eventually, a stable colloidal suspension is formed by diluting the product to a salt concentration below the critical agglomeration concentration.

Cost-effective CNC production via neutralization of the acidic reactant solution facilitates commercialization efforts by overcoming economic market barriers.[56,58] Thus far, we have reported the effect of different sulfate salts on colloidal CNCs isolated by this process.[60] Furthermore, we have successfully applied CNC suspensions containing residual salt from neutralization as an oxygen barrier layer in polymer films.[62] Complementary to these reported works, we hypothesize in this study that CNC suspensions containing residual salt have mechanical

reinforcing ability in starch nanocomposites similar to salt-free CNCs. For this purpose, CNCs were isolated from cotton cellulose by sulfuric acid-catalyzed hydrolysis, and suspensions with and without residual sulfate salt were prepared. Effects of CNCs with and without residual salt on the mechanical performance of CNC-starch nanocomposites were comparatively investigated. CNCs containing residual salt, but having similar performance to salt-free CNCs, offer great potential as a biobased, low-cost filler in sustainable nanocomposites.

2. Results and Discussion

2.1. Disperse Properties of Colloidal CNCs

Suspensions of salt-free CNCs (D-CNCs) and salt-containing CNCs (S-CNCs) were prepared by sulfuric acid-catalyzed hydrolysis of cotton α-cellulose, neutralization with NaOH, and peptization after removing the salt by centrifugation. As previously reported, the applied CNC isolation protocol yields particles with mean length of 120 nm and diameters $\leq$ 10 nm, which have been determined by transmission electron microscopy.[60] S-CNCs had a salt content of 12.8 ± 0.2 mg Na_2SO_4 g^{-1} CNC (90×10^{-3} M). D-CNCs were further dialyzed to remove the remaining salt from the product. Dynamic light scattering (DLS) and electrophoretic light scattering (ELS) were used to determine hydrodynamic apparent particle diameter (z-avg) and zeta potential of CNCs in each sample, respectively. In accordance with our previous study,[60] z-avg of D-CNCs and S-CNCs was 202 ± 3 and 227 ± 5 nm, respectively, which is in the average range of CNCs of 50–200 nm.[63] Larger hydrodynamic apparent particle diameter of S-CNCs indicated salt-induced cluster formation of CNCs in the presence of Na_2SO_4.[64] Furthermore, D-CNCs and S-CNCs showed zeta potentials of -44.3 ± 4.9 mV and -35.5 ± 7.6 mV, respectively. All values were in the commonly reported range of -50 to -20 mV of sulfated CNCs and indicated elevated colloidal stability of D-CNCs in the salt-free suspension.[63,65]

2.2. Characterization of Starch-Based Nanocomposites

Starch-based nanocomposites containing D-CNCs or S-CNCs as reinforcing fillers at mass fractions of 1, 2, and 5 wt% were prepared by solution casting. Bare starch-glycerol films were used as the reference material. The effects of salt on the starch-glycerol films' mechanical properties were also evaluated by casting starch-glycerol films containing equivalent Na_2SO_4 contents to that in S-CNC suspensions. The mass fraction of glycerol as a plasticizer in all formulations was maintained at 30 wt%.

Table 1 shows the mean thickness of starch films and starch-based nanocomposites after conditioning at a relative humidity of 44%. Based on the dry mass of the respective constituents, a thickness of 75 µm was targeted for all films; however, actual film thicknesses exceeded the targeted value due to moisture uptake of the hygroscopic constituents.[66,67] Note that nanocomposites containing S-CNCs and D-CNCs have higher film thicknesses compared to bare starch films and starch films containing Na_2SO_4. Nevertheless, no significant impact of CNC or salt mass fraction on film thickness is deductible from the results shown in Table 1.

Table 1. Mean thickness of starch films and starch-based nanocomposites at a relative humidity of 44%.

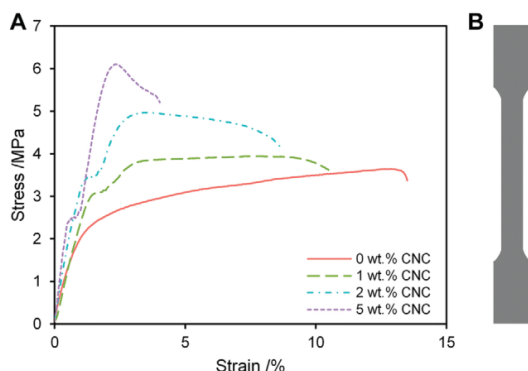| Equivalent CNC mass fraction [wt%]	0	1	2	5
Constituents		Mean film thickness [µm]		
Starch	90 ± 5			
Starch + Na$_2$SO$_4$		87 ± 4	88 ± 8	88 ± 4
Starch + S-CNCs		98 ± 8	92 ± 7	97 ± 5
Starch + D-CNCs		96 ± 7	95 ± 6	98 ± 8

Figure 1. a) Representative stress–strain curves of starch-glycerol films and starch-CNC nanocomposites with different contents of S-CNCs. b) Specimen geometry for uniaxial tensile testing (not to scale), according to ISO 527-3.[73]

The impact of S-CNCs on the mechanical properties of starch nanocomposites is shown in **Figure 1**a and the specimen geometry of all tensile-tested samples is illustrated in Figure 1b. Increasing the filler content caused both strengthening and stiffening of the nanocomposites, recognizable by the increased ultimate tensile strength and Young's modulus, respectively. At the same time, uniform strain and elongation at failure decreased and,

hence, increasing the filler content induced a decrease in ductility. These effects are mainly attributable to the formation of a rigid CNC network in the nanocomposite.[31] Concurrently, mutual entanglement of CNCs and starch, as well as efficient stress transfer from the starch matrix to the nanofiller, promotes improvement of the nanocomposite's mechanical properties, at the expense of ductility.[37,38,68–72] In addition, it has been reported that CNCs have a nucleating effect on the matrix, which causes an increase of the system's overall crystallinity.[39,40,46,47]

Figure 2 shows the mechanical properties of starch films and starch-CNC nanocomposites prepared by all formulations. Overall, the addition of Na$_2$SO$_4$ at equivalent salt contents $\leq$ 5 wt% S-CNCs had no significant impact on the mechanical properties of starch films. Thus, addition of salt at the given concentrations did not alter force transmission within the starch matrix. In contrast, addition of CNCs as nanofiller increased the material's stiffness, while its plastic deformation was constrained. To that effect, the nanocomposites' resistance to elastic deformation increased with increasing filler content, as determined by the increasing Young's modulus from 1.57 ± 0.23 MPa at 0 wt% CNC to 3.42 ± 0.14 MPa at 5 wt% CNC for S-CNCs (+118%) (Figure 2a). As expected, the mechanical properties of the nanocomposites lie between those of bare starch and CNCs, with CNCs having a Young's modulus in the range of 100–130 GPa.[74] Similar to the addition of S-CNCs, addition of 5 wt% D-CNCs increased Young's modulus to 3.63 ± 0.40 MPa (+132%). Although S-CNCs had a lesser effect on the nanocomposites' stiffness than D-CNCs, both were within the corresponding confidence intervals and, hence, residual salt did not significantly affect the elastic behavior of starch-CNC nanocomposites. Figure 2b shows the evolution of ultimate tensile strength as a function of filler content. A filler content of 5 wt% elevated the ultimate tensile strength of the nanocomposites from 3.55 ± 0.79 MPa to 6.35 ± 0.41 MPa (+79%) and 6.59 ± 0.67 MPa (+86%) for S-CNCs and D-CNCs, respectively. Therefore, CNCs strengthened the material by increasing the maximum bearable stress it can endure before failure occurs; however, filler contents of 1 and 2 wt% had no significant impact on σ_{UTS} for both S-CNCs and D-CNCs. Again, S-CNCs show marginally inferior performance compared to D-CNCs; but no significant
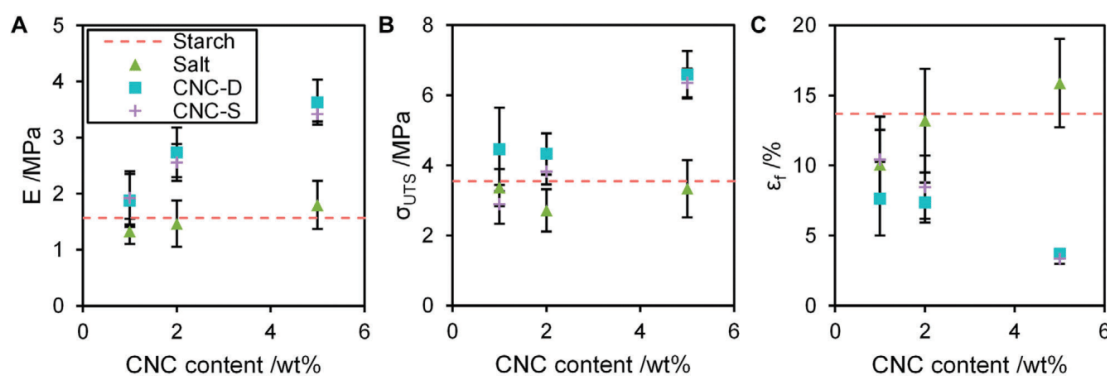

Figure 2. Mechanical properties in terms of a) Young's modulus, b) ultimate tensile strength, and c) elongation at fracture of bare starch films, starch films with equivalent amounts of salt as in S-CNCs, and starch nanocomposites containing D-CNCs or S-CNCs at different filler contents.
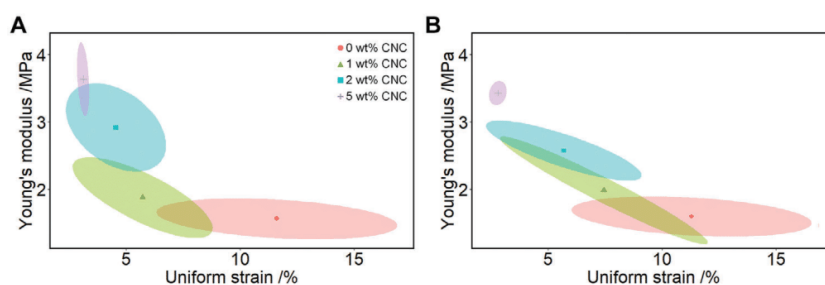
Figure 3. Young's modulus as a function of uniform strain at different filler contents of a) D-CNC or b) S-CNC. The points denote the respective mean values and the ellipses represent the confidence intervals of the means.

difference was found between nanocomposites containing each filler. Furthermore, addition of CNCs to the starch matrix made the nanocomposites more brittle. This is indicated by the reduced elongation at failure, which decreases from $13.7 \pm 3.9\%$ to $3.4 \pm 0.4\%$ (-75%) for S-CNCs and $3.7 \pm 0.4\%$ (-73%) for D-CNCs, respectively (Figure 2c). Overall, the effect of both S-CNCs and D-CNCs on the mechanical properties of starch nanocomposites did not deviate at given CNC mass fractions and, hence, no significant impact of residual salt in CNC suspensions was concluded. Furthermore, the observed increase in strength and concurrent decrease of ductility of starch-CNC nanocomposites lies well within the ranges that have been reported for the relative change of each property.[70,75,76]

Figure 3 presents Young's modulus and uniform strain for starch nanocomposites containing D-CNCs (Figure 3a) or S-CNCs (Figure 3b) at different filler contents. This figure provides a better understanding of the effects of CNCs on the mechanical properties of starch-based nanocomposites. A power law-behavior can approximate the filler content's effect of both D-CNCs and S-CNCs. Stiffness increased with increasing filler content and ductility decreased. Hence, interfacial binding of the hydrophilic CNCs in the starch matrix was good.[31] Note that commonly a linear relationship of Young's modulus and the filler content is determined.[70] In comparison, power law-behavior represents a reinforcing effect in accordance with the percolation model by Favier et al.[52]

Overall, nanocomposites containing S-CNCs exhibit marginally lower stiffness and higher brittleness than D-CNCs at equal filler contents. This effect is tentatively explained by CNC cluster formation in the presence of salt and, therefore, lower aspect ratio.[24] However, both fillers' conformable confidence intervals indicate that the salt content of S-CNCs had no significant impact on the mechanical properties of the resulting starch-based nanocomposites.

2.3. Scanning Electron Microscopy Imaging and Fractography

Figure 4a,b shows scanning electron microscopy (SEM) images on the surface morphology of a) a starch film and b) a starch-CNC nanocomposite film containing 5 wt% S-CNCs, which both contain 30 wt% glycerol as plasticizer. Both films have no pores or cracks; however, the microscopic surface structure indicates the presence of nonplasticized starch granules. Generally, glycerol is

well suited to plasticize starches with high amylose content, such as corn starch.[66,77–79] Nevertheless, some authors recommend plasticizer concentrations > 30 wt% to fully dissolve starch granules and, thus, achieve homogeneous starch films with smooth surface.[66,79] Addition of CNCs containing residual salt and salt-free CNCs (not shown here) have no impact on the surface microstructure of the nanocomposite films.

The fracture pattern of starch-CNC composites was analyzed by SEM using tensile-tested specimens. Figure 4b,c presents SEM images in the vicinity of the fracture sites, indicating that cracks occurred perpendicular to the force vector before failure. No cracks occurred further from the fracture edge. Qualitatively, the distorted texture at the surface of starch-glycerol films implies higher ductility; and the number of perpendicularly oriented cracks decreased as filler content increased. However, there was no assessable difference between the samples containing S-CNCs or D-CNCs.

3. Conclusion

This study evaluated the reinforcing effect of CNCs on starch-based nanocomposite films at filler contents $\leq$ 5 wt%. We devoted particular attention to CNCs containing residual salt from an efficient neutralization-based isolation process (S-CNCs). Salt-free CNCs from dialyzed suspensions (D-CNCs) were used for immediate comparison. The results confirmed the reinforcing effect of CNCs on the nanocomposite's mechanical properties from the increase in stiffness and strength of the material with increasing CNC content; with a concomitant decrease in ductility. In detail, addition of 5 wt% S-CNCs led to an increase of the material's stiffness by 118% and ultimate tensile strength increased by 79%. The improvement of the mechanical properties was at the expense of ductility and elongation at fracture decreased by 75% concurrently. Although the results indicated a good overall dispersion of CNCs in the starch matrix, we assumed that residual salt induces CNC cluster formation. Consequently, reinforcement of starch-based nanocomposites with CNCs containing residual salt resulted in marginally lower performance compared to nanocomposites reinforced with salt-free CNCs. The difference between S-CNCs and D-CNCs was overall <6.1% and statistically not significant. In conclusion, these results will be of particular interest for the production of low-cost, high-volume nanocomposites based on hydrophilic and thermoplastic polymers.
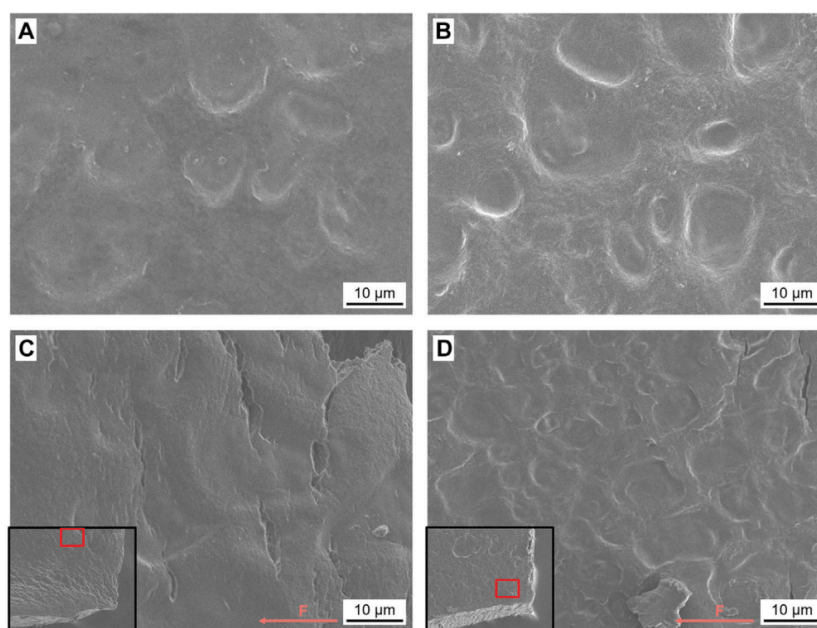
ADVANCED
SCIENCE NEWS
www.advancedsciencenews.com

Macromolecular
Materials and Engineering
www.mame-journal.de

Figure 4. Surface of a) bare starch-glycerol and b) a starch-based nanocomposite film containing 5 wt% S-CNCs at 1000x magnification; and surface of tensile-tested specimens in the vicinity of the fracture of c) a bare starch-glycerol film and d) a starch-based nanocomposite film containing 5 wt% S-CNCs. The arrows indicate the vector of a unidirectionally applied force. The rectangles in the images at the left bottom corners indicate the location of the magnified images. Here, the fracture edge is located at the right side and the sample edge at the bottom.

4. Experimental Section

Reagents: Whatman ashless filter aids (cotton α-cellulose; water content 5 wt%) were purchased from Sigma-Aldrich (Taufkirchen, Germany). Corn starch (water content 15 wt%), glycerol (99.5%), potassium carbonate (K_2CO_3, 99%), and sodium hydroxide (NaOH, 99%) were purchased from Carl Roth (Karlsruhe, Germany). Sulfuric acid (H_2SO_4, 95%) was obtained from VWR (Ismaning, Germany). All chemicals were used as received. Ultrapure (type 1) water with a resistivity of 18.2 MΩ cm (Milli-Q Direct 8 system, Merck Chemicals, Schwalbach, Germany) was used in all experiments.

Preparation of CNC Suspensions: Sulfated CNCs were extracted from cotton α-cellulose by sulfuric acid-catalyzed hydrolysis using the method reported by Cranston and Gray,[80] followed by neutralization with NaOH, according to the methodology reported by Metzger et al.[60,62] and Müller and Briesen.[81] Cellulose was oven-dried for 30 min at 105 °C to evaporate adsorbed water. Dried cellulose was then mixed with preheated sulfuric acid (64 wt%) at 45 °C at an acid-to-cellulose ratio of 10 and stirred for 45 min. Average CNC dimensions resulting from the applied process conditions are 120 nm in length and $\leq$10 nm in diameter, determined by transmission electron microscopy.[60] The reaction was stopped by transferring the reaction solution to an ice bath, followed by incremental neutralization of 85 mol% of the initially provided acid with ice-cold NaOH (aq) (1.25 M). The intermediate product was washed by twofold centrifugation for 15 min at 4500 x g (Centrifuge 5804 R, Eppendorf, Hamburg, Germany), decanted, and diluted. After the first washing step, NaOH (s) was added to adjust the pH to 7 and the amount of water added was adjusted to 110% of the critical peptization concentration of 115 × 10^{-3} M.[60] After the second washing step, the sample was concentrated by vacuum evaporation (Rotavapor R 100, Büchi, Essen, Germany) to a salt concentration above the critical peptization concentration and centrifuged again. Eventually, the precipitate was diluted to a salt concentration below the critical agglomeration

concentration and ultrasonicated with a VS 70 T sonotrode (Sonopuls HD 3400, Bandelin, Berlin, Germany) in an ice bath at an input energy of 5 kJ g^{-1} cellulose and a power of 33.3 W. After ultrasonication, incompletely hydrolyzed cellulosic residues were removed by centrifugation. The sample denoted as S-CNC was stored at 4 °C until further use. A portion of the sample was dialyzed in regenerated cellulose tubes with a molecular weight cutoff of 12–14 kDa (ZelluTrans/ROTH T3, Carl Roth, Karlsruhe, Germany) for 7 d against running water to remove the remaining salt and soluble by-products. The dialyzed sample was denoted as D-CNC.

Plasticized Starch Nanocomposites: Pure starch-glycerol films, nanocomposite films incorporating D-CNCs or S-CNCs, and starch-glycerol films incorporating Na_2SO_4 were prepared by solution casting, as described previously.[62,82] Water was preheated to 70 °C in a water bath. Starch was then added and the suspension was stirred for 1 h to allow gelatinization. D-CNCs, S-CNCs, or salt and glycerol were added, and stirring was continued for 30 min to allow plasticization and mixing of the diluted composite. All precursor solutions with the total mass, m_{total}, had a water content, w_{H_2O}, of 97 wt%. The glycerol weight fraction, w_{gly}, was kept constant at 30 wt% with respect the solid fraction. The nanoparticle loading, w_{CNC}, was varied between 1 and 5 wt% concerning the solid fraction. Residual salt in the S-CNCs was considered in the calculations. The mass fraction of salt, w_{salt}, added to starch-glycerol films was matched with the salt content of the films incorporating S-CNCs. The weighed mass of each chemical was calculated using Equation (1), considering the weight of starch, m_{starch}, and water added, m_{H_2O}, and corrected for the water content of each component

$$m_{total} = \left(1 + w_{gly} + w_{CNC} + w_{salt}\right) \cdot m_{starch} + w_{H_2O} \cdot m_{H_2O} \tag{1}$$

The filmogenic solutions were homogenized in a low-intensity ultrasonic bath for 3 min to remove bubbles and then cast in polystyrene

Petri dishes (Greiner Bio-One, distributed by VWR, Ismaning, Germany). The target dry film thickness was 75 μm. Excess water was evaporated overnight in a climatic chamber (ICH 110, Memmert, Schwabach, Germany) at 40 °C with a relative humidity of 47%. The films were then turned upside down for double-sided drying overnight. Before use, all films were conditioned in a desiccator over a saturated K_2CO_3 solution at 23 °C, resulting in a constant relative humidity of 44%.

Characterization of the CNCs and Nanocomposites: *Dry Mass and Salt Content*: The dry constituents' mass fractions at different production stages were calculated using an aliquot's mass fraction before and after water evaporation by lyophilization (2-4 LSCplus, Christ, Osterode am Harz, Germany). Then, the sample's cellulosic fraction was extrapolated from the mass fraction in the aliquots. The yield refers to the initially provided amount of cellulose, considering the overall mass balance and losses of particular unit operations.

Light Scattering Techniques: The hydrodynamic apparent particle diameter of the CNCs was measured by DLS using a Zetasizer Nano ZSP (Malvern Instruments, Worcestershire, UK). Aliquots of D-CNCs and S-CNCs were filtered through syringe filters with a glass fiber membrane and a pore size of 1 μm (Chromafil Xtra GF, Macherey-Nagel, Düren, Germany). The harmonic intensity-averaged particle diameter (z-avg) from the cumulants analysis was obtained for 0.025 wt% CNC suspensions after equilibration for 3 min at 25 °C. Zeta potentials of D-CNCs and S-CNCs were determined by ELS using the same instrument. Aliquots were similarly filtered, diluted to 0.25 wt%, and equilibrated.

Mechanical Properties: Uniaxial tensile tests were carried out on a zwicki-iLine Z2.5 testing machine (ZwickRoell, Ulm, Germany) according to the standards of the International Organization for Standardization (ISO), ISO 527-1 and ISO 527-3, using screw grips, equivalent to ZwickRoell type 8133.[73,83] Specimens were cut from individual films in a random orientation with a length of 125 mm and a width of 26 mm in the reduced section. After a preload of 0.1 N, a constant extension rate of 25 mm min^{-1} was applied. Film thickness was mechanically measured on three evenly distributed measuring points in the reduced section, using the thickness closest to the point of fracture for stress calculations. Ultimate tensile strength, σ_{UTS}, uniform strain, ϵ_{UTS}, at σ_{UTS}, and the elongation at failure, ϵ_f, were read from the stress-strain curve, σ versus ϵ. Young's modulus, E, was evaluated according to Hooke's law from the linear-elastic relationship in the initial region of the stress–strain curve (Equation (2))

$$E = \frac{\sigma}{\epsilon} \tag{2}$$

SEM Imaging: The film morphology was examined using a JEOL JSM-IT100 scanning electron microscope (Akishima, Japan) with a secondary electron detector at an acceleration voltage of 3 kV. The films were mounted on conducting carbon tape.

Remarks: The weighed mass of each chemical in the experimental section refers to their dry state. Their water content, indicated by the vendor or determined by gravimetric analysis, was considered in all calculations. All measurements were performed at least six times. The results are presented with a 95% confidence interval of the mean. The uncertainty of derived quantities depending on multiple variables is given by the propagation of error.

Conflict of Interest

The authors declare no conflict of interest.

Data Availability Statement

Research data are not shared.

[1] E. S. Medeiros, A. S. Santos, A. Dufresne, W. J. Orts, L. H. Mattoso, in *Polymer Composites, Biocomposites* (Eds: S. Thomas, K. Joseph, S. K. Malhotra, K. Goda, M. S. Sreekala), Wiley, Hoboken **2013**, p. 361.

[2] J. G. Drobny, in *Applications of Fluoropolymer Films: Properties, Processing, and Products* (Ed: J. G. Drobny), William Andrew, Norwich **2020**, p. 3.

[3] S. Gopi, P. Balakrishnan, D. Chandradhara, D. Poovathankandy, S. Thomas, *Mater. Today Chem.* **2019**, *13*, 59.

[4] P. Balakrishnan, S. Gopi, M. S. Sreekala, S. Thomas, *Starch − Stärke* **2018**, *70*, 1700139.

[5] F. M. Pelissari, D. C. Ferreira, L. B. Louzada, F. dos Santos, A. C. Corrêa, F. K. V. Moreira, L. H. Mattoso, in *Starches for Food Application* (Eds: M. T. P. Silva Clerici, M. Schmiele), Academic Press, New York, NY, USA **2019**, p. 359.

[6] A. N. Netravali, S. Chabba, *Mater. Today* **2003**, *6*, 22.

[7] L. Yu, K. Dean, L. Li, *Prog. Polym. Sci.* **2006**, *31*, 576.

[8] P. Balakrishnan, V. G. Geethamma, M. S. Sreekala, S. Thomas, in *Fundamental Biomaterials: Polymers* (Eds: S. Thomas, P. Balakrishnan, M. S. Sreekala), Woodhead Publishing, Cambridge, Sawston, UK **2018**, p. 1.

[9] P. Balakrishnan, M. S. Thomas, L. A. Pothen, S. Thomas, M. S. Sreekala, in *Encyclopedia of Polymeric Nanomaterials* (Eds: S. Kobayashi, K. Müllen), Springer, Berlin, Heidelberg, Germany **2019**, p. 1.

[10] K. K. Sadasivuni, P. Saha, J. Adhikari, K. Deshmukh, M. B. Ahamed, J. -J. Cabibihan, *Polym. Compos.* **2020**, *41*, 32.

[11] K. Van De Velde, P. Kiekens, *Polym. Test.* **2002**, *21*, 433.

[12] D. L. Kaplan, in *Biopolymers from Renewable Resources* (Ed: D. L. Kaplan), Springer, Berlin, Heidelberg, Germany **1998**, p. 1.

[13] K. Hamad, M. Kaseem, M. Ayyoob, J. Joo, F. Deri, *Prog. Polym. Sci.* **2018**, *85*, 83.

[14] M. Biron, in *Thermoplastics and Thermoplastic Composites*, William Andrew, Waltham, MA, USA **2013**, p. 133.

[15] S. Shankar, J. W. Rhim, in *Innovative Food Processing Technologies*, Elsevier, New York, NY, USA **2018**, p. 234.

[16] E. Jamróz, P. Kulawik, P. Kopel, *Polymers* **2019**, *11*, 675.

[17] A. Urvoas, M. Valerio-Lepiniec, P. Minard, C. Zollfrank, in *Bionanocomposites* (Eds: C. Aimé, T. Coradin), John Wiley and Sons, Inc., Hoboken, NJ **2017**, p. 1.

[18] D. R. Paul, L. M. Robeson, *Polymer* **2008**, *49*, 3187.

[19] *Concluded from manual keyword searches on Scopus and Web of Science*.

[20] M. Mucha, S. Ludwiczak, M. Kawinska, *Carbohydr. Polym.* **2005**, *62*, 42.

ADVANCED
SCIENCE NEWS
www.advancedsciencenews.com

Macromolecular
Materials and Engineering
www.mame-journal.de

[21] R. J. Moon, A. Martini, J. Nairn, J. Simonsen, J. Youngblood, *Chem. Soc. Rev.* **2011**, *40*, 3941.
[22] O. Faruk, A. K. Bledzki, H.-P. Fink, M. Sain, *Prog. Polym. Sci.* **2012**, *37*, 1552.
[23] F. Luzi, L. Torre, J. M. Kenny, D. Puglia, *Materials* **2019**, *12*, 471.
[24] A. Babaei-Ghazvini, B. Cudmore, M. J. Dunlop, B. Acharya, R. Bissessur, M. Ahmed, W. M. Whelan, *Carbohydr. Polym.* **2020**, *247*, 116688.
[25] P. Balakrishnan, S. Gopi, V. G. Geethamma, N. Kalarikkal, S. Thomas, *Macromol. Symp.* **2018**, *380*, 1800102.
[26] F. Li, E. Mascheroni, L. Piergiovanni, *Packag. Technol. Sci.* **2015**, *28*, 475.
[27] B. Thomas, M. C. Raj, K. B. Athira, M. H. Rubiyah, J. Joy, A. Moores, G. L. Drisko, C. Sanchez, *Chem. Rev.* **2018**, *118*, 11575.
[28] F. Vilarinho, A. Sanches Silva, M. F. Vaz, J. P. Farinha, *Crit. Rev. Food Sci. Nutr.* **2018**, *58*, 1526.
[29] A. Dufresne, *Curr. For. Rep.* **2019**, *5*, 76.
[30] E. S. Medeiros, A. Dufresne, W. J. Orts, in *Starches* (Ed: A. Bertolini), CRC Press, Boca Raton, FL, USA **2009**, p. 205.
[31] F. Xie, E. Pollet, P. J. Halley, L. Avérous, in *Polysaccharides* (Eds: K. G. Ramawat, J.-M. Mérillon), Springer International Publishing, Cham **2021**, p. 1.
[32] N. L. García, L. Famá, N. B. D'Accorso, S. Goyanes, in *Eco-Friendly Polymer Nanocomposites*, Vol. 75 (Eds: V. K. Thakur, M. K. Thakur), Springer India, New Delhi **2015**, p. 17.
[33] Y. Habibi, L. A. Lucia, O. J. Rojas, *Chem. Rev.* **2010**, *110*, 3479.
[34] J. Kim, G. Montero, Y. Habibi, J. P. Hinestroza, J. Genzer, D. S. Argyropoulos, O. J. Rojas, *Polym. Eng. Sci.* **2009**, *49*, 2054.
[35] D. Klemm, F. Kramer, S. Moritz, T. Lindström, M. Ankerfors, D. Gray, A. Dorris, *Angew. Chem., Int. Ed. Engl.* **2011**, *50*, 5438.
[36] S. Eyley, W. Thielemans, *Nanoscale* **2014**, *6*, 7764.
[37] A. Kaushik, M. Singh, G. Verma, *Carbohydr. Polym.* **2010**, *82*, 337.
[38] G. Siqueira, J. Bras, A. Dufresne, *Biomacromolecules* **2009**, *10*, 425.
[39] A. P. Mathew, A. Dufresne, *Biomacromolecules* **2002**, *3*, 609.
[40] A. P. Mathew, W. Thielemans, A. Dufresne, *J. Appl. Polym. Sci.* **2008**, *109*, 4065.
[41] X. Ma, Y. Cheng, X. Qin, T. Guo, J. Deng, X. Liu, *LWT* **2017**, *86*, 318.
[42] A. Kaushik, J. Kumra, *J. Elastomers Plast.* **2014**, *46*, 284.
[43] X. Cao, Y. Chen, P. R. Chang, M. Stumborg, M. A. Huneault, *J. Appl. Polym. Sci.* **2008**, *109*, 3804.
[44] Y. Chen, C. Liu, P. R. Chang, D. P. Anderson, M. A. Huneault, *Polym. Eng. Sci.* **2009**, *49*, 369.
[45] Y. Lu, L. Weng, X. Cao, *Carbohydr. Polym.* **2006**, *63*, 198.
[46] M. N. Anglès, A. Dufresne, *Macromolecules* **2000**, *33*, 8344.
[47] M. N. Anglès, A. Dufresne, *Macromolecules* **2001**, *34*, 2921.
[48] H. L. Luo, J. J. Lian, Y. Z. Wan, Y. Huang, Y. L. Wang, H. J. Jiang, *Mater. Sci. Eng., A* **2006**, *425*, 70.
[49] M. S. Sreekala, K. Goda, P. V. Devi, *Compos. Interfaces* **2008**, *15*, 281.
[50] A. J. Svagan, M. S. Hedenqvist, L. Berglund, *Compos. Sci. Technol.* **2009**, *69*, 500.
[51] Y. Z. Wan, H. Luo, F. He, H. Liang, Y. Huang, X. L. Li, *Compos. Sci. Technol.* **2009**, *69*, 1212.
[52] V. Favier, R. Dendievel, G. Canova, J. Y. Cavaille, P. Gilormini, *Acta Mater.* **1997**, *45*, 1557.
[53] O. M. Vanderfleet, E. D. Cranston, *Nat. Rev. Mater.* **2021**, *6*, 124.
[54] International Standardization Organization, ISO/TS 20477:2017, Nanotechnologies – Standard Terms and Their Definition For Cellulose Nanomaterial, (**2017**). https://www.iso.org/standard/68153.html (accessed: April 2021).
[55] X. M. Dong, D. G. Gray, *Langmuir* **1997**, *13*, 2404.
[56] C. A. De Assis, C. Houtman, R. Phillips, E. M. (T.) Bilek, O. J. Rojas, L. Pal, M. S. Peresin, H. Jameel, R. Gonzalez, *Biofuels, Bioprod. Biorefin.* **2017**, *11*, 682.

[57] T. Lindstrom, *Tappi J.* **2019**, *18*, 308.
[58] A. Rudie, in *Handbook of Nanocellulose and Cellulose Nanocomposites* (Eds: H. Kargarzadeh, I. Ahmad, S. Thomas, A. Dufresne), Wiley-VCH Verlag GmbH & Co. KGaA, Weinheim, Germany **2017**, p. 761.
[59] C. S. Davis, D. L. Grolman, A. Karim, J. W. Gilman, *Green Mater.* **2015**, *3*, 53.
[60] C. Metzger, D. Auber, S. Dähnhardt-Pfeiffer, H. Briesen, *Cellulose* **2020**, *27*, 9839.
[61] T. Phan-Xuan, A. Thuresson, M. Skepö, A. Labrador, R. Bordes, A. Matic, *Cellulose* **2016**, *23*, 3653.
[62] C. Metzger, S. Sanahuja, L. Behrends, S. Sängerlaub, M. Lindner, H. Briesen, *Coatings* **2018**, *8*, 142.
[63] E. J. Foster, R. J. Moon, U. P. Agarwal, M. J. Bortner, J. Bras, S. Camarero-Espinosa, K. J. Chan, M. J. D. Clift, E. D. Cranston, S. J. Eichhorn, D. M. Fox, W. Y. Hamad, L. Heux, B. Jean, M. Korey, W. Nieh, K. J. Ong, M. S. Reid, S. Renneckar, R. Roberts, J. A. Shatkin, J. Simonsen, K. Stinson-Bagby, N. Wanasekara, J. Youngblood, *Chem. Soc. Rev.* **2018**, *47*, 2609.
[64] A. A. Moud, M. Arjmand, J. Liu, Y. Yang, A. Sanati-Nezhad, S. H. Hejazi, *Cellulose* **2019**, *26*, 9387.
[65] A. Kumar, C. K. Dixit, in *Advances in Nanomedicine for the Delivery of Therapeutic Nucleic Acids* (Eds: S. Nimesh, R. Chandra, G. Nidhi), Woodhead Publishing, Cambridge, Sawston, UK **2017**, p. 43.
[66] E. Basiak, A. Lenart, F. Debeaufort, *Polymers* **2018**, *10*, 412.
[67] X. Guo, Y. Wu, X. Xie, *Sci. Rep.* **2017**, *7*, 14207.
[68] A. Khan, R. A. Khan, S. Salmieri, C. Le Tien, B. Riedl, J. Bouchard, G. Chauve, V. Tan, M. R. Kamal, M. Lacroix, *Carbohydr. Polym.* **2012**, *90*, 1601.
[69] H. Aloui, K. Khwaldia, M. Hamdi, E. Fortunati, J. M. Kenny, G. G. Buonocore, M. Lavorgna, *ACS Sustainable Chem. Eng.* **2016**, *4*, 794.
[70] Z. W. Abdullah, Y. Dong, *J. Mater. Sci.* **2018**, *53*, 15319.
[71] V. Nessi, X. Falourd, J.-E. Maigret, K. Cahier, A. D'orlando, N. Descamps, V. Gaucher, C. Chevigny, D. Lourdin, *Carbohydr. Polym.* **2019**, *225*, 115123.
[72] F. M. Pelissari, M. M. Andrade-Mahecha, P. J. D. A. Sobral, F. C. Menegalli, *J. Colloid Interface Sci.* **2017**, *505*, 154.
[73] International Standardization Organization, ISO 527-3:2018, Plastics – Determination of Tensile Properties – Part 3: Test Conditions for Films and Sheets, (**2018**). https://www.iso.org/standard/70307.html (accessed: April 2021).
[74] A. Dufresne, *Mater. Today* **2013**, *16*, 220.
[75] A. Kaushik, R. Kaur, *Compos. Interfaces* **2016**, *23*, 701.
[76] C. Calvino, N. Macke, R. Kato, S. J. Rowan, *Prog. Polym. Sci.* **2020**, *103*, 101221.
[77] M. G. A. Vieira, M. A. Da Silva, L. O. Dos Santos, M. M. Beppu, *Eur. Polym. J.* **2011**, *47*, 254.
[78] D. Domene-López, J. C. García-Quesada, I. Martin-Gullon, M. G. Montalbán, *Polymers* **2019**, *11*, 1084.
[79] M. I. J. Ibrahim, S. M. Sapuan, E. S. Zainudin, M. Y. M. Zuhri, *Int. J. Food Prop.* **2019**, *22*, 925.
[80] E. D. Cranston, D. G. Gray, *Biomacromolecules* **2006**, *7*, 2522.
[81] Nanocrystalline Cellulose, Its Preparation and Uses of Such Nanocrystalline Cellulose Patent. *US 2017/0306056 A1; EP 3204428; CA 2963698*, https://data.epo.org/gpi/EP3204428B1, **2017**.
[82] J. S. Alves, K. C. Dos Reis, E. G. T. Menezes, F. V. Pereira, J. Pereira, *Carbohydr. Polym.* **2015**, *115*, 215.
[83] International Standardization Organization, ISO 527-1:2019, Plastics – Determination of Tensile Properties – Part 1: General Principles, (**2019**). https://www.iso.org/standard/75824.html (accessed: April 2021).

5. Concluding remarks

Throughout this work, CNCs were investigated with the aim of developing deeper understanding of interactions that control particle agglomeration, forces that facilitate particle dispersion, and effects of CNCs on advanced materials' performance. Specifically, agglomeration behavior of CNCs in the presence of salts was probed through optical measurement techniques; ultrasound-induced dispersion of CNC clusters was analyzed by multi-detector asymmetrical flow field-flow fractionation; and technical properties of packaging films, incorporating CNCs, were assessed. Altogether, these objectives were accomplished in accordance with the goals outlined in section 1.3:

(I) **Develop efficient downstream processing strategy, based on CNC agglomeration behavior.** The work within section 4.1 examined behavior of colloidal CNCs, which were produced through sulfuric acid-catalyzed hydrolysis of cellulose, in the presence of secondary sulfates. Electrostatic particle interaction and, thus, agglomeration behavior can be adjusted by adding salt to CNC suspensions. Resulting CNC nanostructures can be controlled by surface charge density, salt concentration, and species of added salt, among others. Controlling these nanostructures enables production of CNC-based advanced materials with tailored rheological, mechanical, and optical properties (*157, 158*). Critical agglomeration and peptization concentrations of four secondary sulfates were determined. It was found that CNC agglomeration in the presence of sulfates is attributable to electrostatic charge screening, cluster formation, and matching affinities. Not only does this complement studies on CNC agglomeration, which, so far, have only been performed in the presence of chlorides (*251, 263, 365, 412, 413, 402, 414–422*). Furthermore, the results are readily translatable to process design, involving neutralized reactant solutions during downstream processing (section 2.2.4). This contribution is an effort toward control of the structure-property relationship of CNC suspensions, and it will help in product separation at low reactant consumption, for overall efficient CNC production.

(II) **Thoroughly characterize effects of ultrasonication on CNC suspension properties.** Advanced materials based on CNCs demand nanoparticles with predictive and uniform properties. This is commonly achieved by ultrasound-assisted dispersion of clustered CNCs, which inherently form agglomerates during processing, and upon redispersion after drying (*255, 329, 332*). However, process parameters during ultrasonication are not standardized, and the methodology itself is under-reported (*423*). Furthermore, process monitoring and characterization of particle size distribution by common methods, such as DLS, EM, and AFM, cannot quantify CNC size in the particles' native colloidal state. In this regard, on-line multi-detector AF4 and off-line DLS, ELS, and conductometric titration were performed, to elucidate effects of ultrasonication on the process-structure-property relationship of CNCs, in terms of particle size distribution and stability (section 4.2). It was found that mean particle length decreased with increasing ultrasound energy input and, simultaneously, particle length distribution narrowed. Concurrently, colloidal stability remained constant at arbitrary ultrasound energy inputs, whereas the impact of ultrasonication was more lasting for higher energy inputs. These findings are significant for the community, because comprehensive understanding of

effects of ultrasonication on colloidal CNCs facilitates production of well-dispersed CNCs with uniform properties from different cellulose sources. Furthermore, multi-detector AF4 was validated as on-line measurement technique to monitor particle size and shape of colloidal CNCs. Improved control over CNC properties and use of on-line measurement techniques supports standard development on CNC processing and characterization and, therefore, aids commercial adoption of CNCs.

(III) Demonstrate CNC performance in advanced materials. In sections 4.3 and 4.4, CNC suspensions containing residual salt were prepared by sulfuric acid-catalyzed hydrolysis of cellulose and successive neutralization with sodium hydroxide. Nanoparticle suspensions were coated onto polymer films to improve barrier properties and incorporated into nanocomposites as mechanical reinforcement. While CNC coatings and CNC-reinforced nanocomposites have been previously reported (*61, 184, 200, 403, 406, 424–426*), the works herein uniquely examined the impact of residual salt from CNC processing—according to process design presented in section 4.1—on materials' performance. It was found that oxygen barrier properties were significantly increased, compared to bare polymer films. Furthermore, mechanical strength of hydrophilic nanocomposites was improved by minor addition of CNCs, and no negative impact of residual salt on mechanical properties was found. Therefore, good spreadability and dispersion of salt containing CNC suspensions was concluded. These contributions are critical to ongoing development of CNC processing in advanced materials because neutralization-based CNC production provides low-cost potential to packaging applications and, therefore, promotes commercial adoption of CNCs in advanced materials.

Knowledge gained herein deepens understanding of the relationship of process, structure, properties, and performance of CNCs in aqueous suspensions and polymer nanocomposites. For example, agglomeration behavior in the presence of secondary sulfates opens new perspectives to control colloidal stability, aiming at efficient process design. Furthermore, it was found that thermoplastic nanocomposites, reinforced with salt containing CNCs show improved mechanical properties and, hence, excessive purification is not a prerequisite for good CNC dispersion in compatible polymer matrices. This is particularly useful for production of low-cost added value nanomaterials with improved performance. In addition, effects of ultrasonication on colloidal CNCs were quantified. Targeted ultrasonication facilitates control of particle size distribution and stability. As a result, products with uniform and predictable properties can be tailored. This work overall supports ongoing research activities and standard development on CNCs, as sustainable building block in environmentally compatible advanced materials, manufactured in eco-friendly processes.

6. Outlook and future work

Worldwide incentives toward more bio-based economies prompt increasing demand for sustainable materials and processes on a global scale. In this regard, cellulose nanomaterials and, particularly, cellulose nanocrystals have great potential to add value to numerous products and provide a materials platform in versatile sustainable applications. Sulfated CNCs, which constitute their most used form, are produced by sulfuric acid-catalyzed hydrolysis. Reportedly, efforts have been made to control their length, aspect ratio, surface chemistry, surface charge density, and crystallinity index, among others. However, while sulfated CNCs are most uniform and reproducible in properties, adjusting their set of properties to target applications with improved performance is yet to be done. Therefore, contemporary research on CNCs is directed at comprehensive understanding of particle-particle interactions in complex environments to improve dispersibility (*414*), chemical derivatization to expand their use in hydrophobic media and polymeric compounds (*427*), and drying and redispersion for easier storage and handling (*323, 328, 329*). Research on process scaling (*30, 31, 35–39*), on-line characterization in complex environments (*42, 44, 45, 48*), regulation and standardization (*1, 35, 45–49, 428*), and full life-cycle analysis to assess environmental and health impacts (*20, 30, 31, 38, 40–44, 335, 429*) are considered equally important for commercial CNC production.

From the perspective of this work, future studies may be directed at scaling opportunities and full life-cycle analysis of neutralization-based process design, toward resource-efficient CNC isolation. Since critical agglomeration concentration is independent of CNC mass fraction, solid-liquid separation, by centrifugation and concentration, are implementable unit operations to further reduce products' salt concentration. Thereby, a lower degree of agglomeration and, hence, improved dispersibility in hydrophilic media is anticipated. Minor salt residues in the product favor CNC dispersibility after drying (*264, 329*), and neutralization of surface charges reduces CNCs' propensity for autocatalyzed hydrolysis and de-sulfation (*259, 260*). Hence, neutralization-based process design can be adjusted to control CNC structure and stability, along with other CNC properties that depend on ionic strength (*263, 417, 430–432*). While ultrasonication facilitates CNC individualization, combined effects of ionic strength and ultrasound treatment on particle size distribution and stability of CNC suspensions are worthwhile of investigation, and could facilitate the concept's implementation to industrial CNC production and handling, where they are commonly neutralized by sodium counterions (*257*). Process design, targeting predictable dispersibility and control of CNC structure, should be overall aimed at adjusting CNCs' property set to value-added use cases, to make them ready for the market.

7. Lists

7.1. List of publications

Parts of this thesis have been published in following peer-reviewed articles:

Paper I:
Metzger, C.; Auber, D.; Dähnhardt-Pfeiffer, S.; Briesen, H. Agglomeration of cellulose nanocrystals: the effect of secondary sulfates and their use in product separation. *Cellulose* **2020**, 27 (17), 9839–9851. DOI: 10.1007/s10570-020-03476-0.

Paper II:
Metzger, C.; Drexel, R.; Meier, F.; Briesen, H. Effect of ultrasonication on the size distribution and stability of cellulose nanocrystals in suspension: an asymmetrical flow field-flow fractionation study. *Cellulose* **2021**, *(online).* DOI: 10.1007/s10570-021-04172-3.

Paper III:
Metzger, C.; Sanahuja, S.; Behrends, L.; Sängerlaub, S.; Lindner, M.; Briesen, H. Efficiently extracted cellulose nanocrystals and starch nanoparticles and techno-functional properties of films made thereof. *Coatings* **2018**, 8 (4), 142. DOI: 10.3390/coatings8040142.

Paper IV:
Metzger C., Briesen, H. (2021) Thermoplastic starch nanocomposites reinforced with cellulose nanocrystal suspensions containing residual salt from neutralization. *Macromolecular Materials and Engineering* **2021**, 306 (8), 2100161. DOI: 10.1002/mame.202100161.

Parts of this thesis have been presented to the scientific community:

Talk:

Metzger C.; Müller, V.; Briesen, H. One-pot procedure for the isolation of nanocrystalline cellulose. *BioVaria* **2017**, Munich, Germany.

Posters:

Metzger, C.; Müller, V.; Briesen, H. One-pot procedure for the isolation of nanocrystalline cellulose. *BioVaria* **2017**, Munich, Germany.

Metzger, C.; Auber, D.; Briesen, H. Separation efficiency of cellulose nanocrystals from high ionic strength solutions. *PARTEC* **2019**, Nuremberg, Germany.

Metzger, C.; Briesen, H. Cellulose nanocrystals – processing and potential. *NanoCare-Clustertreffen* **2019**, Frankfurt a.M., Germany.

Drexel, R.; Metzger, C.; Briesen, H.; Dähnhardt-Pfeiffer, S.; Meier, F. Electrical asymmetrical flow field-flow fractionation for the characterization of cellulose nanocrystals. *NanoCare-Clustertreffen* **2019**, Frankfurt a.M., Germany.

Following student theses contributed to this work:

7.2. Abbreviations

A

AdM *Advanced material*

AF4 *Asymmetrical flow field-flow fractionation*

AFM *Atomic force microscopy*

AGU *Anhydroglucose unit*

APPTI *Alliance for Pulp & Paper Technology*

B

BBI JU *Bio-based Industries Joint Untertaking*

C

CAC *Critical agglomeration concentration*

CF *Candle filtration*

CMC *Cellulose microcrystal*

CMF *Cellulose microfibril*

CNC *Cellulose nanocrystal*

CNF *Cellulose nanofibril*

CNM *Cellulose nanomaterial*

CPC *Critical peptization concentration*

D

DF *Diafiltration*

DLVO *Theory named after Boris Derjaguin, Lev Landau, Evert Verwey, and Theodoor Overbeek*

DoE *Design of experiments*

E

ELS *Electrophoretic light scattering*

EM *Electron microscopy*

I

ISO *International Standardization Organization*

ISO/CD *Committee draft of the International Organization for Standardization*

ISO/TS *Technical specification of the International Organization for Standardization*

L

LCA *Life-cycle analysis*

M

MALS *Multiangle light scattering*

MNM *Manufactured nanomaterial*

N

NCF *Nanocellulose Forum*

P

PGV *Partikelgrößenverteilung*

pH *Activity of hydrogen ions in solution*

PLA *Poly(lactic acid)*

PPR *Patent-to-publication ratio*

S

SFE *Surface free energy*

T

TAPPI *Technical Association of the Pulp and Paper Industry*

TC *Terminal cellulose synthase complex*

TEM *Transmission electron microscopy*

U

UF *Ultrafiltration*

W

WoS *Web of Science*

WoS-CC *Web of Science Core Collection*

7.3. Symbols

Symbol	Description
α	Alpha phase
β	Beta phase
ε_{sol}	Dielectric constant
ζ	Zeta potential
η	Viscosity
κ^{-1}	Debye length
ρ_s	Surface sulfate group density
a	Reaction order with respect to acid concentration
c_{acid}	Acid concentration
c_{crit}	Critical concentration for liquid crystalline phase separation
c_{enz}	Cellulase concentration
c_{salt}	Salt concentration
CrI	Crystallinity index
d	Particle diameter
D	Dextro conformation of cellulose
E_A	Activation energy
H	Interaction distance
k	Rate constant
k_i	Pre-exponential factor
L	Particle length
m_a	Acid mass
m_c	Pulp mass, or cellulose mass
m_{CNC}	CNC mass
m_P	Product mass
m_B	Mass of byproduct
R	Universal gas constant
t_{mc}	Mechano-chemical treatment time
t_R	Reaction time
t_{US}	Ultrasonication time
T_R	Reaction time
Y	CNC isolation yield
z	Ion valence
$z\text{-}avg$	Hydrodynamic apparent particle size

7.4. Elements, ions, and compounds

Symbol or composition	Name
C	Carbon
H+	Proton, or hydron
NH_4^+	Ammonium ion
Na^+	Sodium ion
ClO_2^-	Chlorine dioxide
K^+	Potassium ion
Ca^{2+}	Calcium ion
H_2O	Water
H_2O_2	Hydrogen peroxide
H_2SO_4	Sulfuric acid
HCl	Hydrochloric acid
CO_2	Carbon dioxide
NH_4OH	Ammonium hydroxide
$(NH_4)_2SO_4$	Ammonium sulfate
Na_2CO_3	Sodium carbonate
NaOH	Sodium hydroxide
NaOCl	Sodium hypochlorite
Na_2SO_4	Sodium sulfate
$NaClO_2$	Sodium chlorite
KOH	Potassium hydroxide
K_2SO_4	Pottasium sulfate
$Ca(OH)_2$	Calcium hydroxide
$CaSO_4$	Calcium sulfate
$R-OSO_3H$	Protonated sulfate half-ester group, where R denominates CNC backbone

7.5. Lists of figures

7.6. List of tables

8. Bibliography

1. International Organization for Standardization. *ISO/TS 20477:2017 - Nanotechnologies - standard terms and their definition for cellulose nanomaterial*, 2017 (20477). https://www.iso.org/standard/68153.html.

2. Dufresne, A. Nanocellulose: a new ageless bionanomaterial. *Materials Today* **2013,** *16* (6), 220–227. DOI: 10.1016/j.mattod.2013.06.004.

3. Klemm, D. O.; Kramer, F.; Moritz, S.; Lindström, T.; Ankerfors, M.; Gray, D. G.; Dorris, A. Nanocelluloses: a new family of nature-based materials. *Angewandte Chemie International Edition* **2011,** *50* (24), 5438–5466. DOI: 10.1002/anie.201001273.

4. Howell, P. *Earth, Air, Fire and Water: Elements of Materials Science;* Kendall Hunt Pub Co, 2008.

5. National Research Council (U.S.). *Materials science and engineering for the 1990s*: *Maintaining competitiveness in the age of materials;* National Academy Press, 1989.

6. National Research Council (U.S.). *Materials science and engineering*: *Forging stronger links to users*; Publication NMAB; Vol. 492; National Academy Press, 1999. DOI: 10.17226/9718.

7. Krausmann, F.; Gingrich, S.; Eisenmenger, N.; Erb, K.-H.; Haberl, H.; Fischer-Kowalski, M. Growth in global materials use, GDP and population during the 20th century. *Ecological Economics* **2009,** *68* (10), 2696–2705. DOI: 10.1016/j.ecolecon.2009.05.007.

8. Ashby, M. F. Introduction. In *Materials Selection in Mechanical Design,* 4th edition; Ashby, M. F., Ed.; Elsevier, 2011, pp 1–13. DOI: 10.1016/B978-1-85617-663-7.00001-1.

9. United Nations. *Transforming our World: The 2030 Agenda for Sustainable Development (Accessed: 15 August 2021)*. https://sustainabledevelopment.un.org/.

10. European Commission. *A sustainable bioeconomy for Europe*: *Strengthening the connection between economy, society and the environment : updated bioeconomy strategy*.

11. Heimann, T. Bioeconomy and SDGs: Does the Bioeconomy Support the Achievement of the SDGs? *Earth's Future* **2019,** *7* (1), 43–57. DOI: 10.1029/2018EF001014.

12. Clarivate Analytics. *Web of Science (Accessed: 15 August 2021)*. https://apps.webofknowledge.com/.

13. Clarivate Analytics. *Web of Science. Research Areas (Categories / Classification) (Accessed: 15 August 2021)*. https://images.webofknowledge.com/images/help/WOS/hp_research_areas_easca.html.

14. Bauer, C.; Buchgeister, J.; Hischier, R.; Poganietz, W. R.; Schebek, L.; Warsen, J. Towards a framework for life cycle thinking in the assessment of nanotechnology. *Journal of Cleaner Production* **2008,** *16* (8-9), 910–926. DOI: 10.1016/j.jclepro.2007.04.022.

15. Dhingra, R.; Naidu, S.; Upreti, G.; Sawhney, R. Sustainable Nanotechnology: Through Green Methods and Life-Cycle Thinking. *Sustainability* **2010,** *2* (10), 3323–3338. DOI: 10.3390/su2103323.

16. Salieri, B.; Turner, D. A.; Nowack, B.; Hischier, R. Life cycle assessment of manufactured nanomaterials: Where are we? *NanoImpact* **2018,** *10*, 108–120. DOI: 10.1016/j.impact.2017.12.003.

17. International Organization for Standardization. *ISO 14044:2006 - Environmental management – Life cycle assessment – Requirements and guidelines*, 2006 (14044). https://www.iso.org/standard/76122.html.

18. International Organization for Standardization. *ISO 14044:2006/AMD 1:2017 - Environmental management - Life cycle assessment - Requirements and guidelines — Amendment 1*, 2017 (14044/AMD 1). https://www.iso.org/standard/72357.html.

19. International Organization for Standardization. *ISO 14044:2006/AMD 2:2020 - Environmental management - Life cycle assessment - Requirements and guidelines - Amendment 2*, 2020 (14044/AMD 2). https://www.iso.org/standard/76122.html.

20. Li, Q.; McGinnis, S.; Sydnor, C.; Wong, A.; Renneckar, S. Nanocellulose Life Cycle Assessment. *ACS Sustainable Chemistry & Engineering* **2013,** *1* (8), 919–928. DOI: 10.1021/sc4000225.

21. Kaplan, D. L. Introduction to Biopolymers from Renewable Resources. In *Biopolymers from Renewable Resources*; Kaplan, D. L., Ed.; Springer, 1998, pp 1–29. DOI: 10.1007/978-3-662-03680-8_1.

22. Krässig, H. A. *Cellulose: Structure, accessibility and reactivity*, 2nd edition; Polymer monographs; Vol. 11; Gordon and Breach, 1996.

23. Klemm, D. O.; Philipp, B.; Heinze, T. J.; Heinze, U.; Wagenknecht, W. Introduction. In *Comprehensive cellulose chemistry*; Klemm, D. O., Ed.; Wiley-VCH, 1998, pp 1–7. DOI: 10.1002/3527601929.ch1.

24. Qi, H. Introduction. In *Novel Functional Materials Based on Cellulose*; Qi, H., Ed.; SpringerBriefs in Applied Sciences and Technology; Springer, 2016, pp 1–9. DOI: 10.1007/978-3-319-49592-7_1.

25. Gilbert, R. D.; Kadla, J. F. Polysaccharides — Cellulose. In *Biopolymers from Renewable Resources*; Kaplan, D. L., Ed.; Springer, 1998, pp 47–95. DOI: 10.1007/978-3-662-03680-8_3.

26. Cambia. *The Lens - Free & Open Patent and Scholarly Search (Accessed: 31 October 2020)*. https://www.lens.org/.

27. Hamad, W. Y. Applications of Cellulose Nanocrystals. In *Cellulose Nanocrystals: Properties, Production and Applications*; Hamad, W. Y., Ed.; Wiley Series in Renewable Resource Ser; John Wiley & Sons, 2017, pp 138–247. DOI: 10.1002/9781118675601.ch5.

28. Shapira, P.; Youtie, J.; Kay, L. National innovation systems and the globalization of nanotechnology innovation. *The Journal of Technology Transfer* **2011,** *36* (6), 587–604. DOI: 10.1007/s10961-011-9212-0.

29. Charreau, H.; Cavallo, E.; Foresti, M. L. Patents involving nanocellulose: Analysis of their evolution since 2010. *Carbohydrate polymers* **2020,** *237*, 116039. DOI: 10.1016/j.carbpol.2020.116039.

30. Rudie, A. W. Commercialization of Cellulose Nanofibril (CNF) and Cellulose Nanocrystal (CNC): Pathway and Challenges. In *Handbook of Nanocellulose and Cellulose Nanocomposites*; Kargarzadeh, H., Ahmad, I., Thomas, S., Dufresne, A., Eds.; Wiley-VCH, 2017, pp 761–797. DOI: 10.1002/9783527689972.ch23.

31. Wu, B.; Wang, S.; Tang, J.; Lin, N. Nanocellulose in High-Value Applications for Reported Trial and Commercial Products. In *Advanced Functional Materials From Nanopolysaccharides*; Tang, J., Lin, N., Dufresne, A., Tam, M. K., Eds.; Springer Series in Biomaterials Science and Engineering; Springer, 2019, pp 389–409. DOI: 10.1007/978-981-15-0913-1_11.

32. Shatkin, J. A.; Wegner, T. H.; Bilek, E. M.; Cowie, J. Market projections of cellulose nanomaterial-enabled products- Part 1: Applications. *TAPPI Journal* **2014,** *13* (5), 9–16.

33. Cowie, J.; Bilek, E. M.; Wegner, T. H.; Shatkin, J. A. Market projections of cellulose nanomaterial-enabled products-- Part 2: Volume estimates. *TAPPI Journal* **2014,** *13* (6), 57–69.

34. Hansen, F.; Brun, V.; Keller, E.; Nieh, W. L. S.; Wegner, T. H.; Meador, M.; Friedersdorf, L. *Cellulose Nanomaterials: A Path Towards Commercialization*: *Workshop Report.* https://tappinano.org/media/1073/2014-usfs-nih-cellulose_nano_workshop_report.pdf.

35. Kargarzadeh, H.; Mariano, M.; Gopakumar, D. A.; Ahmad, I.; Thomas, S.; Dufresne, A.; Huang, J.; Lin, N. Advances in cellulose nanomaterials. *Cellulose* **2018,** *25* (4), 2151–2189. DOI: 10.1007/s10570-018-1723-5.

36. Klemm, D. O.; Cranston, E. D.; Fischer, D.; Gama, M.; Kedzior, S. A.; Kralisch, D.; Kramer, F.; Kondo, T.; Lindström, T.; Nietzsche, S.; Petzold-Welcke, K.; Rauchfuß, F. Nanocellulose as a natural source for groundbreaking applications in materials science: Today's state. *Materials Today* **2018,** *21* (7), 720–748. DOI: 10.1016/j.mattod.2018.02.001.

37. Dunlop, M. J.; Clemons, C.; Reiner, R. S.; Sabo, R.; Agarwal, U. P.; Bissessur, R.; Sojoudiasli, H.; Carreau, P. J.; Acharya, B. Towards the scalable isolation of cellulose nanocrystals from tunicates. *Scientific reports* **2020,** *10* (1), 19090. DOI: 10.1038/s41598-020-76144-9.

38. Trache, D.; Tarchoun, A. F.; Derradji, M.; Hamidon, T. S.; Masruchin, N.; Brosse, N.; Hussin, M. H. Nanocellulose: From Fundamentals to Advanced Applications. *Frontiers in chemistry* **2020,** *8*, 392. DOI: 10.3389/fchem.2020.00392.

39. Vanderfleet, O. M.; Cranston, E. D. Production routes to tailor the performance of cellulose nanocrystals. *Nature Reviews Materials* **2020. DOI:** 10.1038/s41578-020-00239-y.

40. O'Connor, B.; Berry, R.; Goguen, R. Commercialization of Cellulose Nanocrystal (NCC™) Production. In *Nanotechnology, environmental health and safety*: *Risks, regulation, and management,* Second edition; Hull, M. S., Bowman, D. M., Eds.; Elsevier, 2014, pp 225–246. DOI: 10.1016/B978-1-4557-3188-6.00010-4.

41. Shatkin, J. A.; Ong, K. J.; Ede, J.; Wegner, T. H.; Goergen, M. Toward cellulose nanomaterial commercialization: knowledge gap analysis for safety data sheets according to the globally harmonized system. *TAPPI Journal* **2016,** *15* (6), 425–437.

42. Foster, E. J.; Moon, R. J.; Agarwal, U. P.; Bortner, M. J.; Bras, J.; Camarero-Espinosa, S.; Chan, K. J.; Clift, M. J. D.; Cranston, E. D.; Eichhorn, S. J.; Fox, D. M.; Hamad, W. Y.; Heux, L.; Jean, B.; Korey, M.; Nieh, W. L. S.; Ong, K. J.; Reid, M. S.; Renneckar, S.; Roberts, R.; Shatkin, J. A.; Simonsen, J.; Stinson-Bagby, K.; Wanasekara, N.; Youngblood, J. Current characterization methods for cellulose nanomaterials. *Chemical Society reviews* **2018,** *47* (8), 2609–2679. DOI: 10.1039/c6cs00895j.

43. Shatkin, J. A.; Ong, K. J.; Ede, J. Minimizing Risk: An Overview of Risk Assessment and Risk Management of Nanomaterials. In *Metrology and Standardization of Nanotechnology*; Mansfield, E., Kaiser, D. L., Fujita, D., van de Voorde, M., Eds.; Wiley-VCH, 2017, pp 381–408. DOI: 10.1002/9783527800308.ch24.

44. Lindström, T. Research needs for nanocellulose commercialization and applications. *TAPPI Journal* **2019,** *18* (5), 308–311. DOI: 10.32964/TJ18.5.308.

45. International Organization for Standardization. *ISO/TR 19716:2016 - Nanotechnologies — Characterization of cellulose nanocrystals*, 2016 (19716). https://www.iso.org/standard/66110.html.

46. International Organization for Standardization. *ISO/TR 12885:2018 - Nanotechnologies — Health and safety practices in occupational settings*, 2018 (12885). https://www.iso.org/standard/67446.html.

47. Canadian Standards Association. *CSA Z12885-12:2017 - Nanotechnologies-Exposure Control Program for Engineered Nanomaterials in Occupational Settings*, 2017 (Z12885). https://www.scc.ca/en/standards/work-programs/csa/cellulosic-nanomaterials-test-methods-for-characterization.

48. Canadian Standards Association. *CSA Z5100-17:2017 - Cellulose Nanomaterials - Test Methods For Characterization*, 2017 (Z5100). https://www.scc.ca/en/standards/work-programs/csa/cellulosic-nanomaterials-test-methods-for-characterization.

49. Canadian Standards Association. *CSA Z5200-17:2017 - Cellulose nanomaterials - Blank detail specification*, 2017 (Z5200). https://www.scc.ca/en/standards/work-programs/csa/cellulosic-nanomaterials-material-specification-0.

50. Asadi, A.; Bennett, K.; Bilodeau, M.; Binnall, R.; Boyce, S.; Catchmark, J.; Cheng, W.; Ciesielski, P.; Davis, V.; Deng, Y.; Durocher, P.; Eberle, C.; Edwards, M.; Gilman, J. W.; Goergen, M.; Kalatzidou, K.; Khalil, H.; Kippelen, B.; Kitchens, C.; Knox, D.; Kulkarni, S.; Lin, Z.; Luettgen, C.; Marsolan, N.; Meredith, C.; Miller, M.; Nelson, K.; Pendse, H.; Ragauskas, A. J.; Schelling, K.; Shackford, L.; Shatkin, J. A.; Shofner, M.; Simonsen, J.; Tekinalp, H.; Turpin, D. *Cellulose Nanomaterials Research Roadmap*. https://www.appti.org/technology-roadmaps-downloads.html.

51. Dammer, L.; Carus, M.; Iffland, K.; Piotrowski, S.; Sarmento, L.; Chinthapalli, R.; Raschka, A. *Current situation and trends of the bio-based industries in Europe with a focus on bio-based materials*. https://www.bbi-europe.eu/sites/default/files/media/bbiju-pilotstudy.pdf.

52. Miyanishi, T. Unfolding the Future of the Pulp and Paper Industry. *Mokuzai Gakkaishi* **2015,** *61* (3), 196–199. DOI: 10.2488/jwrs.61.196.

53. Boluk, Y.; Ensor, D.; Forsström, U.; Gardner, D. J.; Haydon, B.; Moon, R. J.; Nieh, W. L. S.; Shatkin, J. A.; Teague, C.; Walker, C.; Willis, C.; Wegner, T. H. *Roadmap for the Development of International Standards for Nanocellulose*. https://www.tappinano.org/Media/1070/2011-Roadmapfornanocellulosestandards.Pdf.

54. Himmel, M. E.; Ding, S.-Y.; Johnson, D. K.; Adney, W. S.; Nimlos, M. R.; Brady, J. W.; Foust, T. D. Biomass recalcitrance: engineering plants and enzymes for biofuels production. *Science (New York, N.Y.)* **2007,** *315* (5813), 804–807. DOI: 10.1126/science.1137016.

55. Sugiyama, J.; Vuong, R.; Chanzy, H. Electron diffraction study on the two crystalline phases occurring in native cellulose from an algal cell wall. *Macromolecules* **1991,** *24* (14), 4168–4175. DOI: 10.1021/ma00014a033.

56. Wolfenden, R.; Lu, X.; Young, G. Spontaneous Hydrolysis of Glycosides. *Journal of the American Chemical Society* **1998,** *120* (27), 6814–6815. DOI: 10.1021/ja9813055.

57. Wolfenden, R.; Snider, M. J. The depth of chemical time and the power of enzymes as catalysts. *Accounts of Chemical Research* **2001,** *34* (12), 938–945. DOI: 10.1021/ar000058i.

58. French, A. D. Glucose, not cellobiose, is the repeating unit of cellulose and why that is important. *Cellulose* **2017,** *24* (11), 4605–4609. DOI: 10.1007/s10570-017-1450-3.

59. Nishiyama, Y.; Langan, P.; Chanzy, H. Crystal structure and hydrogen-bonding system in cellulose Ibeta from synchrotron X-ray and neutron fiber diffraction. *Journal of the American Chemical Society* **2002,** *124* (31), 9074–9082. DOI: 10.1021/ja0257319.

60. Nishiyama, Y.; Sugiyama, J.; Chanzy, H.; Langan, P. Crystal structure and hydrogen bonding system in cellulose I(alpha) from synchrotron X-ray and neutron fiber diffraction. *Journal of the American Chemical Society* **2003,** *125* (47), 14300–14306. DOI: 10.1021/ja037055w.

61. Dufresne, A. 1 Cellulose and potential reinforcement. In *Nanocellulose*; Dufresne, A., Ed.; De Gruyter, 2012, pp 1–42. DOI: 10.1515/9783110254600.1.

62. Jacobson, R. A.; Wunderlich, J. A.; Lipscomb, W. N. The crystal and molecular structure of cellobiose. *Acta Crystallographica* **1961,** *14* (6), 598–607. DOI: 10.1107/S0365110X61001893.

63. Meyer, K. H. Neue Wege in der organischen Strukturlehre und in der Erforschung hochpolymerer Verbindungen. *Zeitschrift für Angewandte Chemie* **1928,** *41* (34), 935–946. DOI: 10.1002/ange.19280413402.

64. Norman, N. Cylindrically symmetrical distribution functions and their application in the structure investigation of cellulose. *Acta Crystallographica* **1954,** *7* (5), 462–463. DOI: 10.1107/S0365110X54001442.

65. Viswanathan, A.; Shenouda, S. G. The helical structure of cellulose I. *Journal of Applied Polymer Science* **1971,** *15* (3), 519–535. DOI: 10.1002/app.1971.070150302.

66. French, A. D.; Johnson, G. P. Cellulose and the twofold screw axis: modeling and experimental arguments. *Cellulose* **2009,** *16* (6), 959–973. DOI: 10.1007/s10570-009-9347-4.

67. Khandelwal, M.; Windle, A. Origin of chiral interactions in cellulose supra-molecular microfibrils. *Carbohydrate polymers* **2014,** *106*, 128–131. DOI: 10.1016/j.carbpol.2014.01.050.

68. Bu, L.; Himmel, M. E.; Crowley, M. F. The molecular origins of twist in cellulose I-beta. *Carbohydrate polymers* **2015,** *125*, 146–152. DOI: 10.1016/j.carbpol.2015.02.023.

69. Blackwell, J. The Macromolecular Organization of Cellulose and Chitin. In *Cellulose and Other Natural Polymer Systems*; Brown, R. M., Ed.; Springer, 1982, pp 403–428. DOI: 10.1007/978-1-4684-1116-4_20.

70. Cousins, S. K.; Brown, R. M. Cellulose I microfibril assembly: computational molecular mechanics energy analysis favours bonding by van der Waals forces as the initial step in crystallization. *Polymer* **1995,** *36* (20), 3885–3888. DOI: 10.1016/0032-3861(95)99782-P.

71. Kovalenko, V. I. Crystalline cellulose: structure and hydrogen bonds. *Russian Chemical Reviews* **2010,** *79* (3), 231–241. DOI: 10.1070/RC2010v079n03ABEH004065.

72. Gardner, K. H.; Blackwell, J. The structure of native cellulose. *Biopolymers* **1974,** *13* (10), 1975–2001. DOI: 10.1002/bip.1974.360131005.

73. French, A. D.; Miller, D. P.; Aabloo, A. Miniature crystal models of cellulose polymorphs and other carbohydrates. *International Journal of Biological Macromolecules* **1993,** *15* (1), 30–36. DOI: 10.1016/s0141-8130(05)80085-6.

74. Gross, A. S.; Chu, J.-W. On the molecular origins of biomass recalcitrance: the interaction network and solvation structures of cellulose microfibrils. *The journal of physical chemistry. B* **2010,** *114* (42), 13333–13341. DOI: 10.1021/jp106452m.

75. Nishiyama, Y. Molecular interactions in nanocellulose assembly. *Philosophical transactions. Series A, Mathematical, physical, and engineering sciences* **2018,** *376* (2112). DOI: 10.1098/rsta.2017.0047.

76. Agarwal, U. P.; Ralph, S. A.; Reiner, R. S.; Baez, C. New cellulose crystallinity estimation method that differentiates between organized and crystalline phases. *Carbohydrate polymers* **2018,** *190*, 262–270. DOI: 10.1016/j.carbpol.2018.03.003.

77. Lindman, B.; Medronho, B.; Alves, L.; Costa, C.; Edlund, H.; Norgren, M. The relevance of structural features of cellulose and its interactions to dissolution, regeneration, gelation and plasticization phenomena. *Physical chemistry chemical physics : PCCP* **2017,** *19* (35), 23704–23718. DOI: 10.1039/C7CP02409F.

78. Baker, A. A.; Helbert, W.; Sugiyama, J.; Miles, M. J. High-Resolution Atomic Force Microscopy of Native Valonia Cellulose I Microcrystals. *Journal of structural biology* **1997,** *119* (2), 129–138. DOI: 10.1006/jsbi.1997.3866.

79. Atalla, R. H.; van der Hart, D. L. The role of solid state NMR spectroscopy in studies of the nature of native celluloses. *Solid State Nuclear Magnetic Resonance* **1999,** *15* (1), 1–19. DOI: 10.1016/S0926-2040(99)00042-9.

80. Atalla, R. H.; van der Hart, D. L. Native cellulose: a composite of two distinct crystalline forms. *Science (New York, N.Y.)* **1984,** *223* (4633), 283–285. DOI: 10.1126/science.223.4633.283.

81. O'Sullivan, A. C. Cellulose: the structure slowly unravels. *Cellulose* **1997,** *4* (3), 173–207. DOI: 10.1023/A:1018431705579.

82. Klemm, D. O.; Heublein, B.; Fink, H.-P.; Bohn, A. Cellulose: fascinating biopolymer and sustainable raw material. *Angewandte Chemie International Edition* **2005,** *44* (22), 3358–3393. DOI: 10.1002/anie.200460587.

83. Hieta, K.; Kuga, S.; Usuda, M. Electron staining of reducing ends evidences a parallel-chain structure inValonia cellulose. *Biopolymers* **1984,** *23* (10), 1807–1810. DOI: 10.1002/bip.360231002.

84. Kim, N.-H.; Imai, T.; Wada, M.; Sugiyama, J. Molecular directionality in cellulose polymorphs. *Biomacromolecules* **2006,** *7* (1), 274–280. DOI: 10.1021/bm0506391.

85. Kroon-Batenburg, L. M.; Kroon, J. The crystal and molecular structures of cellulose I and II. *Glycoconjugate journal* **1997,** *14* (5), 677–690. DOI: 10.1023/A:1018509231331.

86. Hess, K.; Trogus, C. Über Ammoniak-Cellulose (Vorläuf. Mitteil.). *Berichte der deutschen chemischen Gesellschaft (A and B Series)* **1935,** *68* (10), 1986–1988. DOI: 10.1002/cber.19350681016.

87. Marrinan, H. J.; Mann, J. Infrared spectra of the crystalline modifications of cellulose. *Journal of Polymer Science* **1956,** *21* (98), 301–311. DOI: 10.1002/pol.1956.120219812.

88. Hayashi, J.; Sufoka, A.; Ohkita, J.; Watanabe, S. The confirmation of existences of cellulose IIII, IIIII, IVI, and IVII by the X-ray method. *Journal of Polymer Science: Polymer Letters Edition* **1975,** *13* (1), 23–27. DOI: 10.1002/pol.1975.130130104.

89. Chanzy, H.; Henrissat, B.; Vincendon, M.; Tanner, S. F.; Belton, P. S. Solid-state 13C-N.M.R. and electron microscopy study on the reversible cellulose I→cellulose IIII transformation in Valonia. *Carbohydrate Research* **1987,** *160*, 1–11. DOI: 10.1016/0008-6215(87)80299-9.

90. Wada, M. In Situ Observation of the Crystalline Transformation from Cellulose III I to I β. *Macromolecules* **2001,** *34* (10), 3271–3275. DOI: 10.1021/ma0013354.

91. Sarko, A. Cellulose - How much do we know about its structure. In *Wood and cellulosics*: *Industrial utilisation, biotechnology, structure and properties*; Kennedy, J. F., Phillips, G. O., Williams, P. A., Eds.; Horwood, 1987, pp 55–70.

92. Sarko, A.; Southwick, J.; Hayashi, J. Packing Analysis of Carbohydrates and Polysaccharides. 7. Crystal Structure of Cellulose IIII and Its Relationship to Other Cellulose Polymorphs. *Macromolecules* **1976,** *9* (5), 857–863. DOI: 10.1021/ma60053a028.

93. Wada, M.; Nishiyama, Y.; Langan, P. X-ray Structure of Ammonia−Cellulose I: New Insights into the Conversion of Cellulose I to Cellulose III I. *Macromolecules* **2006,** *39* (8), 2947–2952. DOI: 10.1021/ma060228s.

94. Hutino, K.; Sakurada, I. Über die Existenz einer vierten Modifikation der Cellulose. *Die Naturwissenschaften* **1940,** *28* (36), 577–578. DOI: 10.1007/BF01483228.

95. Wada, M.; Heux, L.; Sugiyama, J. Polymorphism of cellulose I family: reinvestigation of cellulose IVI. *Biomacromolecules* **2004,** *5* (4), 1385–1391. DOI: 10.1021/bm0345357.

96. Newman, R. H. Simulation of X-ray diffractograms relevant to the purported polymorphs cellulose IVI and IVII. *Cellulose* **2008,** *15* (6), 769–778. DOI: 10.1007/s10570-008-9225-5.

97. Wada, M.; Ike, M.; Tokuyasu, K. Enzymatic hydrolysis of cellulose I is greatly accelerated via its conversion to the cellulose II hydrate form. *Polymer Degradation and Stability* **2010,** *95* (4), 543–548. DOI: 10.1016/j.polymdegradstab.2009.12.014.

98. Chundawat, S. P. S.; Bellesia, G.; Uppugundla, N.; Da Costa Sousa, L.; Gao, D.; Cheh, A. M.; Agarwal, U. P.; Bianchetti, C. M.; Phillips, G. N.; Langan, P.; Balan, V.; Gnanakaran, S.; Dale, B. E. Restructuring the crystalline cellulose hydrogen bond network enhances its depolymerization rate. *Journal of the American Chemical Society* **2011,** *133* (29), 11163–11174. DOI: 10.1021/ja2011115.

99. Nishino, T.; Takano, K.; Nakamae, K. Elastic modulus of the crystalline regions of cellulose polymorphs. *Journal of Polymer Science Part B: Polymer Physics* **1995,** *33* (11), 1647–1651. DOI: 10.1002/polb.1995.090331110.

100. Ishikawa, A.; Okano, T.; Sugiyama, J. Fine structure and tensile properties of ramie fibres in the crystalline form of cellulose I, II, IIII and IVI. *Polymer* **1997,** *38* (2), 463–468. DOI: 10.1016/S0032-3861(96)00516-2.

101. Moon, R. J.; Martini, A.; Nairn, J.; Simonsen, J.; Youngblood, J. Cellulose nanomaterials review: structure, properties and nanocomposites. *Chemical Society reviews* **2011,** *40* (7), 3941–3994. DOI: 10.1039/c0cs00108b.

102. Elias, H.-G. *An introduction to polymer science;* Wiley-VCH, 1997.

103. Glasser, W. G.; Atalla, R. H.; Blackwell, J.; Brown, R. M.; Burchard, W.; French, A. D.; Klemm, D. O.; Nishiyama, Y. About the structure of cellulose: debating the Lindman hypothesis. *Cellulose* **2012,** *19* (3), 589–598. DOI: 10.1007/s10570-012-9691-7.

104. Lindman, B.; Karlström, G.; Stigsson, L. On the mechanism of dissolution of cellulose. *Journal of Molecular Liquids* **2010,** *156* (1), 76–81. DOI: 10.1016/j.molliq.2010.04.016.

105. Medronho, B.; Romano, A.; Miguel, M. G.; Stigsson, L.; Lindman, B. Rationalizing cellulose (in)solubility: reviewing basic physicochemical aspects and role of hydrophobic interactions. *Cellulose* **2012,** *19* (3), 581–587. DOI: 10.1007/s10570-011-9644-6.

106. Zugenmaier, P. Introduction. In *Crystalline Cellulose and Derivatives*; Timell, T. E., Wimmer, R., Zugenmaier, P., Eds.; Springer Series in Wood Science; Springer, 2008, pp 1–6. DOI: 10.1007/978-3-540-73934-0_1.

107. McNamara, J. T.; Morgan, J. L. W.; Zimmer, J. A molecular description of cellulose biosynthesis. *Annual Review of Biochemistry* **2015,** *84,* 895–921. DOI: 10.1146/annurev-biochem-060614-033930.

108. Nevins, D. J. Sugars: their origin in photosynthesis and subsequent biological interconversions. *The American journal of clinical nutrition* **1995,** *61* (4), 915S-921S. DOI: 10.1093/ajcn/61.4.915S.

109. Kimura, S.; Itoh, T. New cellulose synthesizing complexes (terminal complexes) involved in animal cellulose biosynthesis in the tunicateMetandrocarpa uedai. *Protoplasma* **1996,** *194* (3-4), 151–163. DOI: 10.1007/BF01882023.

110. Koyama, M.; Sugiyama, J.; Itoh, T. Systematic survey on crystalline features of algal celluloses. *Cellulose* **1997,** *4* (2), 147–160. DOI: 10.1023/A:1018427604670.

111. Zugenmaier, P. Morphology. In *Crystalline Cellulose and Derivatives*; Timell, T. E., Wimmer, R., Zugenmaier, P., Eds.; Springer Series in Wood Science; Springer, 2008, pp 207–221. DOI: 10.1007/978-3-540-73934-0_7.

112. Nakashima, K.; Sugiyama, J.; Satoh, N. A spectroscopic assessment of cellulose and the molecular mechanisms of cellulose biosynthesis in the ascidian Ciona intestinalis. *Marine genomics* **2008,** *1* (1), 9–14. DOI: 10.1016/j.margen.2008.01.001.

113. Kubicki, J. D.; Yang, H.; Sawada, D.; O'Neill, H.; Oehme, D.; Cosgrove, D. The Shape of Native Plant Cellulose Microfibrils. *Scientific reports* **2018,** *8* (1), 13983. DOI: 10.1038/s41598-018-32211-w.

114. Casey, J. P. *Pulp and paper*, 3rd edition; Wiley-VCH, 1980.

115. Mark, R. E. *Cell Wall Mechanics of Tracheids;* Yale University Press, 1967.

116. Bergander, A.; Salmén, L. Cell wall properties and their effects on the mechanical properties of fibers. *Journal of Materials Science* **2002,** *37* (1), 151–156. DOI: 10.1023/A:1013115925679.

117. Jarvis, M. C. Structure of native cellulose microfibrils, the starting point for nanocellulose manufacture. *Philosophical transactions. Series A, Mathematical, physical, and engineering sciences* **2018,** *376* (2112). DOI: 10.1098/rsta.2017.0045.

118. Hallac, B. B.; Ragauskas, A. J. Analyzing cellulose degree of polymerization and its relevancy to cellulosic ethanol. *Biofuels, Bioproducts and Biorefining* **2011,** *5* (2), 215–225. DOI: 10.1002/bbb.269.

119. Nishiyama, Y.; Kim, U.-J.; Kim, D.-Y.; Katsumata, K. S.; May, R. P.; Langan, P. Periodic disorder along ramie cellulose microfibrils. *Biomacromolecules* **2003,** *4* (4), 1013–1017. DOI: 10.1021/bm025772x.

120. Wickholm, K.; Larsson, P. T.; Iversen, T. Assignment of non-crystalline forms in cellulose I by CP/MAS 13C NMR spectroscopy. *Carbohydrate Research* **1998,** *312* (3), 123–129. DOI: 10.1016/S0008-6215(98)00236-5.

121. Sturcová, A.; His, I.; Apperley, D. C.; Sugiyama, J.; Jarvis, M. C. Structural details of crystalline cellulose from higher plants. *Biomacromolecules* **2004,** *5* (4), 1333–1339. DOI: 10.1021/bm034517p.

122. Wang, T.; Yang, H.; Kubicki, J. D.; Hong, M. Cellulose Structural Polymorphism in Plant Primary Cell Walls Investigated by High-Field 2D Solid-State NMR Spectroscopy and Density Functional Theory Calculations. *Biomacromolecules* **2016,** *17* (6), 2210–2222. DOI: 10.1021/acs.biomac.6b00441.

123. Simmons, T. J.; Mortimer, J. C.; Bernardinelli, O. D.; Pöppler, A.-C.; Brown, S. P.; de Azevedo, E. R.; Dupree, R.; Dupree, P. Folding of xylan onto cellulose fibrils in plant cell walls revealed by solid-state NMR. *Nature communications* **2016,** *7*, 13902. DOI: 10.1038/ncomms13902.

124. Hearle, J. W. S. A fringed fibril theory of structure in crystalline polymers. *Journal of Polymer Science* **1958,** *28* (117), 432–435. DOI: 10.1002/pol.1958.1202811722.

125. Klemm, D. O.; Philipp, B.; Heinze, T. J.; Heinze, U.; Wagenknecht, W. General Considerations on Structure and Reactivity of Cellulose: Section 2.1.5–2.1.7.4. In *Comprehensive cellulose chemistry*; Klemm, D. O., Ed.; Wiley-VCH, 1998, pp 29–43. DOI: 10.1002/3527601929.ch2b.

126. Heux, L.; Dinand, E.; Vignon, M. R. Structural aspects in ultrathin cellulose microfibrils followed by 13C CP-MAS NMR. *Carbohydrate polymers* **1999,** *40* (2), 115–124. DOI: 10.1016/S0144-8617(99)00051-X.

127. Mondragon, G.; Fernandes, S.; Retegi, A.; Peña, C.; Algar, I.; Eceiza, A.; Arbelaiz, A. A common strategy to extracting cellulose nanoentities from different plants. *Industrial Crops and Products* **2014,** *55,* 140–148. DOI: 10.1016/j.indcrop.2014.02.014.

128. Yamanaka, S.; Watanabe, K.; Kitamura, N.; Iguchi, M.; Mitsuhashi, S.; Nishi, Y.; Uryu, M. The structure and mechanical properties of sheets prepared from bacterial cellulose. *Journal of Materials Science* **1989,** *24* (9), 3141–3145. DOI: 10.1007/BF01139032.

129. Sugiyama, J.; Persson, J.; Chanzy, H. Combined infrared and electron diffraction study of the polymorphism of native celluloses. *Macromolecules* **1991,** *24* (9), 2461–2466. DOI: 10.1021/ma00009a050.

130. Hanley, S. J.; Revol, J.-F.; Godbout, L.; Gray, D. G. Atomic force microscopy and transmission electron microscopy of cellulose from Micrasterias denticulata; evidence for a chiral helical microfibril twist. *Cellulose* **1997,** *4* (3), 209–220. DOI: 10.1023/A:1018483722417.

131. Jonas, R.; Farah, L. F. Production and application of microbial cellulose. *Polymer Degradation and Stability* **1998,** *59* (1-3), 101–106. DOI: 10.1016/S0141-3910(97)00197-3.

132. Iguchi, M.; Yamanaka, S.; Budhiono, A. Bacterial cellulose—a masterpiece of nature's arts. *Journal of Materials Science* **2000,** *35* (2), 261–270. DOI: 10.1023/A:1004775229149.

133. van den Berg, O.; Capadona, J. R.; Weder, C. Preparation of homogeneous dispersions of tunicate cellulose whiskers in organic solvents. *Biomacromolecules* **2007,** *8* (4), 1353–1357. DOI: 10.1021/bm061104q.

134. Robertson, G. P.; Hamilton, S. K.; Barham, B. L.; Dale, B. E.; Izaurralde, R. C.; Jackson, R. D.; Landis, D. A.; Swinton, S. M.; Thelen, K. D.; Tiedje, J. M. Cellulosic biofuel contributions to a sustainable energy future: Choices and outcomes. *Science (New York, N.Y.)* **2017,** *356* (6345). DOI: 10.1126/science.aal2324.

135. Heinze, T. J.; El Seoud, O. A.; Koschella, A. Principles of Cellulose Derivatization. In *Cellulose Derivatives*: *Synthesis, structure, and properties*; Heinze, T. J., El Seoud, O. A., Koschella, A., Eds.; Springer Series on Polymer and Composite Materials; Springer, 2018, pp 259–292. DOI: 10.1007/978-3-319-73168-1_4.

136. Liebert, T. F. Cellulose Solvents – Remarkable History, Bright Future. In *Cellulose Solvents: For Analysis, Shaping and Chemical Modification*; Liebert, T. F., Heinze, T. J., Edgar, K. J., Eds.; ACS Symposium Series; American Chemical Society, 2010, pp 3–54. DOI: 10.1021/bk-2010-1033.ch001.

137. Heinze, T. J.; Gericke, M. Ionic Liquids as Solvents for Homogeneous Derivatization of Cellulose: Challenges and Opportunities. In *Production of Biofuels and Chemicals with Ionic Liquids*; Fang, Z., Smith, J. R. L., Qi, X., Eds.; Biofuels and Biorefineries Vol. 1; Springer, 2014, pp 107–144. DOI: 10.1007/978-94-007-7711-8_5.

138. Heinze, T. J.; El Seoud, O. A.; Koschella, A. Production and Characteristics of Cellulose from Different Sources. In *Cellulose Derivatives*: *Synthesis, structure, and properties*; Heinze, T. J., El Seoud, O. A., Koschella, A., Eds.; Springer Series on Polymer and Composite Materials; Springer, 2018, pp 1–38. DOI: 10.1007/978-3-319-73168-1_1.

139. Thomas, B.; Raj, M. C.; Athira K.B.; Rubiyah M.H.; Joy, J.; Moores, A.; Drisko, G. L.; Sanchez, C. Nanocellulose, a Versatile Green Platform: From Biosources to Materials and Their Applications. *Chemical reviews* **2018,** *118* (24), 11575–11625. DOI: 10.1021/acs.chemrev.7b00627.

140. Eyley, S.; Thielemans, W. Surface modification of cellulose nanocrystals. *Nanoscale* **2014,** *6* (14), 7764–7779. DOI: 10.1039/c4nr01756k.

141. Moon, R. J.; Schueneman, G. T.; Simonsen, J. Overview of Cellulose Nanomaterials, Their Capabilities and Applications. *JOM* **2016,** *68* (9), 2383–2394. DOI: 10.1007/s11837-016-2018-7.

142. International Organization for Standardization. *DIN CEN ISO/TS 80004-1:2016 - Nanotechnologies - Vocabulary - Part 1: Core terms*, 2016 (80004). https://www.iso.org/standard/68058.html.

143. Kargarzadeh, H.; Ioelovich, M.; Ahmad, I.; Thomas, S.; Dufresne, A. Methods for Extraction of Nanocellulose from Various Sources. In *Handbook of Nanocellulose and Cellulose Nanocomposites*; Kargarzadeh, H., Ahmad, I., Thomas, S., Dufresne, A., Eds.; Wiley-VCH, 2017, pp 1–49. DOI: 10.1002/9783527689972.ch1.

144. Nickerson, R. F.; Habrle, J. A. Cellulose Intercrystalline Structure. *Industrial & Engineering Chemistry* **1947,** *39* (11), 1507–1512. DOI: 10.1021/ie50455a024.

145. Rånby, B. G.; Ribi, E. Über den Feinbau der Zellulose. *Experientia* **1950,** *6* (1), 12–14. DOI: 10.1007/BF02154044.

146. Siró, I.; Plackett, D. Microfibrillated cellulose and new nanocomposite materials: a review. *Cellulose* **2010,** *17* (3), 459–494. DOI: 10.1007/s10570-010-9405-y.

147. Ribeiro, R. S. A.; Pohlmann, B. C.; Calado, V.; Bojorge, N.; Pereira, N. Production of nanocellulose by enzymatic hydrolysis: Trends and challenges. *Engineering in life sciences* **2019,** *19* (4), 279–291. DOI: 10.1002/elsc.201800158.

148. Blanco, A.; Monte, M. C.; Campano, C.; Balea, A.; Merayo, N.; Negro, C. Nanocellulose for Industrial Use. In *Handbook of nanomaterials for industrial applications*; Hussain, C. M., Ed.; Micro & Nano technologies series; Elsevier, 2018, pp 74–126. DOI: 10.1016/B978-0-12-813351-4.00005-5.

149. Peng, B. L.; Dhar, N.; Liu, H. L.; Tam, K. C. Chemistry and applications of nanocrystalline cellulose and its derivatives: A nanotechnology perspective. *The Canadian Journal of Chemical Engineering* **2011,** *89* (5), 1191–1206. DOI: 10.1002/cjce.20554.

150. Jonoobi, M.; Oladi, R.; Davoudpour, Y.; Oksman, K.; Dufresne, A.; Hamzeh, Y.; Davoodi, R. Different preparation methods and properties of nanostructured cellulose from various natural resources and residues: a review. *Cellulose* **2015,** *22* (2), 935–969. DOI: 10.1007/s10570-015-0551-0.

151. Salas, C.; Nypelö, T.; Rodriguez-Abreu, C.; Carrillo, C.; Rojas, O. J. Nanocellulose properties and applications in colloids and interfaces. *Current Opinion in Colloid & Interface Science* **2014,** *19* (5), 383–396. DOI: 10.1016/j.cocis.2014.10.003.

152. Isogai, A. Wood nanocelluloses: fundamentals and applications as new bio-based nanomaterials. *Journal of Wood Science* **2013,** *59* (6), 449–459. DOI: 10.1007/s10086-013-1365-z.

153. Abitbol, T.; Rivkin, A.; Cao, Y.; Nevo, Y.; Abraham, E.; Ben-Shalom, T.; Lapidot, S.; Shoseyov, O. Nanocellulose, a tiny fiber with huge applications. *Current opinion in biotechnology* **2016,** *39*, 76–88. DOI: 10.1016/j.copbio.2016.01.002.

154. Kargarzadeh, H.; Mariano, M.; Huang, J.; Lin, N.; Ahmad, I.; Dufresne, A.; Thomas, S. Recent developments on nanocellulose reinforced polymer nanocomposites: A review. *Polymer* **2017,** *132*, 368–393. DOI: 10.1016/j.polymer.2017.09.043.

155. Mariano, M.; El Kissi, N.; Dufresne, A. Cellulose nanocrystals and related nanocomposites: Review of some properties and challenges. *Journal of Polymer Science Part B: Polymer Physics* **2014,** *52* (12), 791–806. DOI: 10.1002/polb.23490.

156. Trache, D.; Hussin, M. H.; Haafiz, M. K. M.; Thakur, V. K. Recent progress in cellulose nanocrystals: sources and production. *Nanoscale* **2017,** *9* (5), 1763–1786. DOI: 10.1039/c6nr09494e.

157. Habibi, Y.; Lucia, L. A.; Rojas, O. J. Cellulose nanocrystals: chemistry, self-assembly, and applications. *Chemical reviews* **2010,** *110* (6), 3479–3500. DOI: 10.1021/cr900339w.

158. Lagerwall, J. P. F.; Schütz, C.; Salajková, M.; Noh, J.; Hyun Park, J.; Scalia, G.; Bergström, L. Cellulose nanocrystal-based materials: from liquid crystal self-assembly and glass formation to multifunctional thin films. *NPG Asia Materials* **2014,** *6* (1), e80-e80. DOI: 10.1038/am.2013.69.

159. Rumpf, H. Über die Eigenschaften von Nutzstäuben. *Staub, Reinhaltung der Luft* **1967,** *27* (1), 3–13.

160. Krekel, J.; Polke, R. Qualitätssicherung bei der Verfahrensentwicklung. *Chemie Ingenieur Technik* **1992,** *64* (6), 528–535. DOI: 10.1002/cite.330640609.

161. Rånby, B. G. The cellulose micelles. *TAPPI Journal* **1952,** *35*, 53–58.

162. Rånby, B. G. Fibrous macromolecular systems. Cellulose and muscle. The colloidal properties of cellulose micelles. *Discuss. Faraday Soc.* **1951,** *11* (0), 158–164. DOI: 10.1039/DF9511100158.

163. Rånby, B. G.; Banderet, A.; Sillén, L. G. Aqueous Colloidal Solutions of Cellulose Micelles. *Acta Chemica Scandinavica* **1949,** *3*, 649–650. DOI: 10.3891/acta.chem.scand.03-0649.

164. Rånby, B. G. Über die Feinstruktur der nativen Cellulosefasern. *Die Makromolekulare Chemie* **1954,** *13* (1), 40–52. DOI: 10.1002/macp.1954.020130106.

165. Visanko, M.; Liimatainen, H.; Sirviö, J. A.; Heiskanen, J. P.; Niinimäki, J.; Hormi, O. Amphiphilic cellulose nanocrystals from acid-free oxidative treatment: physicochemical characteristics and use as an oil-water stabilizer. *Biomacromolecules* **2014,** *15* (7), 2769–2775. DOI: 10.1021/bm500628g.

166. Hayashi, N.; Kondo, T.; Ishihara, M. Enzymatically produced nano-ordered short elements containing cellulose Iβ crystalline domains. *Carbohydrate polymers* **2005,** *61* (2), 191–197. DOI: 10.1016/j.carbpol.2005.04.018.

167. Araki, J.; Wada, M.; Kuga, S.; Okano, T. Flow properties of microcrystalline cellulose suspension prepared by acid treatment of native cellulose. *Colloids and Surfaces A: Physicochemical and Engineering Aspects* **1998,** *142* (1), 75–82. DOI: 10.1016/S0927-7757(98)00404-X.

168. Camarero-Espinosa, S.; Kuhnt, T.; Foster, E. J.; Weder, C. Isolation of thermally stable cellulose nanocrystals by phosphoric acid hydrolysis. *Biomacromolecules* **2013,** *14* (4), 1223–1230. DOI: 10.1021/bm400219u.

169. Nelson, K.; Retsina, T. Innovative nanocellulose process breaks the cost barrier. *TAPPI Journal* **2014,** *13* (5), 19–23. DOI: 10.32964/TJ13.5.19.

170. Lu, Q.; Cai, Z.; Lin, F.; Tang, L.; Wang, S.; Huang, B. Extraction of Cellulose Nanocrystals with a High Yield of 88% by Simultaneous Mechanochemical Activation and Phosphotungstic Acid Hydrolysis. *ACS Sustainable Chemistry & Engineering* **2016,** *4* (4), 2165–2172. DOI: 10.1021/acssuschemeng.5b01620.

171. Dong, X. M.; Revol, J.-F.; Gray, D. G. Effect of microcrystallite preparation conditions on the formation of colloid crystals of cellulose. *Cellulose* **1998,** *5* (1), 19–32. DOI: 10.1023/A:1009260511939.

172. Beck-Candanedo, S.; Roman, M.; Gray, D. G. Effect of reaction conditions on the properties and behavior of wood cellulose nanocrystal suspensions. *Biomacromolecules* **2005,** *6* (2), 1048–1054. DOI: 10.1021/bm049300p.

173. Bondeson, D.; Mathew, A.; Oksman, K. Optimization of the isolation of nanocrystals from microcrystalline cellulose by acid hydrolysis. *Cellulose* **2006,** *13* (2), 171–180. DOI: 10.1007/s10570-006-9061-4.

174. Hamad, W. Y.; Hu, T. Q. Structure-process-yield interrelations in nanocrystalline cellulose extraction. *The Canadian Journal of Chemical Engineering* **2010**, n/a-n/a. DOI: 10.1002/cjce.20298.

175. Kargarzadeh, H.; Ahmad, I.; Abdullah, I.; Dufresne, A.; Zainudin, S. Y.; Sheltami, R. M. Effects of hydrolysis conditions on the morphology, crystallinity, and thermal stability of cellulose nanocrystals extracted from kenaf bast fibers. *Cellulose* **2012,** *19* (3), 855–866. DOI: 10.1007/s10570-012-9684-6.

176. Wang, Q. Q.; Zhu, J. Y.; Reiner, R. S.; Verrill, S. P.; Baxa, U.; McNeil, S. E. Approaching zero cellulose loss in cellulose nanocrystal (CNC) production: recovery and characterization of cellulosic solid residues (CSR) and CNC. *Cellulose* **2012,** *19* (6), 2033–2047. DOI: 10.1007/s10570-012-9765-6.

177. Wang, Q.; Zhao, X.; Zhu, J. Y. Kinetics of Strong Acid Hydrolysis of a Bleached Kraft Pulp for Producing Cellulose Nanocrystals (CNCs). *Industrial & Engineering Chemistry Research* **2014,** *53* (27), 11007–11014. DOI: 10.1021/ie501672m.

178. Chen, L.; Wang, Q.; Hirth, K.; Baez, C.; Agarwal, U. P.; Zhu, J. Y. Tailoring the yield and characteristics of wood cellulose nanocrystals (CNC) using concentrated acid hydrolysis. *Cellulose* **2015,** *22* (3), 1753–1762. DOI: 10.1007/s10570-015-0615-1.

179. Bouchard, J.; Méthot, M.; Fraschini, C.; Beck, S. Effect of oligosaccharide deposition on the surface of cellulose nanocrystals as a function of acid hydrolysis temperature. *Cellulose* **2016,** *23* (6), 3555–3567. DOI: 10.1007/s10570-016-1036-5.

180. Vanderfleet, O. M.; Osorio, D. A.; Cranston, E. D. Optimization of cellulose nanocrystal length and surface charge density through phosphoric acid hydrolysis. *Philosophical transactions. Series A, Mathematical, physical, and engineering sciences* **2018,** *376* (2112). DOI: 10.1098/rsta.2017.0041.

181. Dong, S.; Bortner, M. J.; Roman, M. Analysis of the sulfuric acid hydrolysis of wood pulp for cellulose nanocrystal production: A central composite design study. *Industrial Crops and Products* **2016,** *93*, 76–87. DOI: 10.1016/j.indcrop.2016.01.048.

182. Xie, H.; Du, H.; Yang, X.; Si, C. Recent Strategies in Preparation of Cellulose Nanocrystals and Cellulose Nanofibrils Derived from Raw Cellulose Materials. *International Journal of Polymer Science* **2018,** *2018*, 1–25. DOI: 10.1155/2018/7923068.

183. Cao, X.; Dong, H.; Li, C. M. New nanocomposite materials reinforced with flax cellulose nanocrystals in waterborne polyurethane. *Biomacromolecules* **2007,** *8* (3), 899–904. DOI: 10.1021/bm0610368.

184. Favier, V.; Chanzy, H.; Cavaille, J. Y. Polymer Nanocomposites Reinforced by Cellulose Whiskers. *Macromolecules* **1995,** *28* (18), 6365–6367. DOI: 10.1021/ma00122a053.

185. Sacui, I. A.; Nieuwendaal, R. C.; Burnett, D. J.; Stranick, S. J.; Jorfi, M.; Weder, C.; Foster, E. J.; Olsson, R. T.; Gilman, J. W. Comparison of the properties of cellulose nanocrystals and cellulose nanofibrils isolated from bacteria, tunicate, and wood processed using acid, enzymatic, mechanical, and oxidative methods. *ACS Applied Materials & Interfaces* **2014,** *6* (9), 6127–6138. DOI: 10.1021/am500359f.

186. Wang, Z.; Yao, Z.; Zhou, J.; Zhang, Y. Reuse of waste cotton cloth for the extraction of cellulose nanocrystals. *Carbohydrate polymers* **2017,** *157*, 945–952. DOI: 10.1016/j.carbpol.2016.10.044.

187. Brito, B. S. L.; Pereira, F. V.; Putaux, J.-L.; Jean, B. Preparation, morphology and structure of cellulose nanocrystals from bamboo fibers. *Cellulose* **2012,** *19* (5), 1527–1536. DOI: 10.1007/s10570-012-9738-9.

188. Nascimento, S. A.; Rezende, C. A. Combined approaches to obtain cellulose nanocrystals, nanofibrils and fermentable sugars from elephant grass. *Carbohydrate polymers* **2018,** *180*, 38–45. DOI: 10.1016/j.carbpol.2017.09.099.

189. Le Normand, M.; Moriana, R.; Ek, M. Isolation and characterization of cellulose nanocrystals from spruce bark in a biorefinery perspective. *Carbohydrate polymers* **2014,** *111*, 979–987. DOI: 10.1016/j.carbpol.2014.04.092.

190. Bano, S.; Negi, Y. S. Studies on cellulose nanocrystals isolated from groundnut shells. *Carbohydrate polymers* **2017,** *157*, 1041–1049. DOI: 10.1016/j.carbpol.2016.10.069.

191. Jiang, F.; Hsieh, Y.-L. Cellulose nanocrystal isolation from tomato peels and assembled nanofibers. *Carbohydrate polymers* **2015,** *122*, 60–68. DOI: 10.1016/j.carbpol.2014.12.064.

192. Luzi, F.; Fortunati, E.; Puglia, D.; Lavorgna, M.; Santulli, C.; Kenny, J. M.; Torre, L. Optimized extraction of cellulose nanocrystals from pristine and carded hemp fibres. *Industrial Crops and Products* **2014,** *56*, 175–186. DOI: 10.1016/j.indcrop.2014.03.006.

193. Mueller, S.; Weder, C.; Foster, E. J. Isolation of cellulose nanocrystals from pseudostems of banana plants. *RSC Adv* **2014,** *4* (2), 907–915. DOI: 10.1039/C3RA46390G.

194. Marett, J.; Aning, A.; Foster, E. J. The isolation of cellulose nanocrystals from pistachio shells via acid hydrolysis. *Industrial Crops and Products* **2017,** *109*, 869–874. DOI: 10.1016/j.indcrop.2017.09.039.

195. Chanzy, H.; Henrissat, B. Electron microscopy study of the enzymic hydrolysis of Valonia cellulose. *Carbohydrate polymers* **1983,** *3* (3), 161–173. DOI: 10.1016/0144-8617(83)90016-4.

196. Roman, M.; Winter, W. T. Effect of sulfate groups from sulfuric acid hydrolysis on the thermal degradation behavior of bacterial cellulose. *Biomacromolecules* **2004,** *5* (5), 1671–1677. DOI: 10.1021/bm034519+.

197. Habibi, Y.; Goffin, A.-L.; Schiltz, N.; Duquesne, E.; Dubois, P.; Dufresne, A. Bionanocomposites based on poly(ε-caprolactone)-grafted cellulose nanocrystals by ring-opening polymerization. *Journal of Materials Chemistry* **2008,** *18* (41), 5002. DOI: 10.1039/b809212e.

198. Melikoğlu, A. Y.; Bilek, S. E.; Cesur, S. Optimum alkaline treatment parameters for the extraction of cellulose and production of cellulose nanocrystals from apple pomace. *Carbohydrate polymers* **2019,** *215*, 330–337. DOI: 10.1016/j.carbpol.2019.03.103.

199. Collazo-Bigliardi, S.; Ortega-Toro, R.; Chiralt Boix, A. Isolation and characterisation of microcrystalline cellulose and cellulose nanocrystals from coffee husk and comparative study with rice husk. *Carbohydrate polymers* **2018,** *191*, 205–215. DOI: 10.1016/j.carbpol.2018.03.022.

200. Silvério, H. A.; Flauzino Neto, W. P.; Dantas, N. O.; Pasquini, D. Extraction and characterization of cellulose nanocrystals from corncob for application as reinforcing agent in nanocomposites. *Industrial Crops and Products* **2013,** *44*, 427–436. DOI: 10.1016/j.indcrop.2012.10.014.

201. Kallel, F.; Bettaieb, F.; Khiari, R.; García, A.; Bras, J.; Chaabouni, S. E. Isolation and structural characterization of cellulose nanocrystals extracted from garlic straw residues. *Industrial Crops and Products* **2016,** *87*, 287–296. DOI: 10.1016/j.indcrop.2016.04.060.

202. Henrique, M. A.; Silvério, H. A.; Flauzino Neto, W. P.; Pasquini, D. Valorization of an agro-industrial waste, mango seed, by the extraction and characterization of its cellulose nanocrystals. *Journal of environmental management* **2013,** *121*, 202–209. DOI: 10.1016/j.jenvman.2013.02.054.

203. Wijaya, C. J.; Saputra, S. N.; Soetaredjo, F. E.; Putro, J. N.; Lin, C. X.; Kurniawan, A.; Ju, Y.-H.; Ismadji, S. Cellulose nanocrystals from passion fruit peels waste as antibiotic drug carrier. *Carbohydrate polymers* **2017,** *175*, 370–376. DOI: 10.1016/j.carbpol.2017.08.004.

204. Santos, R. M. d.; Flauzino Neto, W. P.; Silvério, H. A.; Martins, D. F.; Dantas, N. O.; Pasquini, D. Cellulose nanocrystals from pineapple leaf, a new approach for the reuse of this agro-waste. *Industrial Crops and Products* **2013,** *50*, 707–714. DOI: 10.1016/j.indcrop.2013.08.049.

205. Chen, D.; Lawton, D.; Thompson, M. R.; Liu, Q. Biocomposites reinforced with cellulose nanocrystals derived from potato peel waste. *Carbohydrate polymers* **2012,** *90* (1), 709–716. DOI: 10.1016/j.carbpol.2012.06.002.

206. Johar, N.; Ahmad, I.; Dufresne, A. Extraction, preparation and characterization of cellulose fibres and nanocrystals from rice husk. *Industrial Crops and Products* **2012,** *37* (1), 93–99. DOI: 10.1016/j.indcrop.2011.12.016.

207. Flauzino Neto, W. P.; Silvério, H. A.; Dantas, N. O.; Pasquini, D. Extraction and characterization of cellulose nanocrystals from agro-industrial residue – Soy hulls. *Industrial Crops and Products* **2013,** *42*, 480–488. DOI: 10.1016/j.indcrop.2012.06.041.

208. Teixeira, E. d. M.; Bondancia, T. J.; Teodoro, K. B. R.; Corrêa, A. C.; Marconcini, J. M.; Mattoso, L. H. C. Sugarcane bagasse whiskers: Extraction and characterizations. *Industrial Crops and Products* **2011,** *33* (1), 63–66. DOI: 10.1016/j.indcrop.2010.08.009.

209. Yoshiharu, N.; Shigenori, K.; Masahisa, W.; Takeshi, O. Cellulose Microcrystal Film of High Uniaxial Orientation. *Macromolecules* **1997,** *30* (20), 6395–6397. DOI: 10.1021/ma970503y.

210. El Achaby, M.; Kassab, Z.; Aboulkas, A.; Gaillard, C.; Barakat, A. Reuse of red algae waste for the production of cellulose nanocrystals and its application in polymer nanocomposites. *International Journal of Biological Macromolecules* **2018,** *106*, 681–691. DOI: 10.1016/j.ijbiomac.2017.08.067.

211. Sheltami, R. M.; Abdullah, I.; Ahmad, I.; Dufresne, A.; Kargarzadeh, H. Extraction of cellulose nanocrystals from mengkuang leaves (Pandanus tectorius). *Carbohydrate polymers* **2012,** *88* (2), 772–779. DOI: 10.1016/j.carbpol.2012.01.062.

212. Cudjoe, E.; Hunsen, M.; Xue, Z.; Way, A. E.; Barrios, E.; Olson, R. A.; Hore, M. J. A.; Rowan, S. J. Miscanthus Giganteus: A commercially viable sustainable source of cellulose nanocrystals. *Carbohydrate polymers* **2017,** *155*, 230–241. DOI: 10.1016/j.carbpol.2016.08.049.

213. Garcia de Rodriguez, N. L.; Thielemans, W.; Dufresne, A. Sisal cellulose whiskers reinforced polyvinyl acetate nanocomposites. *Cellulose* **2006,** *13* (3), 261–270. DOI: 10.1007/s10570-005-9039-7.

214. Li, R.; Fei, J.; Cai, Y.; Li, Y.; Feng, J.; Yao, J. Cellulose whiskers extracted from mulberry: A novel biomass production. *Carbohydrate polymers* **2009,** *76* (1), 94–99. DOI: 10.1016/j.carbpol.2008.09.034.

215. Shaheen, T. I.; Emam, H. E. Sono-chemical synthesis of cellulose nanocrystals from wood sawdust using Acid hydrolysis. *International Journal of Biological Macromolecules* **2018,** *107* (Pt B), 1599–1606. DOI: 10.1016/j.ijbiomac.2017.10.028.

216. Rosa, M. F.; Medeiros, E. S.; Malmonge, J. A.; Gregorski, K. S.; Wood, D. F.; Mattoso, L. H. C.; Glenn, G.; Orts, W. J.; Imam, S. H. Cellulose nanowhiskers from coconut husk fibers: Effect of preparation conditions on their thermal and morphological behavior. *Carbohydrate polymers* **2010,** *81* (1), 83–92. DOI: 10.1016/j.carbpol.2010.01.059.

217. Rhim, J.-W.; Reddy, J. P.; Luo, X. Isolation of cellulose nanocrystals from onion skin and their utilization for the preparation of agar-based bio-nanocomposites films. *Cellulose* **2015,** *22* (1), 407–420. DOI: 10.1007/s10570-014-0517-7.

218. Dai, H.; Ou, S.; Huang, Y.; Huang, H. Utilization of pineapple peel for production of nanocellulose and film application. *Cellulose* **2018,** *25* (3), 1743–1756. DOI: 10.1007/s10570-018-1671-0.

219. Lu, P.; Hsieh, Y.-L. Preparation and characterization of cellulose nanocrystals from rice straw. *Carbohydrate polymers* **2012,** *87* (1), 564–573. DOI: 10.1016/j.carbpol.2011.08.022.

220. César, N. R.; Pereira-da-Silva, M. A.; Botaro, V. R.; Menezes, A. J. de. Cellulose nanocrystals from natural fiber of the macrophyte Typha domingensis: extraction and characterization. *Cellulose* **2015,** *22* (1), 449–460. DOI: 10.1007/s10570-014-0533-7.

221. Fortunati, E.; Luzi, F.; Jiménez, A.; Gopakumar, D. A.; Puglia, D.; Thomas, S.; Kenny, J. M.; Chiralt, A.; Torre, L. Revalorization of sunflower stalks as novel sources of cellulose nanofibrils and nanocrystals and their effect on wheat gluten bionanocomposite properties. *Carbohydrate polymers* **2016,** *149*, 357–368. DOI: 10.1016/j.carbpol.2016.04.120.

222. Cao, X.; Ding, B.; Yu, J.; Al-Deyab, S. S. Cellulose nanowhiskers extracted from TEMPO-oxidized jute fibers. *Carbohydrate polymers* **2012,** *90* (2), 1075–1080. DOI: 10.1016/j.carbpol.2012.06.046.

223. Zhao, X.; Zhou, Y.; Liu, D. Kinetic model for glycan hydrolysis and formation of monosaccharides during dilute acid hydrolysis of sugarcane bagasse. *Bioresource Technology* **2012,** *105*, 160–168. DOI: 10.1016/j.biortech.2011.11.075.

224. Fengel, D.; Wegener, G. Reactions in Acidic Medium. In *Wood: Chemistry, ultrastructure, reactions*; Fengel, D., Wegener, G., Eds.; De Gruyter, 1983, pp 268–295.

225. Xiang, Q.; Lee, Y. Y.; Pettersson, P. O.; Torget, R. W. Heterogeneous Aspects of Acid Hydrolysis of α-Cellulose. In *Biotechnology for Fuels and Chemicals*; Davison, B. H., Lee, J. W., Finkelstein, M., McMillan, J. D., Eds.; Humana Press, 2003, pp 505–514. DOI: 10.1007/978-1-4612-0057-4_42.

226. Timell, T. E. The acid hydrolysis of glycosides: I. General conditions and the effect of the nature of the aglycone. *Canadian Journal of Chemistry* **1964,** *42* (6), 1456–1472. DOI: 10.1139/v64-221.

227. Philipp, B.; Jacopian, V.; Loth, F.; Hirte, W.; Schulz, G. Influence of Cellulose Physical Structure on Thermohydrolytic, Hydrolytic, and Enzymatic Degradation of Cellulose **1979,** *181*, 127–143. DOI: 10.1021/ba-1979-0181.ch006.

228. Nickerson, R. Hydrolysis and Catalytic Oxidation of Cellulosic Materials: A Method for continuous Estimation of Free Glucose. *Industrial & Engineering Chemistry Analytical Edition* **1941,** *13* (6), 423–426. DOI: 10.1021/i560094a020.

229. Chami Khazraji, A.; Robert, S. Interaction Effects between Cellulose and Water in Nanocrystalline and Amorphous Regions: A Novel Approach Using Molecular Modeling. *Journal of Nanomaterials* **2013,** *2013*, 1–10. DOI: 10.1155/2013/409676.

230. Mann, J.; Marrinan, H. J. The reaction between cellulose and heavy water. Part 1. A qualitative study by infra-red spectroscopy. *Transactions of the Faraday Society* **1956,** *52*, 481. DOI: 10.1039/TF9565200481.

231. Mann, J.; Marrinan, H. J. The reaction between cellulose and heavy water. Part 2.—Measurement of absolute accessibility and crystallinity. *Transactions of the Faraday Society* **1956,** *52* (0), 487–492. DOI: 10.1039/TF9565200487.

232. Mann, J.; Marrinan, H. J. The reaction between cellulose and heavy water. Part 3.—A quantitative study by infra-red spectroscopy. *Transactions of the Faraday Society* **1956,** *52* (0), 492–497. DOI: 10.1039/TF9565200492.

233. Matthews, J. F.; Skopec, C. E.; Mason, P. E.; Zuccato, P.; Torget, R. W.; Sugiyama, J.; Himmel, M. E.; Brady, J. W. Computer simulation studies of microcrystalline cellulose Ibeta. *Carbohydrate Research* **2006,** *341* (1), 138–152. DOI: 10.1016/j.carres.2005.09.028.

234. Nickerson, R. F. Hydrolysis and Catalytic Oxidation of Cellulosic Materials. *Industrial & Engineering Chemistry* **1941,** *33* (8), 1022–1027. DOI: 10.1021/ie50380a013.

235. Saeman, J. F. Kinetics of Wood Saccharification - Hydrolysis of Cellulose and Decomposition of Sugars in Dilute Acid at High Temperature. *Industrial & Engineering Chemistry* **1945,** *37* (1), 43–52. DOI: 10.1021/ie50421a009.

236. Daruwalla, E. H.; Shet, R. T. Heterogeneous Acid Hydrolysis of Alpha-Cellulose from Sudanese Cotton. *Textile Research Journal* **1962,** *32* (11), 942–954. DOI: 10.1177/004051756203201110.

237. Nelson, M. L. Apparent activation energy of hydrolysis of some cellulosic materials. *Journal of Polymer Science* **1960,** *43* (142), 351–371. DOI: 10.1002/pol.1960.1204314207.

238. Xiang, Q.; Kim, J. S.; Lee, Y. Y. A Comprehensive Kinetic Model for Dilute-Acid Hydrolysis of Cellulose. *Applied Biochemistry and Biotechnology* **2003,** *106* (1-3), 337–352. DOI: 10.1385/ABAB:106:1-3:337.

239. Nickerson, R. F. Hydrolysis and Catalytic Oxidation of Cellulosic Materials. *Industrial & Engineering Chemistry* **1942,** *34* (1), 85–88. DOI: 10.1021/ie50385a017.

240. Nickerson, R. F. Hydrolysis and Catalytic Oxidation of Cellulosic Materials. *Industrial & Engineering Chemistry* **1942,** *34* (12), 1480–1485. DOI: 10.1021/ie50396a013.

241. Nickerson, R. F.; Habrle, J. A. Hydrolysis and Catalytic Oxidation of Cellulosic Materials. *Industrial & Engineering Chemistry* **1945,** *37* (11), 1115–1118. DOI: 10.1021/ie50431a028.

242. Nickerson, R. F.; Habrle, J. A. Hydrolysis and Catalytic Oxidation of Cellulosic Materials. *Industrial & Engineering Chemistry* **1946,** *38* (3), 299–301. DOI: 10.1021/ie50435a018.

243. Philipp, H. J.; Nelson, M. L.; Ziifle, H. M. Crystallinity of Cellulose Fibers as Determined by Acid Hydrolysis. *Textile Research Journal* **1947,** *17* (11), 585–596. DOI: 10.1177/004051754701701101.

244. Klemm, D. O. *Comprehensive Cellulose Chemistry, Volume 2*: *Functionalization of Cellulose*, Volume 2; Wiley-VCH, 1998. DOI: 10.1002/3527601937.

245. Spinella, S.; Maiorana, A.; Qian, Q.; Dawson, N. J.; Hepworth, V.; McCallum, S. A.; Ganesh, M.; Singer, K. D.; Gross, R. A. Concurrent Cellulose Hydrolysis and Esterification to Prepare a Surface-Modified Cellulose Nanocrystal Decorated with Carboxylic Acid Moieties. *ACS Sustainable Chemistry & Engineering* **2016,** *4* (3), 1538–1550. DOI: 10.1021/acssuschemeng.5b01489.

246. Herlinger; Hoffmann; Husemann; Istel; Kern; Krimm; Müller; Rinke; Schmitz-Josten; Schneider; Schulz; Spielberger; Wegler; Werner. IV. Umwandlung von Cellulose und Stärke (I). In *Makromolekulare Stoffe*; Herlinger, Hoffmann, Husemann, Istel, Kern, Krimm, Müller, Rinke, Schmitz-Josten, Schneider, Schulz, Spielberger, Wegler, Werner, Eds.; Georg Thieme Verlag, 1963. DOI: 10.1055/b-0035-116298.

247. Heinze, T. J.; Liebert, T. F.; Koschella, A. Inorganic Polysaccharide Esters. In *Esterification of polysaccharides*: *With 105 tables and CD-ROM*; Heinze, T. J., Liebert, T. F., Koschella, A., Eds.; Springer laboratory manuals in polymer science; Springer, 2006, pp 129–141. DOI: 10.1007/3-540-32112-8_7.

248. Rowland, S. P.; Howley, P. S. Hydrogen bonding on accessible surfaces of cellulose from various sources and relationship to order within crystalline regions. *Journal of Polymer Science Part A: Polymer Chemistry* **1988,** *26* (7), 1769–1778. DOI: 10.1002/pola.1988.080260708.

249. Verlhac, C.; Dedier, J.; Chanzy, H. Availability of surface hydroxyl groups in valonia and bacterial cellulose. *Journal of Polymer Science Part A: Polymer Chemistry* **1990,** *28* (5), 1171–1177. DOI: 10.1002/pola.1990.080280517.

250. Lemke, C. H.; Dong, R. Y.; Michal, C. A.; Hamad, W. Y. New insights into nano-crystalline cellulose structure and morphology based on solid-state NMR. *Cellulose* **2012,** *19* (5), 1619–1629. DOI: 10.1007/s10570-012-9759-4.

251. Phan-Xuan, T.; Thuresson, A.; Skepö, M.; Labrador, A.; Bordes, R.; Matic, A. Aggregation behavior of aqueous cellulose nanocrystals: the effect of inorganic salts. *Cellulose* **2016,** *23* (6), 3653–3663. DOI: 10.1007/s10570-016-1080-1.

252. Metzger, C.; Auber, D.; Dähnhardt-Pfeiffer, S.; Briesen, H. Agglomeration of cellulose nanocrystals: the effect of secondary sulfates and their use in product separation. *Cellulose* **2020,** *27* (17), 9839–9851. DOI: 10.1007/s10570-020-03476-0.

253. Reid, M. S.; Villalobos, M.; Cranston, E. D. Benchmarking Cellulose Nanocrystals: From the Laboratory to Industrial Production. *Langmuir : the ACS journal of surfaces and colloids* **2017,** *33* (7), 1583–1598. DOI: 10.1021/acs.langmuir.6b03765.

254. Marchessault, R. H.; Morehead, F. F.; Koch, M. Some hydrodynamic properties of neutral suspensions of cellulose crystallites as related to size and shape. *Journal of Colloid Science* **1961,** *16* (4), 327–344. DOI: 10.1016/0095-8522(61)90033-2.

255. Gicquel, E.; Bras, J.; Rey, C.; Putaux, J.-L.; Pignon, F.; Jean, B.; Martin, C. Impact of sonication on the rheological and colloidal properties of highly concentrated cellulose nanocrystal suspensions. *Cellulose* **2019,** *26* (13-14), 7619–7634. DOI: 10.1007/s10570-019-02622-7.

256. Abitbol, T.; Kloser, E.; Gray, D. G. Estimation of the surface sulfur content of cellulose nanocrystals prepared by sulfuric acid hydrolysis. *Cellulose* **2013,** *20* (2), 785–794. DOI: 10.1007/s10570-013-9871-0.

257. Beck, S.; Méthot, M.; Bouchard, J. General procedure for determining cellulose nanocrystal sulfate half-ester content by conductometric titration. *Cellulose* **2015,** *22* (1), 101–116. DOI: 10.1007/s10570-014-0513-y.

258. Reiner, R. S.; Rudie, A. W. Process scale-up of cellulose nanocrystal production to 25 kg per batch at the Forest Products Laboratory. In *Production and applications of cellulose nanomaterials*; Postek, M. T., Moon, R. J., Rudie, A. W., Bilodeau, M., Eds.; TAPPI Press, 2013, pp 21–24.

259. Jiang, F.; Esker, A. R.; Roman, M. Acid-catalyzed and solvolytic desulfation of H2SO4-hydrolyzed cellulose nanocrystals. *Langmuir : the ACS journal of surfaces and colloids* **2010,** *26* (23), 17919–17925. DOI: 10.1021/la1028405.

260. Beck, S.; Bouchard, J. Auto-catalyzed acidic desulfation of cellulose nanocrystals. *Nordic Pulp & Paper Research Journal* **2014,** *29* (1), 6–14. DOI: 10.3183/npprj-2014-29-01-p006-014.

261. Chen, M.; Parot, J.; Mukherjee, A.; Couillard, M.; Zou, S.; Hackley, V. A.; Johnston, L. J. Characterization of size and aggregation for cellulose nanocrystal dispersions separated by asymmetrical-flow field-flow fractionation. *Cellulose* **2020,** *27* (4), 2015–2028. DOI: 10.1007/s10570-019-02909-9.

262. Revol, J.-F.; Godbout, L.; Dong, X. M.; Gray, D. G.; Chanzy, H.; Maret, G. Chiral nematic suspensions of cellulose crystallites; phase separation and magnetic field orientation. *Liquid Crystals* **1994,** *16* (1), 127–134. DOI: 10.1080/02678299408036525.

263. Dong, X. M.; Gray, D. G. Effect of Counterions on Ordered Phase Formation in Suspensions of Charged Rodlike Cellulose Crystallites. *Langmuir : the ACS journal of surfaces and colloids* **1997,** *13* (8), 2404–2409. DOI: 10.1021/la960724h.

264. International Organization for Standardization. *ISO/CD TS 23151:2018 - Nanotechnologies — Particle size distribution for cellulose nanocrystals (under development)*, 2018 (23151). https://www.iso.org/standard/74742.html.

265. Metzger, C.; Drexel, R.; Meier, F.; Briesen, H. Effect of ultrasonication on the size distribution and stability of cellulose nanocrystals in suspension: an asymmetrical flow field-flow fractionation study. *Cellulose* **2021. DOI:** 10.1007/s10570-021-04172-3.

266. Metzger, C.; Sanahuja, S.; Behrends, L.; Sängerlaub, S.; Lindner, M.; Briesen, H. Efficiently Extracted Cellulose Nanocrystals and Starch Nanoparticles and Techno-Functional Properties of Films Made Thereof. Coatings, 8(4), 142. *Coatings* **2018,** *8* (4), 142. DOI: 10.3390/COATINGS8040142.

267. Müller, V.; Briesen, H. Nanocrystalline cellulose, its preparation and uses of such nanocrystalline cellulose: U.S. Patent 20170306056 A1.

268. Assis, C. A. de; Houtman, C.; Phillips, R.; Bilek, E. M.; Rojas, O. J.; Pal, L.; Peresin, M. S.; Jameel, H.; Gonzalez, R. Conversion Economics of Forest Biomaterials: Risk and Financial Analysis of CNC Manufacturing. *Biofuels, Bioproducts and Biorefining* **2017,** *11* (4), 682–700. DOI: 10.1002/bbb.1782.

269. Kontturi, E. Preparation of Cellulose Nanocrystals: Background, Conventions and New Developments. In *Nanocellulose and sustainability*: *Production, properties, applications, and case studies*; Lee, K.-Y., Ed.; Sustainability contributions through science and technology; CRC Press Taylor & Francis Group, 2018, pp 27–44.

270. Ioelovich, M. Study of Cellulose Interaction with Concentrated Solutions of Sulfuric Acid. *ISRN Chemical Engineering* **2012,** *2012*, 1–7. DOI: 10.5402/2012/428974.

271. Mukherjee, S. M.; Woods, H. J. X-ray and electron microscope studies of the degradation of cellulose by sulphuric acid. *Biochimica et Biophysica Acta* **1953,** *10*, 499–511. DOI: 10.1016/0006-3002(53)90295-9.

272. Sluiter, A.; Hames, B.; Ruiz, R.; Scarlata, C.; Sluiter, J.; Templeton, D.; Crocker, D. *Determination of Structural Carbohydrates and Lignin in Biomass*: *Laboratory Analytical Procedure (LAP)*. https://www.nrel.gov/docs/gen/fy11/42618.pdf.

273. Chum, H. L.; Johnson, D. K.; Black, S. K.; Overend, R. P. Pretreatment-Catalyst effects and the combined severity parameter. *Applied Biochemistry and Biotechnology* **1990,** *24-25* (1), 1–14. DOI: 10.1007/BF02920229.

274. Revol, J.-F.; Bradford, H.; Giasson, J.; Marchessault, R. H.; Gray, D. G. Helicoidal self-ordering of cellulose microfibrils in aqueous suspension. *International Journal of Biological Macromolecules* **1992,** *14* (3), 170–172. DOI: 10.1016/S0141-8130(05)80008-X.

275. Box, G. E. P.; Hunter, J. S.; Hunter, W. G. *Statistics for experimenters*: *Design, innovation, and discovery*, 2. ed.; Wiley series in probability and statistics; Wiley-Interscience, 2005.

276. Mason, R. L.; Gunst, R. F.; Hess, J. L. *Statistical design and analysis of experiments*: *With applications to engineering and science*, 2. ed.; Wiley series in probability and statistics; Wiley-Interscience, 2003. DOI: 10.1002/0471458503.

277. Milliken, G. A.; Johnson, D. E. *Analysis of Messy Data Volume 1;* Chapman and Hall/CRC, 2009. DOI: 10.1201/EBK1584883340.

278. Dean, A.; Voss, D.; Draguljić, D. *Design and analysis of experiments*, Second edition; Springer texts in statistics; Springer, 2017. DOI: 10.1007/978-3-319-52250-0.

279. Kandhola, G.; Djioleu, A.; Rajan, K.; Labbé, N.; Sakon, J.; Carrier, D. J.; Kim, J.-W. Maximizing production of cellulose nanocrystals and nanofibers from pre-extracted loblolly pine kraft pulp: a response surface approach. *Bioresources and Bioprocessing* **2020,** *7* (1). DOI: 10.1186/s40643-020-00302-0.

280. Thakur, M.; Sharma, A.; Ahlawat, V.; Bhattacharya, M.; Goswami, S. Process optimization for the production of cellulose nanocrystals from rice straw derived α-cellulose. *Materials Science for Energy Technologies* **2020,** *3*, 328–334. DOI: 10.1016/j.mset.2019.12.005.

281. Wijaya, C. J.; Ismadji, S.; Aparamarta, H. W.; Gunawan, S. Optimization of cellulose nanocrystals from bamboo shoots using Response Surface Methodology. *Heliyon* **2019,** *5* (11), e02807. DOI: 10.1016/j.heliyon.2019.e02807.

282. Kusmono; Listyanda, R. F.; Wildan, M. W.; Ilman, M. N. Preparation and characterization of cellulose nanocrystal extracted from ramie fibers by sulfuric acid hydrolysis. *Heliyon* **2020,** *6* (11), e05486. DOI: 10.1016/j.heliyon.2020.e05486.

283. Liu, W.; Du, H.; Liu, H.; Xie, H.; Xu, T.; Zhao, X.; Liu, Y.; Zhang, X.; Si, C. Highly Efficient and Sustainable Preparation of Carboxylic and Thermostable Cellulose Nanocrystals via FeCl 3 -Catalyzed Innocuous Citric Acid Hydrolysis. *ACS Sustainable Chemistry & Engineering* **2020,** *8* (44), 16691–16700. DOI: 10.1021/acssuschemeng.0c06561.

284. Beltramino, F.; Roncero, M. B.; Torres, A. L.; Vidal, T.; Valls, C. Optimization of sulfuric acid hydrolysis conditions for preparation of nanocrystalline cellulose from enzymatically pretreated fibers. *Cellulose* **2016,** *23* (3), 1777–1789. DOI: 10.1007/s10570-016-0897-y.

285. Ngo, T.-D.; Danumah, C.; Ahvazi, B. Production of Cellulose Nanocrystals at InnoTech Alberta. In *Nanocellulose and sustainability*: *Production, properties, applications, and case studies*; Lee, K.-Y., Ed.; Sustainability contributions through science and technology; CRC Press Taylor & Francis Group, 2018, pp 269–287.

286. *Alberta-Pacific Forest Industries (Accessed: 15 August 2021).* https://alpac.ca/.

287. *InnoTech Alberta (Accessed: 15 August 2021).* https://innotechalberta.ca/.

288. Elazzouzi-Hafraoui, S.; Nishiyama, Y.; Putaux, J.-L.; Heux, L.; Dubreuil, F.; Rochas, C. The shape and size distribution of crystalline nanoparticles prepared by acid hydrolysis of native cellulose. *Biomacromolecules* **2008,** *9* (1), 57–65. DOI: 10.1021/bm700769p.

289. Kontturi, E.; Vuorinen, T. Indirect evidence of supramolecular changes within cellulose microfibrils of chemical pulp fibers upon drying. *Cellulose* **2009,** *16* (1), 65–74. DOI: 10.1007/s10570-008-9235-3.

290. Niinivaara, E.; Faustini, M.; Tammelin, T.; Kontturi, E. Mimicking the Humidity Response of the Plant Cell Wall by Using Two-Dimensional Systems: The Critical Role of Amorphous and Crystalline Polysaccharides. *Langmuir : the ACS journal of surfaces and colloids* **2016,** *32* (8), 2032–2040. DOI: 10.1021/acs.langmuir.5b04264.

291. Hirai, A.; Inui, O.; Horii, F.; Tsuji, M. Phase separation behavior in aqueous suspensions of bacterial cellulose nanocrystals prepared by sulfuric acid treatment. *Langmuir : the ACS journal of surfaces and colloids* **2009,** *25* (1), 497–502. DOI: 10.1021/la802947m.

292. Vasconcelos, N. F.; Feitosa, J. P. A.; da Gama, F. M. P.; Morais, J. P. S.; Andrade, F. K.; Souza Filho, M. s. M. de; Rosa, M. d. F. Bacterial cellulose nanocrystals produced under different hydrolysis conditions: Properties and morphological features. *Carbohydrate polymers* **2017,** *155*, 425–431. DOI: 10.1016/j.carbpol.2016.08.090.

293. Jakubek, Z. J.; Chen, M.; Couillard, M.; Leng, T.; Liu, L.; Zou, S.; Baxa, U.; Clogston, J. D.; Hamad, W. Y.; Johnston, L. J. Characterization challenges for a cellulose nanocrystal reference material: dispersion and particle size distributions. *Journal of Nanoparticle Research* **2018,** *20* (4). DOI: 10.1007/s11051-018-4194-6.

294. Beuguel, Q.; Tavares, J. R.; Carreau, P. J.; Heuzey, M.-C. Ultrasonication of spray- and freeze-dried cellulose nanocrystals in water. *Journal of colloid and interface science* **2018,** *516*, 23–33. DOI: 10.1016/j.jcis.2018.01.035.

295. Brinkmann, A.; Chen, M.; Couillard, M.; Jakubek, Z. J.; Leng, T.; Johnston, L. J. Correlating Cellulose Nanocrystal Particle Size and Surface Area. *Langmuir : the ACS journal of surfaces and colloids* **2016,** *32* (24), 6105–6114. DOI: 10.1021/acs.langmuir.6b01376.

296. Daicho, K.; Saito, T.; Fujisawa, S.; Isogai, A. The Crystallinity of Nanocellulose: Dispersion-Induced Disordering of the Grain Boundary in Biologically Structured Cellulose. *ACS Applied Nano Materials* **2018,** *1* (10), 5774–5785. DOI: 10.1021/acsanm.8b01438.

297. Thygesen, A.; Oddershede, J.; Lilholt, H.; Thomsen, A. B.; Ståhl, K. On the determination of crystallinity and cellulose content in plant fibres. *Cellulose* **2005,** *12* (6), 563–576. DOI: 10.1007/s10570-005-9001-8.

298. Isogai, A.; Usuda, M. Crystallinity indexes of cellulosic materials. *Sen'i Gakkaishi* **1990,** *46* (8), 324–329. DOI: 10.2115/fiber.46.8_324.

299. Sèbe, G.; Ham-Pichavant, F.; Ibarboure, E.; Koffi, A. L. C.; Tingaut, P. Supramolecular structure characterization of cellulose II nanowhiskers produced by acid hydrolysis of cellulose I substrates. *Biomacromolecules* **2012**, 570–578. DOI: 10.1021/bm201777j.

300. Yamane, C.; Aoyagi, T.; Ago, M.; Sato, K.; Okajima, K.; Takahashi, T. Two Different Surface Properties of Regenerated Cellulose due to Structural Anisotropy. *Polymer Journal* **2006,** *38* (8), 819–826. DOI: 10.1295/polymj.PJ2005187.

301. Liu, D.; Chen, X.; Yue, Y.; Chen, M.; Wu, Q. Structure and rheology of nanocrystalline cellulose. *Carbohydrate polymers* **2011,** *84* (1), 316–322. DOI: 10.1016/j.carbpol.2010.11.039.

302. Debye, P.; Hückel, E. Zur Theorie der Elektrolyte. I. Gefrierpunktserniedrigung und verwandte Erscheinungen. *Physikalische Zeitschrift* **1923,** *24* (9), 185–206.

303. Evans, D. F.; Wennerström, H. *The colloidal domain*: *Where physics, chemistry, biology, and technology meet*, 2. ed.; Advances in interfacial engineering series; Wiley-VCH, 1999.

304. Derjaguin, B.; Landau, L. Theory of the stability of strongly charged lyophobic sols and of the adhesion of strongly charged particles in solutions of electrolytes. *Progress in Surface Science* **1993,** *43* (1-4), 30–59. DOI: 10.1016/0079-6816(93)90013-L.

305. Verwey, E. J. W. Theory of the stability of lyophobic colloids. *The Journal of physical and colloid chemistry* **1947,** *51* (3), 631–636. DOI: 10.1021/j150453a001.

306. Sparnaay, M. J. The interaction between two cylinder shaped colloidal particles. *Recueil des Travaux Chimiques des Pays-Bas* **1959,** *78* (9), 680–709. DOI: 10.1002/recl.19590780908.

307. Stigter, D. Interactions of highly charged colloidal cylinders with applications to double-stranded. *Biopolymers* **1977,** *16* (7), 1435–1448. DOI: 10.1002/bip.1977.360160705.

308. Israelachvili, J. N. *Intermolecular and surface forces*, 3. ed.; Academic Press, 2011.

309. Hamaker, H. C. The London—van der Waals attraction between spherical particles. *Physica* **1937,** *4* (10), 1058–1072. DOI: 10.1016/S0031-8914(37)80203-7.

310. Prathapan, R.; Thapa, R.; Garnier, G.; Tabor, R. F. Modulating the zeta potential of cellulose nanocrystals using salts and surfactants. *Colloids and Surfaces A: Physicochemical and Engineering Aspects* **2016,** *509*, 11–18. DOI: 10.1016/j.colsurfa.2016.08.075.

311. Araki, J.; Wada, M.; Kuga, S.; Okano, T. Influence of surface charge on viscosity behavior of cellulose microcrystal suspension. *Journal of Wood Science* **1999,** *45* (3), 258–261. DOI: 10.1007/BF01177736.

312. Hansen, C. M. *Hansen solubility parameters*: *A user's handbook*, 2nd ed.; Taylor & Francis, 2007.

313. Bruel, C.; Tavares, J. R.; Carreau, P. J.; Heuzey, M.-C. The structural amphiphilicity of cellulose nanocrystals characterized from their cohesion parameters. *Carbohydrate polymers* **2019**, 184–191. DOI: 10.1016/j.carbpol.2018.10.026.

314. Gårdebjer, S.; Andersson, M.; Engström, J.; Restorp, P.; Persson, M.; Larsson, A. Using Hansen solubility parameters to predict the dispersion of nano-particles in polymeric films. *Polymer Chemistry* **2016,** *7* (9), 1756–1764. DOI: 10.1039/C5PY01935D.

315. Min, Y.; Akbulut, M.; Kristiansen, K.; Golan, Y.; Israelachvili, J. The role of interparticle and external forces in nanoparticle assembly. *Nature materials* **2008,** *7* (7), 527–538. DOI: 10.1038/nmat2206.

316. Bruel, C.; Davies, T. S.; Carreau, P. J.; Tavares, J. R.; Heuzey, M.-C. Self-assembly behaviors of colloidal cellulose nanocrystals: A tale of stabilization mechanisms. *Journal of colloid and interface science* **2020**, 399–409. DOI: 10.1016/j.jcis.2020.04.049.

317. Esparza, Y.; Ngo, T.-D.; Fraschini, C.; Boluk, Y. Aggregate Morphology and Aqueous Dispersibility of Spray-Dried Powders of Cellulose Nanocrystals. *Industrial & Engineering Chemistry Research* **2019,** *58* (43), 19926–19936. DOI: 10.1021/acs.iecr.9b03951.

318. Honorato-Rios, C.; Lehr, C.; Schütz, C.; Sanctuary, R.; Osipov, M. A.; Baller, J.; Lagerwall, J. P. F. Fractionation of cellulose nanocrystals: enhancing liquid crystal ordering without promoting gelation. *NPG Asia Materials* **2018,** *10* (5), 455–465. DOI: 10.1038/s41427-018-0046-1.

319. Zimmermann, M. V. G.; Borsoi, C.; Lavoratti, A.; Zanini, M.; Zattera, A. J.; Santana, R. M. C. Drying techniques applied to cellulose nanofibers. *Journal of Reinforced Plastics and Composites* **2016,** *35* (8), 628–643. DOI: 10.1177/0731684415626286.

320. Fernandes Diniz, J. M. B.; Gil, M. H.; Castro, J. A. A. M. Hornification?its origin and interpretation in wood pulps. *Wood Science and Technology* **2004,** *37* (6), 489–494. DOI: 10.1007/s00226-003-0216-2.

321. Sokolov, S. V.; Tschulik, K.; Batchelor-McAuley, C.; Jurkschat, K.; Compton, R. G. Reversible or not? Distinguishing agglomeration and aggregation at the nanoscale. *Analytical chemistry* **2015,** *87* (19), 10033–10039. DOI: 10.1021/acs.analchem.5b02639.

322. Peng, Y.; Gardner, D. J.; Han, Y. Drying cellulose nanofibrils: in search of a suitable method. *Cellulose* **2012,** *19* (1), 91–102. DOI: 10.1007/s10570-011-9630-z.

323. Voronova, M. I.; Zakharov, A. G.; Kuznetsov, O. Y.; Surov, O. V. The effect of drying technique of nanocellulose dispersions on properties of dried materials. *Materials Letters* **2012,** *68*, 164–167. DOI: 10.1016/j.matlet.2011.09.115.

324. Quiévy, N.; Jacquet, N.; Sclavons, M.; Deroanne, C.; Paquot, M.; Devaux, J. Influence of homogenization and drying on the thermal stability of microfibrillated cellulose. *Polymer Degradation and Stability* **2010,** *95* (3), 306–314. DOI: 10.1016/j.polymdegradstab.2009.11.020.

325. Han, J.; Zhou, C.; Wu, Y.; Liu, F.; Wu, Q. Self-assembling behavior of cellulose nanoparticles during freeze-drying: effect of suspension concentration, particle size, crystal structure, and surface charge. *Biomacromolecules* **2013,** *14* (5), 1529–1540. DOI: 10.1021/bm4001734.

326. Ng, H.-M.; Sin, L. T.; Tee, T.-T.; Bee, S.-T.; Hui, D.; Low, C.-Y.; Rahmat, A. R. Extraction of cellulose nanocrystals from plant sources for application as reinforcing agent in polymers. *Composites Part B: Engineering* **2015,** *75*, 176–200. DOI: 10.1016/j.compositesb.2015.01.008.

327. Herrero, M.; Cifuentes, A.; Ibanez, E. Sub- and supercritical fluid extraction of functional ingredients from different natural sources: Plants, food-by-products, algae and microalgaeA review. *Food Chemistry* **2006,** *98* (1), 136–148. DOI: 10.1016/j.foodchem.2005.05.058.

328. Khoshkava, V.; Kamal, M. R. Effect of drying conditions on cellulose nanocrystal (CNC) agglomerate porosity and dispersibility in polymer nanocomposites. *Powder Technology* **2014,** *261*, 288–298. DOI: 10.1016/j.powtec.2014.04.016.

329. Beck, S.; Bouchard, J.; Berry, R. Dispersibility in water of dried nanocrystalline cellulose. *Biomacromolecules* **2012,** *13* (5), 1486–1494. DOI: 10.1021/bm300191k.

330. Peng, Y.; Gardner, D. J.; Han, Y.; Kiziltas, A.; Cai, Z.; Tshabalala, M. A. Influence of drying method on the material properties of nanocellulose I: thermostability and crystallinity. *Cellulose* **2013,** *20* (5), 2379–2392. DOI: 10.1007/s10570-013-0019-z.

331. Haouache, S.; Karam, A.; Chave, T.; Clarhaut, J.; Amaniampong, P. N.; Garcia Fernandez, J. M.; Oliveira Vigier, K. de; Capron, I.; Jérôme, F. Selective radical depolymerization of cellulose to glucose induced by high frequency ultrasound. *Chemical Science* **2020,** *11* (10), 2664–2669. DOI: 10.1039/D0SC00020E.

332. Beck, S.; Bouchard, J.; Berry, R. Controlling the reflection wavelength of iridescent solid films of nanocrystalline cellulose. *Biomacromolecules* **2011,** *12* (1), 167–172. DOI: 10.1021/bm1010905.

333. Shojaeiarani, J.; Bajwa, D.; Holt, G. Sonication amplitude and processing time influence the cellulose nanocrystals morphology and dispersion. *Nanocomposites* **2020,** *6* (1), 41–46. DOI: 10.1080/20550324.2019.1710974.

334. Roman, M. Toxicity of Cellulose Nanocrystals: A Review. *Industrial Biotechnology* **2015,** *11* (1), 25–33. DOI: 10.1089/ind.2014.0024.

335. Shatkin, J. A.; Kim, B. Cellulose nanomaterials: life cycle risk assessment, and environmental health and safety roadmap. *Environmental Science: Nano* **2015,** *2* (5), 477–499. DOI: 10.1039/C5EN00059A.

336. Bai, W.; Holbery, J.; Li, K. A technique for production of nanocrystalline cellulose with a narrow size distribution. *Cellulose* **2009,** *16* (3), 455–465. DOI: 10.1007/s10570-009-9277-1.

337. Hu, Y.; Abidi, N. Distinct Chiral Nematic Self-Assembling Behavior Caused by Different Size-Unified Cellulose Nanocrystals via a Multistage Separation. *Langmuir : the ACS journal of surfaces and colloids* **2016,** *32* (38), 9863–9872. DOI: 10.1021/acs.langmuir.6b02861.

338. Mukherjee, A.; Hackley, V. A. Separation and characterization of cellulose nanocrystals by multi-detector asymmetrical-flow field-flow fractionation. *The Analyst* **2018,** *143* (3), 731–740. DOI: 10.1039/c7an01739a.

339. Habibi, Y. Key advances in the chemical modification of nanocelluloses. *Chemical Society reviews* **2014,** *43* (5), 1519–1542. DOI: 10.1039/c3cs60204d.

340. Missoum, K.; Belgacem, M. N.; Bras, J. Nanofibrillated Cellulose Surface Modification: A Review. *Materials (Basel, Switzerland)* **2013,** *6* (5), 1745–1766. DOI: 10.3390/ma6051745.

341. Shen, Q. Surface Properties of Cellulose and Cellulose Derivatives: A Review. In *Cellulose Solvents: For Analysis, Shaping and Chemical Modification*; Liebert, T. F., Heinze, T. J., Edgar, K. J., Eds.; ACS Symposium Series; American Chemical Society, 2010, pp 259–289. DOI: 10.1021/bk-2009-1019.ch012.

342. Eichhorn, S. J. Cellulose nanowhiskers: promising materials for advanced applications. *Soft Matter* **2011,** *7* (2), 303–315. DOI: 10.1039/C0SM00142B.

343. Heux, L.; Chauve, G.; Bonini, C. Nonflocculating and Chiral-Nematic Self-ordering of Cellulose Microcrystals Suspensions in Nonpolar Solvents. *Langmuir : the ACS journal of surfaces and colloids* **2000,** *16* (21), 8210–8212. DOI: 10.1021/la9913957.

344. Podsiadlo, P.; Choi, S.-Y.; Shim, B.; Lee, J.; Cuddihy, M.; Kotov, N. A. Molecularly engineered nanocomposites: layer-by-layer assembly of cellulose nanocrystals. *Biomacromolecules* **2005,** *6* (6), 2914–2918. DOI: 10.1021/bm050333u.

345. Peng, S. X.; Chang, H.; Kumar, S.; Moon, R. J.; Youngblood, J. P. A comparative guide to controlled hydrophobization of cellulose nanocrystals via surface esterification. *Cellulose* **2016,** *23* (3), 1825–1846. DOI: 10.1007/s10570-016-0912-3.

346. Isogai, A.; Saito, T.; Fukuzumi, H. TEMPO-oxidized cellulose nanofibers. *Nanoscale* **2011,** *3* (1), 71–85. DOI: 10.1039/c0nr00583e.

347. Habibi, Y.; Dufresne, A. Highly filled bionanocomposites from functionalized polysaccharide nanocrystals. *Biomacromolecules* **2008,** *9* (7), 1974–1980. DOI: 10.1021/bm8001717.

348. Siqueira, G.; Bras, J.; Dufresne, A. New process of chemical grafting of cellulose nanoparticles with a long chain isocyanate. *Langmuir : the ACS journal of surfaces and colloids* **2010,** *26* (1), 402–411. DOI: 10.1021/la9028595.

349. Dong, S.; Roman, M. Fluorescently labeled cellulose nanocrystals for bioimaging applications. *Journal of the American Chemical Society* **2007,** *129* (45), 13810–13811. DOI: 10.1021/ja076196l.

350. Hasani, M.; Cranston, E. D.; Westman, G.; Gray, D. G. Cationic surface functionalization of cellulose nanocrystals. *Soft Matter* **2008,** *4* (11), 2238–2244. DOI: 10.1039/B806789A.

351. Hoeng, F.; Denneulin, A.; Neuman, C.; Bras, J. Charge density modification of carboxylated cellulose nanocrystals for stable silver nanoparticles suspension preparation. *Journal of Nanoparticle Research* **2015,** *17* (6). DOI: 10.1007/s11051-015-3044-z.

352. Yang, H.; Tejado, A.; Alam, N.; Antal, M.; van de Ven, T. G. M. Films prepared from electrosterically stabilized nanocrystalline cellulose. *Langmuir : the ACS journal of surfaces and colloids* **2012,** *28* (20), 7834–7842. DOI: 10.1021/la2049663.

353. TAPPI. *Standards & Standards Development Activities (Accessed: 15 August 2021)*. https://www.tappinano.org/whats-up/standards-summary/.

354. National Research Council Canada. *Certified reference materials (Accessed: 15 August 2021)*. http://www.nrc.ca/crm.

355. National Research Council Canada. *Certificate of Analysis: CNC-1*: *Cellulose Nanocrystal Powder Certified Reference Material (Accessed: 15 August 2021)*. https://nrc.canada.ca/en/certifications-evaluations-standards/certified-reference-materials/list/32/html.

356. National Research Council Canada. *Certificate of Analysis: CNCD-1*: *Cellulose Nanocrystal Powder Certified Reference Material (Accessed: 15 August 2021)*. https://nrc.canada.ca/en/certifications-evaluations-standards/certified-reference-materials/list/34/html.

357. National Research Council Canada. *Certificate of Analysis: CNCS-1*: *Cellulose Nanocrystal Suspension Certified Reference Material (Accessed: 15 August 2021)*. https://nrc.canada.ca/en/certifications-evaluations-standards/certified-reference-materials/list/36/html.

358. Campano, C.; Lopez-Exposito, P.; Gonzalez-Aguilera, L.; Blanco, Á.; Negro, C. In-depth characterization of the aggregation state of cellulose nanocrystals through analysis of transmission electron microscopy images. *Carbohydrate Polymers* **2021,** *254*, 117271. DOI: 10.1016/j.carbpol.2020.117271.

359. Azzam, F.; Heux, L.; Putaux, J.-L.; Jean, B. Preparation by grafting onto, characterization, and properties of thermally responsive polymer-decorated cellulose nanocrystals. *Biomacromolecules* **2010,** *11* (12), 3652–3659. DOI: 10.1021/bm101106c.

360. Mandal, A.; Chakrabarty, D. Isolation of nanocellulose from waste sugarcane bagasse (SCB) and its characterization. *Carbohydrate polymers* **2011,** *86* (3), 1291–1299. DOI: 10.1016/j.carbpol.2011.06.030.

361. Shinoda, R.; Saito, T.; Okita, Y.; Isogai, A. Relationship between length and degree of polymerization of TEMPO-oxidized cellulose nanofibrils. *Biomacromolecules* **2012,** *13* (3), 842–849. DOI: 10.1021/bm2017542.

362. Postek, M. T.; Vladár, A.; Dagata, J.; Farkas, N.; Ming, B.; Wagner, R.; Raman, A.; Moon, R. J.; Sabo, R.; Wegner, T. H.; Beecher, J. Development of the metrology and imaging of cellulose nanocrystals. *Measurement Science and Technology* **2011,** *22* (2), 24005. DOI: 10.1088/0957-0233/22/2/024005.

363. Bhattacharjee, S. DLS and zeta potential - What they are and what they are not? *Journal of controlled release : official journal of the Controlled Release Society* **2016,** *235*, 337–351. DOI: 10.1016/j.jconrel.2016.06.017.

364. Yang, H.; Alam, M. N.; van de Ven, T. G. M. Highly charged nanocrystalline cellulose and dicarboxylated cellulose from periodate and chlorite oxidized cellulose fibers. *Cellulose* **2013,** *20* (4), 1865–1875. DOI: 10.1007/s10570-013-9966-7.

365. Boluk, Y.; Lahiji, R.; Zhao, L.; McDermott, M. T. Suspension viscosities and shape parameter of cellulose nanocrystals (CNC). *Colloids and Surfaces A: Physicochemical and Engineering Aspects* **2011,** *377* (1-3), 297–303. DOI: 10.1016/j.colsurfa.2011.01.003.

366. Guan, X.; Cueto, R.; Russo, P.; Qi, Y.; Wu, Q. Asymmetric flow field-flow fractionation with multiangle light scattering detection for characterization of cellulose nanocrystals. *Biomacromolecules* **2012,** *13* (9), 2671–2679.

367. Ruiz-Palomero, C.; Laura Soriano, M.; Valcárcel, M. Detection of nanocellulose in commercial products and its size characterization using asymmetric flow field-flow fractionation. *Microchimica Acta* **2017,** *184* (4), 1069–1076. DOI: 10.1007/s00604-017-2106-6.

368. Steyermark, A. Microdetermination of Metals by the Ashing Technique. In *Quantitative Organic Microanalysis*; Steyermark, A., Ed.; Elsevier, 1961, pp 133–150. DOI: 10.1016/B978-0-12-395686-6.50012-X.

369. Steyermark, A. Microdetermination of Nitrogen by the Dumas Method. In *Quantitative Organic Microanalysis*; Steyermark, A., Ed.; Elsevier, 1961, pp 151–187. DOI: 10.1016/B978-0-12-395686-6.50013-1.

370. Steyermark, A. Microdetermination of Sulfur. In *Quantitative Organic Microanalysis*; Steyermark, A., Ed.; Elsevier, 1961, pp 276–315. DOI: 10.1016/B978-0-12-395686-6.50016-7.

371. Steyermark, A. Microdetermination of Halogens. In *Quantitative Organic Microanalysis*; Steyermark, A., Ed.; Elsevier, 1961, pp 316–353. DOI: 10.1016/B978-0-12-395686-6.50017-9.

372. Steyermark, A. Microdetermination of Oxygen. In *Quantitative Organic Microanalysis*; Steyermark, A., Ed.; Elsevier, 1961, pp 377–409. DOI: 10.1016/B978-0-12-395686-6.50020-9.

373. Li, W.; Ding, E. Characterization of PET Fabrics Surface Modified by Graft Cellulose Nano-crystal Using TGA, FE-SEM XPS. *Surface Review and Letters* **2006,** *13* (06), 819–823. DOI: 10.1142/S0218625X06008906.

374. Boujemaoui, A.; Mongkhontreerat, S.; Malmström, E.; Carlmark, A. Preparation and characterization of functionalized cellulose nanocrystals. *Carbohydrate polymers* **2015,** *115*, 457–464. DOI: 10.1016/j.carbpol.2014.08.110.

375. Tian, C.; Fu, S.; Habibi, Y.; Lucia, L. A. Polymerization topochemistry of cellulose nanocrystals: a function of surface dehydration control. *Langmuir : the ACS journal of surfaces and colloids* **2014,** *30* (48), 14670–14679. DOI: 10.1021/la503990u.

376. Kaushik, M.; Moores, A. Review: nanocelluloses as versatile supports for metal nanoparticles and their applications in catalysis. *Green Chemistry* **2016,** *18* (3), 622–637. DOI: 10.1039/C5GC02500A.

377. Zhong, T.; Oporto, G. S.; Peng, Y.; Xie, X.; Gardner, D. J. Drying cellulose-based materials containing copper nanoparticles. *Cellulose* **2015,** *22* (4), 2665–2681. DOI: 10.1007/s10570-015-0646-7.

378. Ruiz-Palomero, C.; Soriano, M. L.; Benítez-Martínez, S.; Valcárcel, M. Photoluminescent sensing hydrogel platform based on the combination of nanocellulose and S,N-codoped graphene quantum dots. *Sensors and Actuators B: Chemical* **2017,** *245*, 946–953. DOI: 10.1016/j.snb.2017.02.006.

379. Missoum, K.; Belgacem, M. N.; Barnes, J.-P.; Brochier-Salon, M.-C.; Bras, J. Nanofibrillated cellulose surface grafting in ionic liquid. *Soft Matter* **2012,** *8* (32), 8338. DOI: 10.1039/C2SM25691F.

380. Cunha, A. G.; Freire, C. S. R.; Silvestre, A. J. D.; Neto, C. P.; Gandini, A. Reversible hydrophobization and lipophobization of cellulose fibers via trifluoroacetylation. *Journal of colloid and interface science* **2006,** *301* (1), 333–336. DOI: 10.1016/j.jcis.2006.04.078.

381. Kalaskar, D. M.; Ulijn, R. V.; Gough, J. E.; Alexander, M. R.; Scurr, D. J.; Sampson, W. W.; Eichhorn, S. J. Characterisation of amino acid modified cellulose surfaces using ToF-SIMS and XPS. *Cellulose* **2010,** *17* (4), 747–756. DOI: 10.1007/s10570-010-9413-y.

382. Mohd Amin, K. N.; Annamalai, P. K.; Morrow, I. C.; Martin, D. Production of cellulose nanocrystals via a scalable mechanical method. *RSC Advances* **2015,** *5* (70), 57133–57140. DOI: 10.1039/C5RA06862B.

383. Cirtiu, C. M.; Dunlop-Brière, A. F.; Moores, A. Cellulose nanocrystallites as an efficient support for nanoparticles of palladium: application for catalytichydrogenation and Heck coupling under mild conditions. *Green Chemistry* **2011,** *13* (2), 288–291. DOI: 10.1039/C0GC00326C.

384. Shi, S.; Chen, S.; Zhang, X.; Shen, W.; Li, X.; Hu, W.; Wang, H. Biomimetic mineralization synthesis of calcium-deficient carbonate-containing hydroxyapatite in a three-dimensional network of bacterial cellulose. *Journal of Chemical Technology & Biotechnology* **2009,** *84* (2), 285–290. DOI: 10.1002/jctb.2037.

385. International Organization for Standardization. *ISO 21400:2018 - Pulp — Determination of cellulose nanocrystal sulfur and sulfate half-ester content*, 2018 (21400). https://www.iso.org/standard/70861.html.

386. Park, S.; Baker, J. O.; Himmel, M. E.; Parilla, P. A.; Johnson, D. K. Cellulose crystallinity index: measurement techniques and their impact on interpreting cellulase performance. *Biotechnology for biofuels* **2010,** *3*, 10. DOI: 10.1186/1754-6834-3-10.

387. Ahvenainen, P.; Kontro, I.; Svedström, K. Comparison of sample crystallinity determination methods by X-ray diffraction for challenging cellulose I materials. *Cellulose* **2016,** *23* (2), 1073–1086. DOI: 10.1007/s10570-016-0881-6.

388. Agarwal, U. P.; Ralph, S. A.; Reiner, R. S.; Baez, C. Probing crystallinity of never-dried wood cellulose with Raman spectroscopy. *Cellulose* **2016,** *23* (1), 125–144. DOI: 10.1007/s10570-015-0788-7.

389. Fukuzumi, H.; Saito, T.; Isogai, A. Influence of TEMPO-oxidized cellulose nanofibril length on film properties. *Carbohydrate polymers* **2013,** *93* (1), 172–177. DOI: 10.1016/j.carbpol.2012.04.069.

390. Park, S.; Johnson, D. K.; Ishizawa, C. I.; Parilla, P. A.; Davis, M. F. Measuring the crystallinity index of cellulose by solid state 13C nuclear magnetic resonance. *Cellulose* **2009,** *16* (4), 641–647. DOI: 10.1007/s10570-009-9321-1.

391. Kim, S. H.; Lee, C. M.; Kafle, K. Characterization of crystalline cellulose in biomass: Basic principles, applications, and limitations of XRD, NMR, IR, Raman, and SFG. *Korean Journal of Chemical Engineering* **2013,** *30* (12), 2127–2141. DOI: 10.1007/s11814-013-0162-0.

392. International Organization for Standardization. *ISO 527-1:2019 - Plastics — Determination of tensile properties — Part 1: General principles*, 2018 (527-1). https://www.iso.org/standard/75824.html.

393. International Organization for Standardization. *ISO 527-3:2018 - Plastics — Determination of tensile properties — Part 3: Test conditions for films and sheets*, 2018 (527-3). https://www.iso.org/standard/70307.html.

394. Deutsches Institut für Normung. *DIN 53122-1:2001-08, Prüfung von Kunststoff-Folien, Elastomerfolien, Papier, Pappe und anderen Flächengebilden_- Bestimmung der Wasserdampfdurchlässigkeit_- Teil_1: Gravimetrisches Verfahren;* Beuth Verlag GmbH: Berlin, 2001 (53122-1). https://www.beuth.de/de/norm/din-53122-1/40508039.

395. Deutsches Institut für Normung. *DIN 53380-3:1998, Prüfung von Kunststoffen - Bestimmung der Gasdurchlässigkeit - Teil 3: Sauerstoffspezifisches Trägergas-Verfahren zur Messung an Kunststoff-Folien und Kunststoff-Formteilen;* Beuth Verlag GmbH: Berlin, 1998 (53380-3). https://www.beuth.de/de/norm/din-53380-3/3725281.

396. Deutsches Institut für Normung. *Rheologie;* Beuth Verlag GmbH, 2019.

397. Österberg, M.; Cranston, E. D. Special issue on nanocellulose- Editorial. *Nordic Pulp & Paper Research Journal* **2014,** *29* (1), 4–5. DOI: 10.3183/npprj-2014-29-01-p004-005.

398. Charreau, H.; Foresti, M. L.; Vazquez, A. Nanocellulose Patents Trends: A Comprehensive Review on Patents on Cellulose Nanocrystals, Microfibrillated and Bacterial Cellulose. *Recent Patents on Nanotechnology* **2013,** *7* (1), 56–80. DOI: 10.2174/187221013804484854.

399. Nelson, K.; Walker, C. *Advancing Commercialization of Nanocellulose*: *Critical Challenges Workshop.* 10.13140/RG.2.2.33789.59363.

400. Vlachy, N.; Jagoda-Cwiklik, B.; Vácha, R.; Touraud, D.; Jungwirth, P.; Kunz, W. Hofmeister series and specific interactions of charged headgroups with aqueous ions. *Advances in colloid and interface science* **2009,** *146* (1-2), 42–47. DOI: 10.1016/j.cis.2008.09.010.

401. Labet, M.; Thielemans, W. Improving the reproducibility of chemical reactions on the surface of cellulose nanocrystals: ROP of ε-caprolactone as a case study. *Cellulose* **2011,** *18* (3), 607–617. DOI: 10.1007/s10570-011-9527-x.

402. Shafiei-Sabet, S.; Hamad, W. Y.; Hatzikiriakos, S. G. Rheology of nanocrystalline cellulose aqueous suspensions. *Langmuir : the ACS journal of surfaces and colloids* **2012,** *28* (49), 17124–17133. DOI: 10.1021/la303380v.

403. Sangroniz, A.; Zhu, J.-B.; Tang, X.; Etxeberria, A.; Chen, E. Y.-X.; Sardon, H. Packaging materials with desired mechanical and barrier properties and full chemical recyclability. *Nature communications* **2019,** *10* (1), 3559. DOI: 10.1038/s41467-019-11525-x.

404. World Economic Forum; Ellen MacArthur Foundation; McKinsey & Company. *The New Plastics Economy: Rethinking the Future of Plastics (Accessed: 15 August 2021).* https://www.ellenmacarthurfoundation.org/publications/the-new-plastics-economy-rethinking-the-future-of-plastics.

405. Gross, R. A.; Kalra, B. Biodegradable polymers for the environment. *Science (New York, N.Y.)* **2002,** *297* (5582), 803–807. DOI: 10.1126/science.297.5582.803.

406. Nair, S. S.; Zhu, J. Y.; Deng, Y.; Ragauskas, A. J. High performance green barriers based on nanocellulose. *Sustainable Chemical Processes* **2014,** *2* (1). DOI: 10.1186/s40508-014-0023-0.

407. Syverud, K.; Stenius, P. Strength and barrier properties of MFC films. *Cellulose* **2009,** *16* (1), 75–85. DOI: 10.1007/s10570-008-9244-2.

408. Saxena, A.; Elder, T. J.; Kenvin, J.; Ragauskas, A. J. High Oxygen Nanocomposite Barrier Films Based on Xylan and Nanocrystalline Cellulose. *Nano-Micro Letters* **2010,** *2* (4), 235–241. DOI: 10.1007/BF03353849.

409. Lagaron, J. M.; Catalá, R.; Gavara, R. Structural characteristics defining high barrier properties in polymeric materials. *Materials Science and Technology* **2004,** *20* (1), 1–7. DOI: 10.1179/026708304225010442.

410. Lindner, M.; Rodler, N.; Jesdinszki, M.; Schmid, M.; Sängerlaub, S. Surface energy of corona treated PP, PE and PET films, its alteration as function of storage time and the effect of various corona dosages on their bond strength after lamination. *Journal of Applied Polymer Science* **2018,** *135* (11), 45842. DOI: 10.1002/app.45842.

411. Chen, Y.; Gan, L.; Huang, J.; Dufresne, A. Reinforcing Mechanism of Cellulose Nanocrystals in Nanocomposites. In *Nanocellulose*: *From Fundamentals to Advanced Materials,* 1. Auflage; Huang, J., Dufresne, A., Lin, N., Eds.; Wiley-VCH Verlag GmbH & Co. KGaA, 2019, pp 201–249. DOI: 10.1002/9783527807437.ch7.

412. Wu, Q.; Li, X.; Fu, S.; Li, Q.; Wang, S. Estimation of aspect ratio of cellulose nanocrystals by viscosity measurement: influence of surface charge density and NaCl concentration. *Cellulose* **2017,** *24* (8), 3255–3264. DOI: 10.1007/s10570-017-1341-7.

413. Moud, A. A.; Arjmand, M.; Liu, J.; Yang, Y.; Sanati-Nezhad, A.; Hejazi, S. H. Cellulose nanocrystal structure in the presence of salts. *Cellulose* **2019,** *26* (18), 9387–9401. DOI: 10.1007/s10570-019-02734-0.

414. Cherhal, F.; Cousin, F.; Capron, I. Influence of charge density and ionic strength on the aggregation process of cellulose nanocrystals in aqueous suspension, as revealed by small-angle neutron scattering. *Langmuir : the ACS journal of surfaces and colloids* **2015,** *31* (20), 5596–5602. DOI: 10.1021/acs.langmuir.5b00851.

415. Peddireddy, K. R.; Capron, I.; Nicolai, T.; Benyahia, L. Gelation Kinetics and Network Structure of Cellulose Nanocrystals in Aqueous Solution. *Biomacromolecules* **2016,** *17* (10), 3298–3304. DOI: 10.1021/acs.biomac.6b01061.

416. Bertsch, P.; Isabettini, S.; Fischer, P. Ion-Induced Hydrogel Formation and Nematic Ordering of Nanocrystalline Cellulose Suspensions. *Biomacromolecules* **2017,** *18* (12), 4060–4066. DOI: 10.1021/acs.biomac.7b01119.

417. Dong, X. M.; Kimura, T.; Revol, J.-F.; Gray, D. G. Effects of Ionic Strength on the Isotropic−Chiral Nematic Phase Transition of Suspensions of Cellulose Crystallites. *Langmuir : the ACS journal of surfaces and colloids* **1996,** *12* (8), 2076–2082. DOI: 10.1021/la950133b.

418. Mikhailov, V. I.; Torlopov, M. A.; Martakov, I. S.; Krivoshapkin, P. V. Stability of nanocrystalline cellulose in aqueous KCl solutions. *Colloid Journal* **2017,** *79* (2), 226–233. DOI: 10.1134/S1061933X17020065.

419. Wu, Q.; Li, X.; Li, Q.; Wang, S.; Luo, Y. Estimation of Aspect Ratio of Cellulose Nanocrystals by Viscosity Measurement: Influence of Aspect Ratio Distribution and Ionic Strength. *Polymers* **2019,** *11* (5). DOI: 10.3390/polym11050781.

420. Liu, L.; Hu, Z.; Sui, X.; Guo, J.; Cranston, E. D.; Mao, Z. Effect of Counterion Choice on the Stability of Cellulose Nanocrystal Pickering Emulsions. *Industrial & Engineering Chemistry Research* **2018,** *57* (21), 7169–7180. DOI: 10.1021/acs.iecr.8b01001.

421. Moud, A. A.; Arjmand, M.; Yan, N.; Nezhad, A. S.; Hejazi, S. H. Colloidal Behavior of Cellulose Nanocrystals in Presence of Sodium Chloride. *ChemistrySelect* **2018,** *3* (17), 4969–4978. DOI: 10.1002/slct.201703152.

422. Qi, W.; Yu, J.; Zhang, Z.; Xu, H.-N. Effect of pH on the aggregation behavior of cellulose nanocrystals in aqueous medium. *Materials Research Express* **2019,** *6* (12), 125078. DOI: 10.1088/2053-1591/ab5974.

423. Girard, M.; Vidal, D.; Bertrand, F.; Tavares, J. R.; Heuzey, M.-C. Evidence-based guidelines for the ultrasonic dispersion of cellulose nanocrystals. *Ultrasonics sonochemistry* **2020,** *71*, 105378. DOI: 10.1016/j.ultsonch.2020.105378.

424. Gicquel, E.; Martin, C.; Garrido Yanez, J.; Bras, J. Cellulose nanocrystals as new bio-based coating layer for improving fiber-based mechanical and barrier properties. *Journal of Materials Science* **2017,** *52* (6), 3048–3061. DOI: 10.1007/s10853-016-0589-x.

425. Herrera, M.; Oksman, K. Moisture and Gas Barrier Properties of Cellulose Nanocrystals in Thin Films. In *Handbook of Green Materials*; Oksman, K., Mathew, A. P., Bismarck, A., Rojas, O. J., Sain, M., Eds.; Materials and Energy; WORLD SCIENTIFIC, 2014, pp 231–246. DOI: 10.1142/9789814566469_0045.

426. Cao, X.; Chen, Y.; Chang, P. R.; Stumborg, M.; Huneault, M. A. Green composites reinforced with hemp nanocrystals in plasticized starch. *Journal of Applied Polymer Science* **2008,** *109* (6), 3804–3810. DOI: 10.1002/app.28418.

427. Kedzior, S. A.; Zoppe, J. O.; Berry, R. M.; Cranston, E. D. Recent advances and an industrial perspective of cellulose nanocrystal functionalization through polymer grafting. *Current Opinion in Solid State and Materials Science* **2019,** *23* (2), 74–91. DOI: 10.1016/j.cossms.2018.11.005.

428. Wegner, T. H.; Ireland, S.; Jones, P. E. Cellulosic Nanomaterials: Sustainable Materials of Choice for the 21st Century. In *Production and applications of cellulose nanomaterials*; Postek, M. T., Moon, R. J., Rudie, A. W., Bilodeau, M., Eds.; TAPPI Press, 2013, pp 3–9.

429. Ma, T.; Hu, X.; Lu, S.; Liao, X.; Song, Y.; Hu, X. Nanocellulose: a promising green treasure from food wastes to available food materials. *Critical reviews in food science and nutrition* **2020**, 1–14. DOI: 10.1080/10408398.2020.1832440.

430. Reid, M. S.; Kedzior, S. A.; Villalobos, M.; Cranston, E. D. Effect of Ionic Strength and Surface Charge Density on the Kinetics of Cellulose Nanocrystal Thin Film Swelling. *Langmuir : the ACS journal of surfaces and colloids* **2017,** *33* (30), 7403–7411. DOI: 10.1021/acs.langmuir.7b01740.

431. Chau, M.; Sriskandha, S. E.; Pichugin, D.; Thérien-Aubin, H.; Nykypanchuk, D.; Chauve, G.; Méthot, M.; Bouchard, J.; Gang, O.; Kumacheva, E. Ion-Mediated Gelation of Aqueous Suspensions of Cellulose Nanocrystals. *Biomacromolecules* **2015,** *16* (8), 2455–2462. DOI: 10.1021/acs.biomac.5b00701.

432. Shafiei-Sabet, S.; Hamad, W. Y.; Hatzikiriakos, S. G. Ionic strength effects on the microstructure and shear rheology of cellulose nanocrystal suspensions. *Cellulose* **2014,** *21* (5), 3347–3359. DOI: 10.1007/s10570-014-0407-z.

433. Salini, S. An Introduction to Bibliometrics. In *Research methods for postgraduates,* Third edition; Greener, S., Greenfield, T., Eds.; John Wiley & Sons, 2016, pp 130–143. DOI: 10.1002/9781118763025.ch14.

434. van Leeuwen, T. Descriptive Versus Evaluative Bibliometrics. In *Handbook of quantitative science and technology research*: *The use of publication and patent statistics in studies of S&T systems*; Moed, H. F., Glänzel, W., Schmoch, U., Eds.; Kluwer Academic Publishers, 2004, pp 373–388. DOI: 10.1007/1-4020-2755-9_17.

435. RStudio Team. *RStudio: Integrated Development for R. Version 1.3.1093.* https://rstudio.com/.

436. Aria, M.; Cuccurullo, C. bibliometrix : An R-tool for comprehensive science mapping analysis. *Journal of Informetrics* **2017,** *11* (4), 959–975. DOI: 10.1016/j.joi.2017.08.007.

437. Wickham, H.; Henry, L. *tidyr: Tidy Messy Data. R package version 1.1.2*. https://cran.r-project.org/web/packages/tidyr/index.html.

438. Wickham, H.; François, R.; Henry, L.; Müller, K. *dplyr: A Grammar of Data Manipulation. R package version 1.0.2*. https://cran.r-project.org/web/packages/dplyr/index.html.

439. Côte, G.; Roberge, G.; Deschamps, P.; Robitaille, N. *Bibliometrics and Patent Indicators for the Science and Engineering Indicators 2018*. Task 21. https://www.science-metrix.com/sites/default/files/science-metrix/publications/bibliometrics_and_patent_indicators_for_the_sei_2018_technical_documentation.pdf.

440. Paillet, M.; Dufresne, A. Chitin Whisker Reinforced Thermoplastic Nanocomposites. *Macromolecules* **2001,** *34* (19), 6527–6530. DOI: 10.1021/ma002049v.

441. Wågberg, L.; Decher, G.; Norgren, M.; Lindström, T.; Ankerfors, M.; Axnäs, K. The build-up of polyelectrolyte multilayers of microfibrillated cellulose and cationic polyelectrolytes. *Langmuir : the ACS journal of surfaces and colloids* **2008,** *24* (3), 784–795. DOI: 10.1021/la702481v.

442. Yuan, H.; Nishiyama, Y.; Wada, M.; Kuga, S. Surface acylation of cellulose whiskers by drying aqueous emulsion. *Biomacromolecules* **2006,** *7* (3), 696–700. DOI: 10.1021/bm050828j.

443. Nooy, A. de; Besemer, A. C.; van Bekkum, H. Highly selective tempo mediated oxidation of primary alcohol groups in polysaccharides. *Recueil des Travaux Chimiques des Pays-Bas* **1994,** *113* (3), 165–166. DOI: 10.1002/recl.19941130307.

444. Suflet, D. M.; Chitanu, G. C.; Popa, V. I. Phosphorylation of polysaccharides: New results on synthesis and characterisation of phosphorylated cellulose. *Reactive and Functional Polymers* **2006,** *66* (11), 1240–1249. DOI: 10.1016/j.reactfunctpolym.2006.03.006.

445. Sassi, J.-F.; Chanzy, H. Ultrastructural aspects of the acetylation of cellulose. *Cellulose* **1995,** *2* (2), 111–127. DOI: 10.1007/BF00816384.

446. Ruiz-Palomero, C.; Soriano, M. L.; Valcárcel, M. β-Cyclodextrin decorated nanocellulose: a smart approach towards the selective fluorimetric determination of danofloxacin in milk samples. *The Analyst* **2015,** *140* (10), 3431–3438. DOI: 10.1039/c4an01967a.

447. Andresen, M.; Stenstad, P.; Møretrø, T.; Langsrud, S.; Syverud, K.; Johansson, L.-S.; Stenius, P. Nonleaching antimicrobial films prepared from surface-modified microfibrillated cellulose. *Biomacromolecules* **2007,** *8* (7), 2149–2155. DOI: 10.1021/bm070304e.

448. Carlmark, A.; Malmström, E. Atom transfer radical polymerization from cellulose fibers at ambient temperature. *Journal of the American Chemical Society* **2002,** *124* (6), 900–901. DOI: 10.1021/ja016582h.

449. Larsson, E.; Boujemaoui, A.; Malmström, E.; Carlmark, A. Thermoresponsive cryogels reinforced with cellulose nanocrystals. *RSC Advances* **2015,** *5* (95), 77643–77650. DOI: 10.1039/C5RA12603G.

450. Roy, D.; Guthrie, J. T.; Perrier, S. Synthesis of natural-synthetic hybrid materials from cellulose via the RAFT process. *Soft Matter* **2007,** *4* (1), 145–155. DOI: 10.1039/b711248n.

451. Lönnberg, H.; Larsson, K.; Lindström, T.; Hult, A.; Malmström, E. Synthesis of polycaprolactone-grafted microfibrillated cellulose for use in novel bionanocomposites--influence of the graft length on the mechanical properties. *ACS Applied Materials & Interfaces* **2011,** *3* (5), 1426–1433. DOI: 10.1021/am2001828.

452. Harrisson, S.; Drisko, G. L.; Malmström, E.; Hult, A.; Wooley, K. L. Hybrid rigid/soft and biologic/synthetic materials: polymers grafted onto cellulose microcrystals. *Biomacromolecules* **2011,** *12* (4), 1214–1223. DOI: 10.1021/bm101506j.

453. Chen, Y.; Liu, C.; Chang, P. R.; Cao, X.; Anderson, D. P. Bionanocomposites based on pea starch and cellulose nanowhiskers hydrolyzed from pea hull fibre: Effect of hydrolysis time. *Carbohydrate polymers* **2009,** *76* (4), 607–615. DOI: 10.1016/j.carbpol.2008.11.030.

454. Morais, J. P. S.; Rosa, M. d. F.; Souza Filho, M. s. M. de; Nascimento, L. D.; do Nascimento, D. M.; Cassales, A. R. Extraction and characterization of nanocellulose structures from raw cotton linter. *Carbohydrate polymers* **2013,** *91* (1), 229–235. DOI: 10.1016/j.carbpol.2012.08.010.

455. Edgar, C. D.; Gray, D. G. Smooth model cellulose I surfaces from nanocrystal suspensions. *Cellulose* **2003,** *10* (4), 299–306. DOI: 10.1023/A:1027333928715.

456. Yue, Y.; Zhou, C.; French, A. D.; Xia, G.; Han, G.; Wang, Q.; Wu, Q. Comparative properties of cellulose nano-crystals from native and mercerized cotton fibers. *Cellulose* **2012,** *19* (4), 1173–1187. DOI: 10.1007/s10570-012-9714-4.

457. Salajková, M.; Berglund, L. A.; Zhou, Q. Hydrophobic cellulose nanocrystals modified with quaternary ammonium salts. *Journal of Materials Chemistry* **2012,** *22* (37), 19798. DOI: 10.1039/c2jm34355j.

458. Leguy, J.; Diallo, A.; Putaux, J.-L.; Nishiyama, Y.; Heux, L.; Jean, B. Periodate Oxidation Followed by NaBH4 Reduction Converts Microfibrillated Cellulose into Sterically Stabilized Neutral Cellulose Nanocrystal Suspensions. *Langmuir : the ACS journal of surfaces and colloids* **2018,** *34* (37), 11066–11075. DOI: 10.1021/acs.langmuir.8b02202.

459. Lalia, B. S.; Samad, Y. A.; Hashaikeh, R. Nanocrystalline-cellulose-reinforced poly(vinylidenefluoride- co -hexafluoropropylene) nanocomposite films as a separator for lithium ion batteries. *Journal of Applied Polymer Science* **2012,** *126* (S1), E442-E448. DOI: 10.1002/app.36783.

460. *Anomera (Accessed: 15 August 2021)*. https://www.anomera.ca/.

461. *Blue Goose Biorefineries (Accessed: 15 August 2021)*. https://bluegoosebiorefineries.com/.

462. *CelluForce (Accessed: 15 August 2021)*. https://www.celluforce.com/.

463. *Cellulose Lab (Accessed: 15 August 2021)*. https://www.celluloselab.com/.

464. *FPInnovations (Accessed: 15 August 2021)*. https://web.fpinnovations.ca/.

465. *GranBio (Accessed: 15 August 2021)*. http://www.granbio.com.br/.

466. *Melodea (Accessed: 15 August 2021)*. https://innotechalberta.ca/.

467. *USDA Forst Products Laboratory (Accessed: 15 August 2021)*. https://www.fpl.fs.fed.us/.

9. Appendix

9.1. Bibliometric indicators

Bibliometry is the objective evaluation and mapping of scientific research, and it facilitates systematization of steadily growing scientific output (*433*). It can be used to describe research activity in certain fields, by applying principles of scientometrics and infometrics. Scientometrics involve mathematical and statistical methods to determine relative associations. Infometrics address quantitative aspects of any information. Most bibliometric indicators are derived from simple quantitative aspects. Based on this, a bibliometric top-down approach addresses descriptive evaluation of scientific output. Advanced bibliometric measures, which include network indicators, are derived from citation networks and co-authorships. Such a bottom up approach focuses on evaluation of scientific activity for qualitative evaluation of scientific performance (*434*).

Export from the Web of Science. Bibliographic data was retrieved from the Web of Science Core Collection (*12*) on 15 August 2021. Both singular and plural forms of each keyword were either manually entered, or they were considered via wildcards. Search queries for multi-word terms were entered as exact phrases. Search results were refined to include only English-language documents, and document types other than articles were excluded. Data was exported as plain text.

Export from The Lens. Patent data was retrieved from The Lens (*26*) on 15 August 2021. Keyword entries were handled analogously to the search for academic publications on the WoS-CC. Search results were refined to English-language patent applications and granted patents. Data was exported in BibTeX format, and it included corresponding cited literature.

Data editing. Data was imported to RStudio (*435*) and converted to DataFrames, using the bibliometrix package (*436*). The packages tidyr (*437*) and dplyr (*438*) were used for data editing.

Data processing. Entries exported from the WoS-CC, which had no DOI assigned and no reference list included, were manually removed (*439*). The DataFrame column, containing research areas on the journal level, was split and matched to subject categories of the database maintainer Clarivate Analytics (*13*). Data was then processed for quantitative presentation by annual number of publications and publications per research area per year. Entries exported from The Lens were processed for quantitative presentation by annual number of granted patents and patent applications. Entries, existing both as cited academic publications in patents and in search results from the WoS-CC, were matched by their DOI, for quantitative presentation.[4]

---

[4] The Python algorithm for processing DOIs from different databases has been provided by Tiaan Friedrich.

9.2. Cellulose surface modification

Table A8: Surface modifications of cellulose in the context of CNMs, according to Moon et al. (*101*), Eyley and Thielemans (*140*), and Thomas et al. (*139*). Surface functional groups are linked to the primary hydroxy groups of the cellulose backbone, R, and can contain a substituent, R'. Surface functional groups are presented in charge-balanced state.

Modification process	Modification technique	Functional group	Reference
Unfunctionalized		$R-Cl$	(*440*)
Imparting of ionic surface charge	Carboxymethylation		(*441*)
	Esterification		(*442*)
	Oxidation		(*443*)
	Phosphorylation		(*444*)
	Sulfonation		(*162*)
Hydrophobization	Acetylation		(*445*)
	Amidation		(*446*)
	Etherification		(*350*)
	Silylation		(*447*)
	Urethanization		(*347*)
Polymer grafting-to	Atom transfer radical polymerization	*	(*448*)
	Free radical	*	(*449*)
	Reversible addition-fragmentation chain transfer	*	(*450*)
	Ring-opening polymerization	*	(*451*)
Polymer grafting-from	Post-polymerization	*	(*452*)

More complex surface functional groups for polymer grafting can be viewed in listed references.

9.3. Biomass sources for CNC production

Table A9: Cellulose sources for CNC production and representative production routes. The list of methods was adopted from Vanderfleet and Cranston (*39*).

Feedstock	Cellulose source	Cellulose isolation	CNC isolation	Reference
Agricultural waste	Apple pomace	Digestion (HCl; NaOH); bleaching (NaOCl)	Hydrolysis (H_2SO_4); mechanical treatment	(*198*)
	Banana pseudostem	Extraction; digestion (NaOH); bleaching (H_2O_2); extraction	Hydrolysis (H_2SO_4)	(*193*)
	Coconut husk	Digestion (NaOH); bleaching ($NaClO_2$); digestion (HNO_3)	Hydrolysis (H_2SO_4)	(*216*)
	Coffee husk	Digestion (NaOH); bleaching ($NaClO_2$)	Hydrolysis (H_2SO_4)	(*199*)
	Corncob	Digestion (NaOH); bleaching ($NaClO_2$)	Hydrolysis (H_2SO_4)	(*200*)
	Garlic straw	Digestion (NaOH); bleaching ($NaClO_2$)	Hydrolysis (H_2SO_4)	(*201*)
	Mango seed	Digestion (NaOH); bleaching ($NaClO_2$)	Hydrolysis (H_2SO_4)	(*202*)
	Onion skin	Bleaching ($NaClO_2$); digestion (Na_2SO_3; NaOH)	Hydrolysis (H_2SO_4)	(*217*)
	Passion fruit peel	Bleaching (NaOH; H_2O_2)	Hydrolysis (H_2SO_4)	(*203*)
	Pea hull	*Not reported*	Hydrolysis (H_2SO_4)	(*453*)
	Peanut shell	Extraction; bleaching ($NaClO_2$); digestion (NaOH)	Hydrolysis (H_2SO_4)	(*190*)
	Pineapple leaf	Digestion (NaOH); bleaching ($NaClO_2$)	Hydrolysis (H_2SO_4)	(*204*)
	Pineapple peel	Bleaching ($NaClO_2$ + HCl); digestion (NaOH)	Hydrolysis (H_2SO_4)	(*218*)
	Pistacio shell	Extraction; digestion (NaOH); bleaching (H_2O_2); extraction	Hydrolysis (H_2SO_4)	(*194*)
	Potato peel	Digestion (NaOH); bleaching ($NaClO_2$)	Hydrolysis (H_2SO_4)	(*205*)
	Rice husk	Digestion (NaOH); bleaching ($NaClO_2$)	Hydrolysis (H_2SO_4)	(*206*)
	Rice straw	Bleaching ($NaClO_2$); digestion (KOH)	Hydrolysis (H_2SO_4)	(*219*)
	Soy hull	Digestion (NaOH); bleaching ($NaClO_2$)	Hydrolysis (H_2SO_4)	(*207*)
	Sugarcane bagasse	Digestion (NaOH); bleaching (H_2O_2)	Hydrolysis (H_2SO_4)	(*208*)
	Tomato peel	Extraction; bleaching ($NaClO_2$; H_2O_2); digestion (KOH)	Hydrolysis (H_2SO_4)	(*191*)
Algae	Cladophora	Digestion (KOH); bleaching ($NaClO_2$)	Hydrolysis (H_2SO_4)	(*209*)
	Gelidium sesquipedale	Digestion (NaOH); bleaching ($NaClO_2$)	Hydrolysis (H_2SO_4)	(*210*)
	Microdictyon tenuius	Digestion (NaOH; HCl)	Hydrolysis (HCl)	(*55*)
	Valonia macrophysa	Digestion (NaOH; HCl)	Hydrolysis (HCl)	(*195*)

Feedstock	Cellulose source	Cellulose isolation	CNC isolation	Reference
Animals	Tunicate	Extraction; bleaching ($NaClO_2$)	Hydrolysis (H_2SO_4)	(*184, 185*)
Bacterial cellulose	Komagataeibacter xylinus	Digestion (NaOH)	Hydrolysis (H_2SO_4)	(*185, 196*)
Cotton	Cotton cloth (waste)	Extraction; digestion (NaOH); bleaching (H_2O_2)	Hydrolysis (H_2SO_4, HCl)	(*186*)
	Cotton linter	None	Hydrolysis (H_2SO_4)	(*454*)
	Filter aid (ashless)	None	Hydrolysis (H_2SO_4)	(*253*)
	Filter paper	None	Hydrolysis (H_2SO_4)	(*455*)
	Mercerized cotton	None	Hydrolysis (H_2SO_4); mechanical treatment	(*456*)
Plants and grasses	Bamboo	Digestion (NaOH); bleaching ($NaClO_2$)	Hydrolysis (H_2SO_4)	(*187*)
	Elephant grass	Digestion (NaOH); bleaching (H_2O_2)	Hydrolysis (H_2SO_4)	(*188*)
	Flax	None	Hydrolysis (H_2SO_4)	(*183*)
	Hemp	Extraction; bleaching ($NaClO_2$); digestion ($NaHSO_4$; NaOH)	Hydrolysis (H_2SO_4)	(*192*)
	Jute	Digestion (NaOH); extraction	TEMPO-mediated oxidation; mechanical treatment	(*222*)
	Kenaf	Digestion (NaOH); bleaching ($NaClO_2$)	Hydrolysis (H_2SO_4)	(*175*)
	Mengkuang leaf	Digestion (NaOH); bleaching ($NaClO_2$)	Hydrolysis (H_2SO_4)	(*211*)
	Miscanthus giganteus	Digestion (NaOH); bleaching ($NaClO_2$)	Hydrolysis (H_2SO_4)	(*212*)
	Ramie	Digestion (NaOH)	Hydrolysis (H_2SO_4); mechanical treatment	(*197*)
	Sisal	Digestion (NaOH); bleaching ($NaClO_2$)	Hydrolysis (H_2SO_4)	(*213*)
	Southern cattail	Bleaching ($NaClO_2$); digestion (NaOH)	Hydrolysis (H_2SO_4)	(*220*)
	Sunflower Stalk	Digestion (NaOH); bleaching ($NaClO_2$); digestion ($NaHSO_4$; NaOH)	Hydrolysis (H_2SO_4)	(*221*)
Wood	Eucalyptus kraft pulp (bleached)	None	Hydrolysis (H_2SO_4)	(*178*)
	Microcrystalline cellulose	None	Hydrolysis (H_2SO_4)	(*173*)
	Mulberry branch bark	Digestion (NaOH; Na_2S); bleaching ($NaClO_2$)	Hydrolysis (H_2SO_4)	(*214*)
	Sawdust waste	Digestion (NaOH); bleaching ($NaClO_2$)	Hydrolysis (H_2SO_4)	(*215*)
	Softwood kraft pulp (bleached)	None	Hydrolysis (H_2SO_4)	(*172, 174*)
	Softwood sulfite pulp	None	TEMPO-mediated oxidation; hydrolysis (HCl)	(*457*)
	Spruce bark	Extraction; bleaching ($NaClO_2$)	Hydrolysis (H_2SO_4)	(*189*)

Feedstock	Cellulose source	Cellulose isolation	CNC isolation	Reference
Wood	Spruce sulfite pulp (microfibrillated)	None	Oxidation ($NaIO_4$); reduction ($NaBH_4$)	(*458*)
	Wood fibers (virgin)	None	Hydrolysis (H_2SO_4)	(*459*)

9.4. Industrial CNC production

Table A10: Industrial CNC production, current and planned. Adopted from Trache et al. (*38*), Vanderfleet and Cranston (*39*), and Moon et al. (*101*).

Company, Country	Cellulose source	CNC isolation	CNC surface	Volume /kg d^{-1}	Reference
Alberta-Pacific Forest Industries Canada	Hardwood kraft pulp, softwood kraft pulp, dissolving pulp	Hydrolysis (H_2SO_4), continuous	Sulfated	500	(*286*)
Anomera Canada	Softwood pulp	Oxidation (H_2O_2)	Carboxylated	30	(*460*)
Blue Goose Biorefineries Canada	Dissolving pulp (viscose-grade)	Oxidation, transition metal	Carboxylated	10	(*461*)
CelluForce Canada	Softwood kraft pulp (bleached)	Hydrolysis (H_2SO_4), discontinuous	Sulfated	1000	(*462*)
Cellulose Lab Canada	Dissolving pulp, commercial pulp, cotton, sisal, tunicate	Hydrolysis (H_2SO_4), discontinuous	Sulfated or derivatized	10	(*463*)
FPInnovations Canada	Chemical wood pulp (bleached)	Hydrolysis (H_2SO_4; H_3PO_4), discontinuous	Sulfated, phosphated	1.5	(*464*)
GranBio Brazil/USA	Eucalyptus chips, agricultural residues, energy crops	AVAP (American Value Added Pulping) process with ethanol and SO_2, continuous	Unmodified or lignin-coated	500	(*465*)
InnoTech Alberta Canada	Hardwood pulp (bleached), softwood pulp (bleached)	Hydrolysis (H_2SO_4), continuous and discontinuous	Sulfated	2	(*287*)
Melodea Sweden/Israel	Hardwood pulp (bleached), softwood pulp (bleached)	Hydrolysis (H_2SO_4), discontinuous	Sulfated	30 (projected)	(*466*)
USDA Forest Products Laboratory USA	Dissolving pulp	Hydrolysis (H_2SO_4), discontinuous	Sulfated	10	(*467*)